NNT : 2017SACLC056

Thèse de doctorat de l'Université Paris-Saclay préparée à CentraleSupelec

Ecole doctorale n°579
Sciences mécaniques et énergétiques, matériaux et géosciences
Spécialité de doctorat: Combustion

par

Elias Rehayem

Modélisation des turbomachines: Dérivation d'un modèle phénoménologique de combustion pour la simulation de transitoires sur hélicoptères

Thèse présentée et soutenue à Rueil-Malmaison, le 20 novembre 2017.

Composition du Jury :

M.	Denis Veynante	Directeur de recherche CNRS CentraleSupelec	(Président)
M.	Angelo Onorati	Professeur École polytechnique de Milan	(Rapporteur)
M.	Luis Le Moyne	Professeur Université de Bourgogne - ISAT	(Rapporteur)
M.	Stéphane Richard	Ingénieur de recherche Safran Helicopter Engines	(Examinateur)
M.	Olivier Colin	Ingénieur de recherche IFP Energies nouvelles	(Directeur de thèse)
M.	Alessio Dulbecco	Ingénieur de recherche IFP Energies nouvelles	(Encadrant de thèse)

à mes parents et mes soeurs,
à Virginie.

Remerciements

Je tiens à remercier Denis Veynante d'avoir présidé à mon jury de thèse, en remerciant également Angelo Onorati et Luis Le Moyne d'avoir accepté avec intérêt le rôle de rapporteurs de ce manuscrit. J'adresse de vifs remerciements à Stéphane Richard pour avoir initié ce sujet, pour m'avoir donné sa confiance par mon recrutement, puis pour avoir suivi mon travail une fois qu'il avait rejoint SAFRAN Helicopter Engines, et d'avoir été examinateur dans mon jury de thèse.

Je remercie surtout Olivier Colin, mon directeur de thèse, pour avoir partagé avec moi une partie de ses compétences en combustion, puis pour m'avoir donné ses conseils et ses avis avec son authentique franc-parler. je remercie spécialement Alessio Dulbecco, mon encadrant, qui en plus d'avoir joué son rôle scientifique avec brio, a eu une bienveillance et une disponibilité constamment exemplaires.

J'aimerais exprimer ma reconnaissance à Fabrice Le-Berr, Antonio Pires Da Cruz, Christian Angelberger et Stéphane Henriot pour m'avoir permis de faire ce travail chez IFP Energies nouvelles. Par ailleurs, plusieurs ingénieurs de la section Systèmes Moteurs et Vehicules m'ont accordé du temps en répondant à mes questions de simulation numérique et d'informatique ; je les en remercie. En particulier j'adresse un grand merci à Gregory Font, Guillaume Alix, Karine Truffin, Jörg Anderlohr, Cecile Pera, Nicolas Gillet et Anthony Velghe.

Je souhaite remercier le service combustion chez SAFRAN Helicopter Engines et en particulier l'équipe de concepteurs, d'abord pour leur accueil chaleureux et sympathique durant mon séjour d'un mois parmi eux, ensuite pour m'avoir fourni les données SGE d'un cas de secteur de brûleur aéronautique. J'adresse également mes remerciements à l'équipe de CFD et combustion du CERFACS de m'avoir donné les fichiers nécessaires pour préparer les simulations du brûleur PRECCINSTA.

Ce travail, bien que laborieux, a été facilité, et ces longues années de thèse ont paru agréables, grâce aux doctorants, post-docs et stagiaires que j'ai côtoyé à l'IFPEN. Je pense à mes voisins de bureau par vagues successives, Stavros et Betty, doyen et doyenne de ce qui fut le village d'irréductibles thésards, Benjamin, alias rouxb le geek grimpeur, Karl, avec qui nous avons maintenu une sérieuse veille technologique sur de sérieux sites comme Autotitre, Zeperfs ou encore Vroom.be. Je n'oublie pas Mamady, Salah, Benoît, Alexis et Julien pour avoir participé à tous ces débats politiquement très incorrects. Plus généralement, je reconnais que je dois beaucoup de bonne humeur à Sophie, Mickael, Lama, Federico, Valerio, Haïfa, Oguz, Damien, Jan, Carlo, Adam, Nicolas, Stéphane, Anthony, Edouard, Elefterios, Fabien, Pablo, Gorka, Mathieu et Antoine. Je souhaite également bon courage à Antoine qui a repris le flambeau en choisissant un sujet de thèse complémentaire à celui-ci.

La musique a été pour moi pendant ces années de thèse un élément dopant ou tranquilisant selon le besoin du moment. Je remercie donc les membres du groupe de rock Upstairs, François, Angela, Stéphane et Vincent, avec qui j'ai pu me changer les idées et participer à des concerts.

Mes remerciements s'adressent aussi à Yvonne, Naomi et Mia qui ont encadré les séances de débats en anglais pour les doctorants et les étudiants de l'IFP School, ce qui m'a permis de progresser à l'oral et à l'écrit.

Enfin, je remercie mes parents pour m'avoir permis d'en arriver là, mes amis qui m'ont encouragé et Virginie qui a dû supporter cette épreuve avec moi.

Résumé

Contexte

L'aéronautique a un poids économique considérable par les flux d'argent et la main d'oeuvre mis en jeu. A ce poids économique s'associe un impact environnemental non-négligeable et croissant, qui inclut une contribution à la dégradation locale de la qualité de l'air, la contribution au réchauffement climatique et aux nuisances sonores. Face à cet impact négatif, des résolutions internationales et européennes ont été adoptées. Par exemple, le plan « Flightpath 2050 » [35], annoncé par la Commission Européenne, vise à diminuer les émissions de CO_2 de 75%, les émissions de NO_x de 90% et le bruit perçu de 65% par rapport aux données des aeronefs des années 2000. Ces résolutions ont de fortes implications sur la conception des turbomachines thermiques, connues également sous le nom de turbines à gaz, qui restent le meilleur choix de motorisation pour l'aviation grâce à leur rapport poids/puissance et leur compacité.
Dans une turbine à gaz, située en amont d'un compresseur et en aval d'une turbine, la chambre de combustion ou brûleur a pour rôle de générer de l'énergie thermochimique et de la fournir à la turbine de puissance. Les constructeurs de brûleurs aéronautiques oeuvrent à en maximiser l'efficacité et la stabilisté de la combustion tout en minimisant les niveaux d'émissions polluantes, de pertes de charges, de masse et de volume tout en limitant les coûts. Ils visent aussi à optimiser plusieurs critères de performance du brûleur tels que les fonctions d'injection d'air et de carburant, d'évaporation du carburant liquide, d'allumage et de réallumage ainsi que la distribution de température à l'intérieur et à la sortie du brûleur. Ces critères mènent souvent à l'élaboration de brûleurs d'architecture complexe, comprenant un compartiment central appelé tube à flamme (TF). Le TF est alimenté en air par des trous primaires et plusieurs types de perforations et il est lié à plusieurs composants assurant respectivement l'injection de carburant, l'allumage, etc. Dans le TF, brûlent des flammes turbulentes dites de prémélange, consommant le mélange gazeux d'air et de carburant, ainsi que des flammes dites de diffusion, vers lesquelles arrivent des flux séparés d'air et de carburant. Afin d'atteindre les performances requises sur tous les critères, les concepteurs utilisent à profusion divers outils de simulation numérique tout au long des étapes de conception des moteurs.

Etat de l'art

La phase de conception du moteur débute par la définition globale du concept, dans laquelle sont décidées les caractéristiques globales de la chambre de combustion envisagée. S'en suit l'étape de pré-étude ou étude préliminaire qui consiste en un pré-dimensionnement sommaire des composants et des sous-systèmes du moteur en rapport avec des critères de performance issus des profils de missions envisagés. Les résultats de l'étape de pré-étude alimentent la dernière étape, la conception détaillée, dans laquelle se poursuit le développement détaillé et commencent les premiers essais de prototypes de brûleurs. Dans cette thèse, l'étape de conception directement concernée est l'étude préliminaire. Cette étape relève essentiellement

de l'ingénierie de performance des moteurs et fait appel à des simulations 0D et 1D basées sur des modèles mathématiques relativement simples des principaux phénomènes physiques en jeu et s'appuient sur des données expérimentales provenant de campagnes de mesures de conceptions précédentes.

Techniques de simulation en pré-étude

En pratique chez les motoristes à ce jour, selon cette approche à l'échelle 0D/1D, les modèles de brûleurs, point focal de cette thèse, sont souvent des volumes recevant un débit d'air à une certaine température et un débit de carburant caractérisé par son pouvoir calorifique inférieur (PCI) [51, 77]. Le PCI détermine le dégagement de chaleur par combustion, et serait souvent multiplié par un facteur de rendement déterminé à partir de campagnes de mesure. Cette démarche ne permet pas de modélisation prédictive de la dynamique de flamme ni de la chimie des polluants. Il existe dans la littérature des modèles d'éfficacité de combustion, qui selon [66], peuvent être exprimés de manière généralisée par :

$$\eta_{comb} = \kappa \left(\dot{m}_A\right)^{-1} \left(\frac{1}{\tau_{vap}} + \frac{1}{\tau_{mix}} + \frac{1}{\tau_{chem}} \right)^{-1} \tag{1}$$

où κ est une constante, $\dot{m}_A$ est le débit d'air, τ_{vap} est un temps caractéristique d'évaporation de carburant, τ_{mix} un temps caractéristique de mélange et τ_{chem} l'échelle temporelle chimique. Selon le poids attribué à tel ou tel terme de l'équation 1, la combustion serait pilotée par l'évaporation, le mélange ou la chimie. L'hypothèse la plus fréquemment adoptée est celle d'une combustion dominée par le temps chimique, notamment dans les modèles dits de réacteurs homogènes. Un réacteur homogène, « Well Stirred Reactor » (WSR), ou parfaitement mélangé, « Perfectly Stirred Reactor » (PSR), est défini par un volume de contrôle dans lequel le mélange est supposé parfait. Les réactions chimiques s'y déroulent donc à la même vitesse en chaque point du volume qui se caractérise alors par une température et une composition unique de fractions massiques évoluant en fonction du temps. Un réacteur à flux monodimensionel, « Plug Flow Reactor » (PFR), est un réacteur 1D stationnaire dans lequel la vitesse d'écoulement est non-négligeable suivant l'axe du réacteur et le mélange est supposé parfait radialement. La caractérisation du mélange se fait donc uniquement en fonction de la coordonnée axiale.Un projet exhaustif de simulation par approche réseau de brûleur en état stabilisé a été réalisé par [119]. Dans ce projet le TF et les veines d'air annulaires périphériques sont discrétisés par des enchaînements de WSR. Un modèle de mélange rudimentaire y a été implémenté, ainsi qu'un modèle de combustion basé sur une équation d'enthalpie libre d'équilibre et un modèle d'échanges thermiques incluant la convection, la conduction et la radiation. Le modèle développé a été validé sur plusieurs configurations aéronautiques et industrielles, donnant des résultats satisfaisants en répartitions de débits, en pertes de charge et en profils de température. Néanmoins, l'approche ne visait pas des simulations de fonctionnement en transitoire et le modèle de mélange utilisé n'était pas compatible avec les injecteurs à tourbilloneurs. Un autre modèle consistant en un assemblage de 16 PSR a été développé par[1]. Ce modèle, dans lequel les hétérogénéités ont été synthétisées à l'aide d'une fonction de distribution basée sur une loi normale [102], est dédié au calcul des émissions de polluants plutôt qu'à la dynamique de flamme.

Modèles à haute fidélité pour la conception détaillée

Dans cette phase, des calculs CFD tridimensionnels sont fortement exploités, permettant de finement reproduire les écoulements turbulents, les phénomènes aérothermochimiques, les mélanges diphasiques et les ondes aéroacoustiques. Ces calculs sont complémentaires au essais sur bancs moteurs et procurent une large panoplie de variables décrivant les phénomènes analysés, permettant une compréhension inégalée de la physique des brûleurs à flux continu.

Un calcul CFD est basé sur les équations de Navier stokes et sur la procédure de découpage du volume de calcul en un ensemble de mailles constituant le maillage. L'un des types de simulations CFD les plus utilisés en aéronautique est celui des Simulations aux Grandes Echelles (SGE), également connues sous le terme anglais « Large Eddy Simulation » (LES), dont la particularité est la résolution directe des équations de Navier-Stokes, des équations régissants les fractions massiques des espèces chimiques et de l'équation d'énergie jusqu'à une certaine échelle de longueur. En pratique, cette échelle correspond à la distance la plus petite entre deux points du maillage. Les échelles de l'écoulement qui sont de taille inférieure sont modélisées. Cette stratégie de calcul offre un bon compromis entre des résultats représentatifs et précis d'une part et un coût abordable en temps de calcul d'autre part. Un modèle de combustion souvent associé aux SGE en aéronautique est le modèle de flammes épaissies qui consiste à épaissir artificiellement la zone de flamme de manière à ce que l'épaisseur de flamme soit plus large que l'échelle minimale du maillage. Cela dispense de raffiner le maillage jusqu'aux échelles d'épaisseur de flamme laminaire, évitant ainsi de rendre le coût en temps des calculs rédhibitoire.

Stratégie de cette thèse

Dans ce travail, un modèle 0D de TF est développé avec un modèle phénoménologique de combustion, pour les simulations systèmes utilisables surtout durant une étape de conception en pré-étude de moteur aéronautique. Le modèle de TF peut représenter un TF complet tout comme il peut être assemblé en une chaîne de composants afin d'avoir une représentation discrétisée du TF. La démarche inédite consiste à s'appuyer sur des simulations à haute fidélité, habituellement utilisées en conception détaillée, afin de développer et valider le modèle 0D. En particulier, les simulations SGE sont réalisées pour analyser et décrire les flammes de brûleurs aéronautiques en faisant appel à un modèle de combustion 3D conjugué à des post-traitements spécifiques permettant une description 0D des flammes turbulentes. La stratégie s'inscrit dans une vision de modélisation qui s'applique aussi bien aux flammes de prémélange qu'aux flammes de diffusion. Cependant, cette thèse est un premier jet par lequel les flammes de prémélange sont d'abord traitées. Après le développement et la validation du modèle 0D, une analyse est réalisée sur un cas réaliste de brûleur aéronautique présentant des flammes de prémélange et de diffusion. Cette analyse permet de définir le périmètre de validité du modèle de TF développé dans cette thèse et de dégager des pistes de développement d'une extension du modèle aux flammes de diffusion.

Description du composant de tube à flamme

En simulation système par approche réseau, un TF de brûleur peut être discrétisé par plusieurs composants ou bien représenté par un seul composant, ce dernier choix étant sélectionné dans cette étude. Cependant, moyennant de légères modifications dans une étude ultérieure, une discrétisation du TF pour une modélisation plus fine. Le composant de tube à flamme est un volume ouvert ici supposé représenter une chambre de combustion complète. D'après le formalisme Bond Graph, ce volume est classé dans une catégorie dite des capacités aerothermiques (C) recevant des débits massiques et enthalpiques et renvoyant une pression statique et une température. Ce choix autorise l'incorporation ultérieure de toute la modélisation mathématique éventuellement requise pour la modélisation aérothermochimique. Le volume de TF modélise des écoulements gazeux potentiellement réactifs, ainsi que l'injection d'un carburant en phase liquide. L'information décrivant l'interaction aérothermochimique du TF avec son evironnement est échangée à travers six bornes ou ports, dont trois entrées et une sortie dédiées aux mélanges gazeux. Les douze espèces chimiques transportées sont $C_xH_yO_z$, N_2, O_2, H_2, H_2O, CO, CO_2, NO, NO_2, HC, NH_3 et les suies représentées en

tant que C. Un port est dédié à l'injection de carburant liquide et un dernier port assure les échanges thermiques à travers la paroi. Une division du volume de TF en deux zones est choisie, permettant de distinguer les gaz frais (zone UG) des gaz brûlés (zone BG). Chaque zone est occupée par un mélange de gaz parfait homogène caracterisé thermodynamiquement et est décrite par sa masse, son volume, sa composition et sa température. La pression P est supposée la même dans les zones UG et BG. L'énergie cinétique turbulente est supposée uniforme dans le volume de contrôle global V.

Caractérisation globale

Bilan de masse, densité et composition

Pour chaque espèce dans le tube à flamme, l'équation de conservation de la masse pour un système ouvert réactif est dérivée en temps sous la forme suivante :

$$\frac{dm_i}{dt} = \frac{d\left(\rho_i V\right)}{dt} = \sum_k^{in/out} \dot{m}_{i,k} + \dot{\Omega}_i \tag{2}$$

La masse globale est obtenue en faisant la somme des masses des espèces. L'indice k représente un port d'entrée ou de sortie. $\dot{\Omega}_i$ est le taux de réaction de l'espèce i. En présence d'un carburant passant de l'état liquide à l'état gazeux, le taux de carburant évaporé, $\dot{m}_F^{vap}$, est rajouté au débit massique de carburant gazeux. Le carburant liquide est isolé en tant que système thermodynamique à part entière échangeant de la masse et de l'enthalpie avec la phase gazeuse. Le taux d'évaporation s'écrit :

$$\dot{m}_F^{vap} = \frac{m_F^{liq}}{\tau} \tag{3}$$

$$\dot{m}_F^{liq} = \dot{m}_{inj,F} - \dot{m}_F^{vap} \tag{4}$$

où m_F^{liq}, variable d'état, est la masse courante de carburant liquide dans la chambre de combustion et τ est le temps caractéristique d'évaporation du carburant qui dépend de la température et qui est spécifique à chaque carburant. $\dot{m}_{inj,F}$ est le débit massique de carburant liquide injecté. A chaque pas de temps, la masse de carburant evaporé en zone UG est supposé instantanément mélangé à la phase gazeuse.
Les densités sont des variables d'état du système. Leurs dérivées sont exprimées à partir des dérivées de conservation de la masse :

$$\dot{\rho}_i = \frac{d\rho_i}{dt} = \frac{d}{dt}\left(\frac{m_i}{V}\right) \tag{5}$$

$$= \frac{\dot{m}_i V - m_i \cancel{\dot{V}}}{V^2} \tag{6}$$

$$\dot{\rho}_i = \frac{\dot{m}_i}{V} \tag{7}$$

Les fractions massiques des espèces sont calculées par $Y_i = \dfrac{\rho_i}{\rho}$.

Bilan d'énergie, température et pression

La forme différentielle du premier principe de thermodynamique est appliqué au TF, 6.12. L'énergie potentielle et l'énergie cinétique sont négligées.

$$dU = \delta Q + \delta W + \sum_k^{in/out} h_k dm_k \tag{8}$$

$$= \delta Q - PdV + \sum_k^{in/out} h_k dm_k \tag{9}$$

La dérivée temporelle s'écrit :

$$\dot{U} = \dot{Q} - P\dot{V} + \sum_{k}^{in/out} h_k \dot{m}_k \tag{10}$$

$$Q = HR + Q_{ex} \tag{11}$$

U étant l'énergie interne, h_k est l'enthalpie spécifique du mélange au port k et $\dot{m}_k$ est le débit massique port k. L'enthalpie spécifique h_i d'une espèce i est évaluée à une température donnée à partir d'une formulation polynomiale JANAF-YAWS de capacité calorifique spécifique à pression constante en fonction de la température. L'énergie calorifique Q inclut le dégagement de chaleur par la combustion, HR, et le terme Q_{ex} inclut l'éventuelle contribution de la conduction, la convection et la radiation thermiques dans des non-adiabatiques. W est le travail mécanique fourni par le système. Dans cette thèse, le TF est supposé adiabatique.

D'après l'équation 12 et l'équation 13, le bilan d'énergie 10 aboutit à l'écriture d'un bilan d'enthalpie, équation 14.

$$H = U + PV \tag{12}$$

$$dH = dU + VdP + PdV \tag{13}$$

$$\dot{H} = \dot{Q} + V\dot{P} + \sum_{k}^{in/out} h_k \dot{m}_k \tag{14}$$

La température T est la température globale du mélange gazeux présent dans le tube à flamme. Ele est calculée à partir de l'enthalpie totale et de la composition du mélange dans le TF par une procédure iterative basée sur la méthode de Newton-Raphson ; sa dérivée temporelle est utilisée pour le calcul de la dérivée de la pression. L'énergie interne s'écrit :

$$U = mu = m\int_T c_v dT = \sum_i m_i \int_T c_{v,i} dT = m\sum Y_i \int_T c_{v,i} dT \tag{15}$$

$$dU = dmu + mdu \tag{16}$$

$$\dot{U} = \dot{m}\sum_i Y_i \int_T c_{v,i} dT + m\sum_i \dot{Y}_i \int_T c_{v,i} dT + m\sum_i Y_i C_{v,i}\dot{T} \tag{17}$$

et c_v est la capacité calorifique spécifique à volume constant.
En injectant l'équation 17 dans l'équation 10 on obtient une expression de $\dot{T}$.

$$\dot{m}\int_T c_v dT + m\sum \dot{Y}_i u_i + mc_v\dot{T} = \dot{Q} - P\dot{V} + h\dot{m}|^{in} - h\dot{m}|^{out} \tag{18}$$

$$\dot{T} = \frac{\sum m_i h_i + \dot{Q} - P\dot{V} - m\sum \dot{Y}_i u_i - \dot{m}\int_T c_v dT}{mc_v} \tag{19}$$

Les fractions massiques des espèces sont dérivées selon :

$$\dot{Y}_i = \frac{d}{dt}\left(\frac{m_i}{m}\right) = \frac{\dot{m}_i}{m} - Y_i\frac{\dot{m}}{m} \tag{20}$$

L'hypothèse de gaz parfait appliquée au TF est dérivée en temps afin d'obtenir la dérivée temporelle de la pression :

$$P = \rho r T \tag{21}$$

$$\dot{P} = \rho\left(\dot{r}T + r\dot{T}\right) + rT\sum \dot{\rho}_i \tag{22}$$

La dérivée de la température $\dot{T}$ s'écrit selon l'équation 19, où r est la constante des gaz parfaits.

Caractérisation des gaz frais

Conservation de la masse, densité, composition et volume

Les ports 1, 4 et 6, dédiés aux flux gazeux, ainsi que le port 5 destiné au carburant liquide, alimentent la zone UG. Le bilan de masse dérivé temporellement, $\dot{m}_{ug,i}$, est calculé chaque espèce i dans la zone UG, permetant ainsi d'obtenir le débit total des gaz frais $\dot{m}_{ug}$ par une simple somme :

$$\frac{dm_{ug,i}}{dt} = \frac{d\left(\rho_{ug,i} V_{ug}\right)}{dt} = \sum_{k}^{in/out} \dot{m}_{k,i} - \dot{m}_{ug,i}^{\rightarrow bg} \tag{23}$$

$$\dot{m}_{ug,i}^{\rightarrow bg} = \dot{\Omega}_F \frac{m_{ug,i}}{m_{ug,F}} \tag{24}$$

$$\dot{m}_{ug} = \sum_{i} \dot{m}_{ug,i} \tag{25}$$

Avec $\sum_{k}^{in/out} \dot{m}_{k,i}$ étant la somme des débits de l'espèce i à travers les ports d'entrée et de sortie et $\dot{m}_{ug,i}^{\rightarrow bg}$ étant le taux de transfert depuis la zone UG vers la zone BG. Dans le cas d'une injection de carburant liquide, ce carburant est traité comme un système thermodynamique à part échangeant de la masse et de l'enthalpie avec the gaz frais durant l'évaporation. Le mélange des débits gazeux est supposé infiniment rapide et l'évaporation du carburant est supposée se dérouler exclusivement dans la région gaz frais.
Les densités des gaz frais sont également des variables d'état du modèle, exprimées et dérivées sous la forme suivante :

$$\rho_{ug,i} = \frac{m_{ug,i}}{V_{ug}} \tag{26}$$

$$\dot{\rho}_{ug,i} = \frac{\dot{m}_{ug,i} V_{ug} - m_{ug,i} \dot{V}_{ug}}{V_{ug}^2} = \frac{\dot{m}_{ug,i}}{V_{ug}} - \rho_{ug,i} \frac{\dot{V}_{ug}}{V_{ug}} \tag{27}$$

De cela découle l'expression des fractions massiques des gaz frais :

$$Y_{ug,i} = \frac{\rho_{ug,i}}{\rho_{ug}} \tag{28}$$

Le volume UG est également dérivé en temps sur la base de la relation $V_{ug} = \frac{m_{ug}}{\rho_{ug}}$, donnant :

$$\frac{dV_{ug}}{dt} = \frac{d}{dt}\left(\frac{mrT}{P}\right)_{ug} \tag{29}$$

$$= \frac{1}{P}\left(\dot{m}rT + m\dot{r}T + mr\dot{T}\right)_{ug} - \frac{\dot{P}}{P} V_{ug} \tag{30}$$

$$\dot{V}_{ug} = V_{ug}\left(\frac{\dot{m}_{ug}}{m_{ug}} + \frac{\dot{r}_{ug}}{r_{ug}} + \frac{\dot{T}_{ug}}{T_{ug}} - \frac{\dot{P}}{P}\right) \tag{31}$$

Conervation de l'énergie, température et pression

L'équation-bilan d'énergie pour système ouvert, equation 14, est appliquée à la région UG :

$$\dot{H}_{ug} = \dot{Q}_{ug} + V_{ug}\dot{P} + \sum_{k}^{in/out} h\dot{m}_{ug,k} - h\dot{m}_{ug}^{\rightarrow bg} \tag{32}$$

avec

$$\delta Q_{ug} = \delta Q \frac{V_{ug}}{V} \tag{33}$$

$$V_{ug} \ll V \tag{34}$$

$$\delta Q_{ug} \simeq 0 \tag{35}$$

Le terme $\sum_{k}^{in/out} h\dot{m}_{ug,k}$ représente le bilan des flux d'enthalpie passant à travers les ports d'entrée et de sortie, et $h\dot{m}_{ug}^{\rightarrow bg}$ est le débit enthalpique transféré des gaz frais vers les gaz brûlés. La température du mélange frais et sa dérivée sont calculés à partir de l'enthalpie totale et la composition du mélange UG par une procédure itérative basée sur la méthode de Newton-Raphson. D'après l'hypothèse d' homogénéité de la pression dans le TF, la dérivée temporelle de la pression est donnée par l'équation 22.

Caractérisation des gaz brûlés

Conservation de la masse,densité, composition et volume

Le volume BG, V_{bg}, est calculé en soustrayant le volume UG du volume total de la chambre de combustion et la masse BG est déduite de la masse globale et de la masse UG :

$$V_{bg} = V - V_{ug} \tag{36}$$

$$m_{bg,i} = m_i - m_{ug,i} \tag{37}$$

$$m_{bg} = \sum m_{bg,i} \tag{38}$$

Par conséquent, la densité en BG et la composition peuvent être directement calculées.

Bilan d'énergie, température et pression

L'enthalpie spécifique en BG est calculée à partir des enthalpies globale et UG :

$$h_{bg} = \frac{(H - H_{ug})}{m_{bg}} \tag{39}$$

La procédure iterative de Newton-Raphson est à nouveau utilisée pour le calcul de T_{bg} :

$$T_{bg} = f^{-1}\left(h_{bg}\right) \tag{40}$$

En accord avec le formalisme CFM, la pression est supposée identique dans les zones UG et BG.

Description de la combustion

En première approche, un schéma global à une réaction, proposé par [100], est utilisé pour synthétiser la réaction de combustion :

$$\begin{aligned} &\alpha_1 \left(C_x H_y O_z + \left(x + \frac{y}{4} - \frac{z}{2} \right) O_2 \longrightarrow x CO_2 + \frac{y}{2} H_2 O \right) \\ &+ (1 - \alpha_1) \left(C_x H_y O_z + \frac{x - z}{2} O_2 \longrightarrow x CO + \frac{y}{2} H_2 \right) \end{aligned} \tag{41}$$

avec α_1 défini d'après un bilan atomique de C, H et O, tel que :

$$\alpha_1 = \frac{\left(0.98\left(4x + y - 2z\right)/\phi - 2(x - z)\right)}{2x + y} \tag{42}$$

et ϕ la richesse donnée par :

$$\phi = \left(\frac{Y_F}{Y_A}\right)\left(\frac{Y_A}{Y_F}\right)_{st} \tag{43}$$

Y_F et Y_A sont les fractions massiques respectives de carburant et d'air, et l'indice st fait référence au cas stochiométrique. Le taux de réaction d'une espèce i, $\dot{\Omega}_i$, s'écrit :

$$\dot{\Omega}_i = \upsilon_i \frac{M_i}{M_F}\dot{\Omega}_F \tag{44}$$

$\dot{\Omega}_F$ est le taux de consommation de carburant, M_i est la masse molaire de l'espèce i et υ_i est son coefficient stoichiométrique dans l'équation-bilan 41.

Le taux de consommation de carburant $\dot{\Omega}_F$ s'exprime sous la forme suivante :

$$\dot{\Omega}_F = \rho_{ug} Y_{ug,F} S_L A_m \Xi \tag{45}$$

avec ρ_{ug} la densité UG, $Y_{ug,F}$ étant la fraction massique du carburant frais, S_L est la vitesse de flamme laminaire, A_m est la surface de flamme moyenne et Ξ est le facteur de plissement, défini par $\Xi = \dfrac{A_T}{A_m}$. Dans l'équation 45, la densité de carburant frais est déterminée par une résolution directe des équations 0D régissant les gaz frais. Les termes de surface, de plissement et de vitesse, liés à la topologie de la flamme et à sa dynamique, doivent être modélisés par des équations supplémentaires.

Fermeture du modèle de combustion 0D à l'aide de la simulation aux grandes échelles

Conformément aux pratiques courantes en conception détaillée des brûleurs aéronautiques, dans ce travail, les calculs SGE sont utilisés avec le modèle de flamme localement épaissie DTFLES [33, 69]. Ce modèle fait appel à un calcul du taux de réaction selon des lois d'Arrhénius, munies de l'épaississement localisé aux régions dans lesquelles un taux de réaction est détecté. Pas de variable d'avancement n'est donc requise contrairement au formalisme CFM, ni de vitesse de flamme laminaire. Afin de pouvoir analyser la flamme selon l'approche CFM, un conditionnement de variables telles que la température et la densité doit être fait aux gaz frais et aux gaz brûlés, et des variables doivent être reconstituées, telles que la vitesse globale de consommation de carburant, la surface de flamme et son facteur de plissement. Cette construction mathématique des variables de caractérisation de la flamme selon le formalisme CFM, présentée dans ce qui suit, a été incorporée aux sources de code du logiciel AVBP. Ensuite, des données de simulation nous on été gracieusement fournies par le CERFACS, correspondant à un brûleur expérimental de flamme prémélangée à pression atmosphérique nommé PRECCINSTA. Le montage consiste en un tourbilloneur recevant du méthane d'un côté et de l'air de l'autre, débitant le mélange air et carburant dans une chambre de section carrée. Ce montage expérimental a fait l'objet de campagnes de mesures [80] et de plusieurs simulations numériques [26, 62, 109, 114, 128]. Les paramètres numériques du cas de simulation ont été optimisés et un point de fonctionnement de référence a été calculé, permettant ainsi une vérification des résultats en les comparant à des résultats expérimentaux de la littérature [80]. Suite à cette vérification, des variations monoparamétriques de débit d'entrée, de richesse, de température de gaz frais et de pression de sortie ont été simulées par calculs SGE. Ces variations sont détaillées au chapitre 5. Les résultats de ces simulations ont servi à caractériser la réponse de la flamme turbulente de prémélange aux variations de conditions opératoires. Dans ce qui suit, pour chaque variable présentant un intérêt pour le développement 0D, son calcul dans l'espace 3D SGE est présenté, puis sa modélisation réduite en 0D est détaillée.

Surface moyenne de flamme

Dans les simulations DTFLES, l'identification d'un volume UG et la définition d'une surface moyenne de flamme et d'une surface totale, FIGURE 1, reposent sur la construction d'une variable d'avancement de combustion ou de progrès, $\tilde{c}$, calculée par ce qui suit :

$$\tilde{c}\left(\vec{x},t\right) = 1 - \frac{Y_F\left(\vec{x},t\right)}{Y_{ug,F}\left(\vec{x},t\right)} \tag{46}$$

$$Y_{F,ug}\left(\vec{x},t\right) = Z_C + Z_H \tag{47}$$

$$Z_C = M_C \sum \frac{n_{C,k} Y_k}{M_k} \tag{48}$$

$$Z_H = M_H \sum \frac{n_{H,k} Y_k}{M_k} \tag{49}$$

avec $Y_F\left(\vec{x},t\right)$ étant la fraction massique de carburant à une position donnée et un instant donné et $Y_{ug,F}$ est la fraction massique de carburant dans les gaz frais. Z_C et Z_H sont les fractions de mélange de carbone et d'hydrogène, obtenus par des bilans atomiques. En

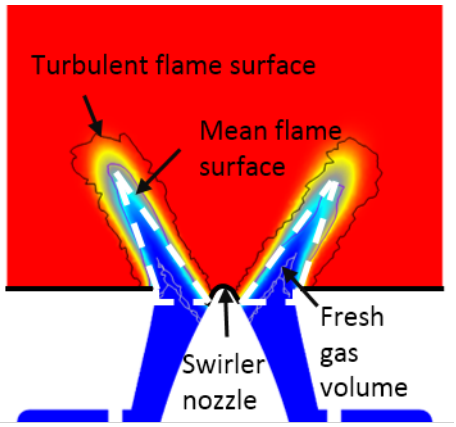

FIGURE 1 – Volume de gaz frais, surfaces de flamme moyenne et turbulente.

calculant la moyenne temporelle de $\tilde{c}$, $\langle\tilde{c}\left(\vec{x}\right)\rangle$ on peut approximer la surface moyenne A_m par l'expression suivante :

$$\langle\tilde{c}(\vec{x})\rangle = \frac{1}{\tau}\int_\tau \tilde{c}\left(\vec{x},t\right) dt \tag{50}$$

$$A_m = \int_V |\nabla\langle\tilde{c}\left(\vec{x}\right)\rangle| dV \tag{51}$$

Le volume UG est obtenu par l'intégrale suivante :

$$V_{ug} = \int_V \left(1 - \langle\tilde{c}\left(\vec{x}\right)\rangle\right) dV \tag{52}$$

Dans l'espace 0D, d'après le formalisme CFM, la surface moyenne de flamme est liée au volume UG qui est défini comme étant le volume enveloppé par la flamme d'une part et délimité par la paroi de la chambre de combustion d'autre part. Une modélisation de cette surface moyenne par approche géométrique a d'abord été investiguée. En effet, la surface de flamme est assimilée à un double-cône tronqué, FIGURE 2. Cela conduit à l'expression de la surface A_m et du volume UG en fonction des paramètres géométriques de l'entrée du brûleur et de la longueur de pénétration de la flamme.

Une autre méthode, de type semi-empirique, a aussi été envisagée et consiste à chercher une corrélation entre la surface moyenne normalisée de flamme et le volume normalisé de

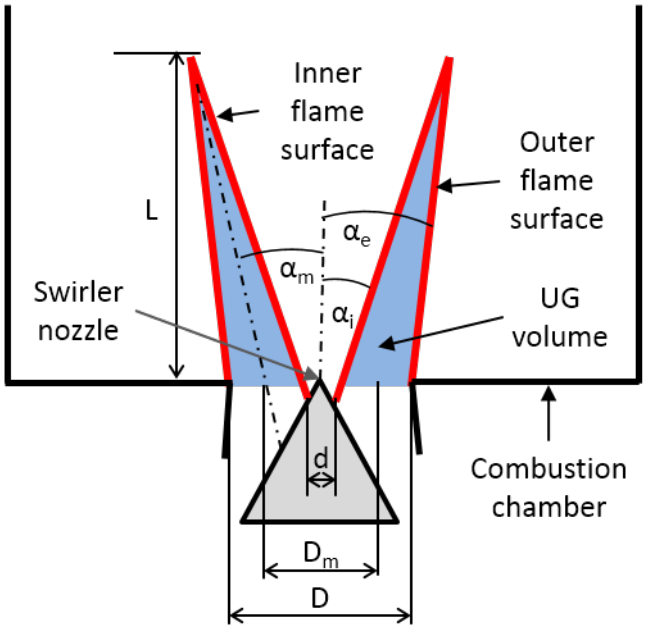

FIGURE 2 – Flamme en M du brûleur PRECCINSTA représentée par un double cône tronqué. D est le diamètre du tourbilloneur, d est le diamètre de la flamme autour du tourbilloneur au point d'ancrage, L est la hauteur de flamme, α_i et α_e sont respectivement les angles interne et externe formés par la flamme avec la verticale, et α_m est l'angle moyen.

gaz frais, pour plusieurs réalisations qui correspondent à des calculs SGE paramétriques qui seront décrits par la suite.

$$A_m = A_{m,0} \cdot a_m\,(v) \tag{53}$$

$$v_{ug} = \frac{V_{ug}}{V_{ug,0}} \tag{54}$$

où a_m est une fonction du volume UG normalisé, v_{ug}. Une dépendance linéaire, f_1, est identifiée entre V_{ug} et A_m d'après les résultats SGE, FIGURE 3, en excluant le point correspondant au cas le plus riche dans lequel la zone d'expansion thermique des gaz frais préchauffés semble particulièrement impacter le calcul du volume de gaz frais. Ainsi, pour $V_{ug} < 2V_{ug,0}$, a_m peut s'écrire sous la forme suivante :

$$f_1 : a_m = 0.903 v_{ug} + 0.034 \tag{55}$$

La comparaison des deux méthodes aux résultats SGE montre que la corrélation semi-empirique serait plus fidèle aux résultats SGE et semble mieux correspondre à la forme moyenne de la flamme étudiée. La corrélation a donc été choisie pour modéliser la surface moyenne de flamme.

Vitesse de flamme laminaire

Destinée à un usage dans un modèle 0D, la vitesse de flamme laminaire, S_L, n'est autre que la vitesse globale de consommation de carburant. Dans un calcul SGE dans l'espace tridimensionnel, le taux d'oxydation global du carburant s'écrit :

$$\dot{\Omega}_F = -\int_V \dot{\omega}_F dV \tag{56}$$

$$\dot{\omega}_F = M_F \dot{\omega}_F^{mol} \tag{57}$$

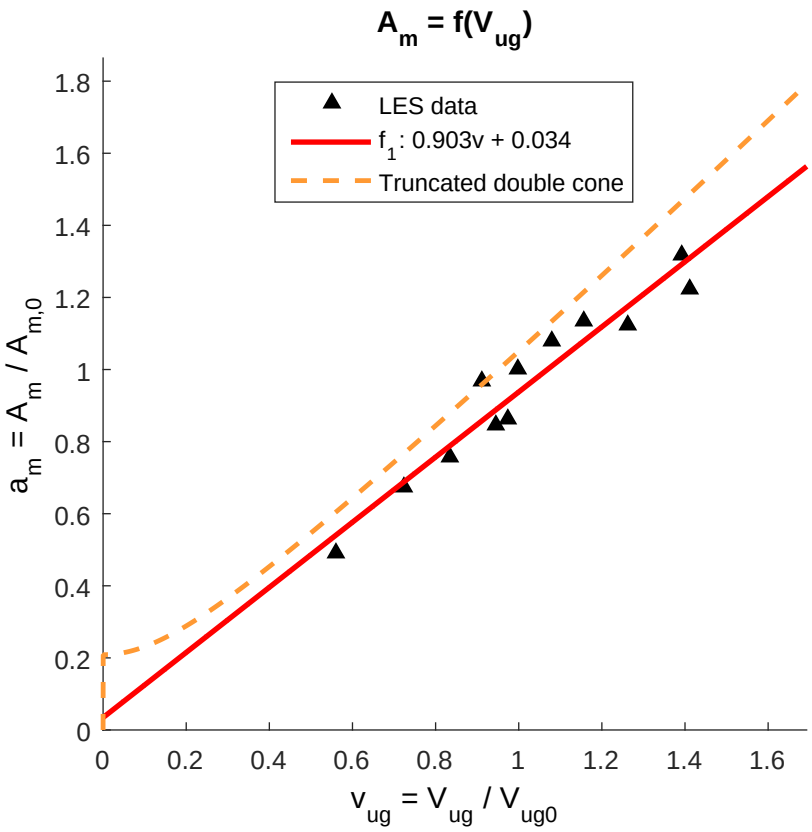

FIGURE 3 – Variation de a_m en fonction de v_{ug} ; comparaison entre les résultats SGE, la corrélation linéaire f_1 et le modèle géométrique de double cône tronqué.

où M_F est la masse molaire du carburant F et $\dot{\omega}_F^{mol}$ est son taux de réaction molaire par unité de volume.
Etant donné que pour une situation de combustion donnée, un formalisme CFM et un formalisme TFLES donnent le même taux global de réaction, en SGE DTFLES, $\dot{\Omega}_F$ peut s'écrire sous la forme suivante :

$$\dot{\Omega}_F(t) = \rho_{ug,F} S_L^{SGE}(t) A_T(t) \tag{58}$$
$$\tag{59}$$

et A_T désigne la surface totale de flamme, qui s'écrit :

$$A_T(t) = \int_V \Xi_{sgs}\left(\vec{x},t\right) \left|\nabla \tilde{c}\left(\vec{x},t\right)\right| dV \tag{60}$$

avec Ξ_{sgs} étant une fonction d'efficacité modélisant le plissement de sous-maille [33] et premettant de compenser le lissage de la surface de flamme artificiellement causé par l'épaississement. S_L^{SGE} est donc égale à $\dfrac{\dot{\Omega}_F}{\rho_{ug,F} A_T}$.

Pour proposer un modèle 0D de vitesse de flamme laminaire, on part du principe que pendant la combustion d'un carburant pleinement évaporé et prémélangé avec l'air, S_L dépend de la richesse, de la pression et de la température du prémélange : $S_L = S_L(\phi, T, P)$. Les valeurs de S_L obtenues par calcul SGE, S_L^{SGE}, s'écartent des vitesses de flamme laminaire calculées à partir de corrélations issues de la littérature. Ces écarts seraient en partie dûs à des effets de courbure ou d'étirement qui ne seraient pas pris en compte par la fonction de plissement de sous-maille en SGE. Il a été démontré qu'une contribution mineure à ces écart provient du procédé d'épaississement de la flamme en SGE et de l'application d'un terme de viscosité numérique afin d'atténuer les instabilités numériques. Pour pallier à ces écarts, une normalisation autour du point de fonctionnement moyen du brûleur, dont les variables correspondantes sont désignées par l'indice 0, a été réalisée sous la forme suivante :

$$S_L = \frac{S_{L,0}^{SGE}}{S_{L,0}^{0D}\left(\phi, T_{ug}, P\right)} S_L^{0D}\left(\phi, T_{ug}, P\right) \tag{61}$$

Pour la flamme de méthane, une corrélation par Metghalchi& Keck [82] est sélectionnée.

$$S_L\left(\phi, T_{ug}, P\right) = a_1 \left[1 + a_2\left(\phi - 1\right) + a_3\left(\phi - 1\right)^2\right] \left(\frac{T_{ug}}{T_{ug,ref}}\right)^{b_1} \left(\frac{P}{P_{ref}}\right)^{b_2} \tag{62}$$

a_i et b_i sont des constantes, $T_{ug,ref}$ et P_{ref} sont respectivement une température et une pression de référence [82]. Cette corrélation a été expérimentalement validée pour :

$$298K < T_{ug} < 650K,\ 1 < P < 40bar,\ 0.8 < \phi < 1.2$$

Il est important de préciser que des modèles de vitesses de flammes existent pour des cas de propagation à travers des mélanges dans lesquels le carburant est présent sous forme d'une combinaison de phases gazeuse et liquide en gouttelettes[68]. De tels modèles seraient intéressants pour traiter des cas réalistes de brûleurs aéronautiques dans lesquels le carburant est injecté à l'état liquide.

Plissement de surface de flamme

En SGE, le plissement de surface de flamme est le rapport entre la moyenne temporelle de la surface totale et la surface moyenne de flamme :

$$\langle \Xi^{SGE} \rangle = \frac{\langle A_T \rangle}{A_m} \tag{63}$$

Dans le formalisme CFM, la flamme turbulente prémélangée est supposée présenter une topologie dite de flammelettes minces plissées infiniment minces par rapport à toutes les structures de l'écoulement. Le plissement de la surface de flamme, quantitativement inclu dans le taux de consommation de carburant, se doit d'être mis en équation. Plusieurs corrélations de plissement de surface de flamme issues de la littérature sont testées, dont quatre sont retenues et comparées aux résultats obtenus par simulations SGE. Il s'agit des modèles de Clavin et Williams [32], de Ballal et Lefebvre [68], Bradley [17] et le modèle « Intermittent Turbulence Net flamme Stretch Model » (ITNFS) [28, 29, 81]. Ces quatre modèles sont respectivement formulés par ce qui suit.

$$\Xi_{Clavin-Williams} = \sqrt{0.5\left(1+\sqrt{1+8C\left(\frac{u'}{S_L}\right)^2}\right)} \tag{64}$$

$$\Xi_{Ballal-Lefebvre} = \sqrt{1+0.003\left(\frac{u' l_T}{S_L \delta_L}\right)^2} \tag{65}$$

$$\Xi_{Bradley} = 1+\frac{0.95}{Le}\sqrt{\frac{l_T}{\delta_L}\frac{u'}{S_L}} \tag{66}$$

$$\Xi_{ITNFS} = 1+\frac{2}{S_L}\sqrt{\Gamma_e \nu_T} \tag{67}$$

avec ν_T étant la viscosité cinématique turbulente, calculée à partir de l'échelle intégrale l_T et de l'énergie cinétique turbulente, elle-même issue de u'. Ces quatre modèles de plissement font intervenir les rapports d'échelles spatiales respectives de turblence, l_T, et d'épaisseur de flamme laminaire, δ_L, ainsi que les rapports de vitesses turbulente, u', et de flamme laminaire, S_L. L'effet des propriétés thermo-diffusives du mélange est également pris en compte à travers le nombre de Lewis, Le, qui est cependant supposé unitaire dans cette thèse conformément à une hypothèse de diffusivité thermique égale à la diffusivité massique. Le calcul des grandeurs δ_L, l_T et u' s'impose donc d'abord en simulation SGE.
L'épaisseur de flamme laminaire (épaisseur thermo-diffusive δ_L^0) contribue à la description de la structure d'une flamme prémélangée et se retrouve dans l'analyse théorique de la combustion turbulente [28, 81]. La corrélation de Blint [9], jugée suffisamment représentative et aussi bien valable dans un post-traitement de résultats SGE DTFLES que dans un modèle 0D CFM, est choisie dans cette étude en SGE et dans le modèle de TF :

$$\delta_L = \frac{2\lambda_{ug}}{\rho_{ug} c_{p_{ug}} S_L}\left(\frac{T_{bg}}{T_{ug}}\right)^{0.7} \tag{68}$$

avec λ_{ug} étant la conductivité thermique du mélange de gaz frais et $c_{p_{ug}}$ en est la capacité calorifique à pression constante.

Intensité turbulente et échelle intégrale

Les fluctuations turbulentes de vitesse suivant chaque direction spatiale i sont calculées en SGE et conditionnées à la zone de flamme d'une part, et à la zone UG d'autre part :

$$u'^2_{flamme,i} = \frac{1}{A_m}\int_V |\nabla\langle\tilde{c}\,(\vec{x})\rangle|\left(\langle\tilde{U}_i^2(\vec{x})\rangle - \langle\tilde{U}_i(\vec{x})\rangle^2\right) dV \tag{69}$$

$$u'^2_{ug,i} = \frac{1}{V_{ug}}\int_V (1-\langle\tilde{c}\,(\vec{x})\rangle)\left(\langle\tilde{U}_i^2(\vec{x})\rangle - \langle\tilde{U}_i(\vec{x})\rangle^2\right) dV \tag{70}$$

L'impact des structures de l'écoulement turbulent sur le plissement de flamme est supposé approximativement similaire à celui qu'aurait un champ de Turbulence Homogène Isotrope

(THI). La vitesse turbulent au sein d'un tel champs est calculée à partir de l'énergie cinétique turbulente k, d'après les relations suivantes :

$$k_{ug} = \frac{1}{2}\sum_i u'^2_{ug,i},\ k_{flamme} = \frac{1}{2}\sum u'^2_{flamme,i} \tag{71}$$

$$u'_{ug,THI} = \sqrt{\frac{2k_{ug}}{3}},\ u'_{flamme,THI} = \sqrt{\frac{2k_{flamme}}{3}} \tag{72}$$

Les différentes valeurs des vitesses $u'_{ug,THI}$ et $u'_{flamme,THI}$ s'avèrent assez proches sur tous les cas des variations paramétriques. Par conséquent, $u'_{ug,THI}$ est choisie pour contribuer au calcul de Ξ en 0D.

Bien que la pression soit supposée homogène dans les zones UG et BG, d'après ce qui est observé en Figure 5.34, les fluctuations de vitesses turbulentes sont linéairement corrélées à la perte de charge relative, $\dfrac{\Delta P_t}{P_{ug,t}}$, avec P_t étant la pression totale. En effet, d'après Figure 5.33, l'intensité turbulente dans les gaz frais est modélisée par :

$$\left.\frac{u'}{u'_0}\right|_{ug} = 0.56\left(\frac{\Delta P_t}{\Delta P_{ug,t}}\right)\left(\frac{P_{ug,t}}{\Delta P_t}\right)_0 + 0.56 \tag{73}$$

où $\left.\dfrac{u'}{u'_0}\right|_{ug}$ est l'intensité turbulente UG normalisée par sa valeur au point moyen et $\left(\dfrac{\Delta P_t}{P_{ug,t}}\right)_0$ est la valeur au point moyen de la perte de charge relative dans la base de résultats SGE. La perte de charge aérodynamique [68] est exprimée par :

$$\frac{\Delta P_t}{P_{ug,t}} = \alpha\frac{r_{ug}}{2}\left(\frac{\dot{m}_{ug}\sqrt{T_{ug}}}{A_{tube}P_{ug,t}}\right)^2 \tag{74}$$

où $\dfrac{\dot{m}_{ug}\sqrt{T_{ug}}}{P_{ug,t}}$ est le débit corrigé, α est une constante et A_{tube} est une section caractéristique du TF, ici égale à la section de la chambre PRECCINSTA. Dans le modèle 0D, cette perte de charge aérodynamique est donc calculée par la relation 74, et u' par la relation 73.

D'après [50], pour une géométrie donnée, l'échelle intégrale, l_T, ne varierait pas en fonction des conditions opératoires. Dans le cas du brûleur PRECCINSTA, l'échelle intégrale est supposée égale au diamètre contournant la pointe du tourbilloneur au point d'ancrage de la flamme, qui vaut en l'occurrence 7mm.

Suite au calcul de δ_L, l_T et u' par post-traitement des résultats des SGE, chaque modèle $\hat{\Xi}_j$ a été ajusté par une constante κ_j, Table 1, afin de donner des résultats du même ordre de grandeur que le plissement $\langle\Xi_0^{SGE}\rangle$ calculé pour le point moyen du cas PRECCINSTA, equation 75.

$$\Xi_0 = 1 + \kappa_j\left(\hat{\Xi}_j - 1\right) \tag{75}$$

Table 1 – Coefficients d'ajustement des différents modèles de plissement testés.

Model	Ballal & Lefebvre	Bradley	Clavin & Williams	ITNFS
κ_j	0.25	0.2	0.84	0.35

Après l'ajustement, le modèle de Bradley semble capturer le mieux les allures observées dans les résultats SGE. Ce modèle a donc été retenu.

Validation du modèle de tube à flamme

Le modèle 0D de tube à flamme est validé en comparant les résultats de simulations système du brûleur PRECCINSTA aux résultats des calculs SGE. Les simulations sont réalisés avec l'environnement LMS Imagine.Lab Amesim, doté d'un solveur à pas de temps variable. Le composant de TF est connecté à une source injectant un mélange d'air et de méthane, permettant de contrôler le débit, la température et la richesse. La sortie du TF est reliée à un tuyau d'échappement convergent avec un rapport de section entrée/sortie de 6/1 et au bout duquel la pression de sortie est imposée. Le TF est considéré comme adiabatique. Les sept epsèces chimiques en jeu sont CH_4, O_2, N_2, CO, CO_2, H_2 et H_2O. Quatre simulations sont réalisées. Dans chacune de ces simulations un paramètre du système varie au cours du temps. Les paramètres sont le débit d'entrée $\dot{m}_{in}$, la richesse ϕ, la température des gaz frais T_{ug} et la pression de sortie P_{out}. Dans ce résumé, quelques résultats sont présentés et correspondent aux cas de validation faisant varier $\dot{m}_{in}$ et P_{out}. Les résultats complets sont détaillés dans le chapitre 6.

Variation du débit d'entrée

Dans cette simulation, le débit $\dot{m}_{in}$ est augmenté de 7.4g/s jusqu'à 13.4g/s en trois étapes durant au total sept secondes, Figure 4. La richesse des gaz frais est de 0.83, leur température T_{ug} est de 320K et la pression de sortie est 1 atm.

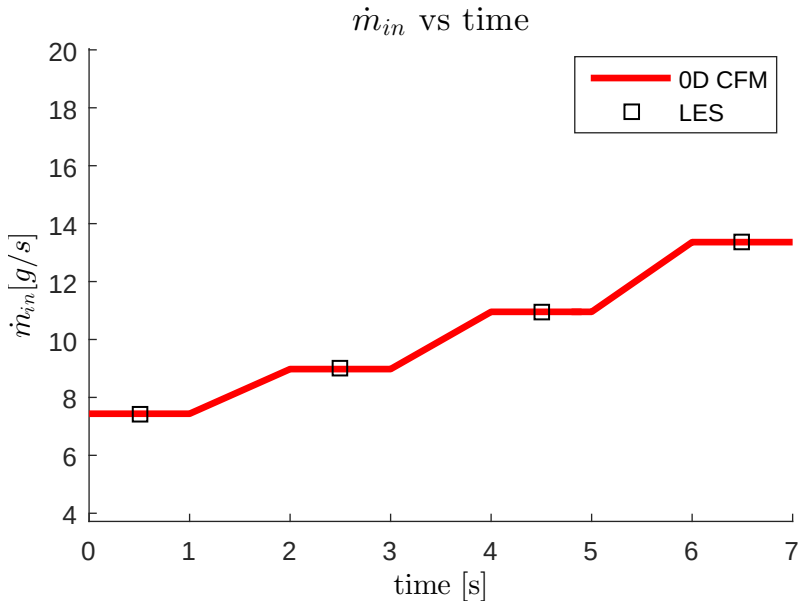

Figure 4 – Variation temporelle du débit d'entrée $\dot{m}_{in}$.

Les volumes de gaz frais prédits par la simulation système concordent bien avec les résultats SGE, Figure 6.11, figure de gauche, ce qui conduit à une bonne prédiction de A_m en fonction de $\dot{m}_{in}$.

Globalement, l'augmentation du débit de 81% entraîne une augmentation de u' en zone UG, tableau 6.3a. Le tableau 6.3b récapitule les variations des grandeurs décrivant la dynamique de flamme. En effet, ni la vitesse ni l'épaisseur de flamme n'augmentent dans le modèle 0D, ce qui est prévisible du fait que la richesse, la température et la pression ne varient pas. L'augmentation de u' engendre naturellement une augmentation de Ξ. Les fluctuations de vitesse turbulente obtenues par le modèle 0D à bas débit diffèrent légèrement de celles calculées en 3D, n'empêchant pas toutefois de maintenir un écart acceptable sur le plissement, Figure 6.

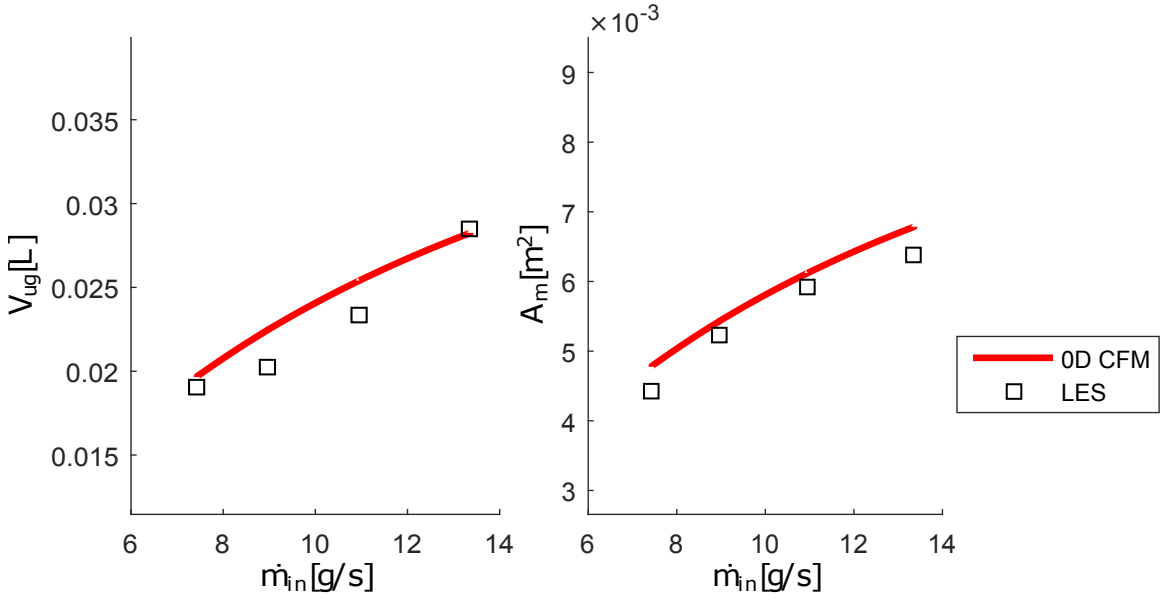

FIGURE 5 – Variation de V_{ug} (gauche) et de A_m (droite) avec le débit d'entrée $\dot{m}_{in}$.

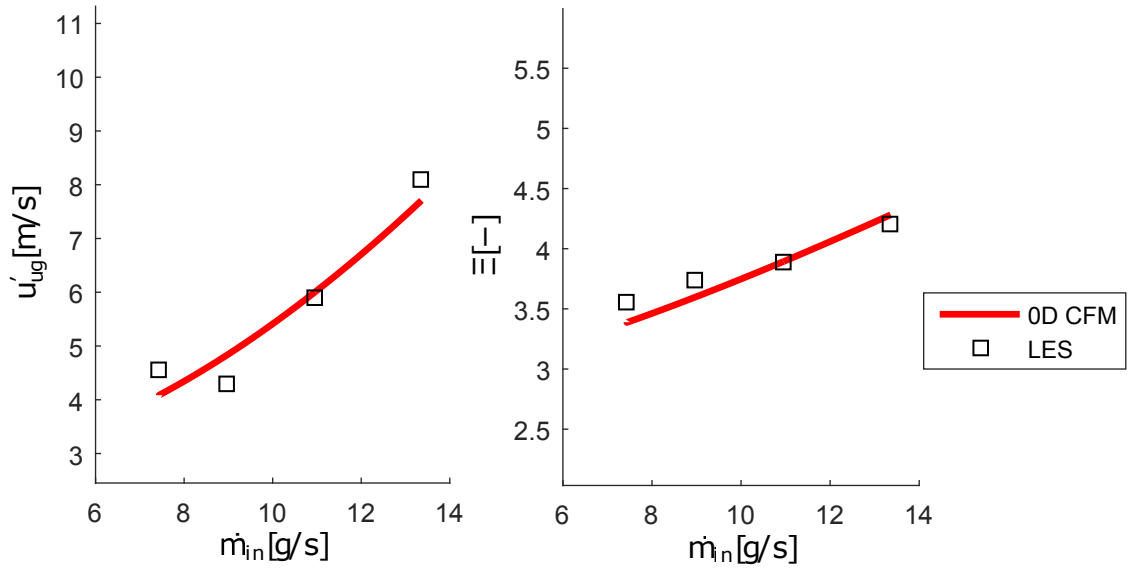

FIGURE 6 – Variation de u'_{ug} (gauche) et de Ξ (droite) avec le débit d'entrée $\dot{m}_{in}$.

TABLE 2 – Réponse dynamique de la zone UG et de la flamme à des variations de débit d'entrée. Symboles : $=$: constante ; $\simeq$: variations négligeables ; $\uparrow$: augmentation ; $\downarrow$: diminution.

ρ_{ug}	$Y_{ug,F}$	T_{ug}	P_{ug}	u'_{ug}
$=$	$=$	$=$	$\simeq$	$\uparrow 89\%$

(a) Bilan des variations en zone UG.

S_L	δ_L	A_m	Ξ	$\dot{\Omega}_F$
$\simeq$	$\simeq$	$\uparrow 41.8\%$	$\uparrow 27.5\%$	$\uparrow 81\%$

(b) Variables de dynamique de flamme.

La réponse du TF à des augmentations de débit est conforme à la physique et en accord avec ce qui est observé en simulations à haute fidélité.

Variation de la pression statique de sortie

La pression P_{out} est augmentée par paliers de 1bar à 3bar en cinq secondes, FIGURE 7. La chambre est alimentée par un débit $\dot{m}_{in} = 8.98g/s$ à une température $T_{ug} = 320K$ et d'une richesse $\phi = 0.83$.

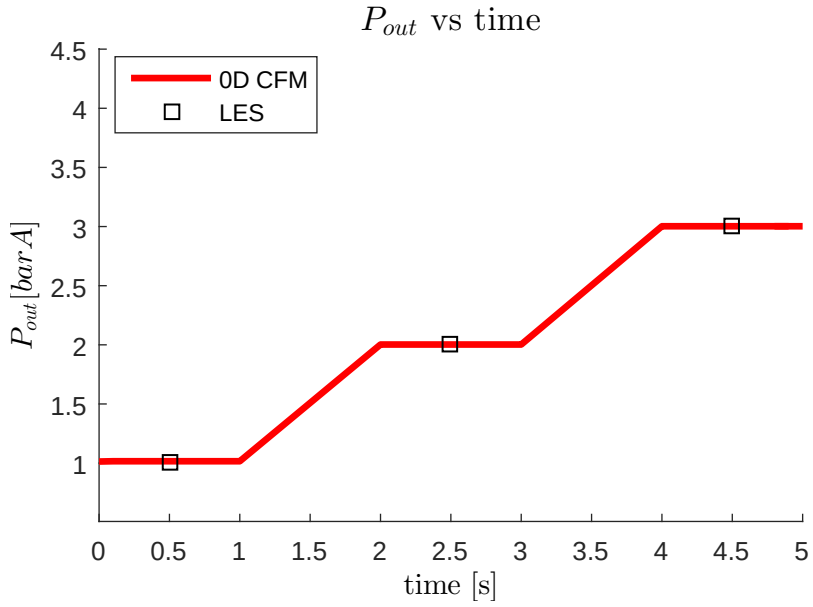

FIGURE 7 – Variation temporelle de la pression statique de sortie P_{out}.

La figure FIGURE 8 montre à gauche une concordance acceptable entre les volumes UG 0D et SGE (LES) malgré une tendance de décroissance plus prononcée avec le modèle 0D. Sur cette même figure, la surface moyenne de flamme calculée en 0D est sensiblement égale à celle obtenue par les SGE. Les vitesses turbulentes en 0D et en 3D ne sont pas exactement identiques à 1bar et à 2bar mais convergent vers le même niveau à 3bar, FIGURE 9 à gauche. Le plissement de surface de flamme dans le modèle 0D de TF présente des valeurs et une allure globalement en accord avec les résultats SGE, FIGURE 9 à droite.

Quant à la vitesse et à l'épaisseur de flamme laminaire, FIGURE 10, la concordance entre les résultats 0D CFM et SGE DTFLES s'avère satisfaisante. La montée en pression imposée au TF réduit le volume UG, ce qui augmente la densité des gaz frais et ralentit l'écoulement, se traduisant par une chute de l'intensité turbulente d'environ 44%, tableau 3a.

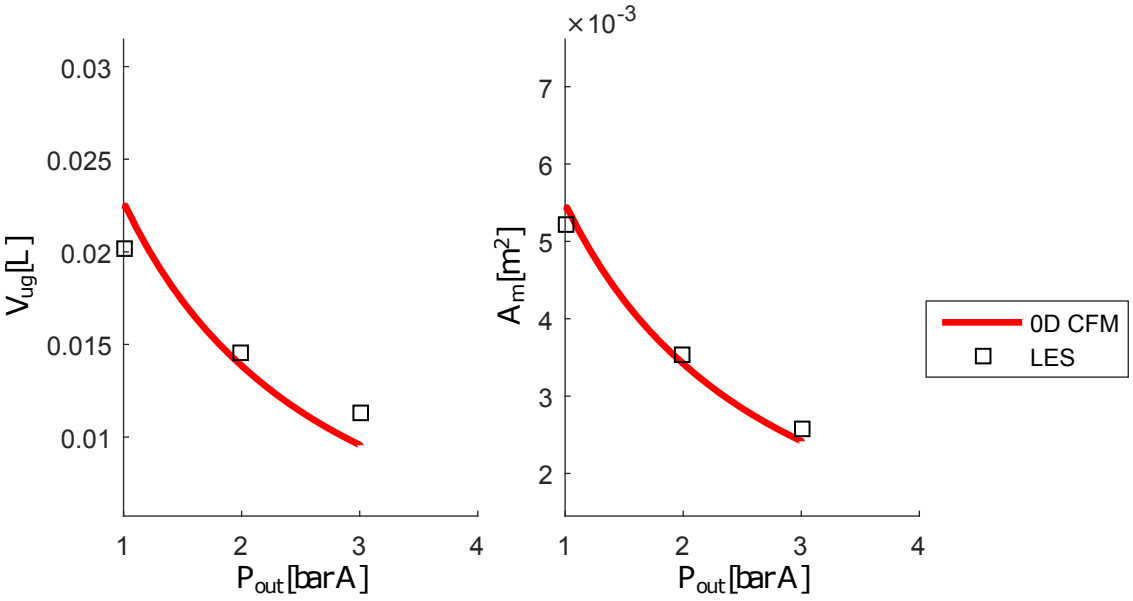

FIGURE 8 – Variation de V_{ug} et de A_m avec la pression statique de sortie P_{out}.

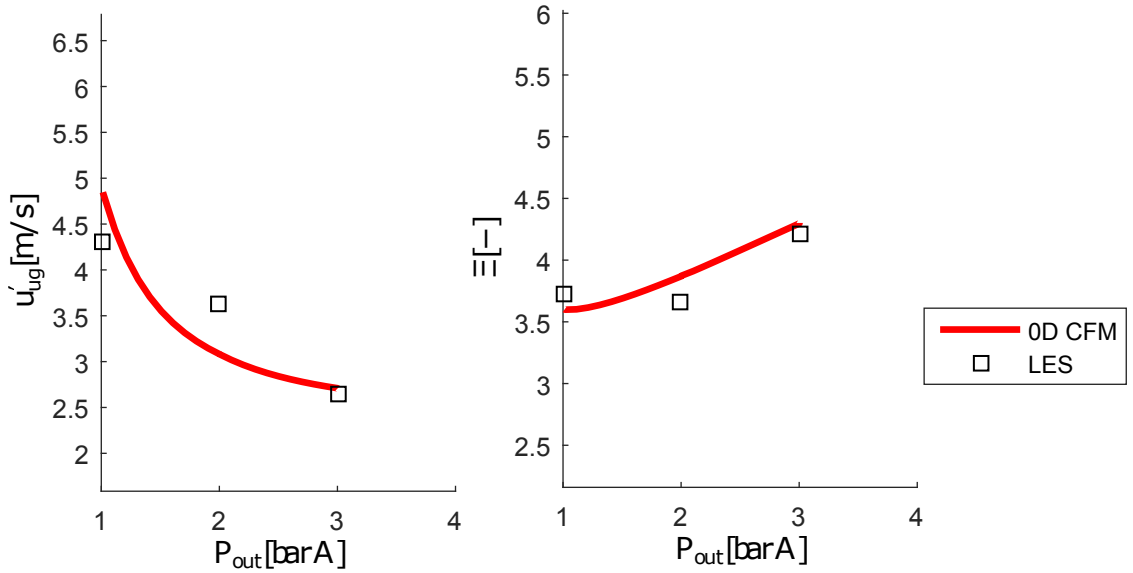

FIGURE 9 – Variation de u'_{ug} et de Xi avec la pression statique de sortie P_{out}.

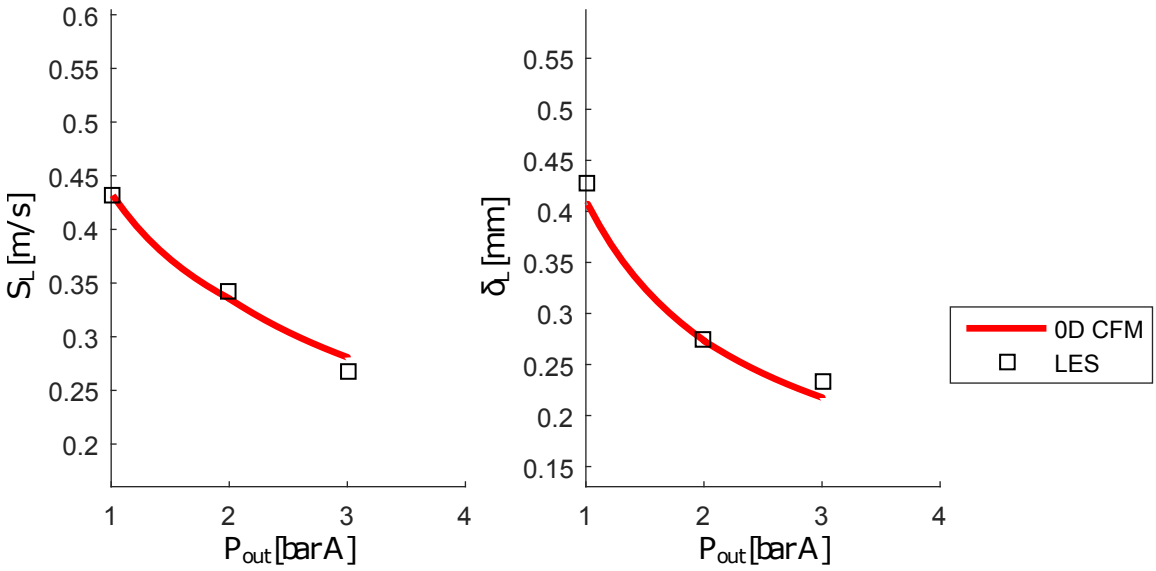

FIGURE 10 – Evolution de S_L et de δ_L en fonction de la variation de P_{out}.

TABLE 3 – Réponse dynamique de la zone UG et de la flamme à des variations de pression de sortie.

ρ_{ug}	$Y_{ug,F}$	T_{ug}	P_{ug}	u'
$\uparrow$ 189%	$=$	$\simeq$	$\uparrow$ 200%	$\downarrow$ 44%

(a) Variables en zone UG.

S_L	δ_L	A_m	Ξ	$\dot{\Omega}_F$
$\downarrow$ 35%	$\downarrow$ 47%	$\downarrow$ 56%	$\uparrow$ 19.4%	$\simeq$

(b) Variables régissant le comportement de la flamme.

D'après le tableau 3b, en plus de la diminution de S_L, l'accroissement de P_{out} réduit l'épaisseur de flamme laminaire. Cela est dû au fait que l'élevation de densité UG se traduit par une diminution du coefficient de diffusivité thermique, $\frac{\lambda}{\rho_{ug} c_{p_{ug}}}$, plus importante que la diminution de S_L. Ces fluctuations sont conformes à ce qui a été décrit en détail par Blint [9]. La décroissance de A_m est une autre conséquence inévitable de la compression du volume UG. Concernant le plissement de flamme, d'une part, la diminution de l'intensité turbulente est plus forte que celle de la vitesse de flamme laminaire. D'autre part, la diminution de l'épaisseur de flamme laminaire de 47% combinée à une invariance de l_T semble dominer l'évolution du plissement de flamme. Toutes les variations s'équilibrent et font que le taux de consommation de carburant n'a pas changé.

Les résultats des simulations sont globalement en accord avec les résultats des calculs SGE. Quelques écarts sont observés et sont principalement dûs aux limites de validité de certaines corrélations telles que la loi d'évolution de la surface moyenne de flamme A_m ou le modèle de vitesse de flamme laminaire, notamment dans le cas des variations de richesse. Le modèle de vitesses turbulentes constitue une approximation acceptable en première approche de u'. L'ensemble des variables caractérisant le système aérothermochimique répond de manière cohérente aux sollicitations appliquées au cours des simulations de validation. Ces simulations ont tourné sans manifester d'instabilités numériques et n'ont nécessité qu'un temps de calcul

de l'ordre d'une demi-seconde pour reproduire des temps simulés de l'ordre de cinq secondes, le tout en occupant une faible quantité de mémoire vive.

Analyse d'un secteur de brûleur d'hélicoptère

Afin d'investiguer en détail la possibilité d'appliquer de modèle de composant de TF à la simulation d'un brûleur de turbomoteur aéronautique réel, un cas de secteur de chambre de combustion annulaire a été considéré. Le motoriste SAFRAN Helicopter Engines nous a confié une mise en données numérique pour calculs SGE similaire à un secteur de chambre annulaire à flux inversé de turbomoteur récent muni d'un injecteur tourbilloneur d'air et d'un tourbilloneur de kérosène gazeux, les deux tourbilloneurs étant coaxiaux et débitant à contre-sens. Le cas est décrit en détail au chapitre 7. Le calcul SGE est réalisé avec le logiciel AVBP et le modèle de combustion DTFLES est choisi. Une analyse initiale du cas a permis de déterminer la dynamique de l'écoulement et d'identifier les structures de flammes du secteur. Suite à cette analyse, un post-traitement spécifique a été développé afin d'évaluer la contribution des flammes de prémélange à la combustion globale et la part de surface de flamme prémélangée. Une analyse des fluctuations de vitesse turbulente a également été réalisée.

Etude préliminaire de l'écoulement et des structures de flammes

Cette analyse s'est focalisée sur un domaine du TF identifié comme étant la zone de flamme. Cette zone est délimitée par les parois du TF, un plan coupant les injecteurs et un plan situé à une certaine distance en aval des injecteurs, désignée comme étant la longeur de pénétration de la flamme, L_p, Figure 11. Cette identification a été établie à partir des taux de dégagement de chaleur par unité de volume, $HRRD$. D'après Figure 11, coupe longitudinale au centre du TF, les zones en bleu révèlent une zone de recirculation centrale et un écoulement à vitesse axiale négative le long de l'axe du secteur, allant vers l'intérieur de l'injecteur interne. Une analyse détaillée des profils radiaux de vitesses axiales, radiales et azimuthales moyennes et turbulentes a été réalisée et détaillée au chapitre 7.

Par ailleurs, une identification sommaire des zones de flammes de prémélange et de diffusion a été établie. Cette identification s'est basée sur l'indice de Takeno normalisé [46, 61], G_{FO}, appliqué aux champs moyens de résultats SGE du secteur :

$$G_{FO} = \frac{\nabla Y_F \times \nabla Y_{O_2}}{|\nabla Y_F \times \nabla Y_{O_2}|} \tag{76}$$

G_{FO} est imposé à zéro aux noeuds à taux de réaction nul. Ainsi, G_{FO} vaut -1 pour une zone de flamme de diffusion, 0 en l'absence de combustion et 1 en zone de combustion prémélangée.

D'après Figure 7.14, des zones centrales à haut $HRRD$ se situent à l'intérieur de l'injecteur interne et au voisinage des sorties d'injecteurs. Une zone supplémentaire de densité de dégagement de chaleur est visible en amont du trou d'air « air feed 2 ». Des contours de G_{FO} indiquent plusieurs zones de flammes de prémélange et de diffusion. Une poche de gaz brûlés chimiquement inerte se trouve au beau milieu de la zone de flamme. L'analyse en post-traitement basée sur G_{FO} est complétée par une analyse basée sur la température en fonction de la fraction de mélange de carburant, Z_F, calculé à chaque noeud et à chaque instant à partir d'un bilan d'atomes de carbone et d'hydrogène. Pour plus de détails concernant cette analyse, consulter le chapitre 7.

Développements pour l'analyse des zones de flamme prémélangée

Pour effectuer cette analyse, la variable d'avancement $\tilde{c}$ introduite dans ce qui précède est modifiée de façon à tenir compte des divers flux d'air de dilution entrant dans le TF à travers

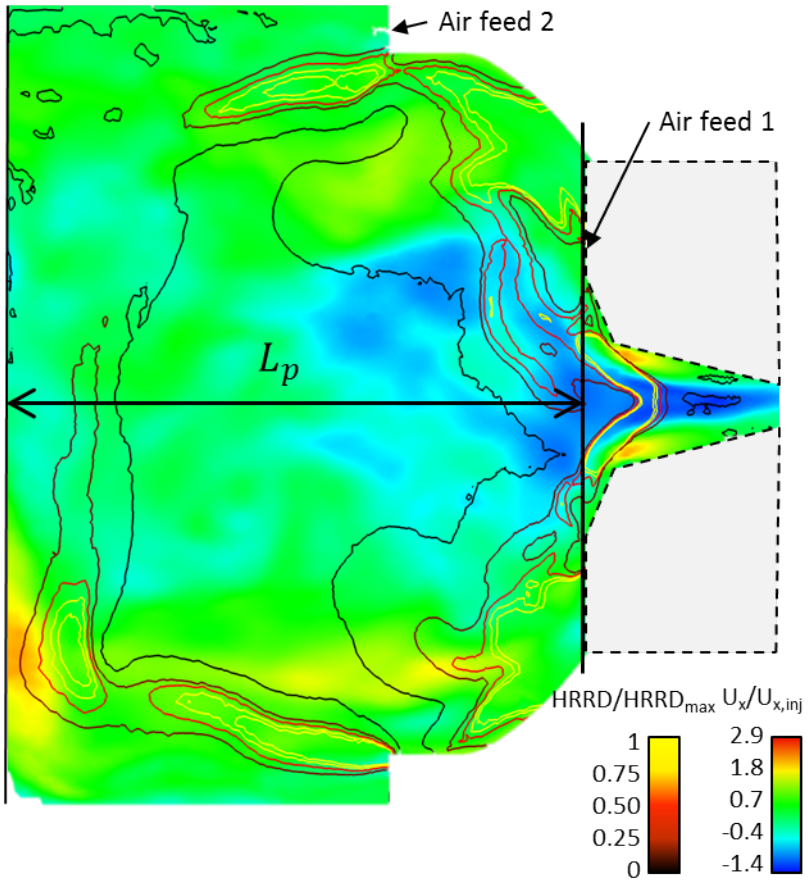

FIGURE 11 – Vue en 2D du champ moyen de vitesse axiale, U_x, normalisé par ça valeur à l'intérieur de l'injecteur, $U_{x,inj}$. Des contours normalisés de $HRRD$ sont superposés au champs de vitesse.

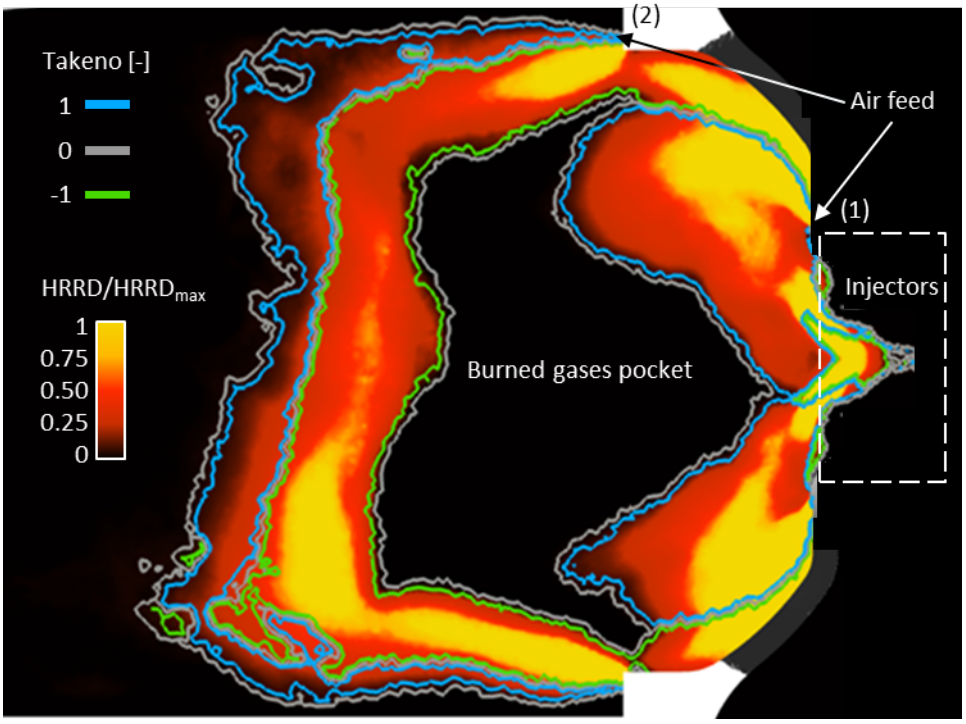

FIGURE 12 – Vue en 2D du champ moyen de $HRRD$ normalisé dans le TF, avec des contours d'indice de Takeno normalisé.

les divers trous et multiperforations. A partir du bilan atomique d'oxygène, la fraction de mélange Z_{O_2} est calculée, et elle est supposée égale à la fraction massique de dioxygène frais, Y_{ug,O_2}. Ensuite, à partir de l'équation de bilan de la réaction d'oxydation du carburant associée au mécanisme cinétique utilisé [48], les fractions de mélange stochiométriques de O_2 et de CO sont calculées. A partir des correspondances basées sur les équation des réactions définissant le mécanisme, Y_{bg,O_2} est également calculée et permet de compléter une relation donnant $\tilde{c}$:

$$\tilde{c} = \frac{Y_{ug,O_2} - Y_{O_2}}{Y_{ug,O_2} - Y_{bg,O_2}} \tag{77}$$

Afin de discriminer les zones de prémélange dans le calcul de surfaces de flamme et de taux de réaction, une fonction de Heaviside, H, est définie à partir de G_{FO} :

$$H \equiv H(G_{FO}) = \begin{cases} 0 & \text{si } G_{FO} < 1 \\ 1 & \text{si } G_{FO} = 1 \end{cases}$$

Le taux de consommation global de O_2, $\dot{\Omega}_{O_2}$, peut être décomposé en taux consommé par flamme de prémélange, $\dot{\Omega}^p_{O_2}$, et taux consommé par flamme de diffusion, $\dot{\Omega}^n_{O_2}$:

$$\dot{\Omega}_{O_2} = -\int_V \dot{\omega}_{O_2} dV \tag{78}$$

$$\dot{\Omega}_{O_2} = \dot{\Omega}^p_{O_2} + \dot{\Omega}^n_{O_2} \tag{79}$$

$$\dot{\Omega}^p_{O_2} = -\int_V H\dot{\omega}_{O_2} dV \tag{80}$$

En réécrivant $\dot{\Omega}^p_{O_2}$ selon le formalisme CFM, on obtient :

$$\dot{\Omega}^p_{O_2} = \rho_{ug} S_L^{eff}\Big|^p (Y_{ug,O_2} - Y_{bg,O_2})^p \, A_T^p \tag{81}$$

avec $S_L^{eff}\Big|^p$ étant la vitesse de flamme lainaire effective en zone de flamme prémélangée. La surface totale de flamme prémélangée, A_T^p, s'obtient de manière similaire à la relation utilisée dans le cas PRECCINSTA en y ajoutant la fonction H :

$$A_T^p = \int_V H \left|\nabla \tilde{c}\right| \Xi_{sgs} dV \tag{82}$$

Résultats

Le taux global instantanné de consommation d'oxygène, FIGURE 13, varie entre 44% et 51 %, tandis que le taux moyen de consommation de O_2 sur l'intervalle de calcul est de 49% en flamme de prémélange contre 51% en flamme non-prémélangée. Ces résultats confirment que les deux types de flammes, prémélangée et non-prémélangée, contribuent selon parts sensiblement égales à la combustion dans le secteur de TF.

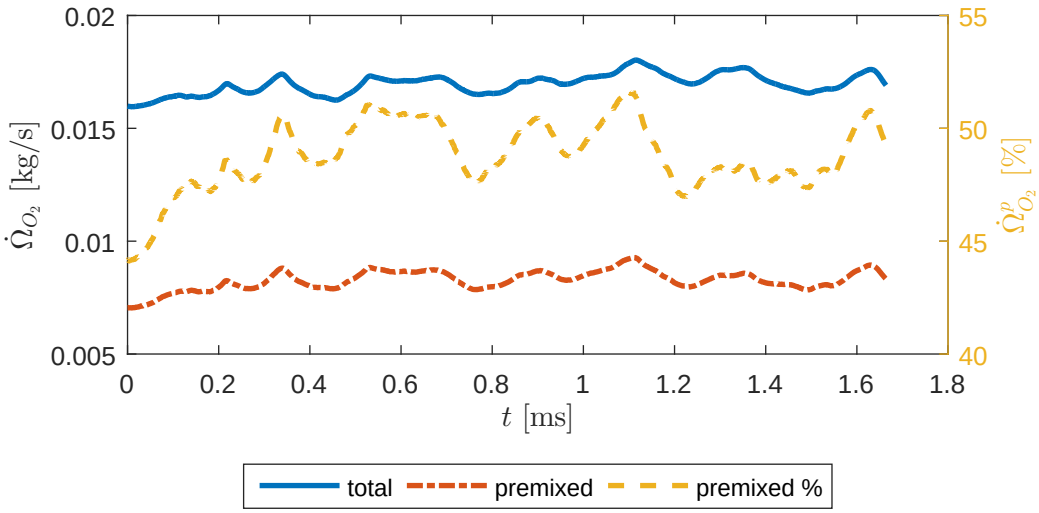

FIGURE 13 – Moyenne spatiale de taux de consommation de O_2 global (ligne bleue en trait continu) et prémélangé (ligne rouge en traits interrompus) ; la ligne orange dashed représente le pourcentage de O_2 consommé par une flamme de prémélange par rapport aux taux de consommation global de O_2.

En outre, la surface totale de flamme, A_T, FIGURE 14, se compose en grande partie d'une surface de flamme prémélangée, notamment 65 à 71%. Cet écart entre les répartitions de taux de réaction et les répartitions de surfaces de flamme serait dû à la différence entre les structures de flammes de prémélange et les flammes de diffusion, mais également aux hétérogénéités de mélange dans le TF, qui entraînent directement des variations spatiales de la quantité $Y_{ug,O_2} - Y_{bg,O_2}$.

Concernant la vitesse de flamme, FIGURE 15, des fluctuations autour de 0.64 m/s sont relevées. Comparer avec précision ce résultat avec les données de la littérature se heurte à l'obstacle de la forte disparité de richesses et de températures en fonction de la position en amont et dans la zone de flamme. Néanmoins, l'ordre de grandeur obtenu semble tout à fait plausible pour du kérosène brûlant aux conditions nominales du cas étudié, FIGURE 16. Des post-traitements aditionnels, présentés au chapitre 7, ont permis d'établir des corrélations pour les vitesses turbulentes du mélange et de la flamme prémélangée.

Le bilan de cette étude de secteur de bûleur de turbomoteur montre clairement des éléments à prendre en compte dans un modèle pour simulation système, tels que les zones de recirculation et les flux axiaux à contre-courant, qui auraient des impacts sur les structures de flammes et sur les réactions chimiques se déroulant dans la zone de flamme. De plus,

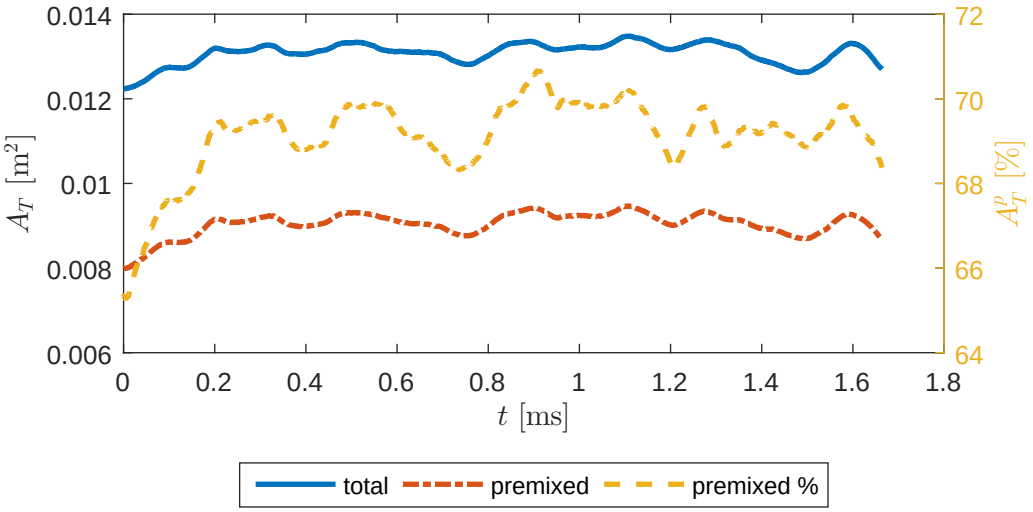

FIGURE 14 – Moyenne spatiale de surface de flame turbulente, $A_T(t)$, sa partie prémélangée, $A_T^p(t)$, et pourcentage de $A_T^p(t)$ par rapport à $A_T(t)$.

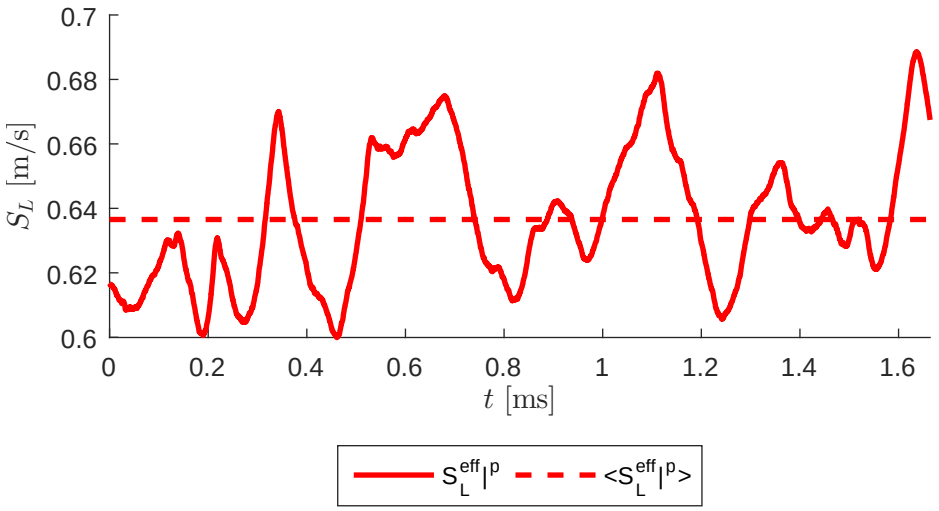

FIGURE 15 – Vitesses instantannée et moyenne de flamme laminaire prémélangée.

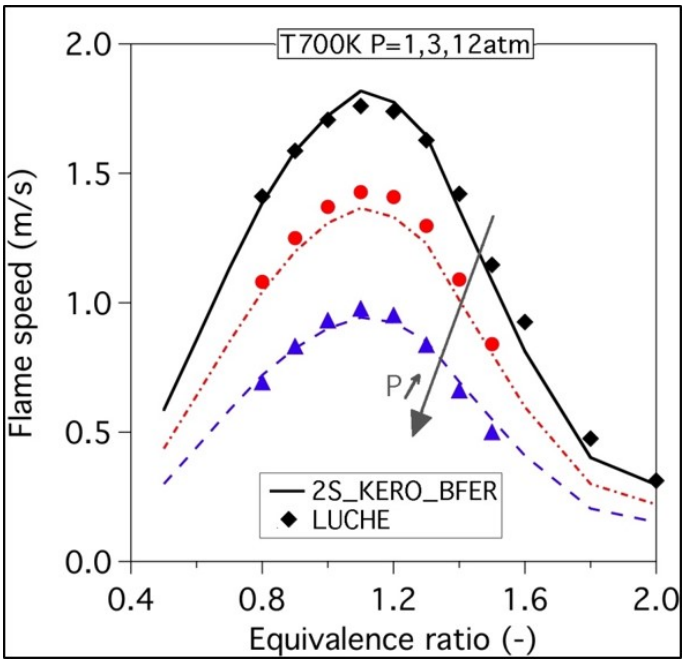

FIGURE 16 – Vitesses de flamme laminaire pour le composé KERO utilisé dans cette étude, obtenu pour les schémas cinétiques chimique 2S_KERO_BFER et LUCHE [76], respectivement représentées par les lignes et les marqueurs.

des répartitions spatiales et globales de flammes de prémélange et de diffusion ont été déterminées par les taux de consommation et les surfaces de flammes turbulentes. Ces répartitions soulignent la nécessité d'élaborer une méthode pour l'analyse et la réduction des flammes non-prémélangées. Identifier des paramètres physiques qui régissent la répartition prémélange/diffusion et qui seraient modélisables en 0D serait un défi de taille.

Conclusion et perspectives

Conclusion

En conclusion, dans cette thèse, une nouvelle approche a été investiguée pour la modélisation de la combustion dans les simulations systèmes des turbines à gaz. Ces simulations système sont intégrées dans un environnement multi-domaine, permettant ainsi une flexibilité de schématisation des systèmes simulés. Cette flexibilité rend l'approche particulièrement adaptée à la phase de pré-étude durant la conception des chambres de combustion aéronautiques, tout en offrant les moyens d'une bonne synergie avec les phases précédente et suivante.

Dans un premier temps, un modèle de composant de TF a été développé pour la simulation système intégrée dans un environnement numérique multi-domaine s'appuyant sur le formalisme Bond-Graph. Ce composant comporte une loi d'évaporation et un modèle 0D de combustion prémélangée basé sur des résultats de simulations SGE. Ces simulations correspondent à un cas de brûleur expérimental à tourbilloneur, PRECCINSTA, dans lequel brûle une flamme de méthane prémélangée dans une chambre de section carrée. Les paramètres numériques de simulation SGE ont été optimisés et une configuration de calcul de référence a été validée par des résultats expérimentaux du brûleur disponibles dans la littérature. Les calculs SGE réalisés font appel au formalisme des flammes épaissies dynamiquement, DTFLES. Des développements spécifiques ont été implémentés dans le code SGE utilisé pour les simulations afin de construire des variables physiques dérivant les flammes selon le

formalisme CFM à partir du formalisme DTFLES. Des variations paramétriques de simulations 3D réalisées avec le code modifié ont permis de caractériser la réponse d'une flamme turbulente de prémélange à des variations de conditions opératoires, et d'élaborer des modèles de surface de flamme, de vitesse et d'épaisseur de flamme laminaire ainsi que de plissement de surface de flamme. Les résultats des variations paramétriques ont également servi pour vérifier le comportement du modèle 0D CFM et la réponse du TF aux variation de conditions opératoires. Le modèle de TF à combustion turbulente prémélangée répond globalement de manière satisfaisante à ces variations et restitue à un premier ordre les principaux phénomènes aérothermochimiques ayant lieu dans un brûleur prémélangé. Les écarts majeurs du modèle par rapport aux résultats de référence obtenus par SGE seraient dûs à l'absence d'un modèle de chimie d'équilibre CO/CO_2.

Dans un second temps, la combustion non-prémélangée a été abordée à travers un cas CFD d'un secteur de brûleur annulaire à flux inversé, similaire à ce qui se retrouve dans des hélicoptères récents. Ce secteur est alimenté en air et en carburant par deux injecteurs à tourbilloneurs à flux contra-rotatifs. Suite à une analyse initiale des écoulements et une identification des structures de flammes présentes dans ce cas, des zones de recirculation ainsi que des flammes de prémélange et de diffusion on été mis en évidence. Les structures des zones réactives présentent des flammes accrochées aux parois et des flammes suspendues par les gaz brûlés. Des post-traitements ont été développés, basés sur une fonction de Heaviside d'indice de Takeno, permettant de filtrer localement des variables ciblées selon le type de flammes présentes à une position donnée. Ces post-traitements ont permis d'évaluer les contributions respectives des flammes prémélangées et non-prémélangées dans la combustion dans le TF. Leurs taux de consommation de O_2 sont quasiment égaux mais la surface de flamme prémélangée est prépondérante.

Perspectives

Des améliorations pourraient être apportées au modèle de TF, notamment sur les corrélations de surface moyenne de flamme, de vitesse de flamme laminaire et de vitesse turbulente. Afin d'améliorer concrètement la prédictivité du modèle, le procédé de réduction par analyse de résultats SGE pourrait être étendu à plusieurs types de chambres de combustion. Un ajout supplémentaire intéressant serait l'implémentation d'un modèle d'échanges thermiques à travers les parois, ce qui aurait sans doute un impact sur les phénomènes d'étirement, de plissement et d'extinction locale de la flamme. Concernant la prise en compte de la turbulence, il serait important d'intégrer un modèle pour le calcul de l'échelle intégrale l_T, éventuellement similaire à la méthode employée par [50]. Une autre alternative serait l'ajout d'une équation de transport de l'énergie turbulente. Par ailleurs, l'intégration d'un modèle de chimie post-flamme serait nécessaire pour simuler les émissions polluantes à évaluer et à maîtriser, tout en améliorant la précision du calcul de température et de composition des gaz brûlés. Une piste prometteuse serait l'intégration des méthodes de relaxation du CO et du NO, respectivement CORA and NORA [14], basées sur une cinétique chimique tabulée. Cela lui confère une bonne précision sans pénaliser le temps de calcul.
Concernant la valorisation du modèle de TF et de la philosophie de modélisation dans laquelle s'inscrit cette thèse, il serait intéressant de mettre le modèle de TF en oeuvre dans des simulations représentant des tubes à flammes aéronautiques discrétisés de manière similaire à l'étude de Stuttaford [119], auquel cas une méthode de prise en compte des hétérogénéités s'imposerait. Des points de fonctionnement stabilisés et des opérations transitoires pourraient être envisagés. Un autre champ d'application serait un cas de turbomoteur complet, par la connexion d'un composant de TF à un compresseur, une turbine de génératrice et une turbine de puissance. Par le choix de l'environnement de développement adopté, il serait possible d'inclure une boucle de contrôle et de commande.

D'après les résultats présentés au dernier chapitre et comme prévu selon la stratégie annoncée au préalable, le modèle de combustion 0D développé dans cette thèse devrait être étendu aux flammes non-prémélangées du fait de leur rôle dans les brûleurs aussi important que celui des flammes de prémélange. Cela impliquerait l'expression d'un taux de réaction non-prémélangée ainsi que d'un taux de transfert de réactifs partiellement brûlés en prémélange vers une zone de flamme de diffusion. Cette extension se doit de tenir compte de la dynamique instable des flammes non-prémélangées, ainsi que du fait qu'elles ne se propagent pas et ne possèdent pas d'épaisseur caractéristique. De surcroît, l'analyse des flammes de diffusion par les taux de dissipation scalaires de fractions de mélange présente une dépendence spatiale intrinsèque. Cette perspective devrait être investiguée à l'aide de calculs SGE et de post-traitements dédiés.

Contents

Nomenclature

Roman Symbols

A_m	Mean flame surface $[m^2]$
A_R	Resolved flame surface $[m^2]$
A_T	Turbulent flame surface $[m^2]$
c_p	Specific heat at constant pressure $[kJ \cdot K^{-1} \cdot kg^{-1}]$
c_v	Specific heat at constant volume $[kJ \cdot K^{-1} \cdot kg^{-1}]$
d, D	Diameter $[m]$
H	Enthalpy $[kJ]$
h	Specific enthalpy $[kJ \cdot kg^{-1}]$
$H(G_{FO})$	Heaviside function of the normalised Takeno flame index
l_T	Integral length scale $[m]$
M	Molar weight $[kg \cdot mol^{-1}]$
m	Mass $[kg]$
$\dot{m}$	Mass flow rate $[kg \cdot s^{-1}]$
Z	Mixture fraction $[-]$
P	Static pressure $[Pa]$
L_p	Flame penetration length $[m]$
P_t	Total pressure $[Pa]$
Q	Heat $[kJ]$
r	Specific gas constant $[kJ \cdot kg^{-1} \cdot K^{-1}]$
R	Radius $[m]$
S_L	Laminar flame speed $[m \cdot s^{-1}]$
S_L	Laminar premixed flame speed $[m \cdot s^{-1}]$
T	Temperature $[K]$
G_{FO}	Normalised Takeno index $[-]$
k	Turbulent kinetic energy $[m^2 \cdot s^{-2}]$

U	Internal energy $[kJ]$
u	Specific internal energy $[kJ \cdot kg^{-1}]$
v	Speed $[m \cdot s^{-1}]$
W	Mechanical work $[kJ]$
Y	Mass fraction $[-]$

Greek Symbols

δ_L	Laminar flame thickness $[m]$
η_{comb}	Combustion efficiency $[-]$
η_k	Smallest turbulent eddy scale or Kolmogorov scale $[m]$
γ	Specific heats ratio $[-]$
Γ_c	Surface stretch efficiency function $[m^{-1}]$
λ	Thermal conductivity $[W \cdot m^{-1} \cdot K^{-1}]$
μ	Absolute viscosity $[Pa \cdot s]$
$\dot{\Omega}$	Reaction rate $[kg \cdot s^{-1}]$
ϕ	Fuel/air equivalence ratio $[-]$
Ψ	Mass transfer rate $[kg \cdot s^{-1}]$
ρ	Density $[kg \cdot m^{-3}]$
σ	Stefan-Boltzmann constant $[5.67 \times 10^{-8} W \cdot m^{-2} \cdot K^{-4}]$
τ	Time constant $[s]$
Θ	Combustion progress variable, also labeled c $[-]$
υ	Stoichiometric coefficient $[-]$
Ξ	Flame surface wrinkling factor $[-]$
ξ	stiffness coefficient $[-]$

Dimensionless numbers

a_m	Normalised mean flame surface $[-]$
c	Combustion progress variable, also labeled Θ $[-]$
Da	Damköhler number $[-]$
Ka	Karlovitz number $[-]$
Le	Lewis number $[-]$
Ma	Mach number $[-]$
PL	Pressure Loss $[-]$
Pr	Prandtl number $[-]$

Re	Reynolds number [−]
v	Normalised fresh gas volume [−]

Superscripts

n	Non-premixed
eff	Effective
p	Premixed

Subscripts

A	Air
ad	Adiabatic
$base$	Baseline
$comb$	Combustion
$conv$	Convection
ex	Exchange
F	Fuel
ff	Flame front
i, j, k	Respectively i^{th}, j^{th} and k^{th} items
inj	Injected
L	Laminar
liq	Liquid
$mixt$	Mixture
O	Oxidiser
pf	Post-flame
rad	Radiation
ref	Reference
RMS, rms	Root Mean Square
st	Stoichiometric
T	Turbulent
th	Thermal
vap	Evaporation
0	Normalisation reference

Other Symbols

$\tilde{c}$	Filtered combustion progress variable

$\dot{b}$ Time derivative of the quantity b

b' Fluctuating part of the quantity b

$\bar{b}$ Reynolds average of a given variable b

Acronyms

$ACARE$ Advisory Council for Aviation Research in Europe

APU Auxiliary Power Unit

$ATAG$ Air Transport Action Group

ATM Air Traffic Management

ATS Air Traffic System

BG, bg Burned Gas

BML Bray Moss Libby

$CAGR$ Compound Annual Growth Rate

CFD Computational Fluid Dynamics

CFM Coherent Flame Model

CI Compression Ignition

CMC Conditional Moment Closure

CO Carbon Oxide

$CORA$ CO Relaxation Approach

CRZ Central Recirculation Zone

DNS Direct Numerical Simulation

DOE Design Of Experiments

$DTFLES$ Dynamically Thickened Flame Large Eddy Simulation model

DZ Dilution Zone

EBU Eddy Break Up

EGR Exhaust Gas Recirculation

EI Emissions Index

EPA Environment Protection Agency

$FADEC$ Full Authority Digital Control

FAR Fuel/Air Ratio

FT Flame Tube

FSD Flame Surface Density

GDP Gross Domestic Product

HIT Homogeneous Isotropic Turbulence

HR Heat Release $[kJ]$

HRR Heat Release Rate Rate $[kW]$

$HRRD$ Heat Release Rate Rate Density $[kW \cdot m^{-3}]$

$ICAO$ International Civil Aviation Organization

ISA International Standard Atmosphere

ITB Interstage Turbine Burner

IZ Intermediate Zone

JTI Joint Technology Initiative

LW Lax-Wendroff numerical scheme

LDI Lean Direct Injection

LES Large Eddy Simulation

LHV Lower Heating Value $[kJ \cdot mol^{-1}]$

LPP Lean Premix Prevaporized

MMC Multiple Mapping Conditioning

$NORA$ NO Relaxation Approach

NOx Nitrogen Oxides

ODE Ordinary Differential Equation

OEM Original Equipment Manufacturer

PDF Probability Density Function

PFR Plug Flow Reactor

PGC Pressure Gain Combustion

PM Particulate Matter

PM Particulate Matter

$PPFM$ Partially Premixed Flame Model

$PRECCINSTA$ PREdiction and Control of Combustion INStabilities in Tubular and Annular gas turbine combustion systems

PZ Primary Zone

$RANS$ Reynolds Averaged Navier-Stokes

RQL Rich burn - quick Quench - Lean burn

SGS, sgs Sub-grid scale

SI Spark Ignition

TBO	Time Between Overhaul
$TFLES$	Thickened Flame Large Eddy Simulation
TIT	Turbine Inlet Temperature $[K]$
$TTGC$	Third order Taylor Galerkin numerical scheme, variant 'C'.
UHC	Unburned Hydro-Carbons
UG, ug	Unburned Gas
VOC	Volatile Organic Compound
WSR	Well Stirred Reactor, also known as Perfectly Stirred Reactor

List of Figures

List of Tables

Part I

Introduction

The Aeronautics Market: Importance and Growth

According to the Air Transport Action Group (ATAG) website [53], nearly 63 million people are employed worldwide in aviation. Of this, 9.9 million people work directly in the aviation industry. Aviation generates $2.7 trillion of Gross Domestic Products (GDP) per year. The aviation industry consumes around 278 billion litres of jet fuel, annually. Worldwide air traffic is predicted to grow at a rate close to 4-5% per year with even higher rates in the Middle East and Asia [35]. More in the specific, the worldwide market for commercial helicopters is expected to witness growth through 2023, driven mainly by the offshore oil and gas exploration, and flourishing demand from Asia, Africa and Latin America. Medium[1] helicopters account for the largest share of the world commercial helicopters market and the heavy helicopter sector is forecast to achieve the largest CAGR[2] during 2013-2023. Demand is increasing thanks to new markets, and the already established markets will go through massive fleet renewals soon. Most of the worldwide air vehicles are powered by gas turbines.

Environmental Impact and Resolutions

Impact

Today the aviation part of responsibility in CO2 emissions is still small compared to the contributions of all the other fuel-burning activities, as shown in Figure 17. However, the air traffic influence on radiative forcing appears to be more complex than just a matter of CO2 emissions index. Indeed studies [65, 112] highlight several mechanisms having both negative and positive contribution to radiative forcing. In any case, the growth of the air transport activity will obviously amplify its impact on radiative forcing.

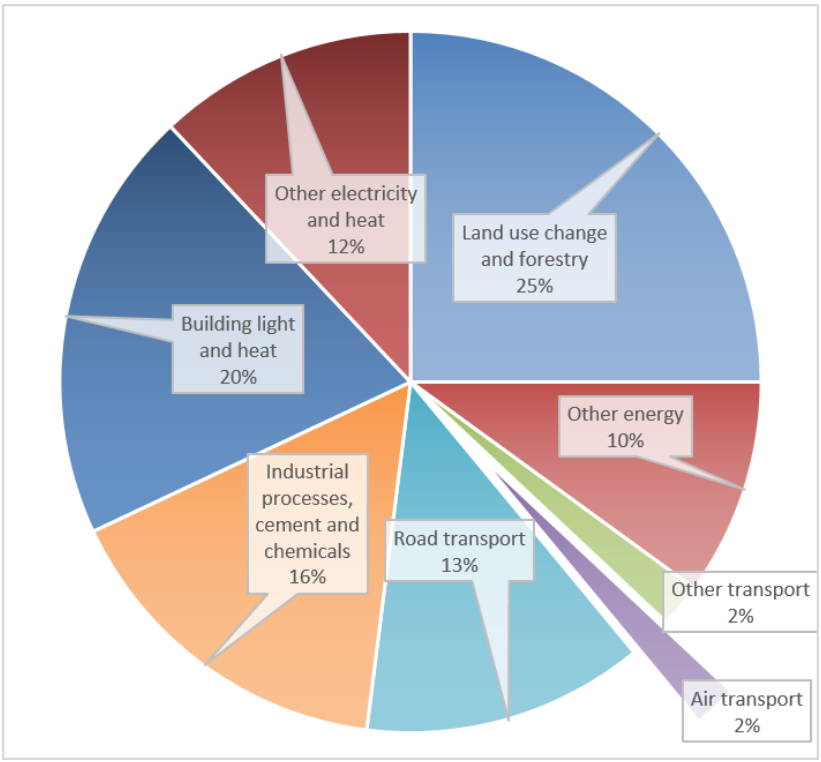

Figure 17 – Global CO2 emissions by activity in 2013 [2].

[1] Civil medium helicopters weight from 1800kg to 7250kg [99].
[2] Compound Annual Growth Rate.

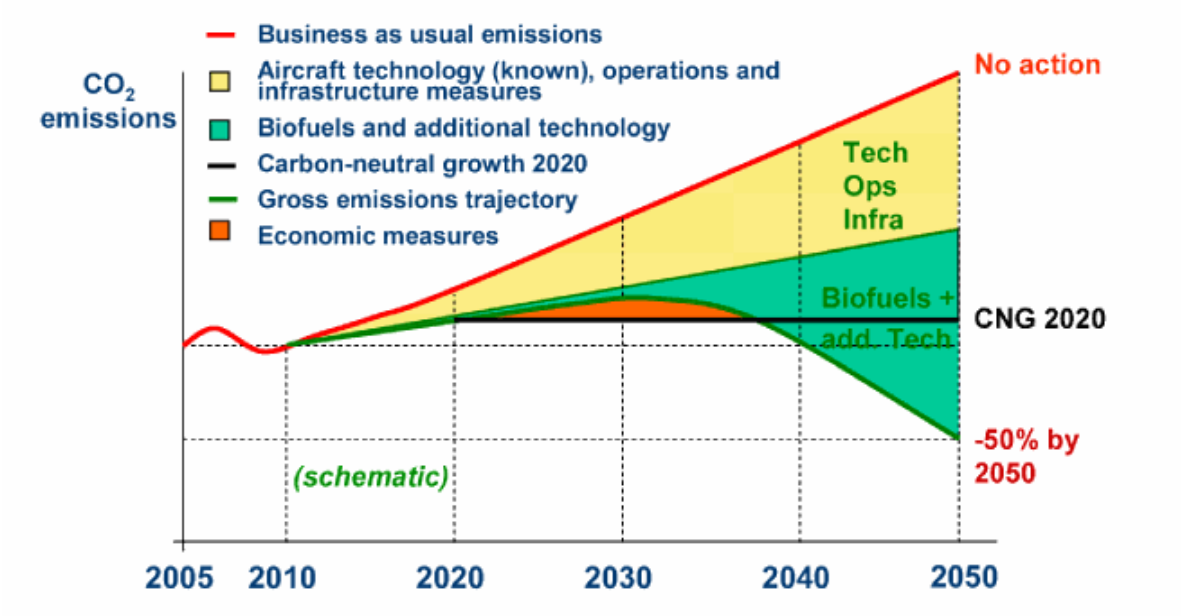

Figure 18 – CO_2 Emissions projection - ATAG.

The ATAG has established several scenarios of CO2 emissions growth until 2050, Figure 18. The most positive scenario grounded on the use of biofuels and new aircraft technologies forecasts an inversion of the CO2 emission trend, from growth to decrease. The worst scenario, relative to no action, forecasts a continuous CO2 emissions growth following the present trend.

Moreover, emissions of Nitrogen Oxides (NOx), Volatile Organic Compounds (VOCs), Carbon Oxide (CO) and Particulate Matter (PM) severely degrade local air quality. Furthermore, an enlarged global fleet of helicopters could have a detrimental effect on the acoustic environment due to a raise of noise radiation.

Resolutions

The aeronautics community defined directions for the next decades and actions are already being taken in several areas of the air transport sector. The ACARE[1] has set improvement targets concerning aircraft, engine and Air Traffic Management (ATM), aiming at reducing the CO2 emissions by 50% in 2020, as shown in Figure 19. The "greener" Air Traffic System (ATS) was one of the main goals of the European Commission 7th Framework Programme for collaborative research, in which a dedicate Joint Technology Initiative (JTI) was launched with the aim of accelerating the required technology development. Advanced flight procedures will be developed in order to minimise pollutant emissions and noise taking care of air navigation / ATM constraints. New aerodynamic designs are being considered. Various engine technologies are being analysed. Electrical system technologies are being developed to increase systems efficiency and reduce the use of hydraulic solutions. Alternative fuels are in the scope as well.

[1] Advisory Council for Aviation Research in Europe.

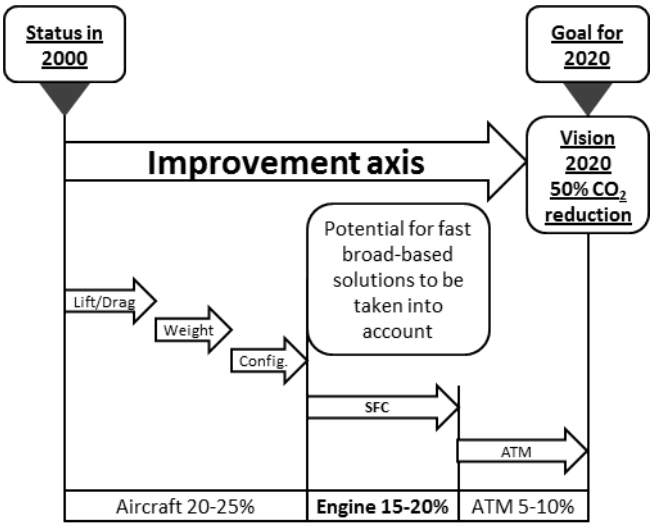

Figure 19 – CO_2 reduction goal, vision 2020 set by ACARE.

Why Thermal Turbomachines

Combustion is still the best means of power production for air vehicles. Spark Ignition (SI) engines and gas turbines[1] have very comparable thermal efficiencies; Compression Ignition (CI) engines are 20 to 30% more efficient than simple conventional gas turbines. However, for a same power output, a thermal turbomachine occupies less volume and is lighter than a piston engine; these two aspects are very important for air transport, overriding engine efficiency. In fact, when higher efficiency yields more weight and volume the aircraft needs more lift area. Increasing lift area adds aerodynamic drag in return, leading to more energy demand. Furthermore, turbomachines offer more reliability and longer Time Between Overhaul (TBO) than aircraft piston engines. The typical TBO for a turboprop engine is 3,000 hours while a piston aircraft TBO is generally 2,000 hours. The higher initial cost of a turboprop aircraft may be compensated by maintenance savings over time. Accordingly, gas turbine engines are still the best choice for the major part of international air fleets.

Modelling and Simulation

The benefits from computer aided modelling and numerical simulation are undeniable. In aeronautics, because of safety purpose and money, time and experiments limitations, modelling and simulation become vital. Nowadays, at each stage in the life cycle of any aircraft unit, computer modelling tools are crucial. The evolution of these tools became tightly linked to the evolution of the aircraft itself. This fact is observed for every component of an air vehicle and the engine definitely follows the same rule. On the one hand, CFD is rapidly spreading over many areas of the detailed engine design phase. On the other hand, engine performance prediction is gaining importance in supporting early conceptual designs. In both cases, the environmental impact of engines is already one of the primary performance criteria.

Thesis Objectives

The primary objective of this thesis was to investigate a new physical approach to 0D combustion modelling for gas turbine system simulation. The development of a new 0D flame tube model was based on a detailed understanding of combustion extracted from CFD. The

[1] Although it refers to a system generally composed of a compressor, a combustor and a turbine, the name "gas turbine" has become commonly used. Others designations are "thermal turbomachine" and "turboprop".

goal was the description of flame structure and dynamics. This implied in a first time the study of an experimental single phase premixed burner case by means of numerical simulation and the development of specific CFD tools. In a second time, the CFD results enabled the analysis of premixed turbulent flame properties. That analysis lead to the assessment and the selection of flame characteristics modelling choices, to build the 0D flame tube model. The achievement of this target set the bearing to the extension of the study to a case of non-premixed single phase aeronautical combustor sector by determining its flame types with their respective contributions to the overall combustion process. These achievements open perspectives for a future work to represent multiple flame type combustion and pollutant formation, in the closest possible scenario to gas turbine burners on duty.

Thesis Presentation

Part I introduces the economic, environmental and industrial contexts of this.
Part II, formed by the chapters 1, 2, 3 and 4, represents the bibliography and the roadmap of the present work. In the first three chapters, engine technology is presented with its relevant modelling approaches.

- **Chapter 1** presents the global picture of aeronautical gas turbines engineering.

- **Chapter 2** gets closer to the details of the burner; the different physical phenomena are briefly discussed, as well as their simulation approaches.

- In order to introduce to turbulent flames modelling choices, as well as to provide an opportunity for pollutants prediction in a future work, some of the basics of flames theory and modelling are briefly stated in **Chapter 3**. In the same chapter, the inventory of pollutant emissions is listed and their current prediction methods are mentioned.

- In a first step, **Chapter 4** summarizes the bibliography and defines the herein investigated gas turbine simulation approach. In a second step, the combustor modelling framework is specified, as well as its interaction with the other engine components.

Parts III and IV deal with the contribution of this thesis. **Part III** treat premixed turbulent combustion through a premixed swirl burner case.

- **Chapter 5** describes the CFD study of the premixed burner case and the analysis of turbulent flame characteristics.

- **Chapter 6** details the 0D combustion model development and validation on the premixed burner case.

In **Part IV**, featuring **Chapter 7**, an aeronautical burner sector is studied by means of CFD and partially premixed turbulent flame characteristics are extracted to understand combustion scenarios in a real burner configuration.

The last part, **Part V**, summarises the conclusions and enumerates the upcoming perspectives.

Part II

Bibliography

Chapter 1

Gas Turbines for Aeronautics - Technology and Modelling

Aeronautical gas turbines are present in a wide range of aeronautical applications from small Auxiliary Power Units (APUs) to vectored thrust engines in modern fighter aircraft. They fill an intermediate power range that goes from 2kW to 80MW. That is, above the microturbine category, rated between 20W to 50kW, and under the power generation turbines, that generate from 4 to 510MW.
This chapter starts by briefly presenting a general description of the current aeronautical gas turbines technology. Then, the most commonly used modelling and simulation tools throughout a typical aeroengine life cycle are summarised. That summary highlights improvement possibilities in the design process, that could be made thanks to both an evolution of simulation tools and more synergy between the teams of engineers working in all the stages of aeroengines design.

1.1 Technology

The compressor - burner - turbine arrangement is common to all gas turbines and it is the gas generator.

Part of the power carried by the high pressure burned mixture sustains the compressor work and the excess power is retrieved by an additional turbine or simply released to the atmosphere, resulting in thrust. As an exemple, Figure 1.1 displays a 2-spool free turbine turboshaft.

1.1.1 Conventional Engines Operation

Gas turbines operate on an open cycle that can be represented by the Joule-Brayton cycle, represented in Figure 1.2. The ideal cycle is described by the four following steps:

- Isentropic compression is done from station 2 to station 3 in the compressor.
- Isobaric combustion rises the gas mixture temperature in the burner from 3 to 4.
- Isentropic expansion is achieved in the turbine from 4 to 5.
- Isobaric heat rejection to the atmosphere.

Figure 1.3 indicates the stations along the gas path of the gas generator, at which thermodynamic states are defined.

The global ideal-cycle gas turbine performance is determined by net specific work, $\frac{\dot{W}_{net}}{\dot{m}}$, according to equation 1.1, and thermal efficiency, η_{th}, according to equation 1.2.

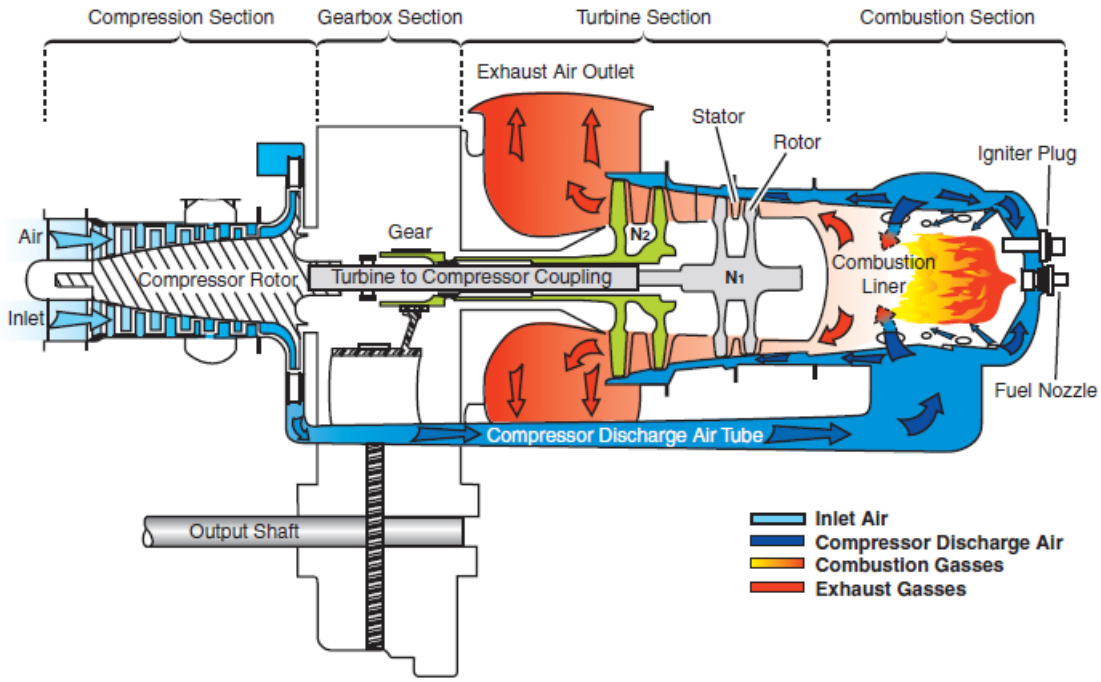

Figure 1.1 – Turboshaft system [126].

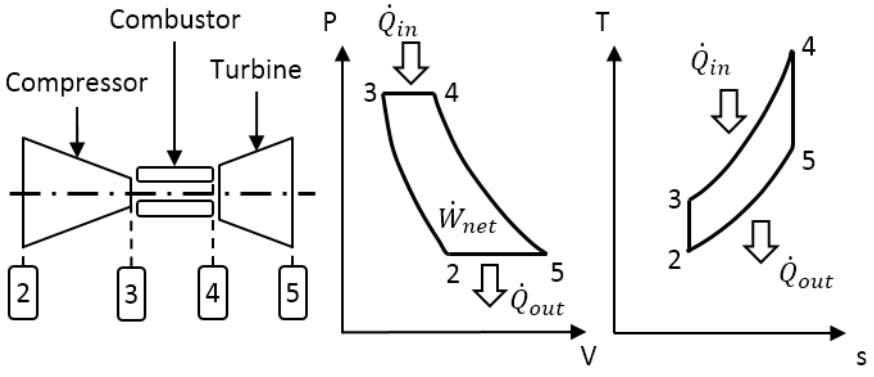

Figure 1.2 – Ideal thermodynamic cycle of a gas turbine. Left: gas generator; center: Clapeyron P-V diagram, where P is the thermodynamic pressure and V is the volume; right: T-s diagram, where T is the gas temperature and s is the entropy.

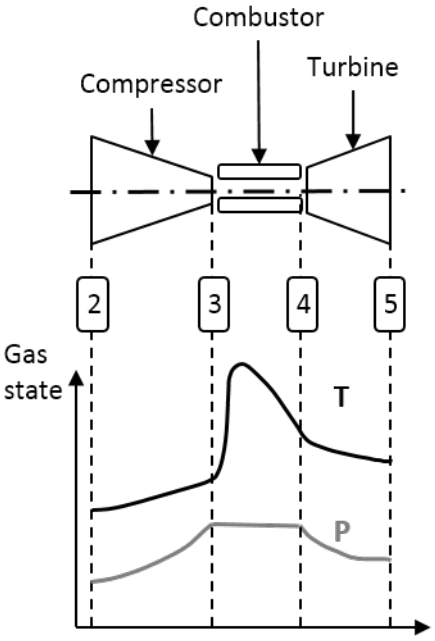

Figure 1.3 – Gas generator components representation and thermodynamic characterization in terms of pressure, P, and temperature, T. From [77].

$$\frac{\dot{W}_{net}}{\dot{m}} = -\frac{\dot{Q}_{in} + \dot{Q}_{out}}{\dot{m}} \tag{1.1}$$

$$\eta_{th} = \left|\frac{\dot{W}_{net}}{\dot{Q}_{in}}\right| = 1 + \frac{\dot{Q}_{out}}{\dot{Q}_{in}} \tag{1.2}$$

where $\dot{m}$ is the total mass flow rate of gas crossing the gas turbine, $\dot{Q}_{in}$ is the rate of heat released by combustion, $\dot{Q}_{out}$ is the power used by the gas turbine and η_{th} is the thermal efficiency. $\dot{Q}_{in}$ and $\dot{Q}_{out}$ are respectively given by:

$$\dot{Q}_{in} \approx \dot{m} c_p \left(T_4 - T_3\right) \tag{1.3}$$

$$\dot{Q}_{out} \approx \dot{m} c_p \left(T_2 - T_5\right) \tag{1.4}$$

where c_p is the specific heat of the gaseous mixture at constant pressure, and T_n is the temperature at the station n. Accordingly, equations 1.1 and 1.2 can be expressed as it follows:

$$\frac{\dot{W}_{net}}{\dot{m}} \approx c_p \left(T_3 - T_4 + T_5 - T_2\right) \tag{1.5}$$

$$\eta_{th} \approx 1 + \frac{T_2 - T_5}{T_4 - T_3} \tag{1.6}$$

For given air flow conditions, according to equation 1.6, the thermal efficiency depends on T_4 and T_3. In real systems, T_4, also known as the Turbine Inlet Temperature (TIT), is limited by the theromechanical properties of turbine blades and stator vanes. Therefore, a given TIT is matched with an optimal compression ratio. Design precautions taken in order to protect the turbine blades and stator vanes as well as their impact on combustion chambers design are briefly explained in chapter 2. T_3 depends on the compression ratio, $\frac{P_3}{P_2}$, given by:

$$T_3 = T_2 \left(\frac{P_3}{P_2}\right)^{\frac{\gamma-1}{\gamma}} \tag{1.7}$$

where γ is the specific heats ratio. The compressor and turbine operation is characterized by reduced gas mass flow rate, $\dot{m}\frac{\sqrt{T}}{P}$, reduced shaft speed, $\frac{N}{\sqrt{T}}$, pressure ratios and efficiency. Typical compressor and turbine maps are shown in Figure 1.4.

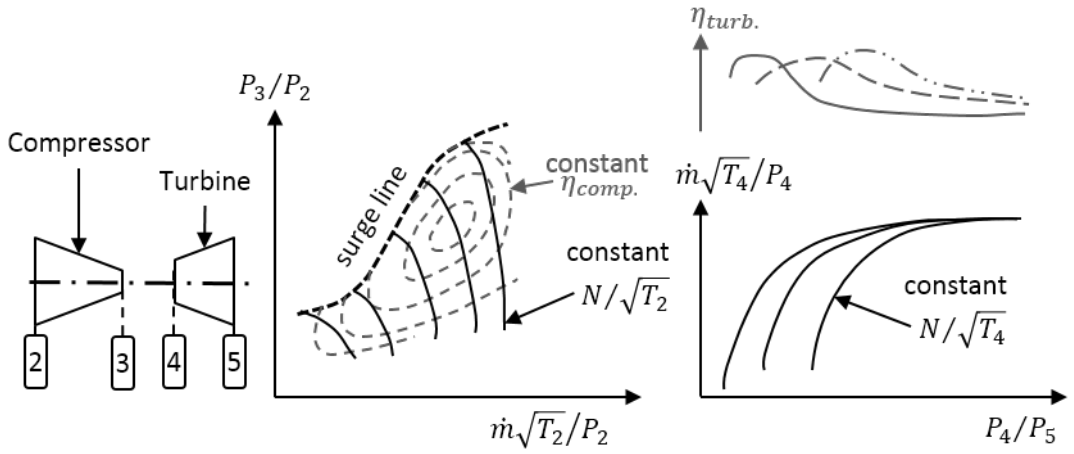

Figure 1.4 – Compressor and turbine thermodynamic characterization, where $\eta_{comp.}$ is the compression efficicency and $\eta_{turb.}$ is the expansion efficiency. From [77].

On an industrial scale, the technical peculiarities of aeronautical gas turbines presented above are tackled throughout their life cycle by means of various experiments mathematical models and numerical simulations, as detailed in what follows.

1.2 Engine Life Cycle and Modelling Tools

In aircraft industry the life cycle of a product can be defined by four stages: definition, development, manufacturing and support. Definition can be subdivided into preliminary design or pre-design and detailed design. The pre-design phase starts with the engine architecture definition, in which performance targets are set for the whole engine and for each of its main components. During that phase, several designs and technical solutions are considered for the main components, and their impact on performance is estimated. Finally, thanks to CFD, component design is completed down to the smallest details, and experimentally validated. In addition to rough operation conditions, today aeronautical engines follow extremely severe standards of reliability and performance at minimal manufacturing cost along with a maximal TBO (Time Between Overhaul) and optimal maintainability. All these criteria have become design constraints, subjected to evaluation and measurement from cradle to end-of-service time.

The importance of the aeronautics sector and the complexity of the aircraft engines combined with manufacturing costs have led the aeronautics community to establish technical standards and publish reports worldwide in order to enable decision-making instances to wisely plan for research and development priorities and adequate funding. In some of the latter reports, engine performance modelling peculiarities are specified [87].

1.2.1 Overview

Aeroengine design treats several systems such as the gas path, fuel system, rotors and other moving mechanical components, and FADEC[1]. From the conceptual design stage to the detailed design stage, all the systems of the aeroengine are parametered and engineered in order to achieve a performance target. Today aeroengine performance includes the following criteria:

- Design point
- Off-design and transients
- Exhaust pollutant emissions
- Noise
- Starting time
- Acceleration time

The design point matches with typical customer use. Concerning gas path design, design point analysis includes the optimization of the gas path components. Three categories of factors can be manipulated: the choice of compressor pressure ratios and TITs, the comparison of different engine configurations such as single, twin or three spools, the numbers and types of stages for compressors and turbines.

Gas turbine models used in numerical simulations can be classified by means of accuracy, fidelity and detail criteria. **Accuracy** is the ability of a model to match target values linked to performance or internal conditions. **Fidelity** reflects the depth and sophistication of the model representation with respect to the real physical phenomena involved in the gas turbine and **Detail** represents the amount of simulated parts of the engine. Table 1.1 gives an example of the way the importance of these three criteria changes during the engine life cycle.

Table 1.1 – Model fidelity, accuracy and detail needs through the engine life cycle, from [87]

	Accuracy	Fidelity	Detail
Conceptual	Low	Low	Low
Detail Design	Medium	High	High
Test & Validation	High	Medium	Low
Fleet Support	High	Low	Medium

1.2.2 System Modelling for Preliminary Design

In that phase, many teams of engineers proceed with sizing and sensitivity studies. These studies typically address parameters related to full aeroengine control and sub-systems with respect to mission analysis, such as the injection and the cooling systems, as well as main gas path components features. These activities are conducted with the help of 0D and 1D simulations featuring relatively simple mathematical models and data from previous studies. According to [77], three modelling methods are commonly used for gas turbine performance analysis.

[1] Full Authority Digital Engine Control

1. The linear small-perturbation modelling method [113], is based on a linear approximation of the engine functional parameters developed about a specific operating point. Such a method is used for dynamic response and stability analyses mainly associated with actuators and other types of moving mechanical parts.

2. The full range linearized approach model is obtained by extending the linear small-perturbation method presented above, and modelling the partial derivatives as functions covering the full system operating range. Such an approach facilitates the study of full-range fuel throttle changes.

3. The component-based approach relies on mathematical relations developed from the aerodynamic, thermodynamic, and mechanical properties of the main modules of the engine, which are the compressors, combustor, turbines, etc. The component-based models are integrated to form a complete model of the aeroengine, Figure 1.5.

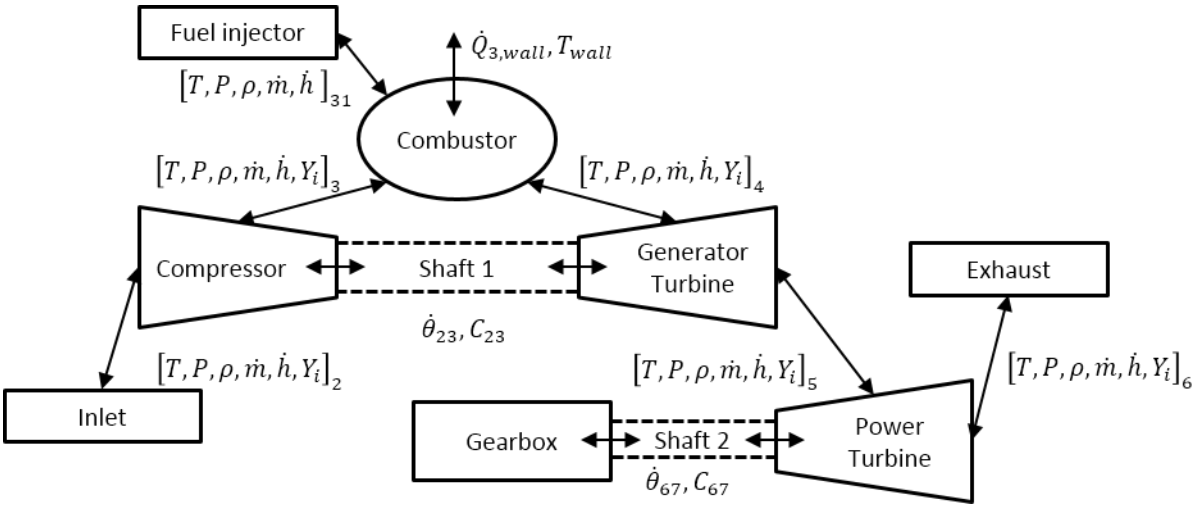

Figure 1.5 – Schematic representation of a helicopter turboshaft system. The arrows and double-sided arrows between components represent the exchange of aerothermal information; namely temperature, T, static pressure, P, density, ρ, mass flow rate, $\dot{m}$, specific enthalpy flow rate, $\dot{h}$, heat flow rate exchanged through combustor walls, $\dot{Q}_{wall}$, and species mass fractions, Y_i. The variable $\dot{\theta}$ stands for shaft angular velocity and C is torque.

Also according to [113], the component-based modelling approach is the most rigorous and the most complete of the three techniques listed above. Therefore, the component-based approach is selected and focused on in this work. According to that 0D/1D level approach, the compressor and turbine models are respectively based on tables matching with compressor and turbine maps similar to the maps shown in Figure 1.4. However, the combustor, which is the focal point of this thesis, is commonly considered as a box that receives hot air with given thermodynamic coordinates, and a mass flow rate of fuel characterized by a given Lower Heating Value (LHV) [51, 77]. Then energy rise and pressure drop are calculated. Emissions may also be computed either by correlations [1, 121, 127] or using chemical kinetics [84].

As a matter of fact, component-based performance simulations can involve local or global iteration schemes. In local schemes the equations for each component are solved locally inside nested loops, whereas global schemes simultaneously handle all the variables from all the components at each iteration. In opposition to local iteration schemes, global iteration

schemes are more advantageous since they can be easily used for different engine types and have better convergence properties. Indeed, local schemes are intrinsically model-dependent, which makes them impractical to apply on different engine types.

1.2.3 High-Fidelity Models for Detailed Design

Moving from the preliminary design phase to the detailed design phase leads towards a more refined definition of the engine and also more commitment to the chosen system and component specifications. In that phase, in addition to fully detailed component modelling and prototyping, extensive experimental measurements conducted on component test rigs and even whole engines prototypes may also be tested. In the meanwhile, CFD is massively used for compressors, burners and turbines. However, nowadays each component cannot be fully modelled in one computation yet because of high CPU time cost. This high cost currently discards the possibility to address several components at once, or several physical domains at once. Nevertheless, coupled computations are being considered between several 3D simulations; that would allow avoiding to mesh very large volumes and focusing the computational resources on the most critical zones; for instance a reactive CFD simulation of the flame region of a combustor would be coupled to a non-reactive CFD simulation of the outlet of that combustor along with a turbine inlet vane and rotor. Another coupling alternative can be the association of high-fidelity 3D CFD with 1D or 0D system simulations.

Chapter 2

Aeronautical Combustors - Technology and Modelling

The combustor also known as burner increases the temperature of a gaseous mixture thanks to the exothermic reaction involving fuel and high-pressure air coming from the compressors. Since World War II, developing this component was a major obstacle that the German, British and American engineers had to overcome in the way to achieve a proper turbojet engine. Today, in addition to its importance for performance, the combustor is a key component to master the environmental impact of aircraft and rotorcraft.

2.1 Burner Technology

The burner is a melting pot of physical phenomena and engineering techniques, and has not completely reached a universal, optimal design yet. Nevertheless, the majority of aeroengine combustors, as depicted in Figure 2.1 and Figure 2.2, feature the following parts: a diffuser, an injector, an igniter, internal and external annuli and the flame tube. The main gas path inside the burner is usually organized in three zones: the Primary Zone, (PZ), in which the flame is anchored and combustion of the incoming fuel-air mixture is achieved; the Intermediate Zone, (IZ), in which the gaseous mixtutre temperature is reduced by the addition of air, allowing the burnout of soot and the combustion of CO and any other unburned hydrocarbons to be completed; and the Dilution Zone (DZ) that allows providing the turbine a gaseous stream with an acceptable temperature in terms of temperature level and distribution.

Fuel is provided by an injector, air is conveyed by a diffuser to three different pathways, the first being the flame tube where combustion takes place, delimited by liner walls, the second and the third being the internal and external annuli that progressively supply additional air to the flame tube through perforations across the liner walls for dilution and walls cooling.

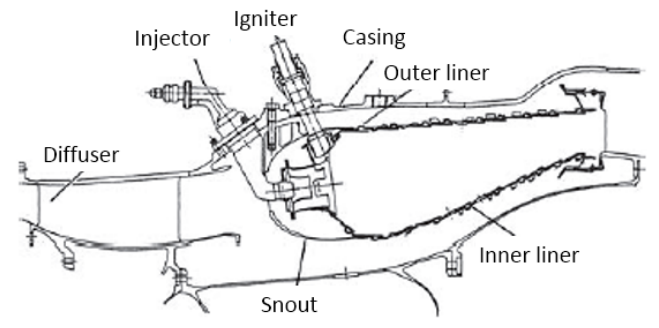

Figure 2.1 – $CF6-50$ annular combustor, from [68].

High-pressure air crosses the diffuser, which allows to recover some of the air dynamic pressure. This passage reduces air velocity and shares the air mass flow rate between the flame tube inlet and the two annuli. In the flame tube, fuel is injected and combustion is triggered. The triggering is done by a start-up igniter on engine start-up, or by a flame if the burner was already lit. Combustion carries on to the intermediate zone in which additional air is introduced through dilution holes. This process maintains temperature below 2000K for reducing pollutant emissions formation. In the dilution zone burned gases are mixed with additional air. Dilution further reduces temperature and improves temperature distribution, in order to protect the turbine blades and the stator vanes.

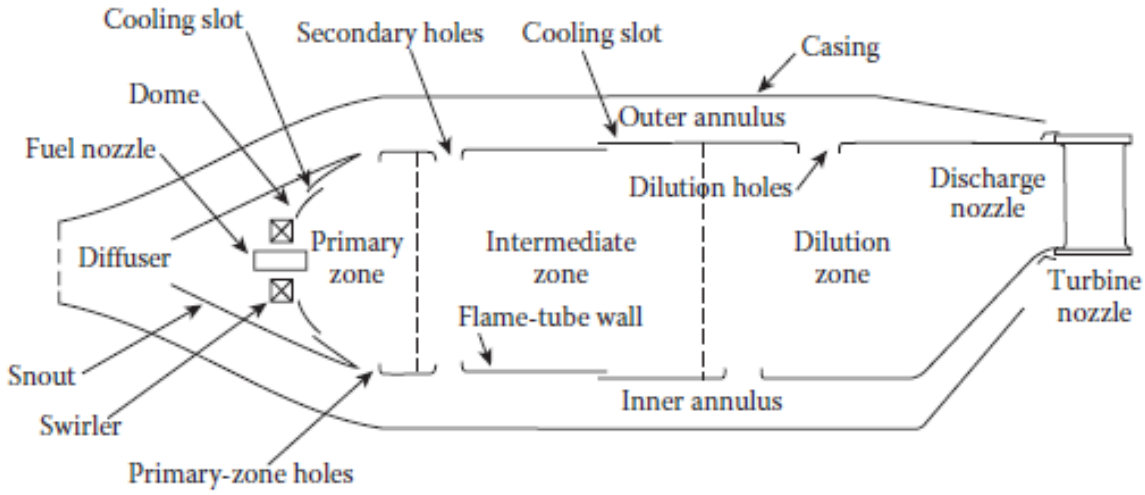

Figure 2.2 – Conventional combustor, from [68].

2.1.1 Combustor Requirements

A gas turbine combustor must satisfy a wide range of requirements whose relative importance varies depending on engine types. However, according to [68], the basic requirements of all combustors may be listed as it follows:

1. High combustion efficiency (i.e. the fuel should be completely burned).
2. Reliable ignition, both on the ground and after a flameout in altitude.
3. Low pressure loss (drop due to aerodynamics and drop due to heat release).
4. Wide combustion stability limits (wide ranges of pressure and air/fuel ratio).
5. No pressure pulsations or other combustion-induced instabilities.
6. An outlet temperature distribution (pattern factor) that maximizes the lives of the turbine blades and nozzle guide vanes.
7. Size and shape compatible with engine flight envelope.
8. Design for minimum cost and ease of manufacturing.
9. Maintainability.
10. Durability.
11. Low emissions of smoke and gaseous pollutant species.

In current aeronautical burners, combustion efficiency has reached a very good level. In 1992, literature [51] stated a value of 0.99 when the engine is running on its design point, and 0.9 when idle. Operation in high altitude, especially relight, is less mastered. According to [68], pressure loss ranges between 2.5% and 5%. Satisfying the above requirements necessitates collaborative multidisciplinary research.

2.1.2 Low Emission Strategies

As mentioned in Part I, low pollutant emissions became a priority. This priority led to the investigation and the development of low-emission gas turbine burners. The key strategy for low NOx burners is to reduce the reaction temperature while achieving temperature homogeneity. Wet low NOx techniques have been previously used: steam or water was injected either directly or via the fuel line or air line within the burner. The method was successful in reducing NOx but caused higher CO and Unburned Hydro-Carbons (UHC) emissions. Wet low NOx also involved high capital and maintenance costs while resulting in increased fuel consumption and corrosion. Thus, engine makers moved to dry low NOx methods. Three main categories of dry-low NOx technologies are currently considered; they are presented in what follows.

The Rich Burn - Quick Quench - Lean Burn Combustor (RQL)

The RQL concept relies on shifting from a fuel-rich combustion to lean-burn combustion and avoid the near-stoichiometric reactions associated with high NOx formation rates, as shown in Figure 2.3. The transition is performed with air jets into the intermediate zone for the reduction of equivalence ratio and temperature.

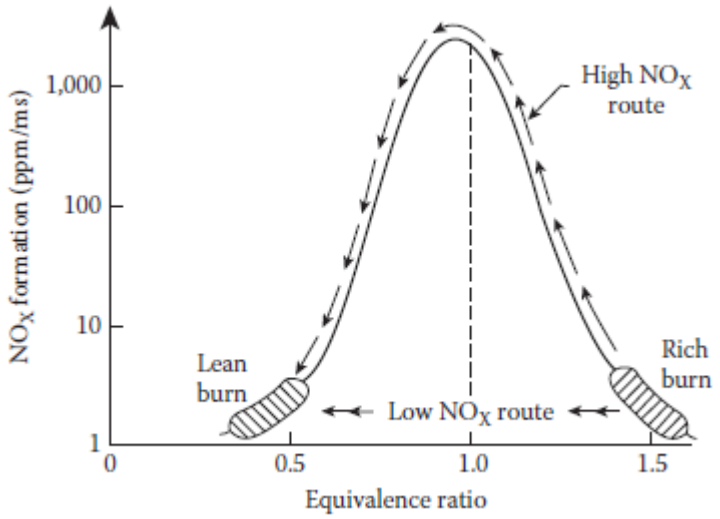

Figure 2.3 – NOx formation associated to the RQL principle, from [68].

This technique can work only if the intermediate zone design is mastered. High soot formation may occur if liquid fuel is used. This results in high flame radiation and exhaust smoke.

Lean Premix Prevaporized Combustor (LPP)

The LPP concept represents the ultimate way for eliminating local regions of high temperature within the flame by mixing the fuel and air and feeding this completely homogeneous mixture to the combustion zone. Its underlying principle is to operate the combustion zone at the

leanest possible equivalence ratio, near the lean blowout limit. The smaller the margin between stable combustion and flame blowout, the lower the output of NOx. A typical LPP combustor can be divided into three main regions. The first region is for fuel injection, fuel vaporization, and fuel/air mixing. It achieves complete evaporation and complete mixing of fuel and air before combustion. In the second region where combustion is completed, one or more recirculation zones stabilize the flame. The flame temperature does not exceed 1900K. Thus the NOx production does not increase with an increase of residence time. The products move to the third region which can be a conventional dilution zone. The main drawback of LPP burners is the high risk of autoignition due to the coexistence of premixed fuel-air reactive mixture at high pressures and temperatures. Another problem, common to well-stirred combustion systems, is that of possible acoustic resonances.

Multipoint Lean Direct Injection(LDI)

In LDI systems, the fuel is directly introduced through multiple injection points into the combustor. Then it is almost instantaneously vaporized, mixed and burned. LDI combustors emit NOx levels comparable to those in LPP burners, while being operated leaner. The critical point in LDI is the fact that it is permanently operated in the near-lean-blowout limit. Thermoacoustic instabilities and flashback often occur in such a kind of combustor.

2.2 The Major Modelling Strategies

Many interacting physical phenomena happen inside a burner on duty. Fuel is injected, vaporized and mixed to high pressure air. Flowing air and fuel are highly turbulent. Turbulence interacts with chemistry and heat transfer. In an industrial context, driven by the requirements listed in section 2.1.1, burner design highly relies on cutting-edge modelling and simulation techniques. At every step of a combustor design cycle, depending on the targeted phenomena and the required fidelity level, a variety of modelling techniques is available. Rule-of-thumb formulae, semi-empirical correlations based on the industry know-how, and system simulation are often used in the early stages of the cycle, in order to determine the bulk features of the combustor. Results obtained in these early stages serve as input to high-fidelity simulations, which are fully deployed in the middle of the detailed design and development cycle.

2.2.1 High Fidelity Simulation

High-fidelity or dimensional methods are extremely useful when it comes to getting spatial and temporal precision for studying turbulent flows, thermodynamic fluctuations and chemical mechanisms. Fidelity and accuracy increase with computation time, Figure 2.4. A comparison between RANS, LES and experiments has been done by [12]. That comparison confirms that LES is much more suitable for turbulent combustion in burners. However, the study also points out the fact that engine makers and OEM would still need RANS in conjunction with LES for DOE (Design Of Experiments) and sensitivity studies. A more detailed overview of the different modelling approaches is given in what follows.

Direct Numerical Simulation (DNS) Method

Running a DNS is the most straight-forward way to solve the balance equations for mass, momentum, species and energy. This technique requires discretizing the computational domain into a very fine mesh. The distance between grid points should be small enough so that all the physical scales of the phenomena involved in the problem are captured. Hence, a full burner would require an extremely dense grid, which is prohibitively costly even on

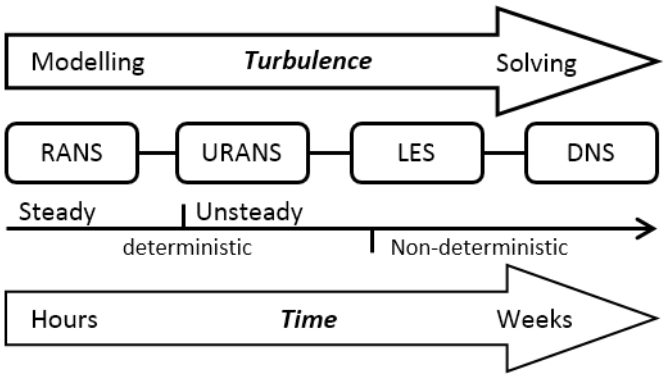

Figure 2.4 – CFD methods overview.

the latest massively parallel computer clusters. Another drawback is the great amount of data generated by the calculation, which requires a non-negligible storage space, and post-processing effort and time. The DNS computations allow a highly detailed observation in fluid dynamics, which allows an in-depth analysis and good unerstanding of the physics, and remain more advantageous than real experiments in many cases [39, 83]. The DNS computations can be very helpful in developing models for other classes of methods. For instance, [81] used DNS computations for the investigation of flame-turbulence interactions; this understanding was then used to develop RANS models based on physical considerations. Among the subjects assessed by DNS one can cite combustion, multiphase flows, radiation, primary and secondary break-up of liquid sheets, thermoacoustic instabilities, aeroacoustics, etc.

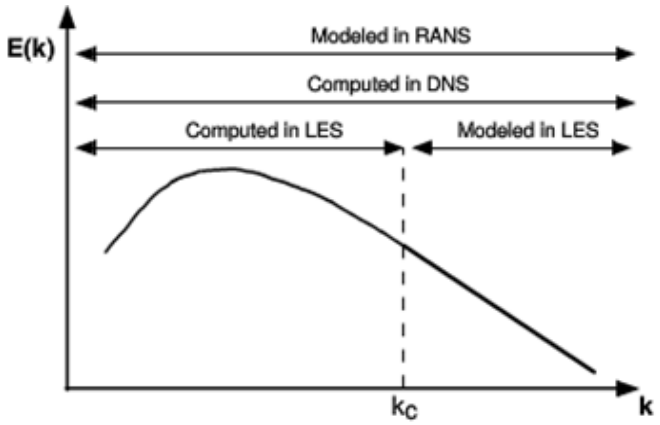

Figure 2.5 – Turbulent kinetic energy spectrum from [96]. The full range is modelled in RANS, while DNS solves the Navier-Stokes equations all along the spectrum and LES solves up to a wave number value k_c and models what is beyond.

Large Eddy Simulation (LES) Method

In this type of simulations, the structures which are larger than the mesh element or volume size are resolved, while the smaller structures are modelled. In the conservation equations for mass, momentum, species and energy, all the quantities are spatially filtered [111], either by using an explicit filtering function, or implicitly filtered as a consequence of the mesh refinement. In the resulting set of equations, unclosed terms remain and need to be modelled. These parts correspond to the sub-grid scale. Many models were suggested for the unclosed

terms. Reactive LES allows a fairly accurate prediction of unsteady velocity and temperature fields inside the combustor, which is very beneficial to addressing its challenging design. In the detailed design phase of a given gas turbine burner, LES can be considered today as the best compromise between physical understanding and computational resources. However, the boundary conditions setup can be delicate. The combustor liner, for instance, often features multiple small-diameter cooling and dilution perforations. These perforations would greatly increase the computational cost if they were to be explicitly represented in the mesh. Thus, multi-perforations are often lumped into equivalent porous surfaces. These surfaces are generally characterized by semi-empirical correlations. These correlations are often established by the designers using experimental measurements.

Reynolds Averaged Navier-Stokes (RANS) Method

All the quantities of the conservation equations are split using the Reynolds and Favre average operators. However, there is no spatial filtering.

$$\text{Reynolds average:} \qquad \bar{g} = g - g' = \frac{1}{t}\int_0^t g(t)dt \tag{2.1}$$

where g' is the fluctuating part and $\bar{g}$ is the mean value of the variable g. The mean parts are considered to be the deterministic components of the quantities. The fluctuating parts can not be directly resolved and therefore must be modelled. Reynolds stresses, species and enthalpy laminar and turbulent fluxes and species chemical reaction rates remain unclosed and require modelling. The pressure-velocity correlation term is usually neglected in RANS numerical codes.

2.2.2 Global System Simulation

System simulation of combustors is a crucial support for early design stages and it is also a useful tool for supplying input data to detailed design and simulation. System simulation of combustion focuses on combustion efficiency, η_{comb}, which can be expressed as in [66] by:

$$\eta_{comb} = \kappa\,(\dot{m}_A)^{-1}\left(\frac{1}{evaporation\,rate} + \frac{1}{mixing\,rate} + \frac{1}{reaction\,rate}\right)^{-1} \tag{2.2}$$

where κ is a constant coefficient and $\dot{m}_A$ is the air mass flow rate.

Depending on the relative contribution of each term in the RHS of equation 2.2, a reactor modelling approach can be formulated. Thus, these models rely on the assumption that combustion would be either evaporation-controlled, mixing-controlled or chemistry-controlled. The latter assumption is the most frequent in current high-speed simulation software, in particular in the Stirred Reactor Models, detailed in the following.

Elementary Stirred Reactor Models

A Well Stirred Reactor (WSR) or Perfectly Stirred Reactor (PSR) is defined by a control volume, an inlet and an outlet. In the control volume of a WSR, perfect mixing is assumed, Figure 2.6. Accordingly, chemical reactions occur at the same rate at each and every location within the gas volume, and a single temperature and set of species concentrations describe the evolution of this system.
A Plug Flow Reactor (PFR), displayed in Figure 2.7, is a steady-state 1D reactor with no mixing in the axial direction. A perfectly mixed fluid is assumed in the radial direction. The working fluid is a perfect gas, the flow is non-viscous and thermal conduction is assumed to be null. The reactor flow properties can be expressed as functions of the distance.

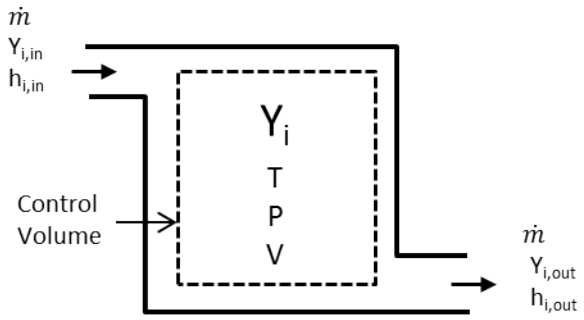

Figure 2.6 – Well Stirred Reactor, also known as PErfectly Stirred Reactor.

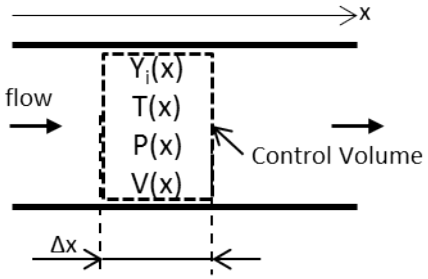

Figure 2.7 – Plug Flow Reactor.

These elementary models stand-alone are not suitable for modelling aeronautical combustors, but they can be connected to form networks, Figure 2.8.

Stirred Reactors Network: Combinations of Mixing-Controlled and Chemistry-Controlled Models

A real combustor can be thought of as a combination of WSR and PFR, Figure 2.8. In 1973, Swithenbank presented a model based on this concept [121], predicting blow-off stability limits, combustion efficiency and intensity, as well as pressure losses. It enabled the access to other variables by means of further analysis. Some of these are NOx and UHC emissions, noise efficiency, ignition capability and flame-system oscillations. This conceptual model is represented in Figure 2.8.

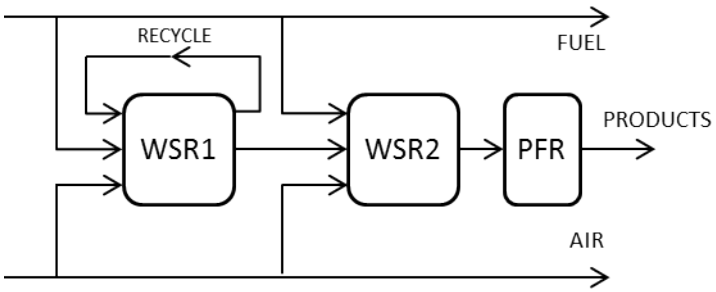

Figure 2.8 – Conceptual model of a gas turbine combustor using combinations of WSRs and PFRs, from [121].

An exhaustive steady state combustor simulation project [119], was also based on a

network approach representing the flame tube and the annuli by chains of WSR. It featured a simple mixing model, a constrained equilibrium combustion model as well as a conductive, convective and radiative heat transfer model. The approach was validated against several aeronautical and industrial configurations, and good agreements of pressure loss, mass flow rate split and liner temperatures were obtained with experimental measurements. However, the mixing model featured in that approach was not adapted to swirl combustors, and it was only meant for steady-state design operating conditions. Another physical burner model with a primary zone, Figure 2.2, made of 16 PSR was also developed [1]. In this model, unmixedness was represented by a normal distribution function [102]. The model was dedicated to pollutant emissions prediction, Section 3.3.1. More details about this approach are given in Section 3.3.1.

Chapter 3

Combustion and Pollutants

In gas turbine burners, both turbulent premixed and non-premixed flames can be observed; one type prevails on the other depending on the air and fuel injection technologies and the physical state of the injected fuel. Conventional aeronautical burners, in which liquid fuel is directly injected inside the flame tube, mostly feature non-premixed jet flames. Conversely, when fuel is prevaporized and efficiently mixed with air before reaching the flame, as in LPP burners, the flame would be considered as premixed. However, perfect mixing is impossible to reach, and for security reasons, fuel and oxidiser are always separately stored and separately injected in aeroengines. Therefore, the most common scenario combines premixed and non-premixed flame regions. In addition, when operating conditions are varied, shares of premixed and non-premixed flames contributions may vary in return.

The flame type provides the conditions that enable the formation of different pollutants. Accordingly, a multi-flame-type burner can potentially emit all pollutant types at once. The next sections refer to the phenomenology of the flames, and brielfy summarize some combustion modelling approaches. In turbulent combustion, chemistry and mixing can be approached by means of different paradigms. These paradigms have been reviewed and discussed by [5], and briefly summarized in Table 3.1.

3.1 Premixed Flames

When fuel and oxidizer are perfectly mixed before reaching the reaction zone, the flame is called premixed. In that case, the heat released by the reaction enables the flame to propagate towards the fresh gases mixture, Figure 3.1.

A key variable for describing premixed combustion is the progress variable, c, given by:

$$c\left(\vec{x},t\right)=1-\frac{Y_F\left(\vec{x},t\right)}{Y_{ug,F}\left(\vec{x},t\right)} \tag{3.1}$$

where $Y_F\left(\vec{x},t\right)$ is the fuel mass fraction at a given time t, at the spatial coordinates defined by $\vec{x}$, and $Y_{ug,F}$ is the fuel mass fraction present in the fresh gases zone. The progress variable c is equal to zero in the fresh gases zone and it becomes equal to one in the burned gases zone.

Premixed flames were characterized by reaction rates [45, 129], temperature, thickness [9], stretch [25, 31, 41, 79] and speed [9, 41, 82, 95, 122] as they propagate towards reactant streams. These features as well as the main premixed flame modelling paradigms are discussed in what follows.

3.1.1 Laminar Premixed Flames

Laminar premixed flames have a few practical applications such as heating appliances and Bunsen burners. Neverthless, according to [96], the importance of studying laminar premixed

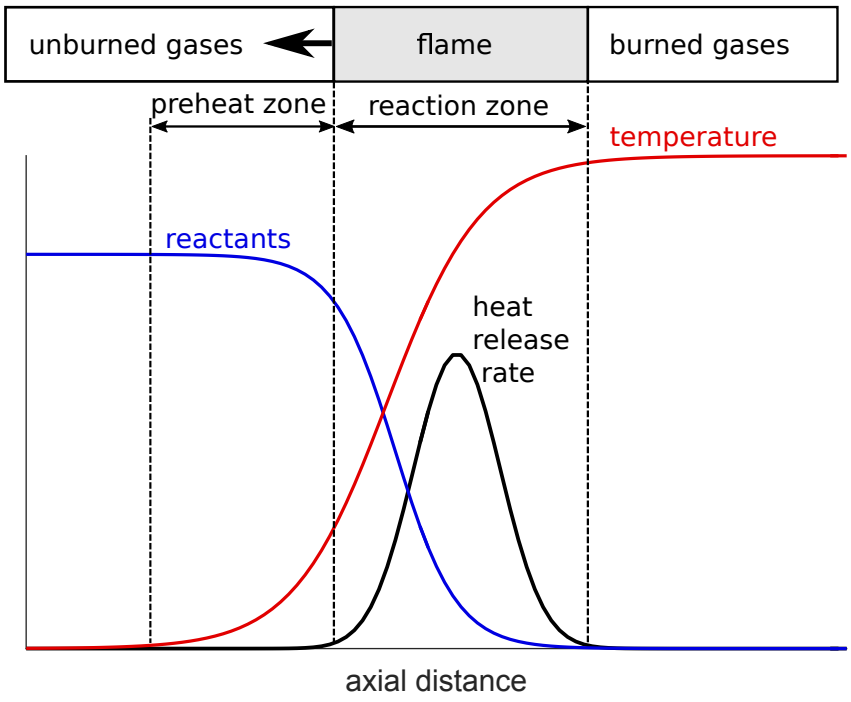

Figure 3.1 – Basic configuration and structure of a laminar premixed flame.

flames configurations, and one-dimensional laminar flames in particular, goes beyond these few applications because:

- Detailed comparisons between theory, experiments and computations can be performed.
- Chemical models can be validated.
- Flame structures and instabilities can be studied by theoretical approaches.
- In many paradigms of turbulent combustion modelling, laminar flames are seen as the elementary entities building turbulent flames.

Laminar Premixed Flame Speed

According to combustion theory [96], there is no unique definition of the laminar flame speed but rather three definitions:

- Global consumption speed, $S_{L,GC}$, which may be defined from the integral of the fuel burning rate across the flame, giving the following relation:

$$S_{L,GC} = -\frac{1}{\rho_{ug} Y_{ug,F}} \int_{-\infty}^{+\infty} \dot{\omega}_F dx \tag{3.2}$$

  where $\rho_{ug,F}$ is the unburned fuel density, $Y_{ug,F}$ is the unburned fuel mass fraction, $\dot{\omega}_F$ is the fuel reaction rate, and x is the spatial coordinate along which the flame propagates.

- Absolute displacement speed, $S_{L,A}$, is the local speed at which a given point of the flame front represented by an iso-level of progress variable c moves relative to the laboratory

frame, and it is given by:

$$S_{L,A} = \vec{v}_{fl}\vec{n} = \frac{1}{|\nabla c|}\frac{\partial c}{\partial t} \tag{3.3}$$

where $\vec{v}_{fl}$ is the flame speed in the laboratory coordinate system, and $\vec{n}$ is the normal to the flame front, given by:

$$\vec{n} = -\frac{\nabla c}{|\nabla c|} \tag{3.4}$$

- Relative displacement speed, $S_{L,D}$, is the difference between the gas stream speed, $\vec{v}_{gas}$, and the flame front speed, $\vec{v}_{fl}$. $S_{L,D}$ is given by:

$$S_{L,D} = (\vec{v}_{fl} - \vec{v}_{gas})\,\vec{n} \tag{3.5}$$

$$= \frac{1}{|\nabla c|}\frac{\partial c}{\partial t} + \vec{v}_{gas}\frac{\nabla c}{|\nabla c|} \tag{3.6}$$

Local flame speeds, $S_{L,A}$ and $S_{L,D}$, represented in Figure 3.2, depend on the iso-level of c at which they are measured, while $S_{L,GC}$ results from an integral over all c values accross the flame.

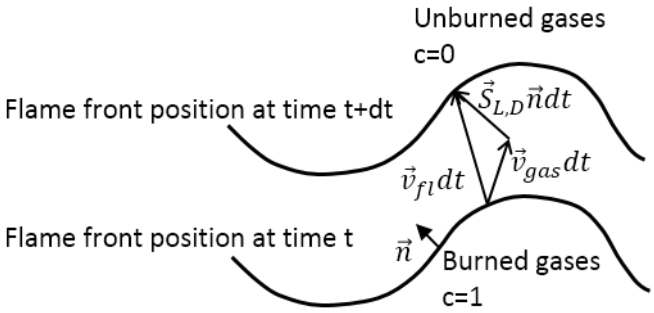

Figure 3.2 – Local flame speed definitions, after [96].

Laminar Premixed Flame Thickness

As summarized by [15], laminar flame thickness can be defined in many ways such as total thickness, δ_L^t, diffusion thickness, δ_L^0, and reaction thickness, δ_r^0. All these definitions can be compared by referring to a premixed combustion characteristic 1D temperature profile, Figure 3.3. Total thickness is the thickness over which the temperature changes from its value in the fresh gases zone, T_{ug}, to its value in the burned gases zone, T_{bg}. Diffusion thickness, which is considered in this thesis, is the ratio of the fresh gas thermal diffusivity, $D_{th,ug}$, to la minar flame speed, S_L:

$$\delta_{L,0} = \frac{D_{th,ug}}{S_L} = \frac{\lambda_{ug}}{\rho_{ug} c_{p_{ug}} S_L} \tag{3.7}$$

where λ_{ug} is the thermal conductivity of the fresh gases mixture and $c_{p_{ug}}$ is the unburned mixture specific heat at constant pressure. δ_L^0 can also be approximated from the temperature profile as reported in [96] by:

$$\delta_L^0 = \frac{T_{bg} - T_{ug}}{max\left(\left|\frac{\partial T}{\partial x}\right|\right)} \tag{3.8}$$

The thickness of the reaction zone, δ_r^0, is commonly considered as being equal to the half-height width of the total combustion heat release rate.

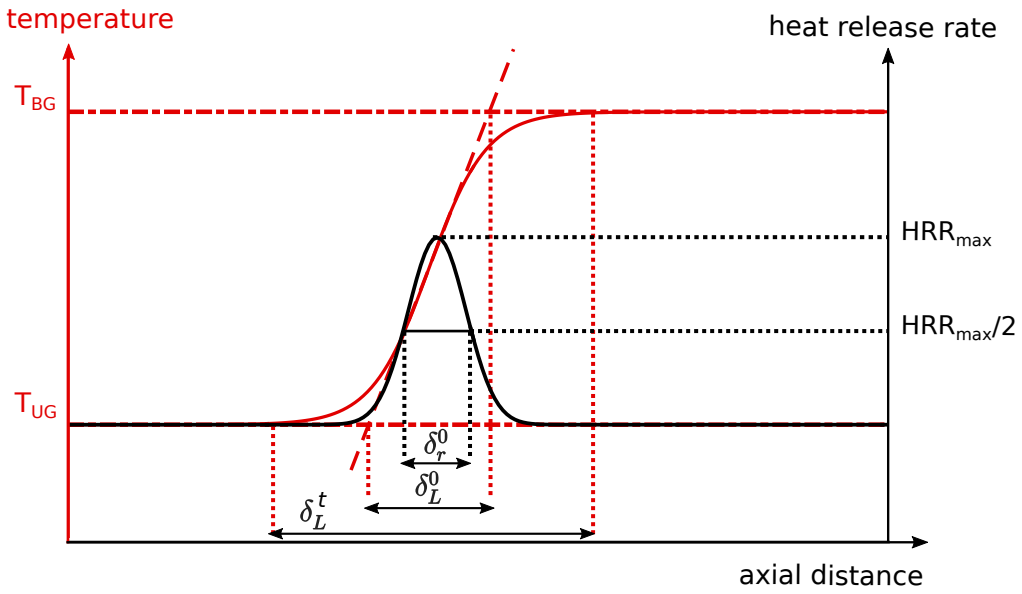

Figure 3.3 – Laminar premixed flame thicknesses, from [15].

3.1.2 Turbulent Premixed Flames

In most of the industrial applications based on combustion systems, reactant streams are turbulent, which often yields turbulent flames. Turbulent flames feature higher combustion rates than laminar flames, and their description combines attributes similar to those of laminar flames, such as flame speed, and also temporal and spatial scales that characterize turbulent flows.

Turbulent Premixed Flame Speed

As pointed out by [41], there is no unique definition for S_T, but rather three definitions:

- Global consumption speed $S_{T,GC} = \dfrac{\dot{m}_F}{\rho_{ug,F} A_T}$
  where $\dot{m}_F$ is the fuel mass flow rate. $S_{T,GC}$ is obviously the speed at which fuel consumed. To use this definition it is necessary that all of the reactants pass through the flame.

- Local consumption speed $S_{T,LC} = S_L I_0 \int_{-\infty}^{+\infty} \Sigma dn$
  where I_0 is the turbulent flame stretch factor, Σ represents flame surface density , and $\vec{n}$ is the coordinate normal to the flame front defined by an iso-value of combustion progress variable, namely $c = 0.5$.

- Local displacement speed $S_{T,LD} = (\vec{v}_{fl} - \vec{v}_{gas})\,\vec{n}_L$ where $\vec{v}_{fl}$ is the flame speed in the laboratory coordinate system, while $\vec{v}_{gas}$ is the velocity of the reactant stream through which the flame is propagating, and $\vec{n}_L$ is the coordinate normal to the leading edge of the flame.

Global consumption speed was considered in this thesis.

Turbulent Premixed Flame Regimes

Attempts have been made to categorize turbulent premixed flames, such as in [11, 17, 94], by comparing the various time and length scales characterising turbulent structures and flames,

in order to ease their physical analysis. In that process, the key flow scales are the turbulent integral length scale, l_T, the turbulent velocity fluctuations, u'. Flame characterising variables are those of laminar flames, S_L and δ_L^0. Comparing flame and flow velocities and length scales allowed the classifiation of turbulent premixed combustion configurations into several combustion regimes, Figure 3.4. In the wrinkled flamelets regime, chemical reactions are faster than mixing, and they occur in thin sheets. According to Damköhler's paradigm [37], which is considered in this work, flame surface wrinkling affects thin reaction layers, which retain the characteristics of a laminar flame. Flame wrinkling is usually expressed as ratio of turbulent to laminar flame speeds, respectively S_T and S_L, equivalent to the ratio of turbulent to laminar flame surfaces, respectively A_T and A_m:

$$\Xi = \frac{S_T}{S_L} = \frac{A_T}{A_m} \tag{3.9}$$

In the thickened wrinkled flames regime, according to [91], chemical characteristic time is very close to turbulent time scale and turbulent structures which enter the flame can penetrate into the preheat zone and broaden it, but cannot modify the flame structure. However, another study [41] discards the idea of attributing preheat zone broadening to turbulence and suggests that it would be due to high strain rates instead. The third combustion regime is the thickened flames regimes, also called distributed-reaction regime. In this reaction regime, small turbulent scales may enter the flame front. According to [125], flames reactions cannot be sustained in such conditions, in opposition to slow reactions like nitric oxide formation.

3.1.3 Premixed Combustion Modelling

Many models were developed for RANS and LES of turbulent premixed combustion, and were detailed and reviewed by several sources [5, 41, 96]. Models that rely on the assumption that the flame front is infinitely thin, such as the level set approach and the Flame Surface Density (FSD) paradigm, are often extensions of the Damköhler paradigm, and address the flamelet regime. Other models like the Eddy Break Up (EBU) model [117] rather match with the distributed reaction regime.

In the level set approach detailed by [94], the flame front is assumed to be infinitely thin. A function, $G(\vec{x}, t)$, is used to identify the flame surface, taking the iso-value G_0 on the flame front. $G < G_0$ in the unburned mixture while values of $G > G_0$ represent fully burned gas. A transport equation for G is obtained by means of kinematic considerations and flame surface density is directly linked to $|\overline{\nabla G}|$.

The FSD paradigm, initiated by [18, 25, 78, 98], is in many ways similar to the level-set approach. In the FSD paradigm, the flame is once again assumed to be infinitely thin and mean reaction rates are determined by the product of the available flame area per unit volume by the local consumption rate per unit of flame area. This paradigm has lead to the Coherent Flame Model (CFM), detailed in the next paragraph.

The idea behind the EBU model [117] is to assume that the reaction rate is controlled by turbulence rather than chemistry. The hypotheses are a Reynolds number and a Damköhler number both much greater than unity. The reaction zone is represented as an assembly of fresh and burned zones transported by turbulent structures.

The Bray Moss Libby (BML) paradigm [19] assumptions allow to express the mixture thermochemistry as a function of a progress variable. That variable can be a normalized temperature or a normalized concentration product. Mean quantities are expressed in terms of Probability Density Functions (PDF), written in three parts, respectively associated to

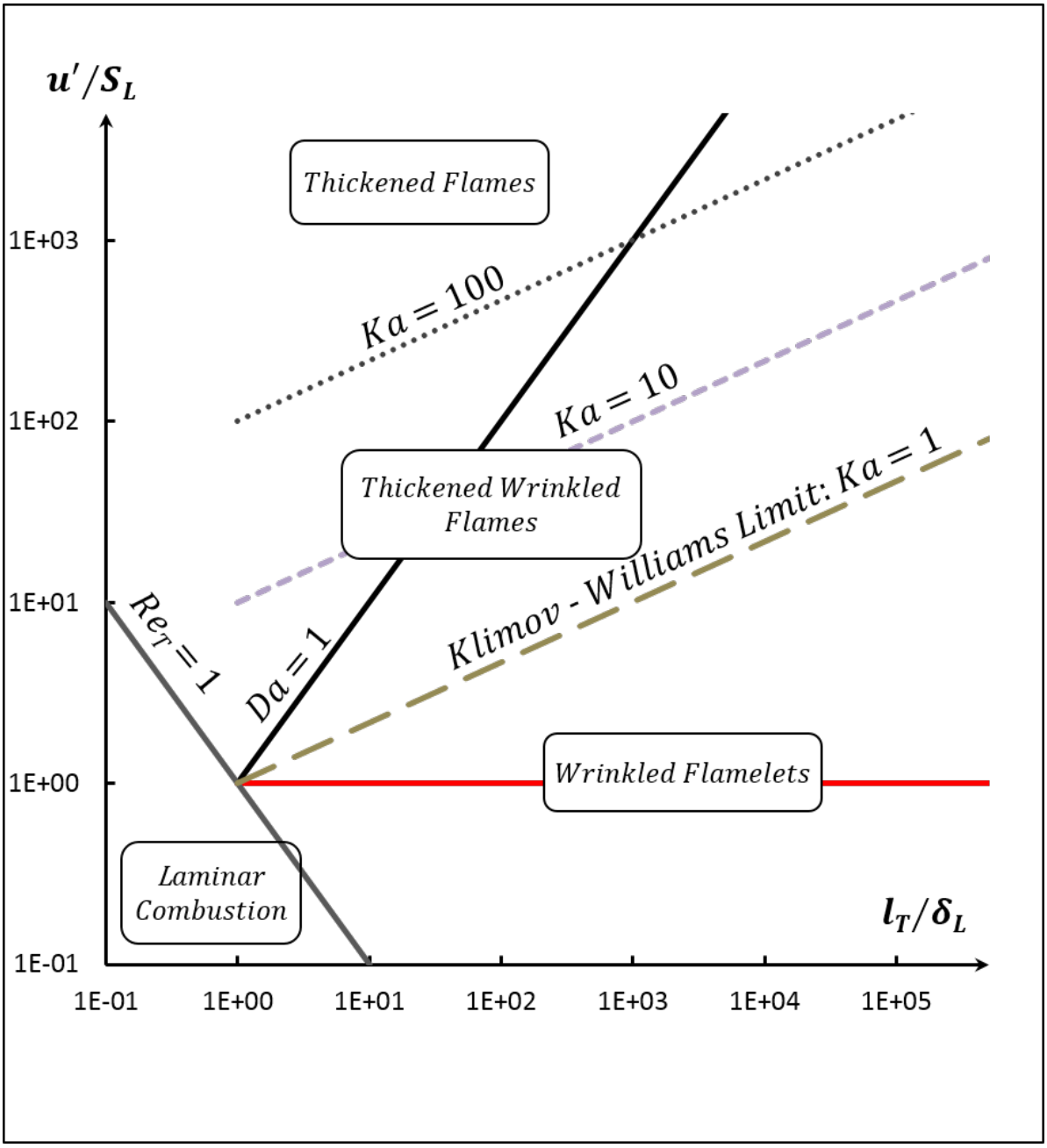

Figure 3.4 – Turbulent premixed combustion regimes diagram, from [91].

unburned reactants with probability $\alpha(x)$, burning mixture with probability $\gamma(x)$, and burned products with probability $\beta(x)$.

Thickened Flame Models

Rather than assuming an infinitely thin flame front and dealing with it, the thickened flame paradigm multiplies the flame thickness by a given factor, so that it can be resolved on a computational mesh. That paradigm was initiated by [23]. One of its modelling variants is the TFLES method [33]. Figure 3.5 illustrates the flame front thickening approach.

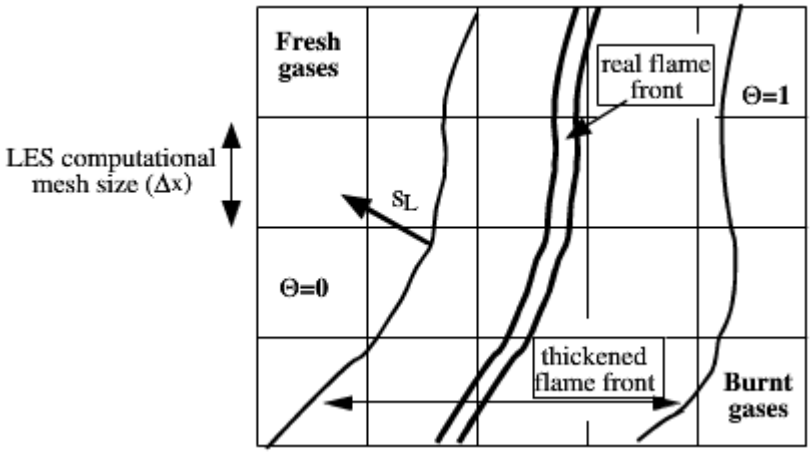

Figure 3.5 – Artificially thickened flame. The flame speed is conserved, Θ represents the combustion progress variable, S_L is the laminar flame speed. From [96].

One commonly used variant of the tickened flame paradigm is the Dynamically Thickened Flame LES combustion model [69], in which thickening only occurs where a flame is detected by means of a given sensor function.

CFM Models

This formalism was initially proposed in [13, 24, 42]. It generated several variants. Some of them were thoroughly used for automotive engines [101] and reactive CFD simulation of aeronautical combustors [64]. In the CFM formalism, Fresh Gases (FG) and Burned Gases (BG) are separated by a flame front propagating from the burned region towards the fresh gases mixture. The flame front is seen as an infinitely thin surface wrinkled by the turbulent flow field, and it propagates at the laminar flame speed, S_L. Fuel oxidation occurs in the flame front, which is very thin compared to turbulent scales.

3.2 Non-Premixed Flames

In non-premixed or diffusion flames, the oxidizer and fuel are separated and located on different sides with respect to the reaction zone where the flame front is located. The structure of a diffusion flame in its basic configuration is represented in Figure 3.6. According to [96], diffusion flames do not propagate; therefore a non-premixed flame cannot be characterised by a reference speed. Diffusion flames cannot be characterised by reference thicknesses neither, since the thickness of an unstrained diffusion flames increases with time, while the thickness of a strained flame is not an intrinsic characteristic of the flame but rather depends on flow

motions. Non-premixed turbulent flames can be analysed in the scope of flame/vortedx interactions. The flame stabilizes in mixtures close to stoichiometric conditions. In the case of turbulent non-premixed combustion, diffusion flames dynamics highly depend on turbulence and need stabilization, which becomes a crucial design criterion for burners. The stabilization method depends on the inlet oxidizer speed with respect to S_L^0, the stoichiometric laminar premixed flame speed [96]. The inlet oxidizer flow velocity ranges from 8m/s in a reverse flow combustor to 41m/s in a straight-through turbojet chamber [16]. In gas turbines fuelled with Jet-A1, the inlet speeds are greater than $10S_L^0$ so the flame is stabilized by recirculation. A non-premixed flame problem can be split in a mixing study and flame structure study. In a flame structure problem, chemistry can be infinitely fast or happen at a finite rate or not occur. Each of these three possibilities obviously involves different physical hypotheses and implies a different mathematical treatment. The infinitely fast chemistry case generates the maximum possible flame temperature for a given combination of reactant species. Diffusion flames drew the interest of many researchers [3, 6, 7, 73, 93].

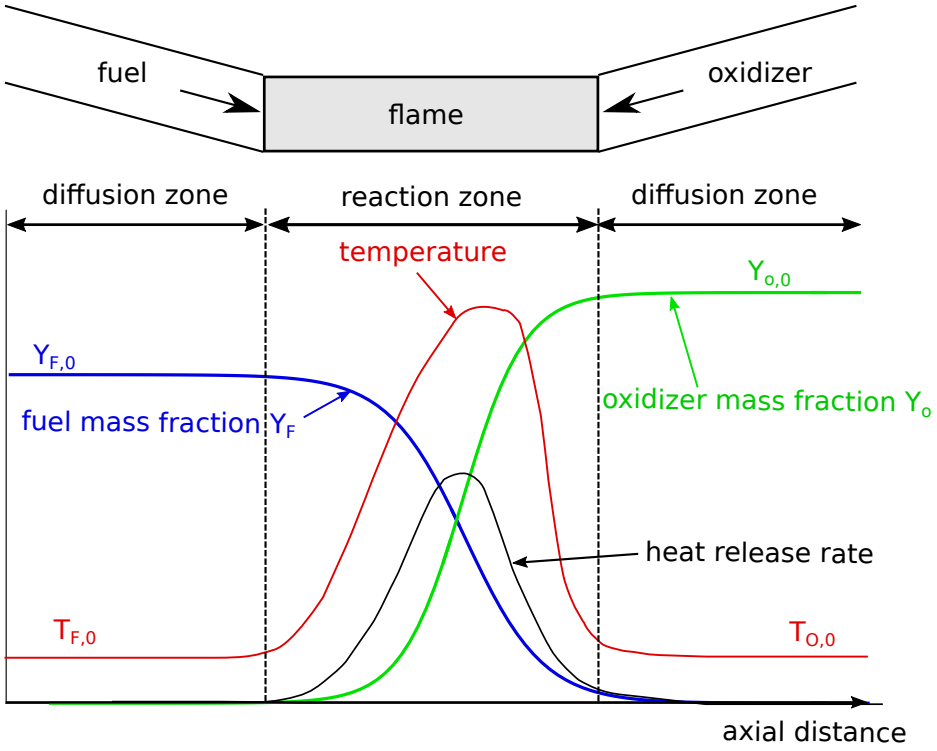

Figure 3.6 – Configuration and structure of a basic non-premixed flame.

3.2.1 Non-Premixed Combustion Modelling

According to‘[5], turbulent non-premixed combustion modelling paradigms were categorized depending on their respective underlying assumptions and modelling strategies for dealing with chemistry and mixing, Table 3.1. The first traceable paradigm was studied by [22]. In that early work, the mixing occurs in a laminar flow by molecular diffusion and the flame is located at the surface where the oxidant and fuel proportions are stoichiometric. The main idea was that chemical rates were faster than mixing due to molecular diffusion. A similar paradigm for turbulent diffusion flames, called mixing-controlled paradigm, was suggested by [54].

The laminar flamelet paradigm emerged after a finding by [92]: the species equations can be locally and instantaneously expressed into the stationary laminar flamelet equation (SLFM)

under particular assumptions. The first assumption is that transient terms are negligible; the second one is to neglect gradients parallel to the surface of the instantaneous surface of the mixture fraction.
According to [5], PDF approach was provided as a more general modelling approach and has become one of the major areas of research. PDF methods have also reached commercial CFD codes for industrial applications.
The Conditional Moment Closure (CMC) is a modelling viewpoint based on the idea that temperature and composition variations in turbulent combustion can be closely cross-linked to key variables such as the fuel mixture fraction [8, 59, 60].
As reported by [5], the CMC and PDF paradigms were unified into Multiple Mapping Conditioning (MMC). In MMC, in place of mixture fractions, m reference variables are considered where m can vary between one and the number of species. These variables may have different natures, e.g. mixture fraction, velocity, scalar dissipation, or other quantities. The distribution of the compositions is then represented by two quantities: the joint PDF of the reference variables and the mean of the species conditioned on the reference variables.
Initially thought for premixed flames, the Thickened Flames approach, described in section 3.2.1, was extended to non-premixed flames and even two-phase flames [10].

Table 3.1 – Paradigms in non-premixed turbulent combustion, after [5].

Paradigm	Chemistry	Mixing
Mixing controlled	Fast for major species	Scaling laws / second order closures
Laminar flamelet	Pre-calculated tables	Laminar counter-flow / second order closure
PDF approach	Already closed / reduced mechanisms	Mixing models
Conditional Moment Closure	Closure in terms of conditional moments	PDF integrals
Multiple Mapping Conditioning	Closure in terms of conditional means	Mapping closure

Modelling Partially Premixed Flames

In modern aeronautical combustion systems, several flames with various levels of mixture fraction can take place at the same time. An effort was made to identify the different combustion modes that occur in such systems. The Takeno flame index, ξ, was proposed by [130]:

$$\xi = \nabla Y_{Fuel} \times \nabla Y_{Oxidizer} \tag{3.10}$$

where Y_i is the mass fraction of the species i. This index is positive for a premixed flame and negative for a non-premixed flame. A normalisation of the Takeno flame index was also proposed by [46, 61]:

$$G_{FO} = \frac{\nabla Y_{Fuel} \times \nabla Y_{Oxidizer}}{|\nabla Y_{Fuel} \times \nabla Y_{Oxidizer}|} \tag{3.11}$$

Accordingly, this dimensionless index, G_{FO}, is equal to -1 in non-premixed regions, and equals to $+1$ in premixed regions. It was experimentally measured by [107], using an NO_2

tracer added to the air, and an acetone tracer added to the fuel. Many combustion models were developed for both premixed and non-premixed flames, and most of them use on variants of G_{FO} or Heaviside functions of G_{FO} and rely on flamelet paradigms for premixed and non-premixed combustion [39, 44, 55]. Other models for partially premixed combustion were proposed based on PDF approaches [72, 105], offering the advantage of being able to handle many different inflow streams of unrelated temperatures and compositions.

3.3 Pollutant Emissions

The major species constituting aircraft exhaust gas are species relative to the excess of atmospheric air (oxygen and nitrogen), mixed with combustion products such as vapour of water, H_2O, carbon dioxide, CO_2, carbon monoxide, CO, unburned hydrocarbons, UHC, Particulate Matter, (PM) and nitrogen oxides (NO_x). CO_2 is not strictly a pollutant but it positively contributes to radiative forcing. The major pollutants are CO, UHC, PM and NO_x. Regulations are getting more stringent. Pollutant emissions measurements and modelling are now key subjects both for air vehicle and engine makers, as well as organisations and agencies like the ICAO, ACARE, ATAG and EPA. The major pollutants generation mechanisms are described below and Table 3.2 summarizes the effects and formation mechanisms of the major aeronautical exhaust gas species.

Carbon Oxide

Large amounts of CO are generated by combustion of rich mixtures. CO can also be formed by CO_2 dissociation in cases of close-to-stoichiometric combustion where temperatures are higher. In combustors, incomplete combustion of the fuel and CO production occurs if the residence time of gases inside the combustion chamber is insufficient, inadequate fuel/air mixing and quenching of the burned gases by entrainment into the liner wall-cooling film in the primary zone. In conventional combustors, as depicted in Figure 3.7, temperatures below 1700K correspond to a rise in CO generation.

Unburned Hydrocarbons

Unburned hydrocarbons include fuel drops and vapours, and hydrocarbons resulting from thermal degradation of fuel into lighter species. They are linked to poor atomization, film-cooling air or inadequate burning rates. The factors that influence CO emissions related to incomplete combustion influence UHC formation in the same manner.

Particulate Matter

Particulates and carbon smoke are generated by the production of soot in the fuel-rich zones inside the burner, i.e. in the vicinity of the fuel spray [68]. In practice, soot formation is governed more by atomization and mixing than by chemical kinetics.

Nitrogen Oxides

Combustion-generated oxides of nitrogen include NO_x and nitrous oxide (N_2O). NO_x include the combined concentrations of nitric oxide (NO) and nitrogen dioxide (NO_2).
The main mechanisms through which NO is formed during combustion are Thermal NO, Prompt NO, Fuel NO and N_2O pathway. Fuel NO results from the combustion of fuels containing organically bounded nitrogen and it is not a major issue for aeroengines.

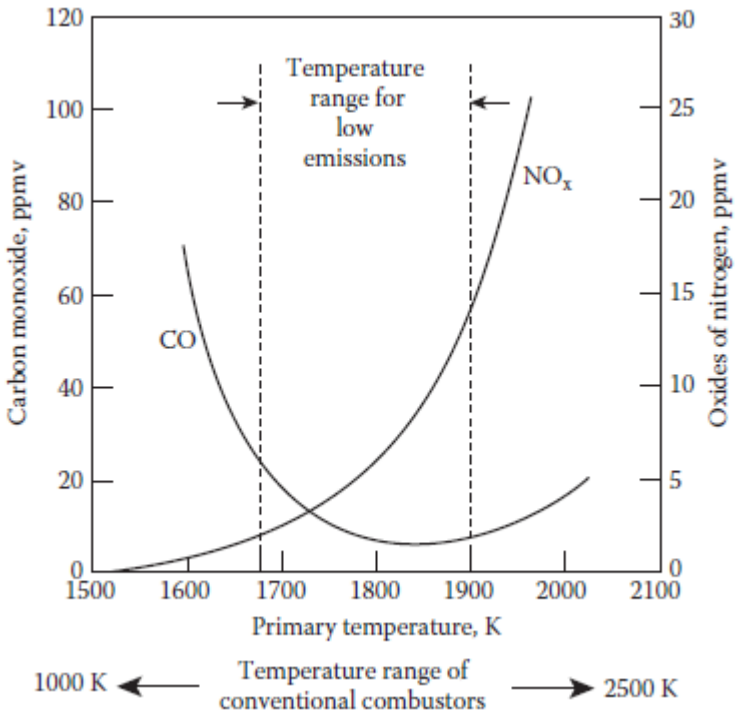

Figure 3.7 – NO_x and CO emissions with respect to temperature, from [68].

The thermal NO reaction scheme can be synthesized by the extended Zeldovich mechanism:

$$O + N_2 \longleftrightarrow NO + N \tag{3.12}$$
$$N + O_2 \longleftrightarrow NO + O \tag{3.13}$$
$$N + OH \longleftrightarrow NO + H \tag{3.14}$$

These reactions take place mainly in high-temperature lean mixture postflame regions of combustion processes and dominate NO_x generation when temperature exceeds 1850K, Figure 3.7. Thermal NO formation rates also depend on pressure. For conventional combustors characterized by high temperatures of combustion, NO increases linearly with residence time [68]. Again according to [68], for lean-premixed burners and equivalence ratios under 0.5, NO formation is independent of residence time.
Prompt NO pathway was first observed by Fenimore as the rapid formation of NO in the flame region. One of the most valid and the most accepted Prompt NO mechanisms is summarized by the following reactions [47]:

$$CH + N_2 \longleftrightarrow HCN + N \tag{3.15}$$
$$N + O_2 \longleftrightarrow NO + O \tag{3.16}$$
$$HCN + OH \longleftrightarrow CN + H_2O \tag{3.17}$$
$$CN + O_2 \longleftrightarrow NO + CO \tag{3.18}$$

N_2O is formed by the following reaction [85]:

$$N_2 + O \longleftrightarrow N_2O \tag{3.19}$$

and the N_2O can be oxidized to NO mainly by the reaction:

$$N_2O + O \longleftrightarrow NO + NO \tag{3.20}$$

and also by the reactions:

$$N_2O + H \longleftrightarrow NO + NH \tag{3.21}$$
$$N_2O + CO \longleftrightarrow NO + NCO \tag{3.22}$$

Table 3.2 – Exhaust gas species effects and mechanisms, from [30].

Species	**Effect**	**Formation mechanism**
CO	Toxic	Incomplete combustion, dissociation of CO_2
UHC	Toxic	Poor atomization, insufficient flame speed, quenching by liner cooling air
C	Toxic	High temperature fuel oxidation under rich FAR in the primary zone, short intermediate zone, poor atomization
NO, NO_2 & N_2O	Toxic, smog precursor, ozone depletor	Thermal, Prompt, Fuel & N_2O
CO_2 and H_2O	Global warming	Fossil fuels combustion

3.3.1 Pollutant Emissions Modelling

There are three major modelling approaches for pollutants formation: *a*) Semi-empirical correlations used for system simulation are based on experimental measurements of pollutant emissions with respect to combustor design and operation parameters; *b*) physical models of ideal chemical reactors such as PSR and PFR are combined pollutant formation models; *c*) detailed chemical kinetics models for CFD codes allow to account for spatial dimensions. All these emissions prediction methods are detailed below.

Semi-empirical Correlations for System Simulation

In engine performance modelling approaches, correlations are generally used for evaluating global pollutant emissions. That choice is based on the availability of sufficient data for the empirical or semi-empirical function identification. Correlation adaptation techniques for gas turbines were reviewed by [123]. This review noted that adaptation is done either through scaling formulas involving measurements and prediction errors, or through optimization algorithms. Many correlations address CO and NO Emission Indices (EI) [68], while only a few such as [103, 104] deal with UHC and soot.

CO According to [67], the primary zone average temperature, T_{pz}, pressure, P_4, and fuel evaporation volume, V_{vap}, are the essential variables for CO formation. A similar formulation was proposed by [104], giving less weight for temperature effect and slightly more importance to pressure, which leads to the following:

$$EI_{CO} = 0.18 \times 10^9 \exp\left(7800/T_{pz}\right)/P^2 \left(t - 0.4t_{vap}\right) \left(\Delta P/P\right)^{0.5} \tag{3.23}$$

where t_vap is a characteristic fuel evaporation time.

NO_x NO_x are the species that have witnessed the greatest effort of prediction through correlation. A short list is presented in Table 3.3. In most of these semi-empirical models the NO_x Emissions Index, $EINO_x$, is based on the Arrhenius equation of the form:

$$EINO_x \propto A \exp kT \tag{3.24}$$

where A is a pre-exponential constant, k is an empirical coefficient and T is temperature. Some of these models introduce pressure [36, 71] and some of them include air mass flow rate, $\dot{m}_A$ [67]. Some formulations feature, ϕ, the fuel/air equivalence ratio [106]. Gases residence and/or spray evaporation characteristic times were added to some models [68, 104]. One NO_x Emissions Index prediction model developed by [74], was validated against a set of 2124 experimental data points realized with 11 different gas turbine chambers, and the standard deviation was only 25%, which is considered to be satisfactory for a rough estimation of global emissions indices.

Table 3.3 – NO_x estimation correlations, from [56, 68].

No.	Author	Year	Engines	Parameters
1	Lewis [56]	1981	wet low-NO_x	calibrated constants
2	Lefebvre [68]	1984	GE J79-17A, F101	burner volume
3	Odgers & Kretschmer [68]	1985	aircraft, industrial	$0.8ms \leq t_{form} \leq 2.0ms$
4	Lewis [68]	1991	dry low-NO_x	
5	NASA [36]	1992	used in Gasturb	*war*
6	Rokke [68]	1993	natural gas industrial, 1.5 to 34MW	
7	Rizk & Mongia [68]	1994	conventional spray burners	t_e fuel evaporation time
8	Bakken & Skogly	1995		
9	Dopelheuer & Lecht [40]	1998	CF6-80C2B1F	
10	Tsague [74]	2006	J79, F101, T56 etc.	

Semi-empirical correlations for predicting pollutants indices are rather simple to use and yield roughly acceptable accuracy after being calibrated. However, their accuracy is highly reduced as soon as significant modifications are brought to the design of the combustion chamber. Moreover, correlations usually give pollutants emissions indices for complete combustion chambers and do not enable zone-by-zone assessement of pollutants concentrations whithin the flame tube.

Physical Models (Ideal Chemical Reactors) for System Simulation

Different zones having different temperatures and equivalence ratios can be macroscopically identified within aircraft and helicopter engine burners, as shown in the findings of [124]. Accordingly, as previously mentioned in chapter 2, in a combustor model, the primary, intermediate and dilution zones can be represented by PSR and PFR components connected with each other [121, 127]. The success of these models depends on the input parameters of each of the reactors, such as temperature, equivalence ratio, residence time and mixing rate. These input parameters are approximated by CFD simulations. Comparisons between

physical pollutant models and empirical correlations for NO_x and CO have been made [1]. These comparisons show that both physical and semi-empirical modelling approaches can successfully predict NO_x at high power conditions, while they can only predict the trends of CO emissions without being able to provide accurate levels of $EICO$. Another finding was that with physical models the generalization to several fuel injection technologies can be done without losing the ability to predict emission indices by using model calibrations previously assessed for specific technologies. Recently, detailed jet fuel chemistry was incorporated in a 0D/1D aircraft engine emission model, representing the combustor, turbine and nozzle as a network of aerothermochemical control volumes characterised by different equivalence ratios and gaseous mixtures residence times [84]. Heterogeneities of equivalence ratios as well as species mixing rates were approximated by a PDF approach. That PDF approach was based on 3D CFD computations representing several configurations of combustors. The model combined formation mechanisms for PAH, soot, NO_x and sulphur chemistry. The complete set features 369 chemical species and 2657 reversible reactions. Results were consistent with measurements for many of the species taken into consideration. However, the high number of chemical species considered in the approach add a non-negligible computational cost to the numerical simulations. Furthermore spray evaporation was not accounted for and the complex structure of the gaseous flow whithin the combustor as well as flame/turbulence interactions were not represented. These modelling choices dedicate the modelling approach proposed by [84] to the study of air quality near aircraft emission sources, which can be helpful to the overall aeroengines design process, but not directly involved in the gas path design that takes place between preliminary studies and detailed design.

Detailed Chemical Kinetics Models for CFD

Many pollutant emissions prediction models were deployed in RANS software. According to a review by [127], in reactive RANS simulations, du to computational cost constraints, either turbulence models are highly detailed and pollutants formation chemistry is reduced and simplified, or chemistry is highly detailed and turbulent flow features are roughly modelled. An unsteady flamelets method was used in a staged combustor case, assuming infinitely fast chemistry [4], and it yielded good agreement on NO_x emissions with experimental measurements. Regarding LES computations that include pollutants prediction, several studies were made as well. For instance, the Presumed Conditional Moments - Flame Prolongation of ILDM[1] (PCM-FPI) was extended to NO_x chemistry and it helped in scouting into the subgrid scale modelling of reactive LES [52]. Another example is the 1D-Manifold model for modelling NO_x in presence of air-dilution [90]. The main drawbacks of detailed chemical kinetics models for CFD are high computational costs and the fact that validating such models requires DNS computations coupled to detailed chemical kinetics or experimental measurements, which can be both even more time-consuming than RANS and LES computations. However, pollutant formation modelling through high-detail CFD allows addressing real configurations of combustion systems and it also helps in examining many combustion and pollutants modelling hypotheses used in simpler models. LES results in this context can be used to provide 0D models with precious information that consolidates high-speed simulation while preserving accuracy.
In this regard, detailed chemistry data can be tabulated and used in system simulation software, and that would allow accurate pollutant emissions predictions by system simulation software. For instance, a NO Relaxataion Approach (NORA) and CO Relaxataion Approach (CORA) were developed and coupled to a 0D CFM model for system simulations of automotive SI engines, which gave good agreements with experimental results [14]. In the NORA and CORA approaches, both CO and NO reaction rates, respectively $\dot{\omega}_{CO}$ and $\dot{\omega}_{NO}$, were expressed by:

[1] Intrinsic Low-Dimensional Manifold.

$$\dot{\omega}_{CO} = \dot{m}_{CO} = \frac{\left(Y^{eq}_{bg,CO} - Y_{bg,CO}\right) m_{bg}}{\tau_{CO}} \tag{3.25}$$

$$\dot{\omega}_{NO} = \dot{m}_{NO} = \frac{\left(Y^{eq}_{bg,NO} - Y_{bg,NO}\right) m_{bg}}{\tau_{NO}} \tag{3.26}$$

where m_{CO} and m_{NO} are the respective CO and NO masses in the combustion chamber, Y is the species mass fraction, the superscript eq refers to the state of chemical equilibrium, the subscript bg stands for the burned gases zone, and τ is a constant parameter representing the time needed to relax the current burned gases composition towards the chemical equilibrium.

Chapter 4

Summary and Modelling Strategy

Achieving continuous aeroengines improvement, minimising potential drawbacks, and maintaining acceptable design time and manufacturing cost, pass through the improvement of the engine design workflow and simulation tools. The literature review done in part I indicates that a new class of system simulation methods for combustor pre-design wouold have the potential to efficiently fulfil current and upcoming requirements. With the herein proposed system modelling approach, more concurrent engineering and synergies would become possible in definition stages such as conceptual, preliminary and detailed combustor design phases. On the one hand, high-fidelity CFD of turbulent flames is used for synthesizing the behaviour of turbulent flames in burners and incorporating that synthesis into a 0D flame tube combustion model. On the other hand, the new flame tube model would help in improving the assessment of combustor designs and hence improve the input given to CFD simulations of the detailed design phase. Such a synergy would allow more efficient low emission aeroengine development at lower costs.

4.1 Summary

4.1.1 System Model Platform Requirements

The new approach consists in extending the 0D combustor submodel from a simplified black-box to a multi-component combustor, as it is the case for the physical models described in section 2.2, along with the elaboration of a combustion model that takes turbulent flame physics into account: separating between fresh gases and burned gases, considering a multi-species mixture instead of a lumped mixture and accounting for turbulent flame physics, bridging the gap between High-Fidelity and High-Speed models. This result is achieved with the insight given by 3D CFD burner simulations, thoroughly validated against experiments.

From a general point of view, the numerical tool that would perfectly fill the gap between current 0D engine performance simulation and 3D CFD combustor simulation should fulfil the following requirements:

1. Adapted for studying design and off-design engine operating points, and mission profiles.

2. Compressor and turbine stages can be simply defined by OEM maps or generic built-in maps.

3. Possibility of representing novel technologies such as alternative thermodynamic cycles, combining gas turbines and electric motors, etc.

4. Sensitive to regulation and control systems such as the fuel system or FADEC.

5. For a given simulation case and setup, the computational time should remain of the same order of magnitude of the time commonly required by state-of-the-art 0D software.
6. Intuitive and user-friendly interface.
7. The combustor submodel should fulfil the specific requirements detailed in section 4.1.2.
8. For a given engine, the model should be able to represent combustion and give an estimate of pollutant emissions for different engine operating conditions, without the need to adjust empirical parameters.

Meeting requirements from the first to the sixth depends on the simulation and the development framework of the new approach. The seventh and the last requirements directly depend on the flame tube model.

4.1.2 Combustor Model Requirements

The ideal combustor submodel should comply with the requirements below:

1. General features:
   - Topological distinction between primary, intermediate and dilution zones.
   - Easily configurable into the widest possible range of aircraft burner technologies.
   - Accurate representations of inlet (compressor diffuser and injector), outlet (flame tube exhaust) and wall (casing and liners) boundary conditions.
   - Reasonable CPU times.
2. Gas and fluid:
   - Sensitive to variations of atmospheric conditions (especially with respect to altitude).
   - Sensitive to fuel properties and formulation.
   - Adapted to manage multiphase flows.
   - Gas properties should guarantee the best compromise between fidelity, accuracy, computation time penalty, etc.
   - Computing of mean fluid-motion variables, including those related to turbulence.
3. Combustion:
   - Combustion modelling for all the aircraft-relevant fuel air mixture conditions.
   - Accurate fresh and burned zones description (temperature, volume, composition).
   - Address premixed and non-premixed flames structures that are the most commonly used in aeronautical burners.
   - Pollutant emissions kinetics evaluation: NOx, CO, Soot and Unburned Hydro-Carbons.
   - Ignition and reignition modelling.
   - Lean blowout.

According to chapter 2, the biggest potential for added modelling value would be carried by flame tube modelling, since the available aerothermal models for diffusers, multi-perforated liners and primary holes have reached satisfactory levels of detail and accuracy. As highlighted in the beginning of chapter 3, the flame types encountered in real burners mostly depend on two factors: first, technological choices defining the burner type, such as LPP or LDI,

define the flame types burning inside the flame tube; secondly, operating conditions, and in particular power settings, may highly affect respective contributions of the different flame types, by modifying turbulence and mixing properties; e.g. mostly non-premixed spray combustion turns into partially or almost fully premixed combustion when the engine is operated at full power, thanks to favorable aerothermal conditions, according to section 3.3.1.

4.2 System Simulation and Combustion Modelling Strategies

In what follows, the system representation level is chosen in a way to benefit from information made available by LES computations to feed global system simulations, and to compute first order physical phenomena enabling to set proper boundary conditions for 3D CFD burner simulations. The retained combustion modelling strategy is then detailed.

4.2.1 System Simulation Strategy

The system simulation strategy retained in this study is a component-based Bond Graph approach, deployed in the framework of the LMS Imagine.Lab Amesim software, developed by SIEMENS. The chosen software as well as the Bond Graph approach are described in Appendix A1. Like any component-based system simulation approach, in the present method, a given system is sketched as a component network, as depicted in Figure 1.5. The system can be a combustor, a full gas turbine or even a whole helicopter. Each component communicates with its neighbouring components by exchanging information through a given number of interfaces. For instance, as depicted in Figure 1.5, the combustor communicates aerothermal information with other components of the system such as the injector, the compressor, the generator turbine, etc.

Since the keystone of the herein developed method is the combustion model, in what follows, the combustion system is isolated from the gas generator. In particular, diffuser aerodynamics is not considered, and dilution and cooling through the annuli liner holes and multi-perforations are out of the investigation perimeter. Therefore, the flame tube PZ, shown in Figure 4.1, is studied separately from the rest of the system and assumed to be a stand-alone combustor, in **part III** and **part IV**.

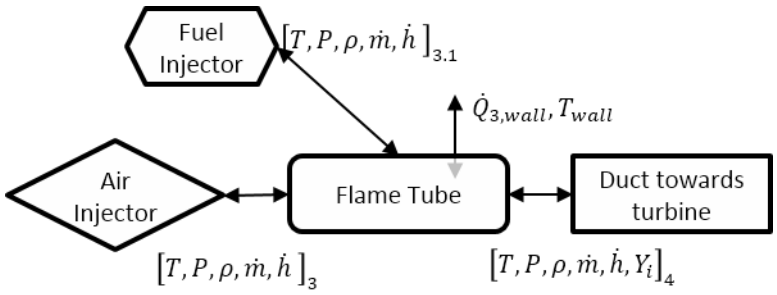

Figure 4.1 – Schematic representation of an aeroengine combustor. The arrows and double-sided arrows between components represent the exchange of aerothermal information; namely temperature, T, static pressure, P, density, ρ, mass flow rate, $\dot{m}$, specific enthalpy flow rate, $\dot{h}$, heat flow rate exchanged through combustor walls, $\dot{Q}_{wall}$, and species mass fractions, Y_i.

According to the Bond Graph formalism, a specific causality for the exchange of information was defined in order to allow the developed flame tube component to communicate with all of the other components. In the same fashion, each component is defined by a submodel that handles the information of interest and interpret the physics of that component. The submodel that represents the combustor flame tube component has to be characterised by

physical variables allowing to describe the aerothermal and chemical phenomena that occur in aeroengines flame tubes. Variables that physically fully characterise the system conditions are referred to as state variables and they are computed by means of Ordinary Differential Equations (ODE). During system simulations, temporal derivatives of the state variables are integrated at each time step. The numerical methods and integration algorithms available in Amesim are detailed in appendix A1.

4.2.2 Combustion Model Derivation Roadmap

Development of a Reference Model

In order to estimate the potential of the new combustion modelling approach, a reference model representing existent Flame Tube (FT) models for system simulation is necessary. Accordingly, as a first step, such a reference model was developed. The reference model computes liquid fuel evaporation and solves for heat release out of a simple one step combustion process inside one homogeneous zone. Emissions of NOx and CO are also calculated through correlations discussed in section 3.3. The reference FT model formulation is detailed in appendix A2.

Computation of a Parametric LES Results Database

Addressing flame dynamics in a combustor submodel for system simulation implies a synthesis of flames behaviour under various operating conditions. That synthesis requires a systematic characterisation of flames response to the targeted operating conditions. For that matter, reactive CFD simulations of a gas turbine burner were performed as a numerical DOE. Therefore, an adequate turbulence model and an appropriate combustion model for the simulation of flames in contemporary aeronautical burners are selected. The numerical setup is thoroughly elaborated and reference configuration results are validated against experimental measurements. A specific post-processing of the 3D results is developed in order to build a parametric flame characterisation database, the parameters being the gas mass flow rate across the combustor, temperatures and compositions of incoming fresh gas, and combustor outlet pressures. As a starting point for developing the new approach, for the sake of reducing the complexity of the real combustion systems, a well-documented academic single-phase burner case was chosen, featuring a flame that can be reasonably considered as a premixed flame. These topics are treated in Chapter 5.

Development of a Flame Tube Model for System Simulation

Based on the homogeneous FT model, a two-zone FT model was created. The parametric LES results database enabled synthesizing flame characteristics and elaborating mathematical formulations that permitted to close terms of a reaction rate equation. The CFM paradigm was a first and promising lead for the 0D combustion model. According to section 3.1, mean flame surface, surface wrinkling, and laminar flame speed and thickness had to be modelled. For each of these terms, several approaches were compared with respect to LES results. Furthermore, the most physical choice was made in a way to make the model as suitable as possible to predict physical behaviours and generate results directly comparable to experimental measurements or 3D computations for validation purposes. Hypotheses concerning turbulence were made for computing the integral length scale and turbulent velocity. Finally, the 0D flame tube model was validated against LES results and its transient response to unsteady operating conditions is verified. This topic is the object of Chapter 6.

Investigation of a Non-Premixed Combustor Sector by Means of LES

LES computations and specific post-processings were carried out for evaluating prospective leads for extending the flame tube model to a level that would be more representative of a real gas turbine flame tube. Indeed turbulent flow velocities and recirculation streamlines were observed, and flame structures were identified in order to estimate the potential validity of the 0D model presented in Chapter 6, and to initiate the discussion concerning a prospective extension of the 0D combustion model. For that matter, specific filtering was performed by applying the Heaviside function of a normalised Takeno flame index onto LES results such as mixture fractions, temperature fields and heat release rates. This investigation is detailed in Chapter 7.

Part III

A Premixed Burner Case

Chapter 5

Large Eddy Simulation of the PRECCINSTA Experiment

Addressing turbulent premixed single phase combustion of swirling flames is necessary for developing aeronautical combustors. For that matter, the well-known PRECCINSTA burner was designed and employed for investigating the physics, prediction and control of combustor instabilities. In this work this same experiment was used as a reference to perform Thickened Flame LES (TFLES) with the AVBP software in order to get a deeper insight of the combustion process. In a first step, a reference configuration was run and validated against experimental measurements. In the following step, impacts on simulation of some relevant numerical parameters were assessed. Afterwards, with respect to the reference case, single parameter variations of flame equivalence ratio, inlet temperature, inlet mass flow rate and pressures were simulated. The flame response to the parametric variations was characterized using specific post-processing, which was applied to time-averaged 3D results and space-averaged results. Finally, the post-processed results were checked for consistency vis-à-vis of the results of the literature and in the aim to the development of a 0D combustion model.

5.1 Determination of Flame Characteristics

The herein conducted LES computations are based on a thickened flame paradigm. However, according to the selected 0D modelling approach, section 4.2.2, the flame has to be analysed from the perspective of a FSD paradigm which is the CFM approach. Hence, the premixed flame must be characterized by its mean surface, wrinkling factor and global fuel consumption speed. In addition, some variables need to be evaluated both in the unburned zone and the burned zone, to enable the comparison with the system simulation approach for validation purposes. For that matter, an unburned gas zone was identified in LES, Figure 5.1, downstream the swirler and prior to the flame. An unburned gas volume was defined accordingly as being delimited by the swirler nozzle exit and the flame.

Accordingly, the source code of the AVBP software was modified, by introducing the mathematical formulations detailed below, in order to extract valuable information for the interpretation of the simulation results.

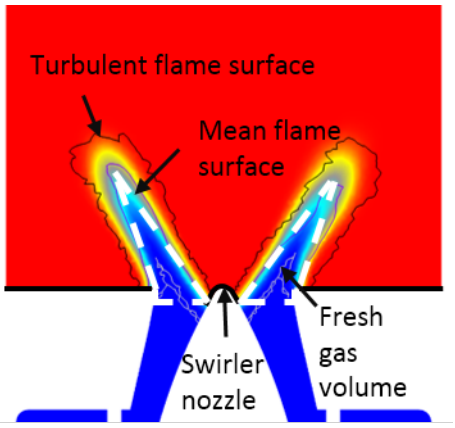

Figure 5.1 – Unburned gases volume, mean and turbulent flame surfaces.

5.1.1 Flame Surface

Combustion Progress Variable $\tilde{c}$

Since no progress variable is calculated in a standard thickened flame formalism, a progress variable had to be constructed. The following formulation was chosen:

$$\tilde{c}\left(\vec{x},t\right) = 1 - \frac{Y_F\left(\vec{x},t\right)}{Y_{ug,F}\left(\vec{x},t\right)} \tag{5.1}$$

where

$$Y_{F,ug}\left(\vec{x},t\right) = Z_C + Z_H \tag{5.2}$$

$$Z_C = M_C \sum \frac{n_{C,k} Y_k}{M_k} \tag{5.3}$$

$$Z_H = M_H \sum \frac{n_{H,k} Y_k}{M_k} \tag{5.4}$$

where $Y_F\left(\vec{x},t\right)$ is the fuel mass fraction solution, $Y_{ug,F}$ is the fuel mass fraction present in the fresh gases zone. In the present case, this quantity is imposed as a boundary condition at the inlet of the plenum upstream the swirler.

Total and Mean Flame Surface, A_T and A_m

Some authors define the flame surface as the iso-surface $A_{\tilde{c}=0.5}$ where the progress variable equals 0.5. In this work, instead of considering a fixed $\tilde{c}$ iso-surface, the norm of the $\tilde{c}$ gradient is used to determine the resolved flame surface. The total flame surface at a given time t is based on a resolved flame surface augmented by subgrid scale wrinkling. The total surface is expressed by:

$$A_T(t) = \int_V \Xi_{sgs}\left(\vec{x},t\right) \left|\nabla \tilde{c}\left(\vec{x},t\right)\right| dV \tag{5.5}$$

where Ξ_{sgs} is the sub-grid wrinkling efficiency function defined by [33] as the wrinkling ratio of the non-thickened reference flame to the thickened flame:

$$\Xi_{sgs} = \frac{\Xi\left(\delta_L^0\right)}{\Xi\left(\delta_L^1\right)} \tag{5.6}$$

where δ_L^0 is the non-thickened reference flame thickness and δ_L^1 is the thickened flame thickness. The mean flame surface A_m is based on the time-averaged progress variable $\langle\tilde{c}(\vec{x})\rangle$:

$$\langle\tilde{c}(\vec{x})\rangle = \frac{1}{\tau}\int_\tau \tilde{c}\,(\vec{x},t)\,dt \tag{5.7}$$

$$A_m = \int_V |\nabla\langle\tilde{c}\,(\vec{x})\rangle| dV \tag{5.8}$$

The total flame surface wrinkling is the ratio of the time-averaged total flame surface $\langle A_T\rangle$ to the mean flame surface A_m:

$$\langle\Xi\rangle = \frac{\langle A_T\rangle}{A_m} \tag{5.9}$$

5.1.2 Fresh and Burned Gas Volumes

The unburned gas volume is found as being delimited by the swirler nozzle and the flame. The average fresh gas volume is computed by means of the following expression:

$$V_{ug} = \int_V \left(1 - \langle\tilde{c}\,(\vec{x})\rangle\right) dV \tag{5.10}$$

The considered burned gas volume begins downstream the flame and ends with the exhaust section of the combustion chamber. It is computed by a simple subtraction:

$$V_{bg} = V_{comb.\ chamber} - V_{ug} \tag{5.11}$$

5.1.3 Flame Speed and Thickness

The flame speed is the global fuel consumption speed, equation 3.1.2, which can be expressed from the CFM reaction rate:

$$\dot{\Omega}_F(t) = \rho_{ug,F} S_L^{eff}(t) A_T(t) \tag{5.12}$$

$$S_L^{eff}(t) = \frac{\dot{\Omega}_F(t)}{\rho_{ug,F}(t) A_T(t)} \tag{5.13}$$

where $\rho_{ug,F}$ is the unburned fuel density, $\dot{\Omega}_F$ is the fuel consumption rate, given by

$$\dot{\Omega}_F = -\int_V \dot{\omega}_F dV \tag{5.14}$$

$$\dot{\omega}_F = M_F R_1 \tag{5.15}$$

where M_F is the fuel Molar weight, and R_1 is the rate progress of the chemical reaction detailed in equation 5.23.
The laminar flame thickness, δ_L^{eff}, is obtained by means of post-processing by using the Blint's formula [9]:

$$\delta_L^{eff} = \frac{2\lambda_{ug}}{\rho_{ug} c_{p_{ug}} S_L^{eff}} \left(\frac{T_{bg}}{T_{ug}}\right)^{0.7} \tag{5.16}$$

where λ_{ug} is the thermal conductivity of the fresh gases mixture, $c_{p_{ug}}$ is the unburned mixture specific heat at constant pressure, and T_{bg} and T_{ug} are the respective burned gas and unburned gas temperatures.

Burned gas temperature results of the LES database were compared against adiabatic flame temperatures calculated by using the GRI-Mech. 3.0 mechanism [116], Figure 5.2. Results discrepancies do not exceed 2% and temperature evolution is well predicted.

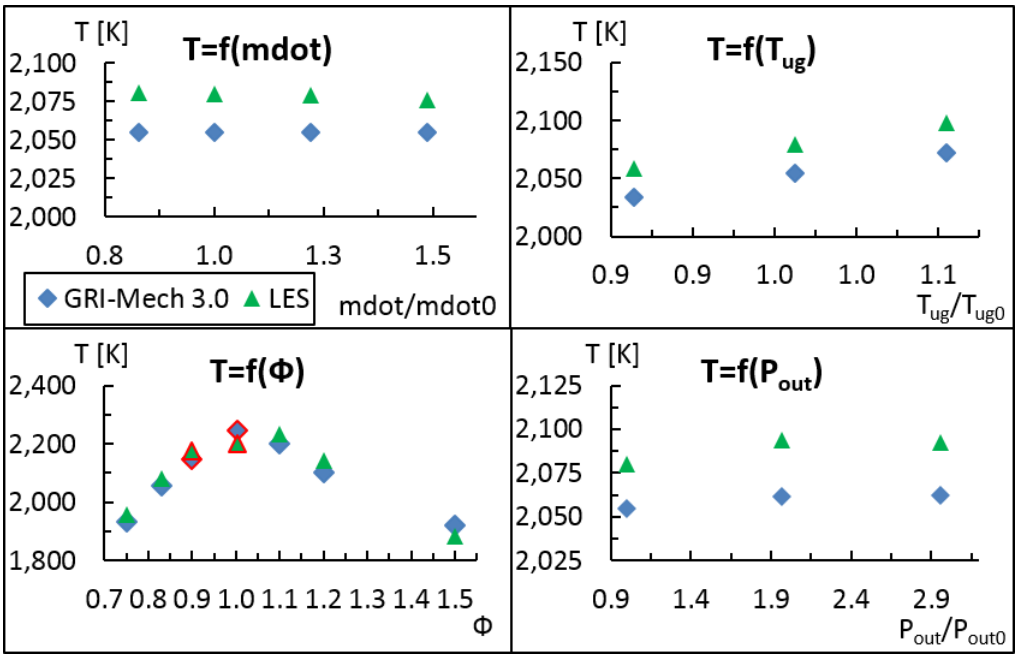

Figure 5.2 – Comparison of the burned gas temperature predicted in the LES computations against adiabatic flame temperatures calculated by using the GRI-Mech. 3.0 mechanism.

5.1.4 Turbulent Intensity and Length Scale

The turbulent intensity is evaluated inside the unburned gas zone and in the flame region, in order to assess the flame/turbulence interaction and its dependency on the parametric variations operated in this study, section 5.3. For that matter, the resolved turbulent intensity is post-processed in the unburned gas zone and in the flame zone by using the following expressions:

$$u'^2_{flame,i} = \frac{1}{A_m}\int_V |\nabla\langle\tilde{c}\,(\vec{x})\rangle| \left(\langle\tilde{U}_i^2(\vec{x})\rangle - \langle\tilde{U}_i(\vec{x})\rangle^2\right) dV \tag{5.17}$$

$$u'^2_{ug,i} = \frac{1}{V_{ug}}\int_V (1-\langle\tilde{c}\,(\vec{x})\rangle) \left(\langle\tilde{U}_i^2(\vec{x})\rangle - \langle\tilde{U}_i(\vec{x})\rangle^2\right) dV \tag{5.18}$$

As global flame wrinkling is targeted, global turbulent velocity fluctuations were calculated for both flame and unburned gas zone, under the Homogeneous Isotropic Turbulence assumption (HIT), from the turbulent kinetic energy, k, according to the following equations:

$$k_{ug} = \frac{1}{2}\sum_i u'^2_{ug,i},\ k_{flame} = \frac{1}{2}\sum u'^2_{flame,i} \tag{5.19}$$

$$u'_{ug,HIT} = \sqrt{\frac{2k_{ug}}{3}},\ u'_{flame,HIT} = \sqrt{\frac{2k_{flame}}{3}} \tag{5.20}$$

In the present case, the turbulent length scale l_T is estimated to be in the order of 7mm, which is the diameter of the flame contour at the swirler nozzle. A more rigorous estimate of l_T could be computed by using the autocorrelation matrix as it was done by [50]. However, the latter source shows that l_T is not significantly influenced by the variations of mass flow rate, pressure or temperature. Thus, for one burner design and a first order study dedicated to 0D modelling, it is acceptable to consider l_T as being constant for all the investigated operation points.

5.2 Simulation Setup and Validation

5.2.1 Case Description

The well-known PRECCINSTA burner, [58], was assembled by the German Aerospace Center (DLR) for the investigation of premixed combustion pulsations. A schematic of the burner is displayed in Figure 5.3. It features a plenum, a swirl u' designed by TURBOMECA and

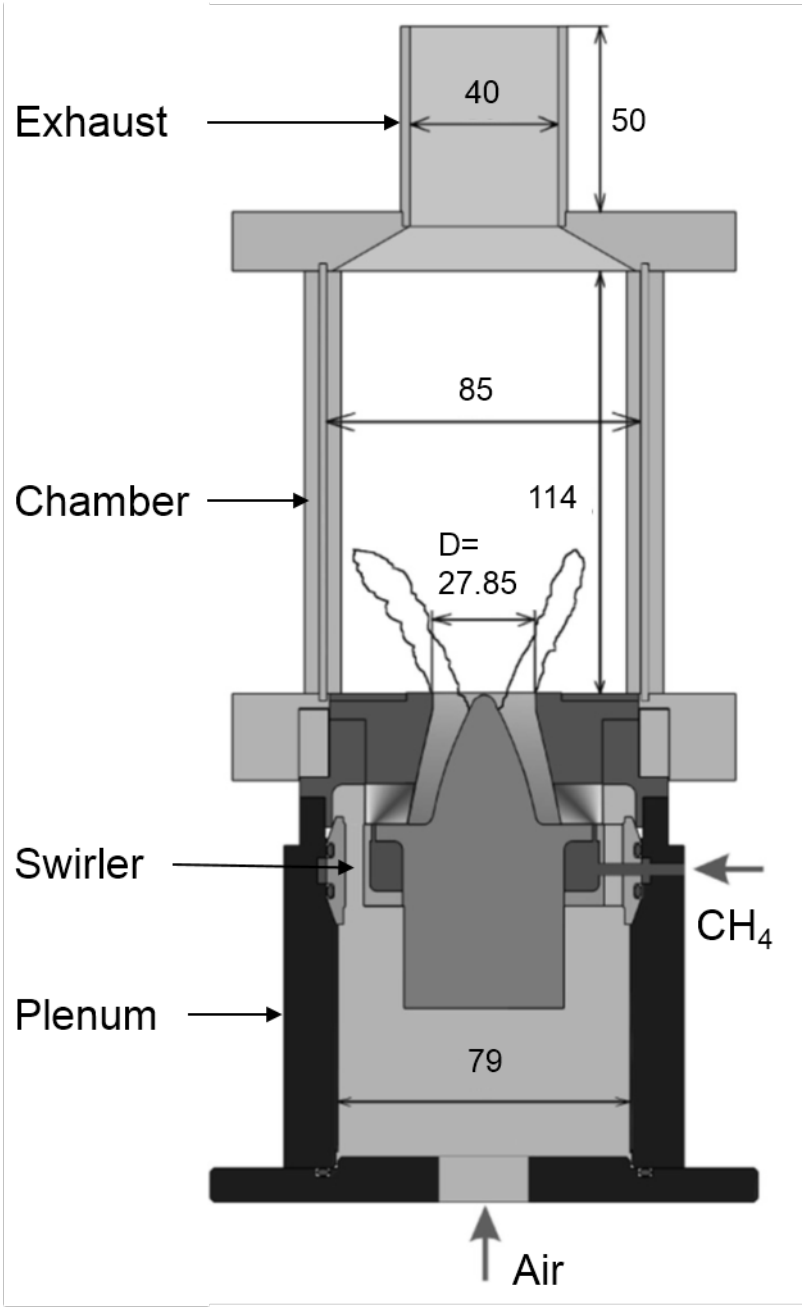

Figure 5.3 – schematic of the PRECCINSTA burner setup by [128], lengths in mm.

a square cross-section combustion chamber. Dry air is fed at ambient temperature via the plenum, and the gaseous fuel is injected into the air flow through the radial swirler. The swirler nozzle exit has a diameter of 27.85mm. In addition to swirl, a central hub stabilizes the flame and controls its position. The combustion chamber is made of quartz windows for optical access. It has a cross section of $85 \times 85\text{mm}^2$ and its length is 114mm. The combustion

chamber operates at atmospheric pressure and ends into a convergent exhaust duct with a cross-section diameter of $40mm$. The thermal power output is around 30kW for an inlet mass flow rate of 12.8g/s and a flame with $\phi = 0.83$. The PRECCINSTA case was subjected to laser and optical diagnostics by [80] on several cases, Table 5.1, RANS computations by [26] and LES computations by [62, 109, 114, 128].

Table 5.1 – Experimental cases of stable, quiet flames, and unstable, pulsating flames, investigated by [80]. $\dot{m}_A$ and $\dot{m}_F$ are the respective air and fuel mass flow rates, and P_{th} is the thermal power output of the burner.

	Case	$\dot{m}_A$ [g/s]	$\dot{m}_F$ [g/s]	ϕ	P_{th} [kW]
1	pulsating	12.23	0.50	0.70	25.1
2a	quiet	12.23	0.60	0.83	30.0
2b	quiet	12.23	0.54	0.75	27.0

During the experimental measurements conducted by [80], the fuel/air mixtures were measured to reach temperatures between 320K and 380K prior to entering the combustion chamber.

5.2.2 Reference and Baseline Operating Conditions

The experimental configuration 2b, Table 5.1, was reproduced in a CFD simulation as a reference operating condition. For this study, another configuration, Table 5.2, was set as a baseline operating point from which the effective single-parametric variations, section 5.3, were derived. That shift with respect to the reference configuration allows a sufficient margin for the single-parametric variations without risking numerical or thermo-acoustic instabilities.

Table 5.2 – Reference case and baseline operating point. $\dot{m}_{in}$ is the combined air and fuel mass flow rate, T_{ug} is the inlet temperature and P_{out} is the outlet pressure.

Case	$\dot{m}_{in}$ [g/s]	ϕ	P_{th} [kW]	T_{ug} [K]	P_{out} [bar]
Reference	12.77	0.70	27	320	1.013
Baseline	9.0	0.83	20.8	320	1.013

5.2.3 Numerical Case Peculiarities

In this work, LES computations were performed with the finite-volume code AVBP, developed by IFPEN and CERFACS. Compressible Navier-Stokes equations are solved. All the species are gaseous and assumed as ideal gases, characterized by using the JANAF thermochemical tables [118]. The Lewis number, Le, equals unity for all the species. The viscosities are modelled by means of Sutherland's law [120]. Steady flows with fully developed turbulence and stable anchored flames are considered in this study. Hence, turbulence production and destruction balance is assumed to be null. Thus, the Smagorinsky-Lilly subgrid scale model, [115], is used, as the present work only aims at a first order analysis of swirl flames for a system simulation modelling purpose.

Boundary Conditions

As it was done by [110], the computational domain was extended upstream the swirler inlet, and downstream the exhaust outlet, in order to set the inlet and outlet boundary conditions off the actual inlet and outlet of the real experimental setup. This choice diminishes the

influence of boundary conditions on results. The numerical setup is shown in Figure 5.4. A mass flow rate composed of air and methane is imposed on the inlet at a given temperature. A plenum is placed upstream the swirler in order to minimize the impact of the inlet boundary condition on the combustion chamber. Absolute pressure is imposed on the outlet, and once again a large plenum is placed downstream the exhaust in order to minimize the impact of the outlet condition on the combustion chamber. A mass flow rate boundary condition is introduced into the outlet plenum to force a co-flow; this co-flow constitutes an additional precaution against spurious numerical effects. In order to properly represent the acoustic waves propagation and reflection, the inlet and outlet are set as Navier-Stokes Characteristic Boundary Conditions (NSCBC) [86, 97]. All the walls are no-slip adiabatic walls.

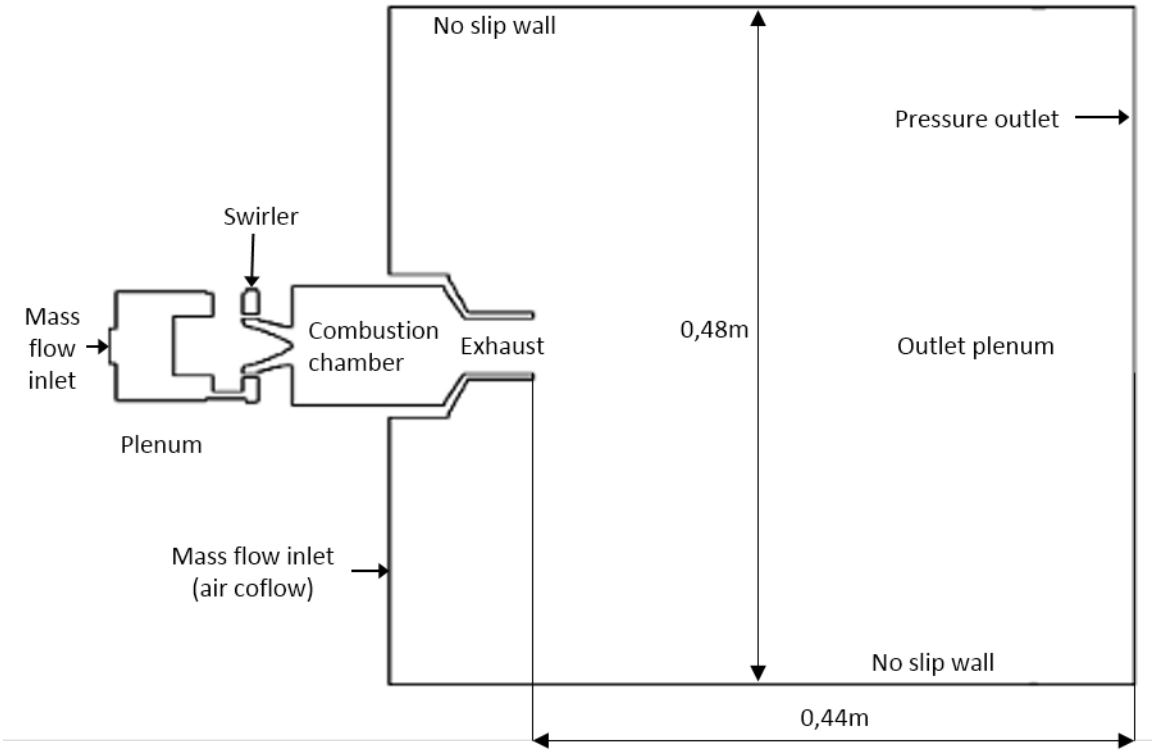

Figure 5.4 – Computational domain and boundary conditions.

Combustion Model

In the aeronautical industry, the Dynamically Thickened Flame (DTF) model for LES [69] is widely used, thanks to its capability of handling all types of flame regimes without compromising the prediction of pure mixing. This is achieved by locally applying a thickening factor, F_{thick}, only where reaction zones are detected by a sensor, [69], and avoiding the thickening in non reactive zones, to avoid modifying the description of pure mixing. Consequently, the flame is resolved without the need of an extremely fine mesh and without altering the turbulent mixing dynamics. Therefore, the DTFLES model is very suitable for the present approach. The reduced chemical scheme 2S_CH_4_BFER for methane/air combustion [49] is used. It takes into account six species (CH_4, O_2, CO_2, CO, H_2O, and N_2) and two reactions:

$$CH_4 + \frac{3}{2}O_2 \longrightarrow CO + 2H_2O \tag{5.21}$$

$$CO + \frac{1}{2}O_2 \longleftrightarrow CO_2 \tag{5.22}$$

The CH_4 oxidation reaction, equation 5.21, is irreversible, whereas the CO-CO_2 equilibrium reaction, equation 5.22, is reversible. The forward rates of the reactions, equations, 5.21 and 5.22, are respectively given by:

$$R_1 = A_1 f_1(\phi) \left[CH_4\right]^{n_{CH_4,1}} \left[O_2\right]^{n_{O_2,1}} \exp\left(-\frac{E_{a,1}}{RT}\right) \tag{5.23}$$

$$R_2 = K_2 \left(\left[CO\right]^{n_{CO,1}} \left[O_2\right]^{n_{O_2,2}} - \left[CO_2\right]^{n_{CO_2,1}}\right) \tag{5.24}$$

$$K_2 = A_2 f_2(\phi) T^{0.7} \exp\left(-\frac{E_{a,2}}{RT}\right) \tag{5.25}$$

where, for the reaction j, R_j is the rate progress, A_j is the pre-exponential factor, f_j is a pre-exponential adjustment factor, function of the equivalence ratio, ϕ, $E_{a,j}$ is the activation energy, and $n_{i,j}$ is the reaction exponent for the species i. According to [49], the values of activation energies, pre-exponential factors and reaction exponents were fitted to match the flame speed in the lean combustion regime at the temperature of 300K and the pressure of 1atm. These values are summarized in Table 5.3.

Table 5.3 – Activation energy $E_{a,j}$, pre-exponential factors A_j and reaction exponents $n_{i,j}$ used in the 2S_CH_4_BFER mechanism [49].

Reaction	CH_4 oxidation (5.21)	CO-CO_2 equilibrium (5.22)
Activation energy [cal/mol]	3.55×10^4	1.2×10^4
Pre-exponential factor (cgs)	4.90×10^9	2.0×10^8
Reaction exponents [-]	$n_{CH_4,1}$ 0.50 $n_{O_2,1}$ 0.65	$n_{CO,2}$ 1.00 $n_{O_2,2}$ 0.50 $n_{CO_2,2}$ 1.00

The pre-adjustment functions $f_j(\phi)$ allow to recover flame speeds for rich mixtures and help in quickly reaching equilibrium states in cases of a laminar premixed flames at atmospheric pressure, fed by fresh gases at 300K.
In the AVBP software, a centred spatial numerical scheme was used, which caused the generation of wiggles in the presence of high gradients of solution variables, such as density, total energy, pressure or species mass fractions. Thus, according to [27], a second order artificial viscosity term, $smu2$, was applied where very strong gradients or shocks are detected, and a fourth order term, $smu4$, was applied in order to damp high frequency wiggles. No shocks were observed in the PRECCINSTA rig simulation, and therefore the factor $smu2$ was kept to a standard value throughout the PRECCINSTA case study. Nonetheless, $smu4$ and F_{thick} parameters might have an impact on the LES results. Therefore, the effects of the flame thickening factor and the 4^{th} order artificial viscosity parameter on the laminar flame speed were assessed on the baseline case, Table 5.2. For that assessment and for further validation purposes, DNS computations featuring a laminar premixed stationary methane flame configuration, were performed with the AVBP software. The results of the assessment are shown in Figure 5.5. As shown in the figure, on the one hand, raising F_{thick} reduces the laminar flame speed and brings it slightly closer to the theoretical reference value calculated from 1D DNS computations. The reason would be an improvement of the flame resolution with the increase of the thickening factor, leading to a better prediction of the flame surface. On the other hand, lowering $smu4$ yields the same effect of lowering S_L. This effect would owe to sharpening the gradients in the vicinity of the flame, which would enhance the flame resolution. Below a certain value of $smu4$, the wiggles amplify and corrupt the computation. The combination of a 6 points thickening with a fourth order viscosity coefficient equal to 5e-3 is technically the most suitable for the baseline case, as the flame brush is sufficiently resolved and the wiggles are prevented from amplifying. Unfortunately it was found that

in order to prevent wiggles from growing, the *smu*4 coefficient had to be raised to 1.0e-2 for some computational cases of the parametric study described in section 5.3. For the sake of consistency and precision, the *smu*4 coefficient was finally set to 0.01 in all the LES computations performed in this study.

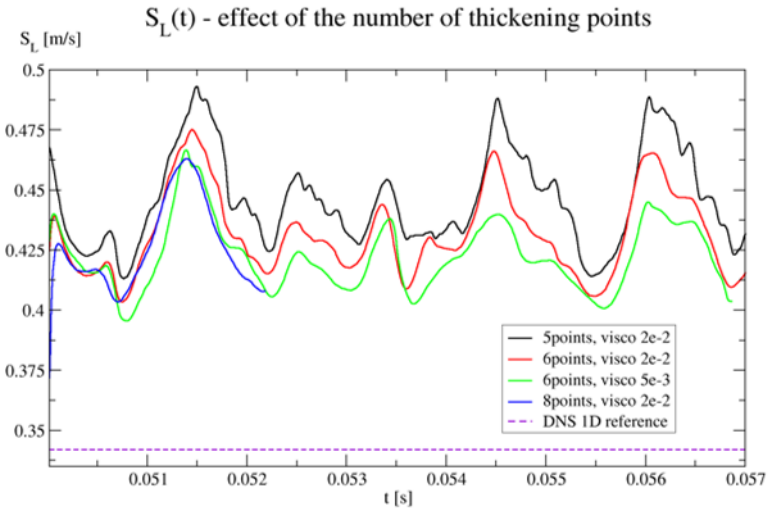

Figure 5.5 – Effect of the thickening factor, specified in terms of grid points, and of the 4th order artificial viscosity coefficient on the instantaneous laminar flame speed, S_L.

CFD Mesh

To build a fairly accurate LES database at an acceptable CPU cost, the CFD mesh was assessed. Three hybrid mesh designs, of different refinement levels, were generated and compared over the baseline operating point, Table 5.2. The characteristics of the three mesh designs are presented in Table 5.4. The additional refinement is progressively applied in the

Table 5.4 – Characteristics of the three mesh designs generated for the LES of PRECCINSTA.

Mesh	R4	R45	R5
Cells total number	4.42×10^6	5.2×10^6	8.6×10^6
Nodes total number	8.06×10^5	9.20×10^5	1.52×10^6
Nodes in chamber	2.0×10^5	3.2×10^5	9.0×10^5
Smallest volume $[m^3]$	5.25×10^{-12}	4.17×10^{-12}	2.53×10^{-12}
Smallest length $[mm]$	0.172	0.161	0.136

swirler and in the flame region, inside the combustion chamber, which are the regions where the highest gradient are localised. In Figure 5.6, the meshes of the different designs and their impact on the CH_4 profile can be seen. The flame thickening factor and the 4^{th} order artificial viscosity were unchanged during the mesh assessment, and corresponds to 6 grid points. As shown in Figure 5.6, by increasing the mesh refinement the flame front is more resolved, and the transition from the unburned gas region to the burned gas region is steeper. The effect of the mesh on the instantaneous flame characteristics, detailed in section 5.2, can be observed in Figure 5.7. As shown in the figure, the subgrid wrinkling efficiency, Ξ_{sgs}, the resolved wrinkling Ξ, the total flame surface A_T and the laminar flame speed S_L fluctuate over time when the mesh is refined. The sgs wrinkling efficiency gets closer to unity when the mesh is more refined. This evolution is expected, as the subgrid scale is reduced when the

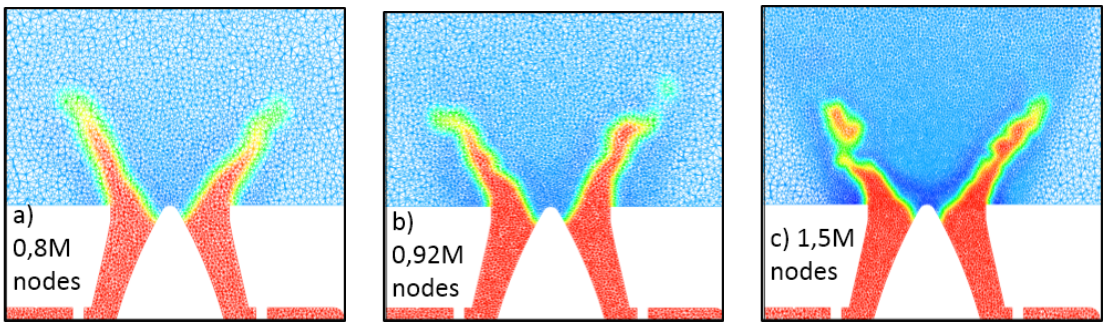

(a) R4 (b) R45 (c) R5

Figure 5.6 – Resolution of the three meshes R4, R45 and R5 in the flame region; CH_4 mass fraction.

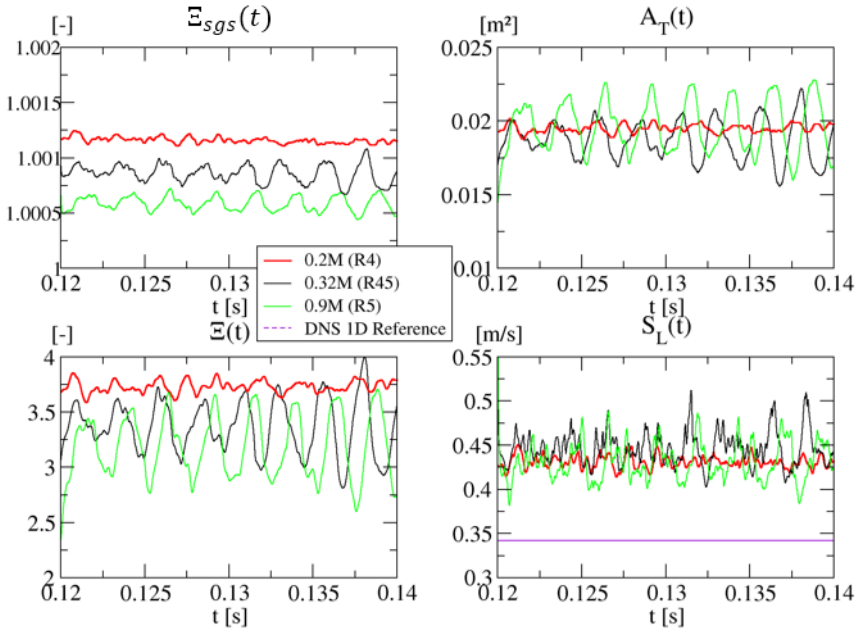

Figure 5.7 – Impact of the mesh refinement on instantaneous subgrid wrinkling efficiency, resolved wrinkling Ξ, total flame surface A_T and laminar flame speed S_L.

mesh refinement increases. However, the resolved wrinkling decreases with the refinement as well. This might be due to an increase of the mean flame surface that is much greater than the increase of turbulent flame surface. Indeed, the total flame surface seem to oscillate around the same average, Table 5.5, but with higher amplitude oscillations as the refinement increases. The laminar speed is affected by the mesh refinement in the same way as the total flame surface is. The Table 5.5 summarizes the comparison of time-averaged results. The averaged fresh gas volume, V_{ug}, and the averaged flame surface, A_m, increased with the

Table 5.5 – Comparison of time-averaged results obtained with the three mesh designs. The time sample is 20ms.

Mesh	R4	R45	R5
V_{ug} $[ml]$	20.2	20.4	22.8
A_m $[m^2]$	5.2×10^{-3}	5.6×10^{-3}	6.2×10^{-3}
Ξ [-]	3.7	3.37	3.2
u' $[m/s]$	4.5	4.6	5.1
S_L^{eff} $[m/s]$	0.43	0.44	0.43
δ_L^{eff} $[mm]$	4.2	4.1	4.2
CPU time for 20ms	$5h$	$6h50min$	$10h45min$

mesh refinement while the flame wrinkling, Ξ, decreased. The decrease of Ξ is obviously the direct result of an increase of A_m greater than the increase of A_T. The turbulent intensity u', computed according to section 5.2.4, grows as the mesh gets finer. However, the laminar flame speed and thickness do not change significantly. The CPU time ratio between the R4 and the R5 is slightly greater than two while the cell number ratio is slightly lower than two. The coarsest mesh, labelled R4, is then selected for its minimal computational cost. The selected mesh provides average results close to those of finer meshes, but with a lower level of oscillations.

Numerical scheme

As recommended by the AVBP guidelines the simulations were started with the Lax-Wendroff scheme (LW)[63], to allow turbulence to develop, and then continued with the TTGC scheme[34], third order in time and space, for more accuracy. However, the TTGC scheme is known to be less stable than the LW scheme and costs about 2.5 times more in terms of CPU time. For the sake of saving time and avoiding spurious numerical instabilities, the effect of the numerical scheme on flame characteristics is assessed. Flame characteristics behaviour as a function of the numerical scheme is shown in Figure 5.8. Unexpectedly, the computations done with TTGC are more stable than those using LW. With TTGC, the total flame surface and the resolved wrinkling are raised, the sgs wrinkling contribution is lower, and the global laminar fuel consumption speed is slightly lower. The CPU time with TTGC is about twice the LW time. Finally, in what follows, LES computations were performed by using the coarse mesh, R4, with the TTGC numerical scheme and a local flame thickening factor of 6 grid points.

5.2.4 Reference Point Simulation Results and Comparison to Experimental Measurements

For simulation setup validation purposes, the CFD results of the reference configuration were compared to experimental results from [80] and LES results corresponding to the same operating conditions from [109] at different heights from the swirler nozzle, Figure 5.9.

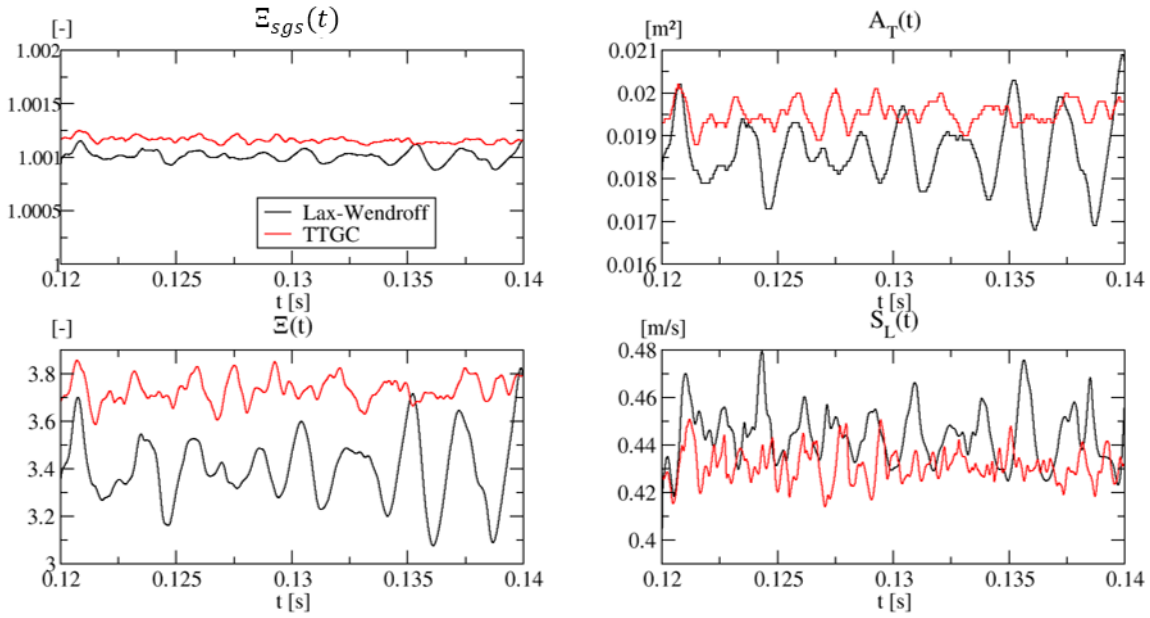

Figure 5.8 – Effect of the numerical scheme on instantaneous laminar flame speed S_L, total flame surface A_T, subgrid and resolved wrinkling.

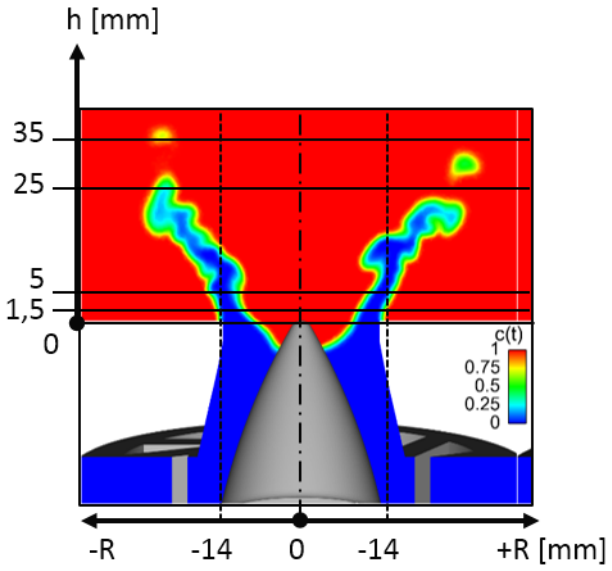

Figure 5.9 – Position of the reference planes in the combustion chamber case retained for the radial profiles analysis. An instantaneous position of the flame is represented by the combustion progress variable, c.

Validation of Velocity Profile Results

Results of mean and RMS (Root Mean Square) velocity profiles were compared against values from the literature, [80, 109], obtained for the reference configuration.

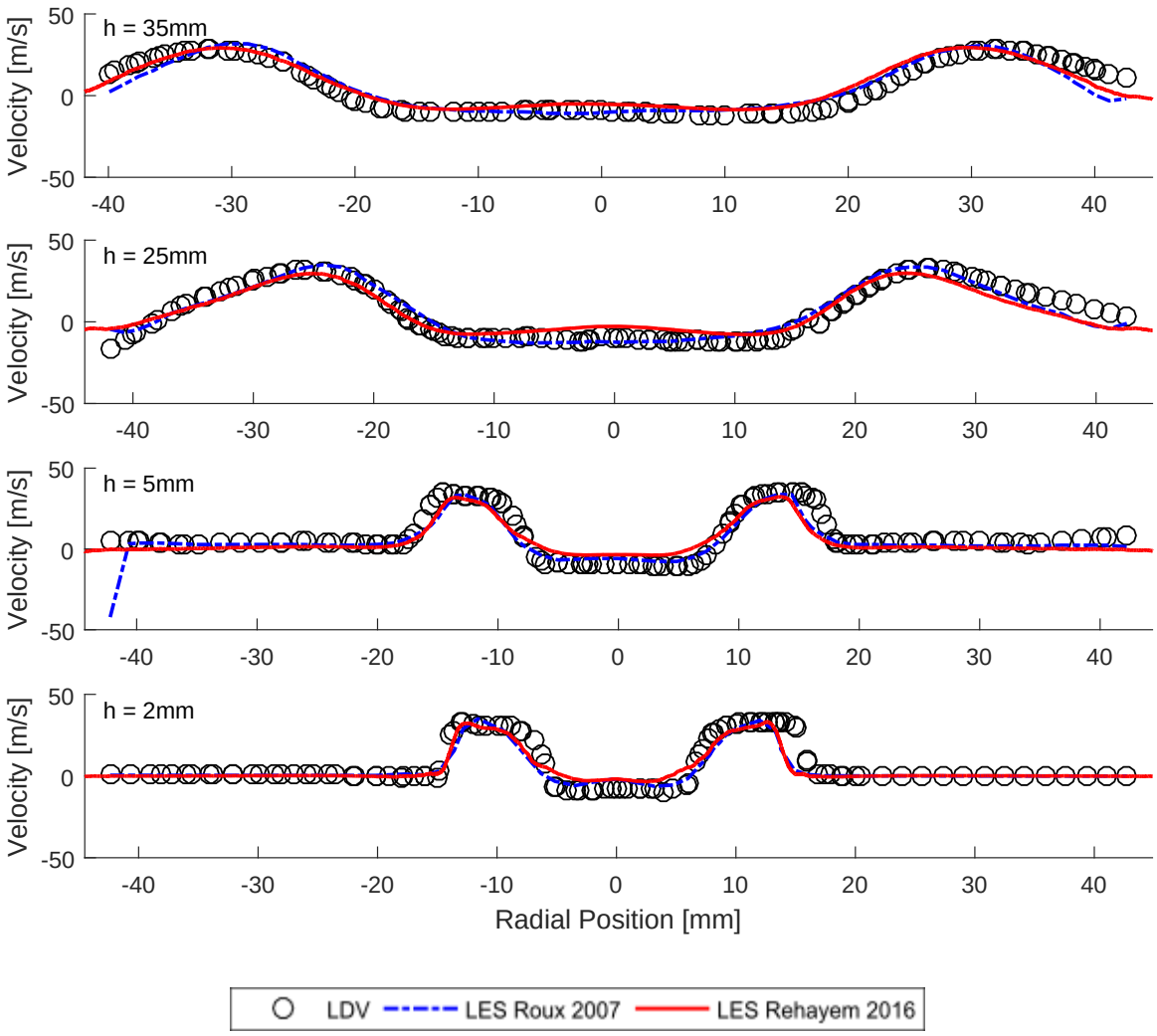

Figure 5.10 – Comparison of the mean axial velocity profiles against LDV measurements by [80] and LES results by [109].

The mean axial velocity profiles, Figure 5.10, mean azimuthal velocity profiles, Figure 5.11, and mean radial velocity profiles, Figure 5.12, show very good agreement with the experimental measurements, the LES profiles obtained by [109] and the LES results of the present study.

The RMS (Root Mean Square) axial profiles, Figure 5.13, are globally well predicted by the herein described LES computation, except at a heights of 2mm and 25mm from the swirler nozzle, where the LES computation underestimated the axial RMS velocity peaks. Conversely, the comparison of RMS azimuthal velocity profiles, Figure 5.14, reveals that the LES computation captured the velocity profiles in terms of radial peak locations and velocity levels, successfully at a height of 2mm and fairly at 5mm. Discrepancies amplify at 25 and 35mm. The computed radial RMS profiles globally agree with the experimental profiles, Figure 5.15.

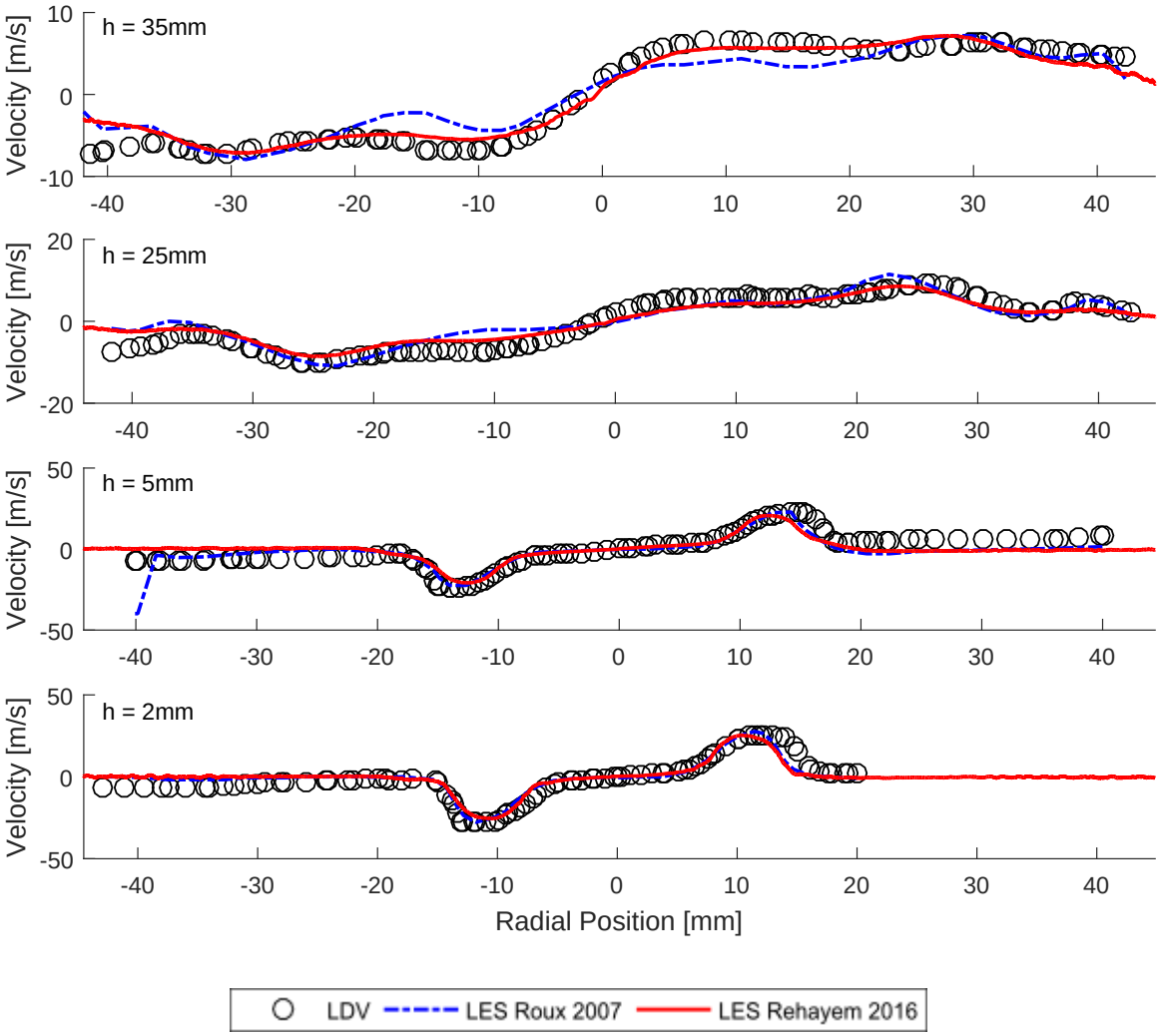

Figure 5.11 – Comparison of the mean azimuthal velocity profiles against LDV measurements by [80] and LES results by [109].

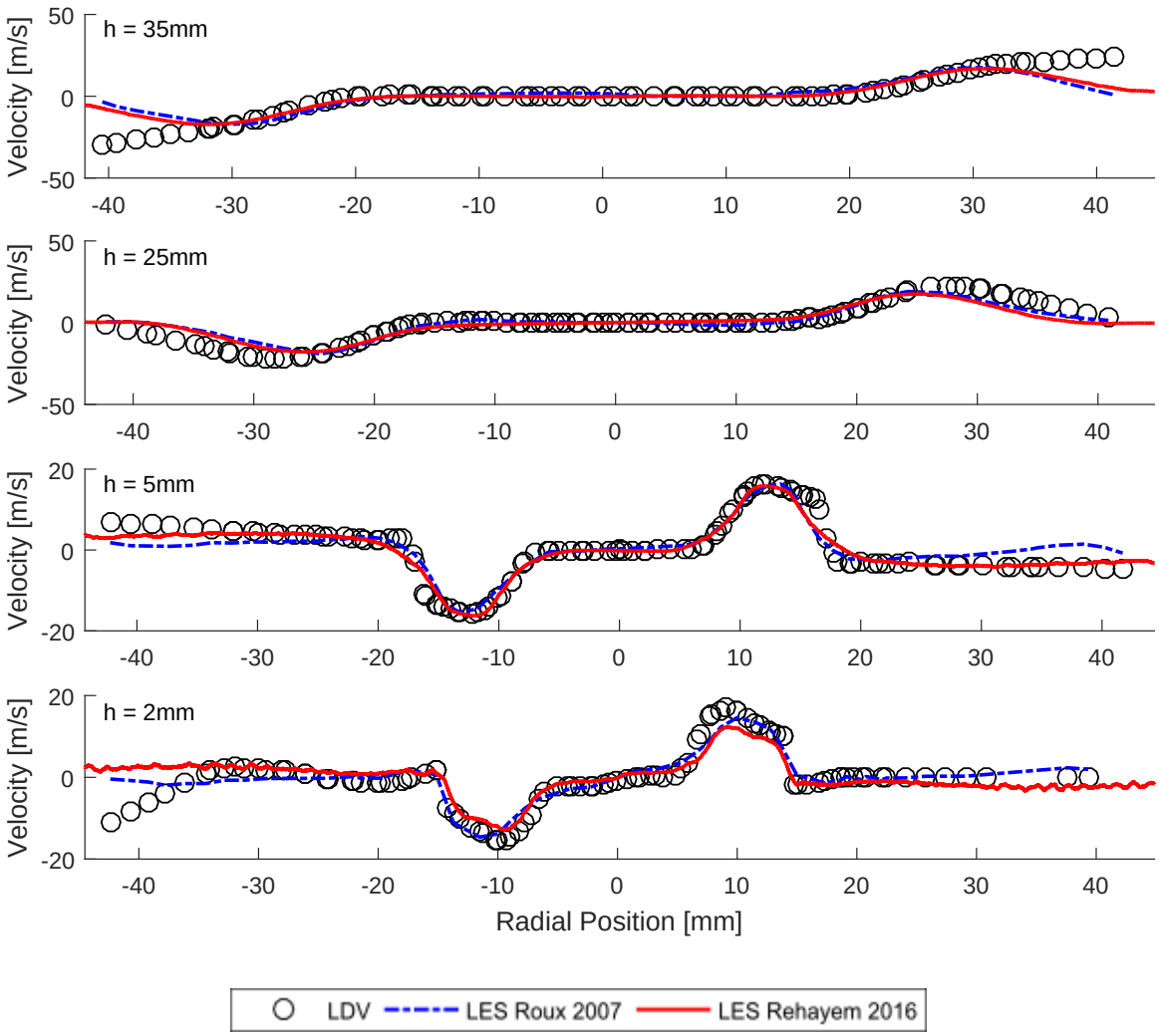

Figure 5.12 – Comparison of the mean radial velocity profiles against LDV measurements by [80] and LES results by [109].

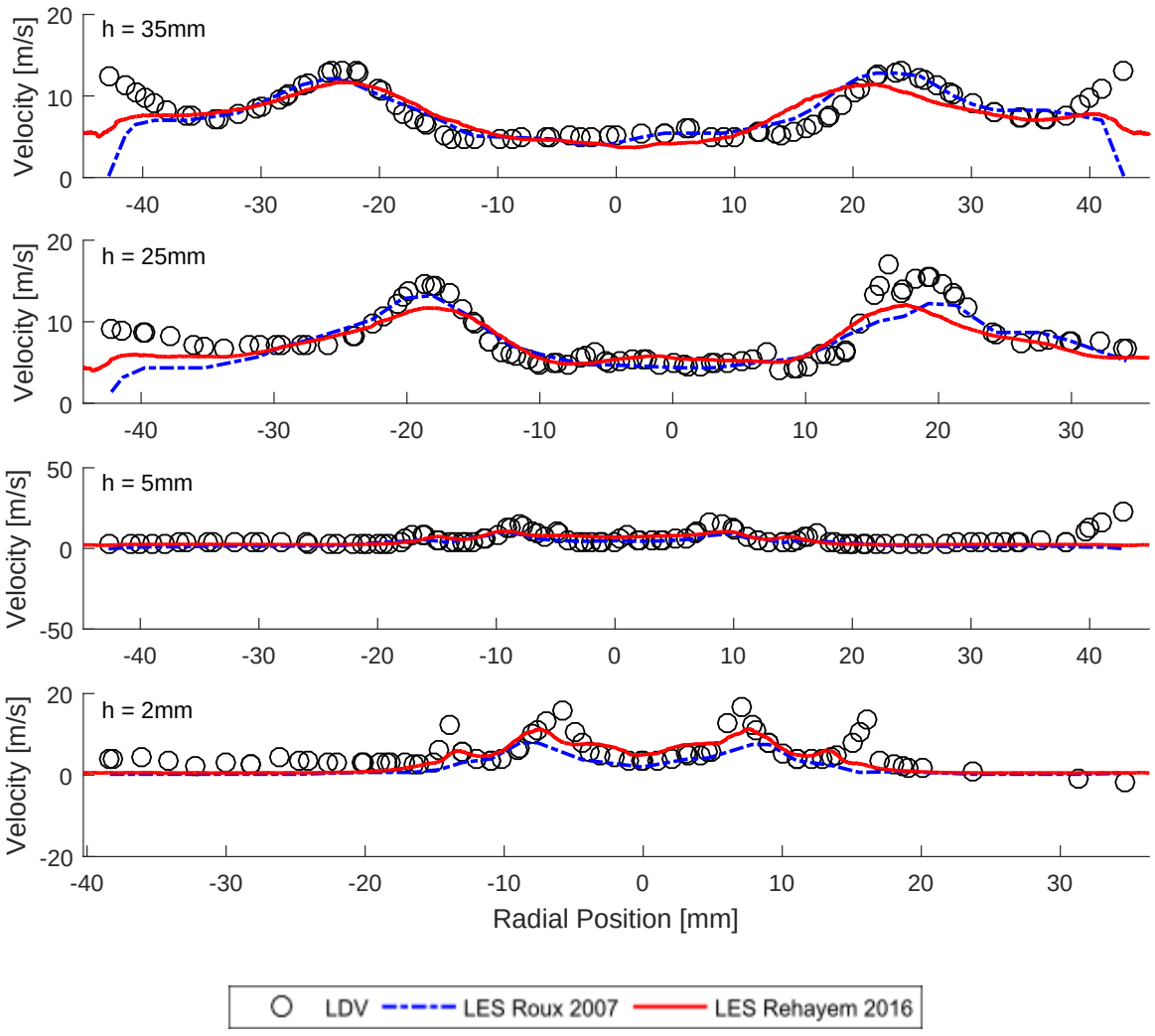

Figure 5.13 – Comparison of the RMS axial velocity profiles against LDV measurements by [80] and LES results by [109].

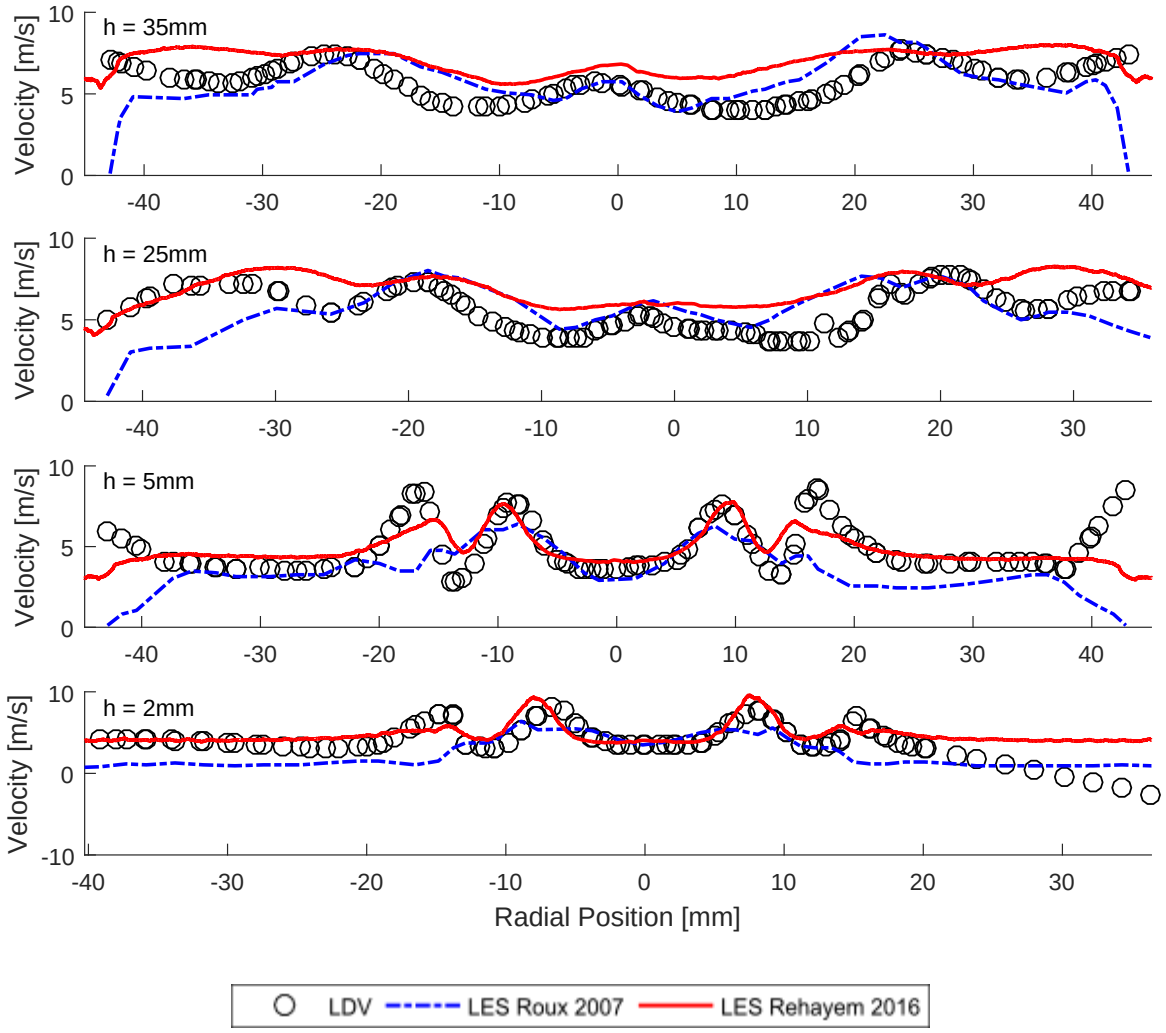

Figure 5.14 – Comparison of the RMS azimuthal velocity profiles against LDV measurements by [80] and LES results by [109].

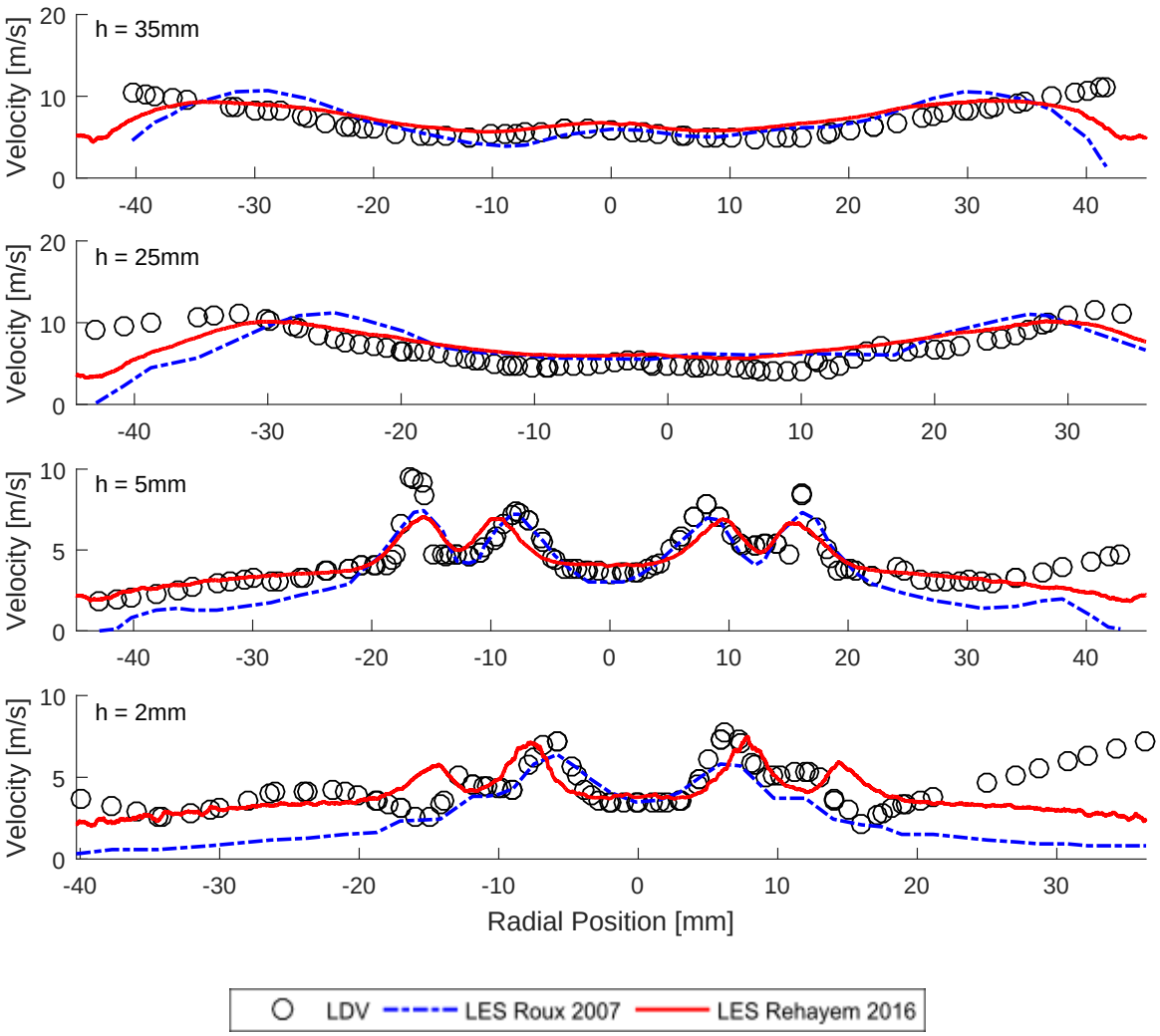

Figure 5.15 – Comparison of the RMS radial velocity profiles against LDV measurements by [80] and LES results by [109].

Validation of Temperature and Species Molar Fraction Profiles Results

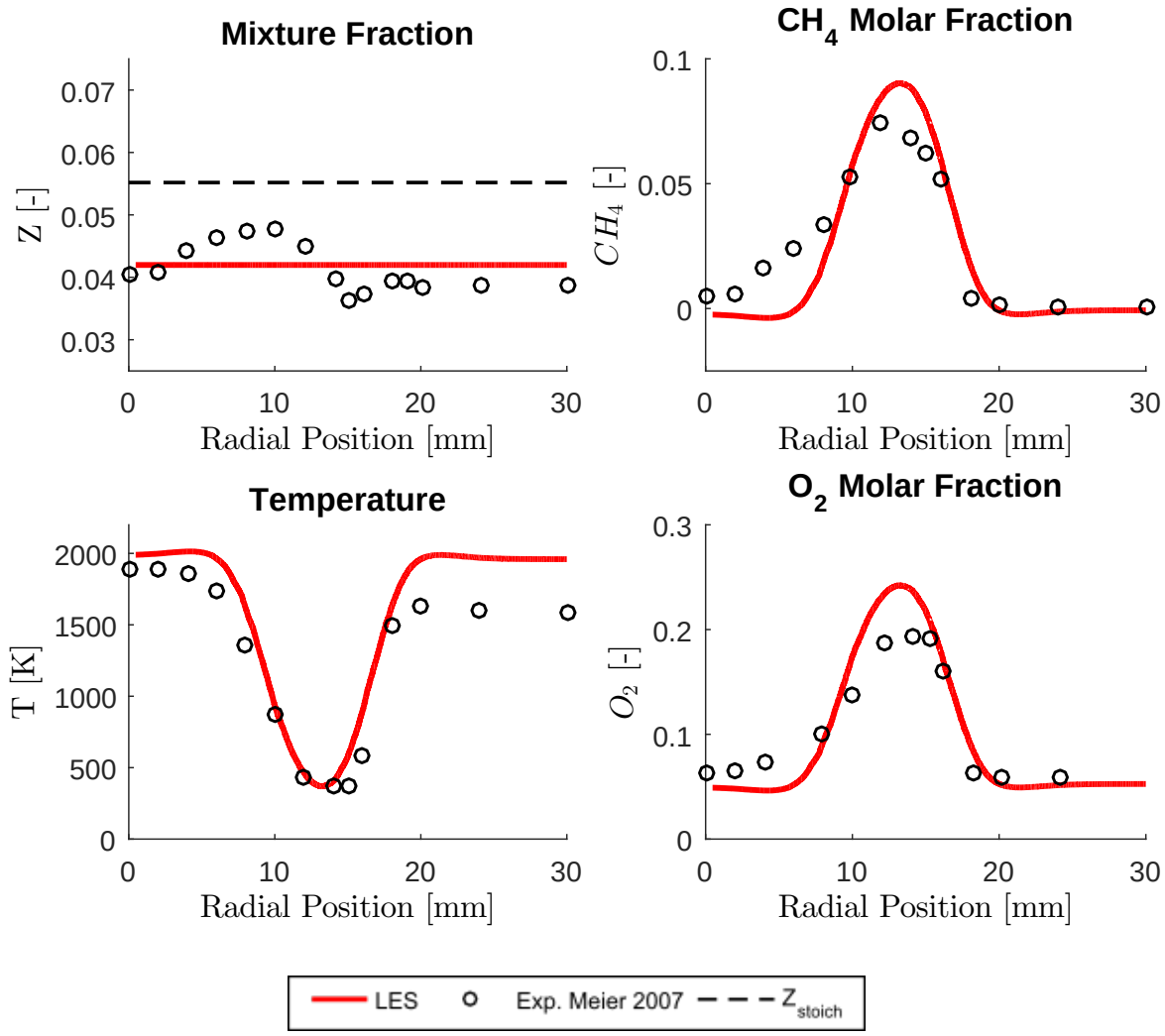

Figure 5.16 – Comparison of time averaged LES results of the baseline and reference points to experimental results by [80] at a height of 6mm over the swirler nozzle; mixture fraction Z, temperature T, methane and oxygen molar fractions.

Radial profiles of fuel mixture fraction, fuel and oxidizer molar fractions, and temperature were compared between the present study LES results and experimental measurements by [80], Figure 5.16. The experimental setup is separately fed by fuel and oxidizer mass flow rates, causing the mixture fraction, Z, to vary along the burner radial coordinate. In the experiment, Z reaches its maximal value at around 10mm along the radial coordinate, and goes down to its minimum at nearly 15mm. That variation is not present in the LES results since all the reactants are introduced through the same section under the hypothesis of perfectly homogeneous mixture. The impact of this hypothesis on comparisons can also be observed in the variations of the molar fractions of methane and oxygen, as well of the temperature. Nevertheless, the inverted temperature bell curves and the methane and oxygen molar fractions bell curves are in good agreement from 7 to 17mm. Hence, the comparisons confirm that the location and the extent of the flame in LES fairly agree with experiments.

5.3 Generation of a Parametric Computational Database

In the herein conducted parametric study of the burner PRECCINSTA, the inlet and outlet operation parameters were modified, one at a time, Figure 5.18. All the computed configurations are detailed in Table 5.6. The range of variation of each parameter aims at

Table 5.6 – Operating conditions of the different configurations of the PRECCINSTA burner simulations computed in this work.

Configuration	$\dot{m}_{in}$	ϕ	T_{ug}	P_{out}	t_{flow}	$t_{eff.}$	Stability	
	[g/s]	[-]	[K]	[Pa]	[ms]	[ms]	Physical	Numerical
reference	12.8	0.75	320	101325	65	80	stable	stable
baseline	8.98	0.83	320	101325	90	120	stable	stable
$\dot{m}_{in} = 7.44$	7.44	0.83	320	101325	108	120	unknown	stable
$\dot{m}_{in} = 10.95$	10.95	0.83	320	101325	74	85	stable	stable
$\dot{m}_{in} = 13.36$	13.36	0.83	320	101325	60	80	stable	stable
$\phi = 0.75$	8.98	0.75	320	101325	92	100	stable	stable
$\phi = 0.9$	8.98	0.9	320	101325	92	100	unknown	unstable
$\phi = 1$	8.98	1.0	320	101325	91	200	unknown	unstable
$\phi = 1.1$	8.98	1.1	320	101325	88	100	unknown	stable
$\phi = 1.2$	8.98	1.2	320	101325	89	100	unknown	stable
$\phi = 1.5$	8.98	1.5	320	101325	102	40	unknown	stable
$T_{ug} = 288$	8.98	0.83	288	101325	100	100	unknown	stable
$T_{ug} = 350$	8.98	0.83	350	101325	83	100	stable	stable
$P_{out} = 2 \times 10^5$	8.98	0.83	320	200000	170	170	unknown	stable
$P_{out} = 3 \times 10^5$	8.98	0.83	320	300000	270	170	unknown	stable

significantly influencing the flow as well as the flame/turbulence interaction, in order to highlight the physical response of the flame to that parameter. The limitations to these variations are linked to the burner geometry and the numerical setup of LES in the AVBP framework. Reducing the flow below 7.4g/s or increasing it above 13.4g/s strongly amplifies numerical instabilities. The computed fuel to air equivalent ratios equal to 0.9 and 1.0 are excluded due to very high numerical instability, Figure 5.17. A reactant mixture leaner than 0.75 triggers acoustic instabilities, according to [80, 109]. A mixture as rich as 1.5 causes a radical change of the flame aspect and structure, Figure 5.19. In addition to changes in the boundary conditions specification files, the variations of FAeR are operated by re-initialising the unburned gas zone and the burned gas zone with the appropriate respective species composition. Similarly, the variations of fresh gas temperature are performed by a re-initialisation of the temperature on the computational nodes, setting the nodes upstream the combustion chamber to the unburned gas temperature, and setting all the rest of the computational domain to an estimation of the burned gas temperature. The increase of the outlet pressure is done by adding a pressure offset to all the nodes of the mesh in order to save time while properly shifting the simulation to the target pressure. The mass flow rate value specification was only changed on the inlet section. After every parametric variation, the computation is launched for a given time, t_{eff}, at least equal to one flow-through time, t_{flow}, equation 5.26, which corresponds to the time required to re-stabilize the flow and to ensure that solution across all the combustion chamber is consistent with the current parametric

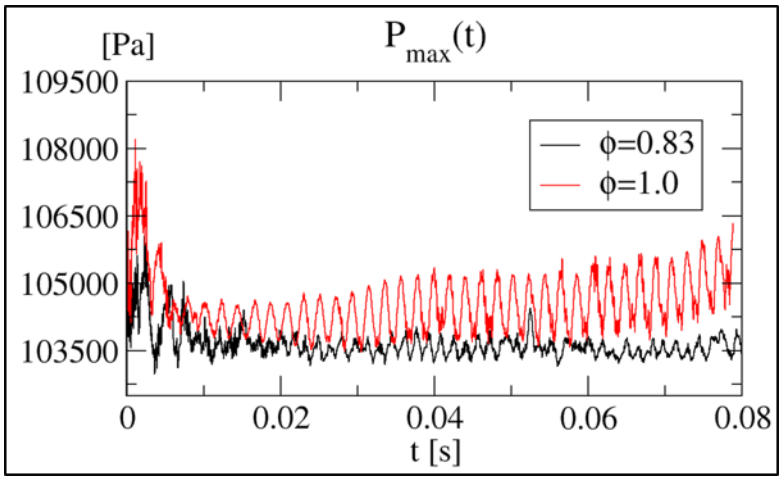

Figure 5.17 – Pressure wave pulsing at 475Hz observed for $\phi = 1$, with a peak-to-peak amplitude reaching 1500Pa and an average increasing from 104000 to 105000 Pa.

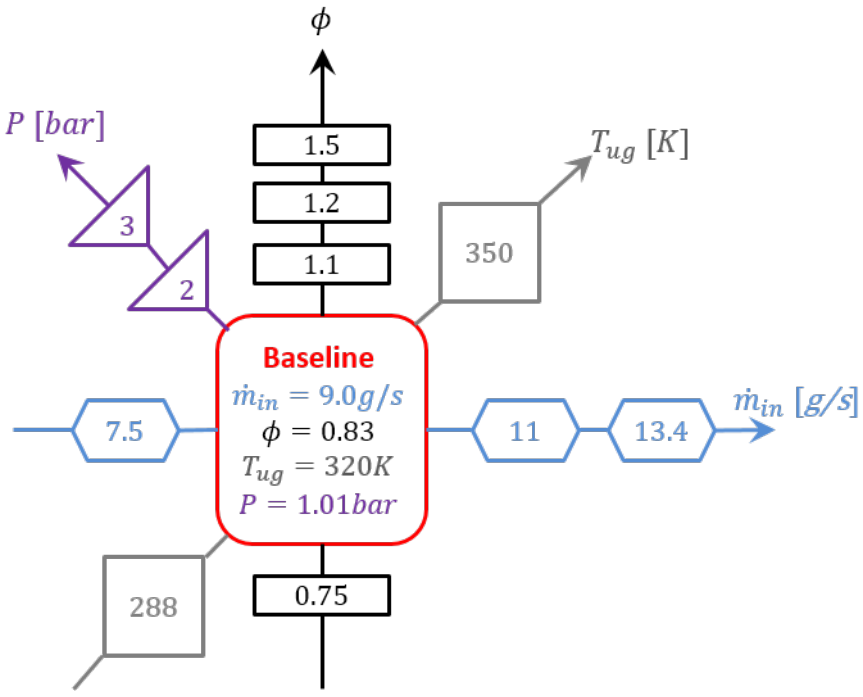

Figure 5.18 – Single parameter variations around the baseline operating point.

variation.

$$t_{flow} = t_{swirl} + t_{comb.} \tag{5.26}$$

$$t_{swirl} = \frac{\rho_{ug} V_{swirl}}{\dot{m}_{in}} \tag{5.27}$$

$$t_{comb.} = \frac{\rho_{comb.} V_{comb.}}{\dot{m}_{in}} \tag{5.28}$$

$$\rho_{comb.} = \frac{\rho_{ug} V_{ug} + \rho_{bg} V_{bg}}{V_{comb.}} \tag{5.29}$$

where t_{swirl} is the flow time through the inlet plenum and the swirler, V_{swirl} is the volume of the inlet plenum and the swirler approximated as a cylinder, $t_{comb.}$ is the flow time through the combustion chamber, $\rho_{comb.}$ and $V_{comb.}$ are the combustion chamber mean gas density and its volume. The fresh gas volume is obtained from the simulation results post-processing, and the other volumes are computed by using the geometrical dimensions of the respective features, Figure 5.3 and Figure 5.4. Depending on the case, the flow through time ranges from 60ms for the case $\dot{m}_{in} = 13.4g/s$ to 260ms for the case $P_{out} = 3bar$. Unfortunately, the minimal simulation times could not be reached for the cases $P_{out} = 3bar$ and $\phi = 1.5$. Nevertheless, the temporal evolution of the flame-characterising variables reached a steady state; this criterion allowed to exploit results for physical understanding. After reaching the time t_{eff}, computations of 20ms of all the parametric variations were performed for time-averaging.

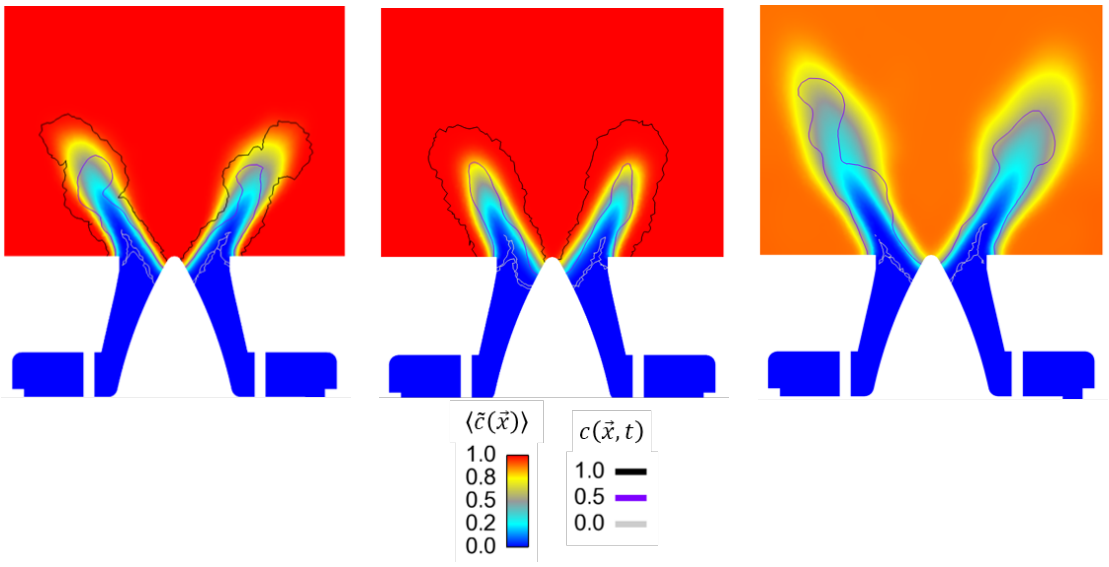

(a) $\phi = 0.75$ (b) $\phi = 1.1$ (c) $\phi = 1.5$

Figure 5.19 – 2D view of $\langle \tilde{c}(\vec{x}) \rangle$ and iso-contours of $\tilde{c}(\vec{x}, t)$ for different FAeR.

5.4 Analysis of the Computational Database

The numerical database results were analysed in order to understand and extract the main physical phenomena holding the response of the flame to a given variation of each operating parameter of the burner. In what follows, as a first step, the different physical variables allowing to determine the CFM reaction rate, equation 5.12, were investigated with the aim to identify and quantify their mutual interactions. The values of the operating parameters and the values of the different physical variables were normalized by the respective values of the operating parameters and physical variables of the baseline configuration. In a second step,

that understanding was interpreted and summarized to get to a formulation of a representative combustion model for system simulation.

5.4.1 Flame Characteristics

Laminar Flame Speed

The evolution of the laminar flame speed depending on the operating conditions is well known in the premixed combustion literature. Under the CFM hypothesis, changing the reactants mass flow rate while keeping the thermochemical properties of the mixture unchanged is not supposed to modify the global laminar consumption speed. However, according to section 5.1.3, S_L^{eff} is impacted by numerical settings of LES computations. Furthermore, the LES computations are subject to numerical perturbations, and therefore, non-physical perturbations can occur. Indeed, the laminar flame speed is affected by the reactants mass flow rate variation, Figure 5.20. Decreasing $\dot{m}_{in}$ to almost 83% of its baseline value causes S_L^{eff} to decrease of 0.3%. Increasing the mass flow rate by 50% increases S_L^{eff} of 8%. These discrepancies are linked to the numerical stability of the computation, which cannot be totally annihilated, neither accurately restricted to the same level for all the computations.

One of the predictable physical evolutions of S_L^{eff} with respect to an increase of ϕ is the

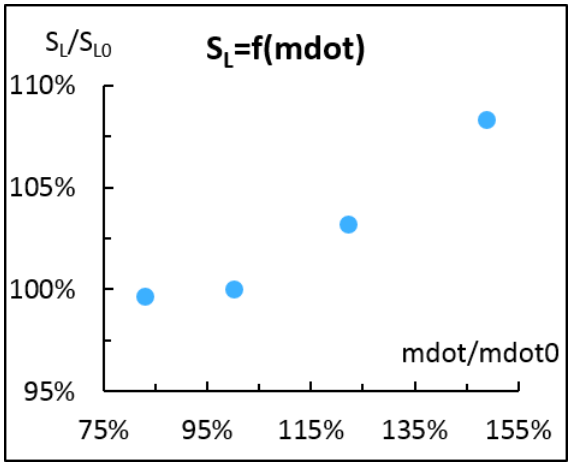

Figure 5.20 – Perturbation of the laminar flame speed S_L^{eff} with variations of inlet mass flow rate $\dot{m}_{in}$.

parabolic curve that peaks close to $\phi = 1.1$, Figure 5.21. The LES flame laminar speed is greater than S_L^{eff} in the 1D DNS results and the one given in [82]. The normalised values are in an acceptable agreement, except for the FAeR of 1.1 and 1.5.

The variation of S_L^{eff} with respect to unburned gas temperature, T_{ug}, Figure 5.22, is compared to the correlations given in [68] and in addition to the 1D DNS computations. One should note that the correlation made by [82] for methane was only meant for $\phi \in [0.8, 1.2]$. The speed increase is conformal to the predictions but the absolute values given by the LES are higher. However, the discrepancy is roughly constant through all the temperature range and the normalised results match.

Regarding the effect of pressure variation on S_L^{eff}, for the slow burning fuels ($S_L < 0.6$) employed in gas turbines [68], the literature states a power law expression of the form:

$$S_L \propto 10^{-x},\ x \in [0.1, 0.5] \tag{5.30}$$

The LES comply with the power law from the literature, and gives for equation 5.30 an exponent of 0.41, Figure 5.23.

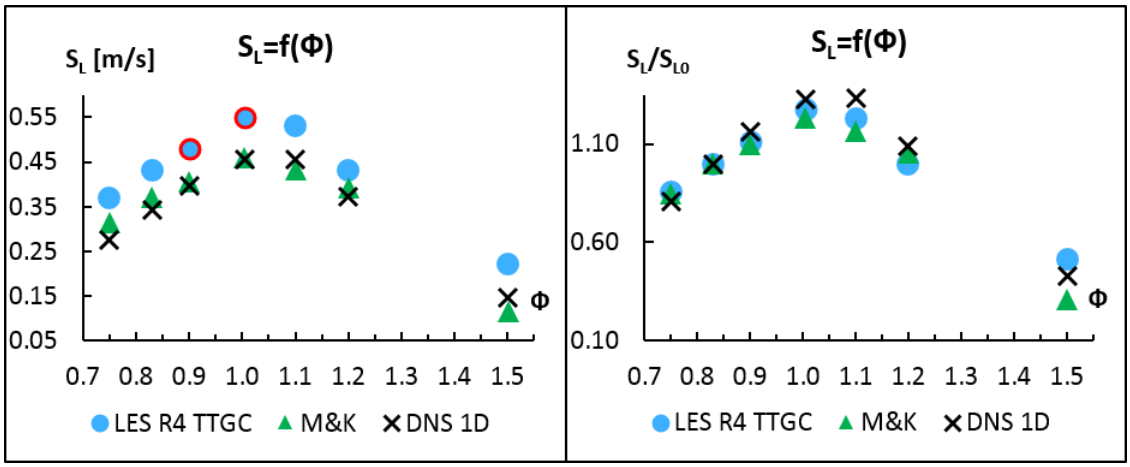

Figure 5.21 – Evolution of the laminar flame speed, S_L^{eff}, with variations of ϕ; comparison between the LES, 1D DNS, and literature correlation [82]. Left: absolute speed; Right: Speed normalised by the baseline value. The points circled in red refer to unstable computations.

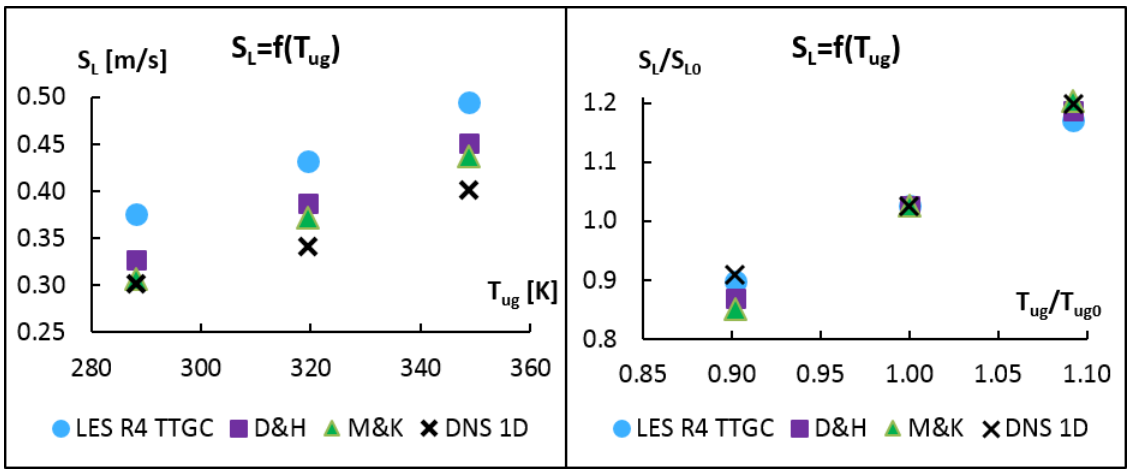

Figure 5.22 – Evolution of the laminar flame speed, S_L^{eff}, with variations of fresh gases temperature, T_{ug}; comparison of the LES results to literature correlations [43, 82], and DNS 1D computations.

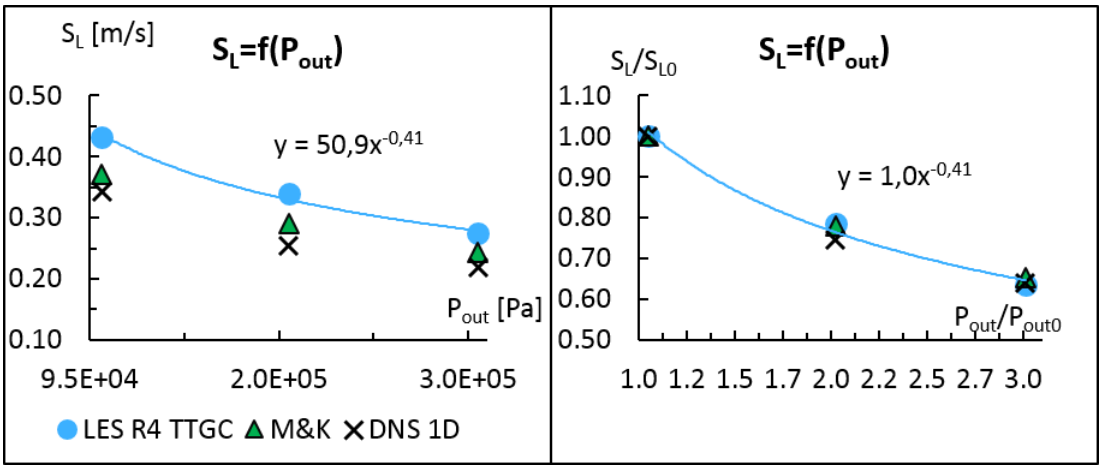

Figure 5.23 – Evolution of the laminar flame speed, S_L^{eff}, with variations of outlet pressure, P_{out}; comparison between LES, correlation [82] and 1D DNS.

Laminar Flame Thickness

The flame thickness response to changes in the various operating parameters, is shown in Figure 5.24. The decrease of the thickness with an increase of $\dot{m}_{in}$ would be due to the spurious increase of S_L^{eff}.

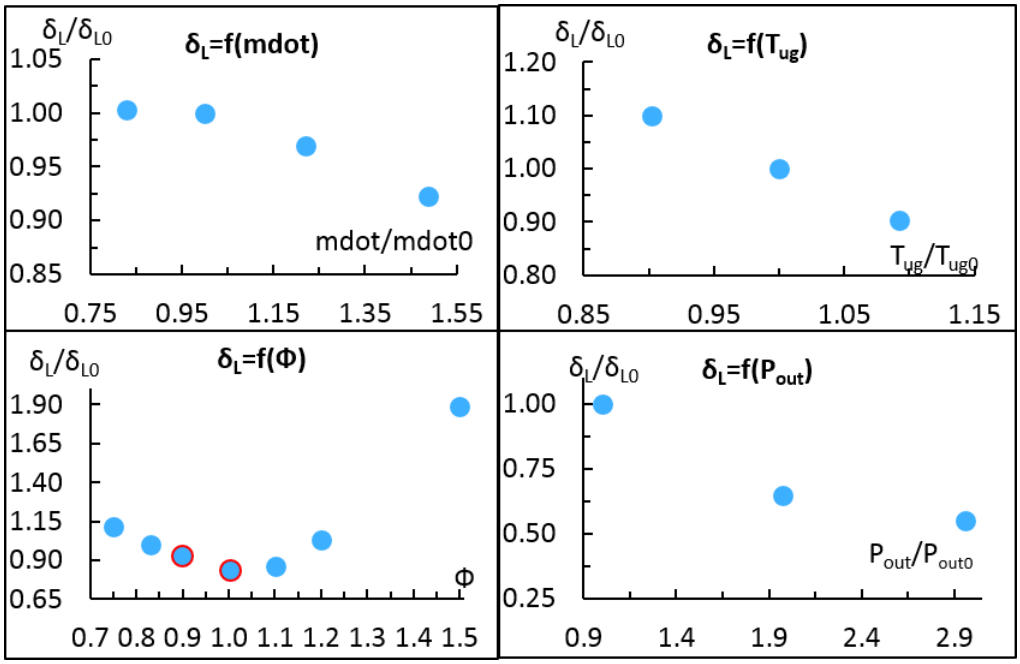

Figure 5.24 – Evolution of the laminar flame thickness, δ_L^{eff}, with variations of inlet mass flow rate, $\dot{m}_{in}$, FAeR, ϕ, fresh gases temperature, T_{ug}, and outlet pressure, P_{out}.

5.4.2 Unburned Zone Volume

Changes of the flame speed and surface directly modify the fresh gas volume. These changes were highlighted and quantified by means of the numerical database, Figure 5.25, and analysed.

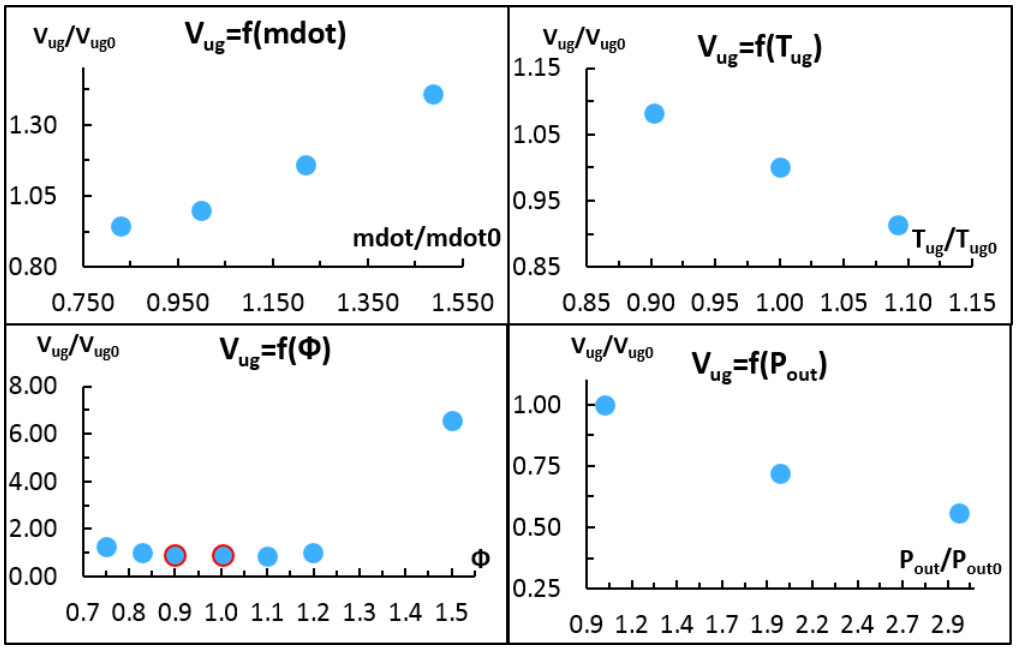

Figure 5.25 – Evolution of the unburned volume, V_{ug}, with variations of $\dot{m}_{in}$, ϕ, T_{ug} and P_{out}. Unstable points $\phi = 0.9$ and $\phi = 1.0$ are circled in red.

The fresh gas volume raises in a nearly linear fashion with the increase of $\dot{m}_{in}$. The increase of V_{ug} is around 40% at a 50% augmentation of the mass flow rate, going from the baseline to the maximal inlet flow rate value. As the flow velocity increases before the burning rate adapts, the flame is pushed and the unburned volume grows.
Conversely, V_{ug} decreases slightly and linearly with an increase of the unburned gas temperature or pressure, but not for the same reasons. A raise of inlet temperature induces a higher burning rate, which pulls the flame upstream towards the reactants flow source, before the combustion system stabilises.
When the static pressure builds up, the density increases, and the laminar flame speed decreases, but not to an extent that compensates the density growth. For instance, a pressure increase from 1bar to 3bar leads a density increase from 1.065kg/m^3 to 3.11kg/m^3, which corresponds to a ratio of 2.93. In the meanwhile, S_L decreases from 0.43m/s to 0.27m/s, which gives a ratio of 1.61. The density growth larger that the slowing down of the laminar flame velocity would explain the decrease of fresh gas volume.
The modification of the FAeR has a non-linear effect on V_{ug} between $\phi = 0.75$ and $\phi = 1.2$, and it is due to S_L change. In particular, a shift from lean combustion to $\phi = 1.1$ translates into an increase of laminar flame speed. The increase in S_L, which would reduce the unburned volume, is countered by an increase of flame wrinkling, which would have the opposite impact on fresh gas volume. Flame wrinkling is discussed in a following section. As the inlet mixture gets richer than $\phi = 1.1$, the burning rate is slowed down again, increasing the fresh gas volume. That mechanism seems to prevail at a FAeR of 1.5: V_{ug} grows remarkably faster from 1.2 to 1.5 than from 1 to 1.2. The accelerated growth suggests a change in the flame structure, Figure 5.29.

5.4.3 Mean Flame Surface

The mean flame surface evolution, Figure 5.26, evolves in a way roughly similar to the evolution of V_{ug}, with two exceptions though. First, when $\dot{m}_{in}$ increases, A_m does not increase following a linear pattern, unlike V_{ug}. Second, the mean flame surface growth

between the FAeR 1.2 and 1.5 is not as strong as the growth of V_{ug}. A plot of the mean flame surface evolution with respect to the fresh gases volume variation, Figure 5.27, shows a correlation between A_m and V_{ug} except for $V_{ug} = 6.5V_{ug,0}$, which is obtained for a FAeR of 1.5.

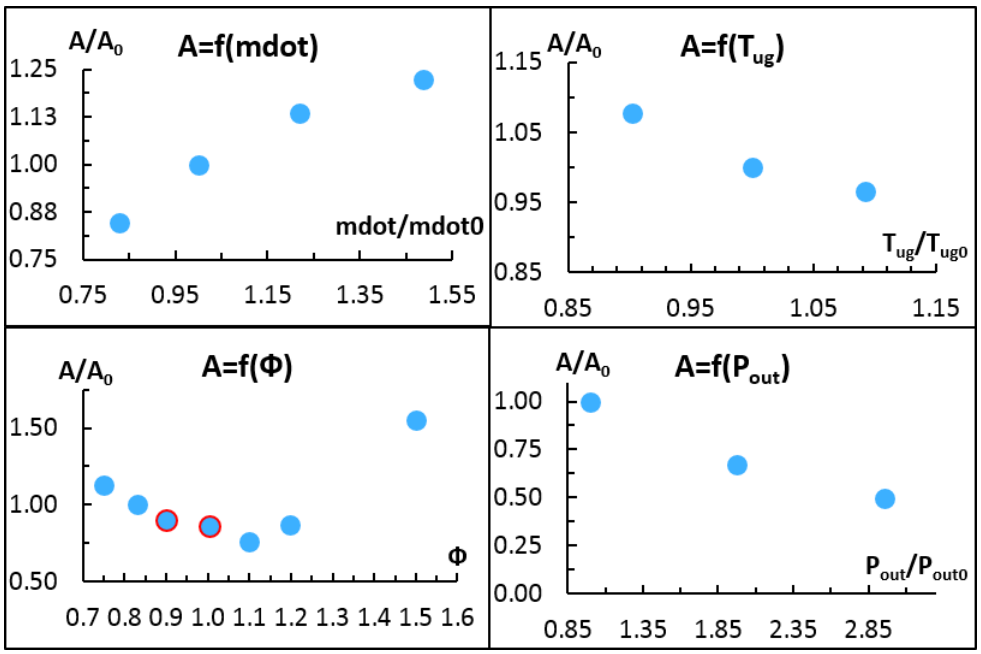

Figure 5.26 – Evolution of the mean flame surface A_m with variations of inlet mass flow rate $\dot{m}_{in}$, ϕ, fresh gases temperature T_{ug} and outlet pressure P_{out}.

A visualisation of the 2D fields of $\langle\tilde{c}(\vec{x})\rangle$ and the iso-contours of $\tilde{c}(\vec{x},t)$, provides a clear understanding of the flame response to the different parametric variations. The increasing

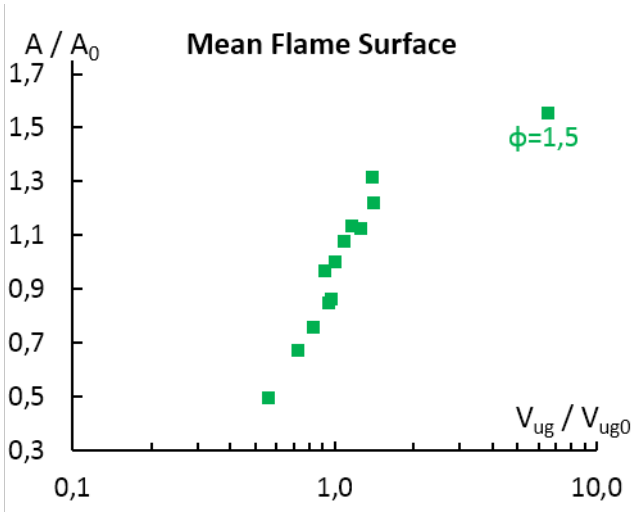

Figure 5.27 – Evolution of the normalised mean flame surface $^{A_m}/_{A_{m0}}$ with respect to $^{V_{ug}}/_{V_{ug0}}$ in response to the variations of $\dot{m}_{in}$, ϕ, T_{ug} and P_{out}.

of the mass flow rate condition slightly stretches the flame by its tip, Figure 5.28, but the anchoring points of the flame on the swirler outlet do not move. When the FAeR condition is enriched from 0.75 to near-stoichiometry, the flame is shortened Figure 5.29. It is enlarged as the mixture is further enriched from $\phi = 1.1$, and almost doubles its penetration length for

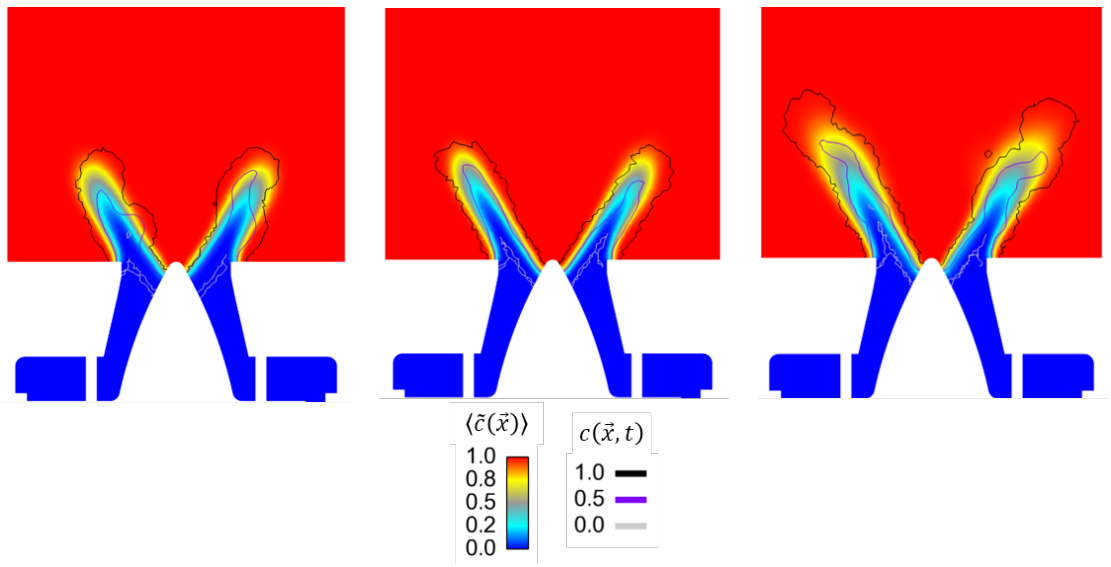

(a) $\dot{m}_{in} = 7.4g/s$ (b) $\dot{m}_{in} = 9.0g/s$ (c) $\dot{m}_{in} = 13.4g/s$

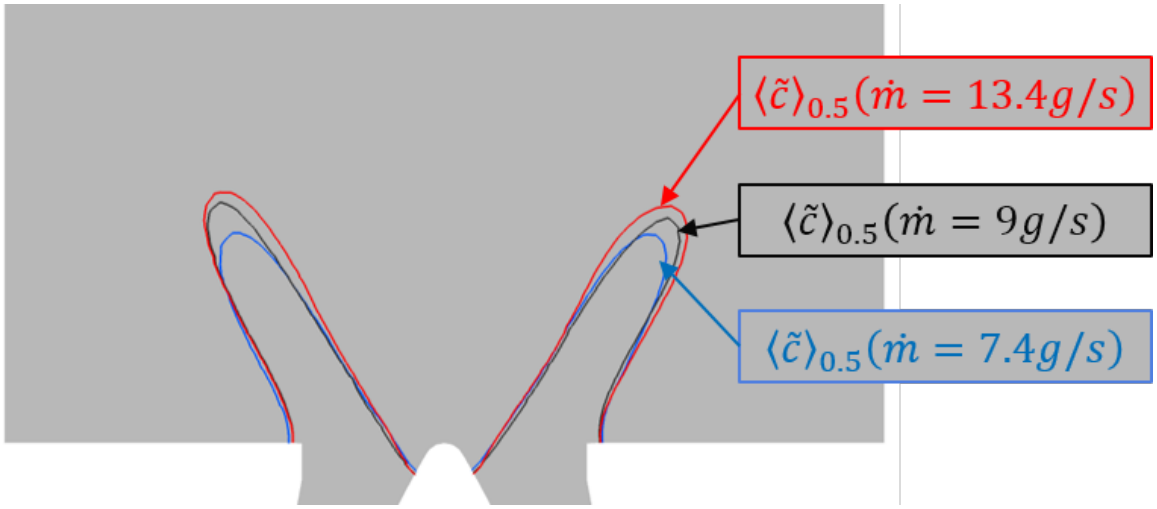

(d) Iso-contour $\langle\tilde{c}\rangle_{0.5}$ of the minimal, baseline and maximal values of $\dot{m}_{in}$.

Figure 5.28 – 2D view of $\langle\tilde{c}(\vec{x})\rangle$ and iso-contours of $\tilde{c}(\vec{x}, t)$ for different inlet mass flow rates.

$\phi = 1.5$. At the maximal FAeR, the flame edges are curved, which spreads wider in the region prior to its tip. The flame anchoring is slightly widened at $\phi = 1.5$. The flame response to a static pressure build-up, Figure 5.30, is characterised by a decrease of the fresh gas volume, and the angle formed by the internal flame edges is slightly narrower than the internal angle of the baseline flame. In addition, the mean flame surface is reduced, Figure 5.26.

5.4.4 Flame Wrinkling

The response of the flame wrinkling with respect to the mono-parametric variations, Figure 5.31, does not exceed the baseline wrinkling by more than 15% in few points. With the mass flow rate increase, Ξ builds up with a nearly constant slope. When the inlet temperature changes from baseline, the wrinkling decreases by a small percentage, between 1 and 5%. These fluctuations of Ξ are of the same order than the uncertainty of the LES results. Consequently, no conclusions can be drawn in the case of temperature variation.

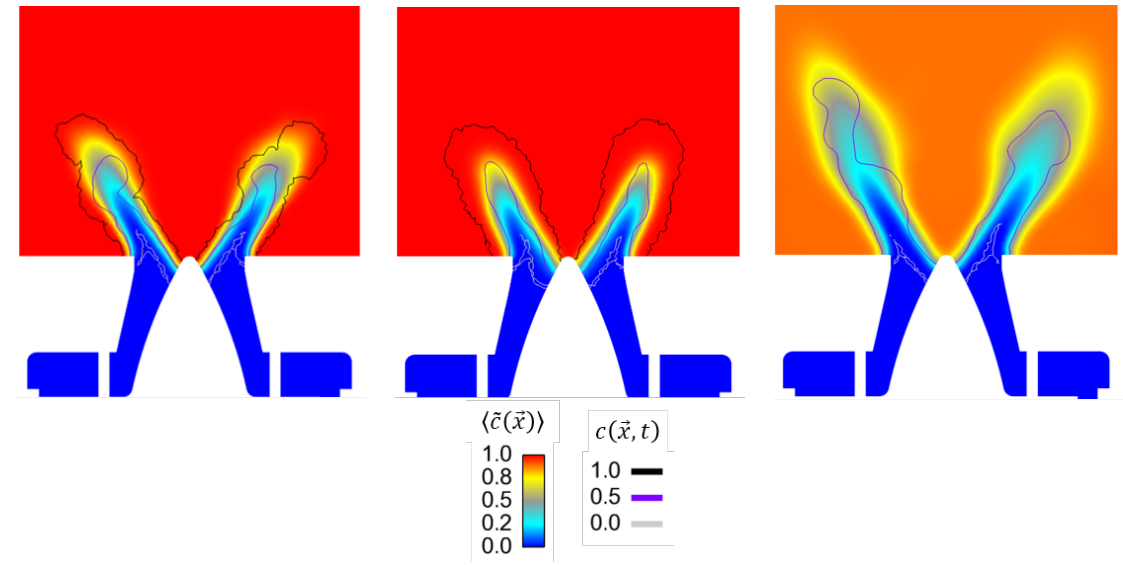

(a) $\phi = 0.75$ (b) $\phi = 1.1$ (c) $\phi = 1.5$

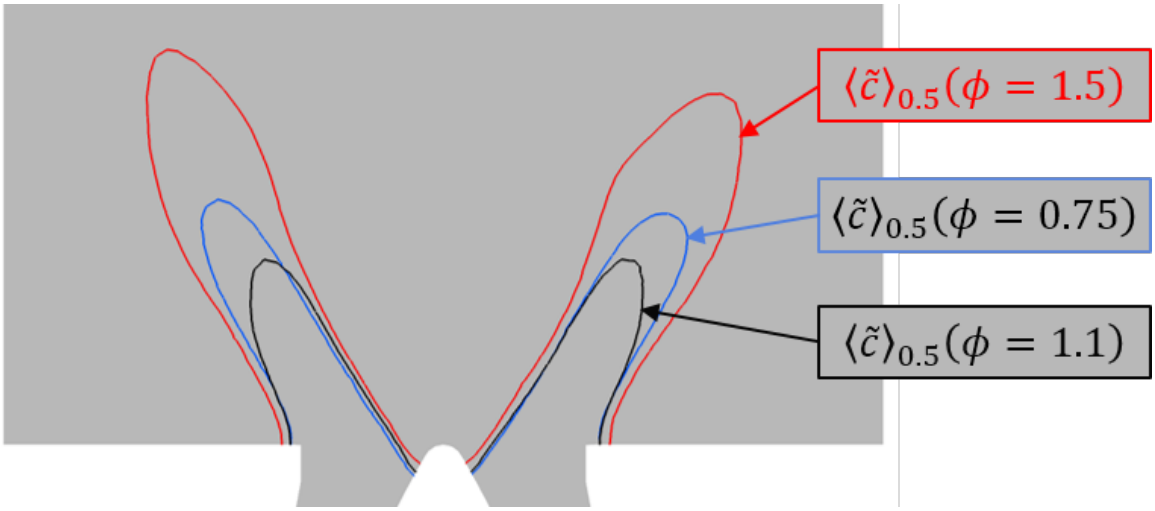

(d) Iso-contour $\langle\tilde{c}\rangle_{0.5}$ of lean, near-stoichiometric and rich mixture conditions.

Figure 5.29 – 2D view of $\langle\tilde{c}(\vec{x})\rangle$ and iso-contours of $\tilde{c}(\vec{x},t)$ for different FAeR.

5.4.5 Turbulent Velocity Fluctuations

The turbulent intensity response to the single-parametric variations listed in Table 5.6, Figure 5.32, is quite similar for what concerns its estimation in the unburned volume and in the flame. The exception remains for a few points: For $\phi = 1.1$ and $P_{out} = 2bar$, u' is greater in the UG zone than in the vicinity of the flame. For $\phi = 1.5$, u' increases in the flame comparing to its value in the UG zone. Turbulence gets more intense as the inlet flow rate raises, and decreases when the static pressure increases. The reason for a low turbulent intensity associated with a high wrinkling level at $\phi = 1.2$ could not be determined.

Adimensional aerodynamic pressure drop

In gas turbines, recirculation zones help in stabilizing the flames. However, these zones are also linked to aerodynamic pressure drop, and host high turbulence intensities. In an attempt to correlate the turbulent intensity to the aerodynamic pressure drop, total pressure

is computed using equation 5.31 both in the unburned and the burned gas zones:

$$\frac{\Delta P_t}{P_t} = \frac{P_{ug,t} - P_{bg,t}}{P_{ug,t}} \tag{5.31}$$

$$P_{ug,t} = P_{ug,s}\left(1 + \frac{\gamma_{ug}-1}{2} Ma_{ug}^2\right)^{\frac{\gamma_{ug}}{\gamma_{ug}-1}} \tag{5.32}$$

$$P_{bg,t} = P_{bg,s}\left(1 + \frac{\gamma_{bg}-1}{2} Ma_{bg}^2\right)^{\frac{\gamma_{bg}}{\gamma_{bg}-1}} \tag{5.33}$$

$$Ma_{ug} = \left.\frac{\left|\vec{U}\right|}{\sqrt{\gamma r T}}\right|_{ug}, \; Ma_{bg} = \left.\frac{\left|\vec{U}\right|}{\sqrt{\gamma r T}}\right|_{bg} \tag{5.34}$$

$$\left|\vec{U}\right| = \sqrt{U_x^2 + U_y^2 + U_z^2} \tag{5.35}$$

where P_s is the static pressure and P_t is the total pressure. Ma is the Mach number, and r is the perfect gas constant. The normalised turbulent velocity fluctuations ${}^{u'}/_{u'_0}$ appear to be correlated to normalised pressure drop, ${}^{\frac{\Delta P_t}{P_t}}/_{\frac{\Delta P_{t,0}}{P_{t,0}}}$, Figure 5.33.

In gas turbine literature [68, 77], aerodynamic pressure drop is often expressed as

$$\frac{\Delta P}{P} = \alpha \frac{r}{2}\left(\frac{\dot{m}\sqrt{T}}{AP}\right)^2 \tag{5.36}$$

where α is an non-dimensional constant, and A is a representative cross-section of the combustion chamber. Plotted against the pressure drop calculated in equation 5.36, u' shows a good correlation as well.

Equations 5.31 and 5.36, plotted in Figure 5.35, match well. A correlation between ${}^{u'_{ug}}/_{u'_{ug,0}}$ and the normalised aerodynamic pressure drop is presented in the next chapter.

Location of the LES points on a theoretical premixed turbulent combustion diagram

Once u', S_L^{eff} and δ_L^{eff} computed, by assuming a constant l_T equal to 7mm, the twelve LES operationg points are plotted on a turbulent premixed flames diagram, Figure 5.36. All the points are located in the area known as the wrinkled flamelets domain except the point ϕ =1.5, which is slightly above the $Ka = 10$ line. However, according to [41], the flamelet domain doesn't stop precisely at $Ka = 10$. Accordingly, the hypothesis of wrinkled flamelets seems to be well-suited for a 0D CFM flame tube model.

Conclusion

The premixed burner PRECCINSTA was studied by means of LES, and featured a turbulent envelope flame fed with methane. The results were validated against experimental measurements. Computations of specific variables and post-processing were developed. A database of twelve points was computed and included variations of inlet mass flow rate, inlet temperature and FAeR, as well as outlet pressure. The results of the database were analysed and verified against literature values and 1D DNS results. The next chapter presents the development and validation of the 0D CFM combustion model.

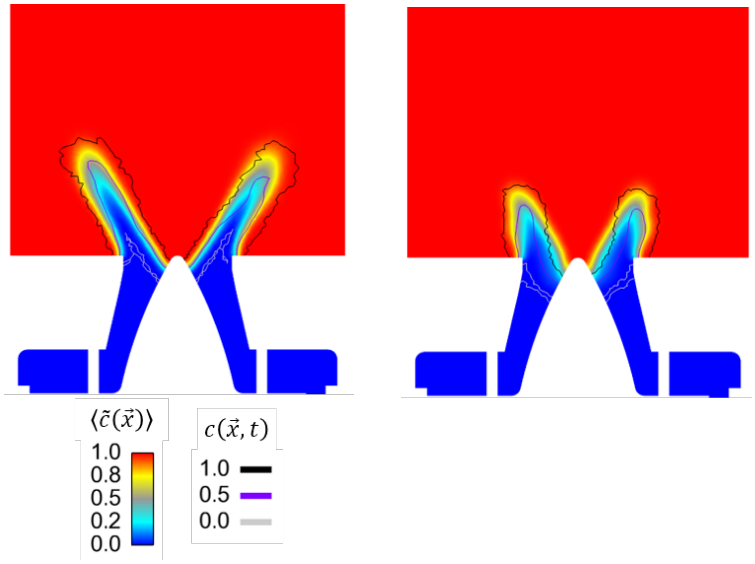

(a) $P_{out} = 1.01bar$ (b) $P_{out} = 3.0bar$

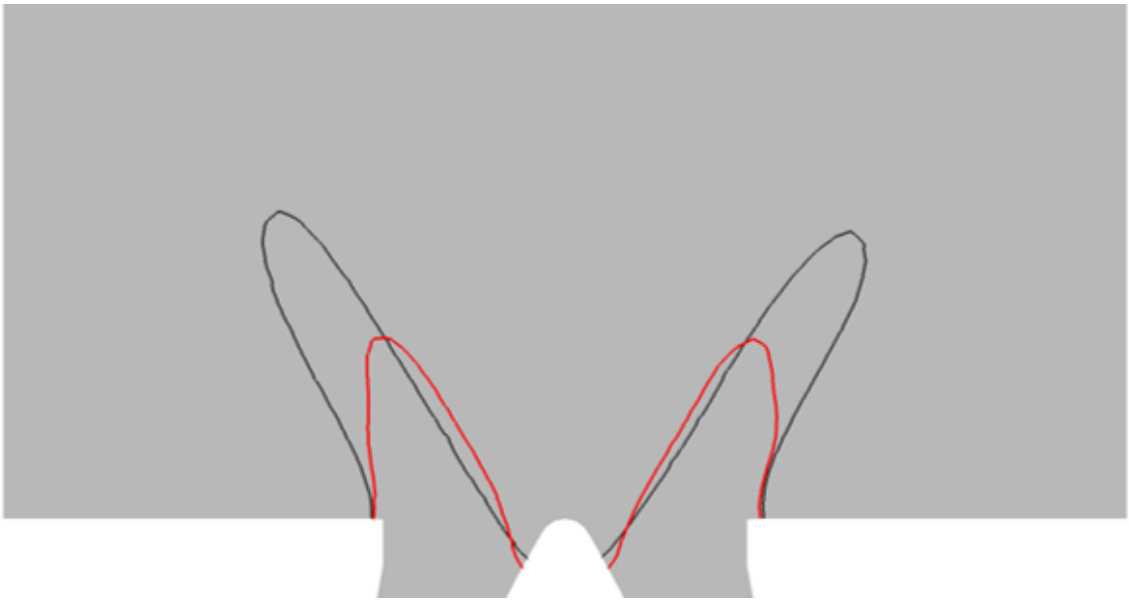

(c) Iso-contour $\langle\tilde{c}\rangle_{0.5}$ of the baseline configuration and the maximal pressure configuration.

Figure 5.30 – 2D view of $\langle\tilde{c}(\vec{x})\rangle$ and iso-contours of $\tilde{c}(\vec{x},t)$ for different outlet pressure conditions.

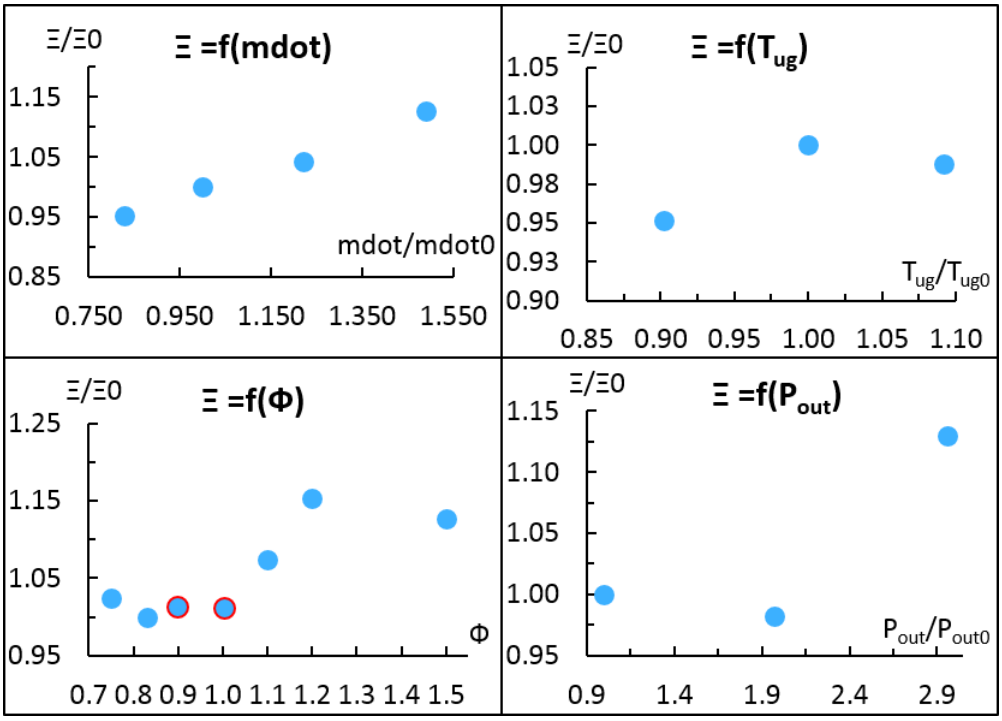

Figure 5.31 – Evolution of the flame wrinkling Ξ with variations of inlet mass flow rate $\dot{m}_{in}$, ϕ, fresh gases temperature T_{ug} and outlet pressure P_{out}.

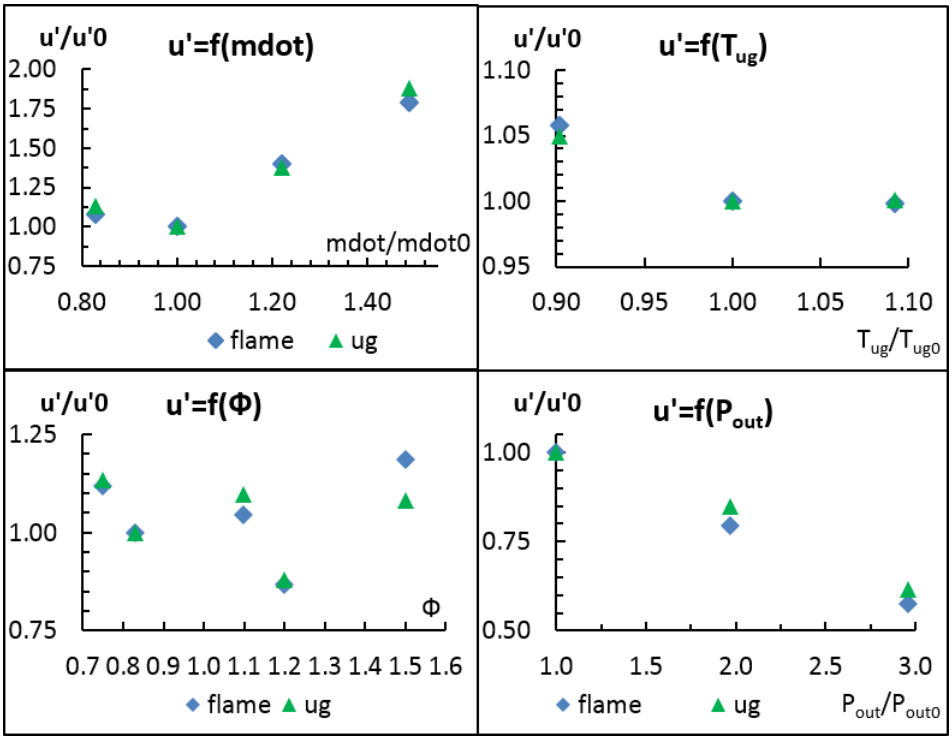

Figure 5.32 – Evolution of the turbulent intensity u' normalised by its baseline value, in the unburned volume and the flame, with variations of inlet mass flow rate $\dot{m}_{in}$, ϕ, fresh gases temperature T_{ug} and outlet pressure P_{out}.

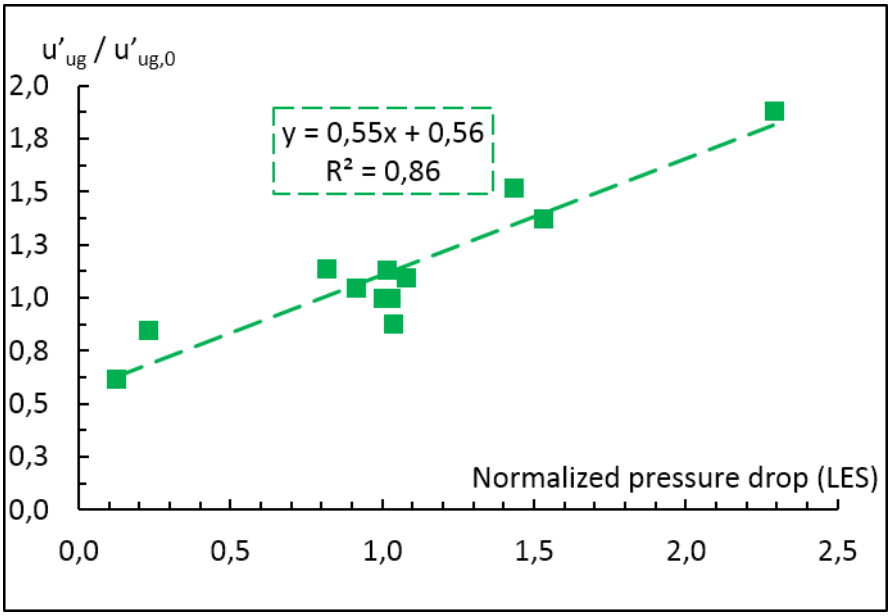

Figure 5.33 – Evolution of $^{u'_{ug}}/_{u'_{ug,0}}$, with the normalised aerodynamic pressure drop; LES data in green squares follows a linear trend.

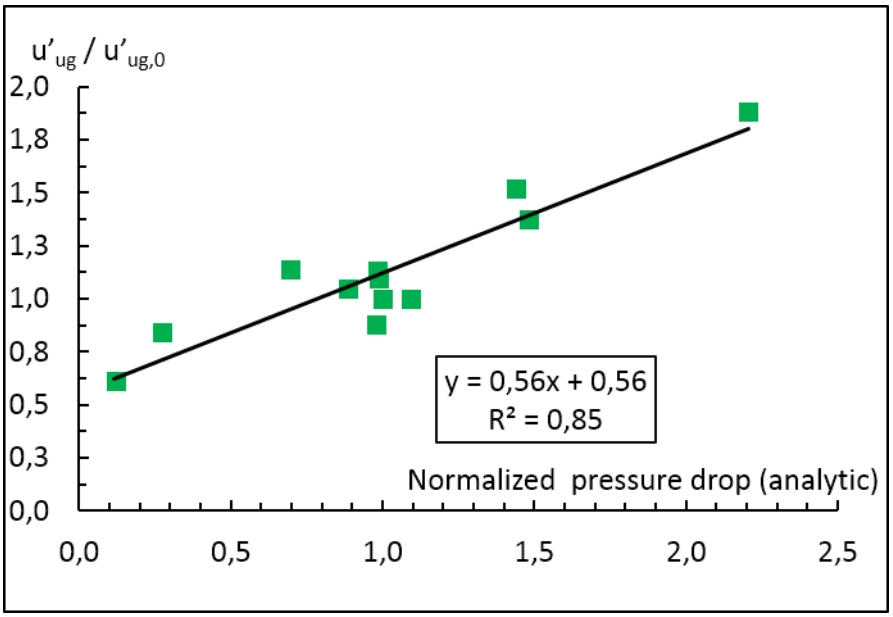

Figure 5.34 – Evolution of $^{u'_{ug}}/_{u'_{ug,0}}$, with the normalised aerodynamic pressure drop modelled by the analytic expression 5.36; LES data in green squares follows a linear trend.

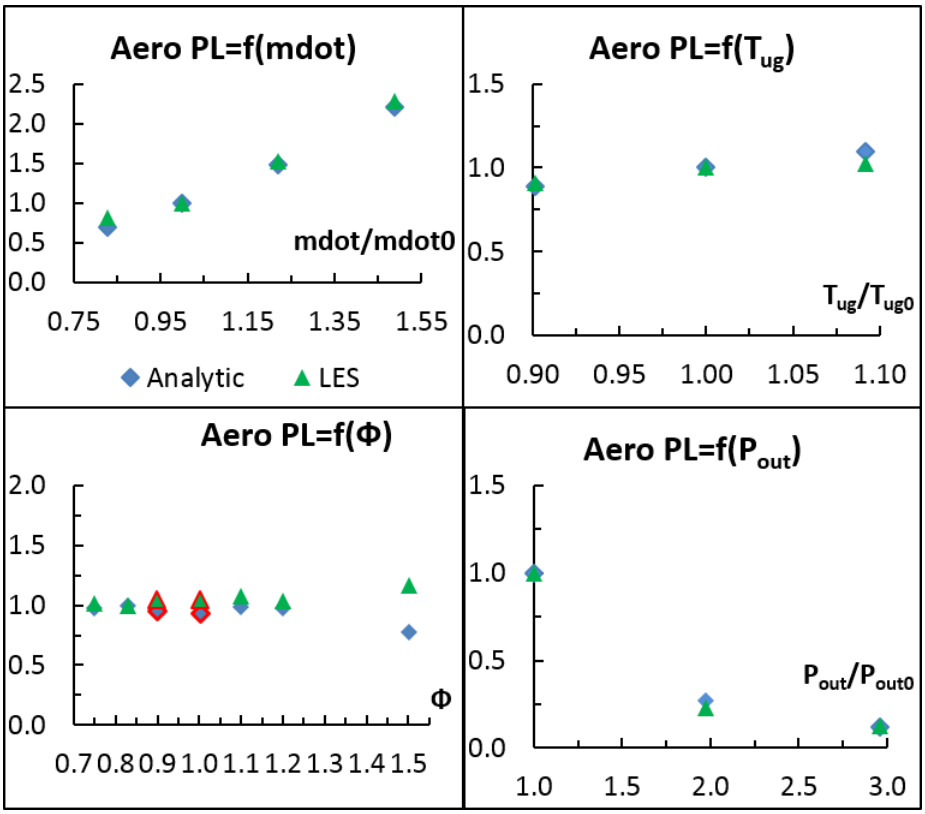

Figure 5.35 – Pressure drop between the unburned zone and the burned zone; comparison between the pressure drop measured from the LES, equation 5.31, and the analytic formula 5.36.

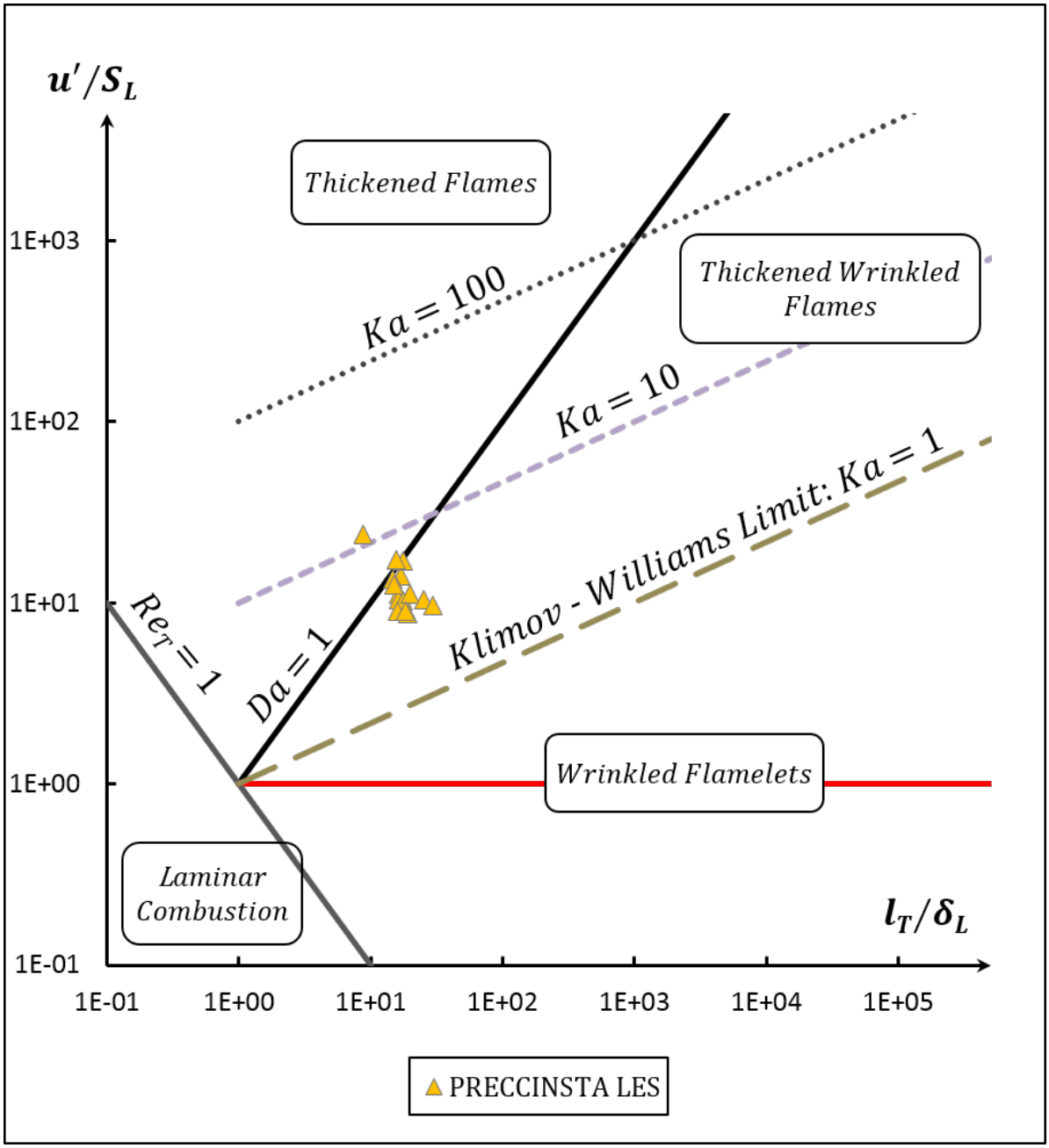

Figure 5.36 – Position of the PRECCINSTA computations on the premixed turbulent combustion diagram from [91] accounting for the remarks from [41].

Chapter 6

The 0D CFM Flame Tube Model

In a system simulation based on a network approach, a gas turbine combustor flame tube can be represented by one or several components. In this study, the flame tube was represented by one component. However, the model can be adapted to a multi-component flame tube representation schemes in a future work. According to the strategy announced in chapter 4, a 0D combustion model based on the CFM approach to premixed combustion is developed. Accordingly, part of the flame tube volume has to be identified as the fresh or Unburned Gases (UG) zone, filled with a homogeneous gaseous mixture fully characterised from a thermodynamic point of view. The complementary part of the flame tube component is the Burned Gases (BG) zone. Each zone is described by its mass, volume, composition and temperature. The flame surface represents the interface between the two zones. Reactants are consumed at the global consumption speed, equation 3.1.2, for which the modelling of some terms is based on the analysis of the PRECCINSTA LES database results, section 5.4. The same results are also used for the validation of the 0D flame tube model. This chapter presents the governing equations of the 0D model in the case of an already established turbulent premixed combustion.

6.1 The Flame Tube Component

The flame tube component, Figure 6.1, is an open volume that represents a complete combustion chamber such as PRECCINSTA. According to the Bond Graph formalism, it is designated as an aerothermal Capacity (C) receiving mass flow rates and returning static pressure. This choice gives the largest possible array of connectivity possibilities while giving the freedom to incorporate all the eventually required mathematical modelling for aerothermochemistry.

Therefore, the 0D flame tube model must be able to handle a reactive/non-reactive gaseous mixture that flows through it, as well as to deal with gaseous/liquid fuel injection. Information describing the interaction of the thermodynamic system contained into the combustion chamber with its external environment is exchanged at the six ports of the component. In details, ports 1, 4 and 6 are inlets and port 2 is an outlet. All these flow ports handle gaseous mixtures of up to twelve species, being oxygenated hydrocarbon fuel $C_xH_yO_z$, N_2, O_2, H_2, H_2O, CO, CO_2, NO, NO_2, HC, NH_3 and *soot*. Port 5 is an inlet restricted to fuel, feeding the flame tube mass and enthalpy flow rates of liquid or gaseous fuel. Port 3 is a thermal port that receives the wall temperature information, designated by T_{ex}, and allows heat exchange between the flame tube system and its surrounding environment, represented by the variable Q_{ex}.

The mixture is considered as ideal gas and as homogeneous in each of the two zones. The pressure P is assumed to be the same in UG and BG zones, and the turbulent kinetic energy field is assumed to be uniform in the total control volume V.

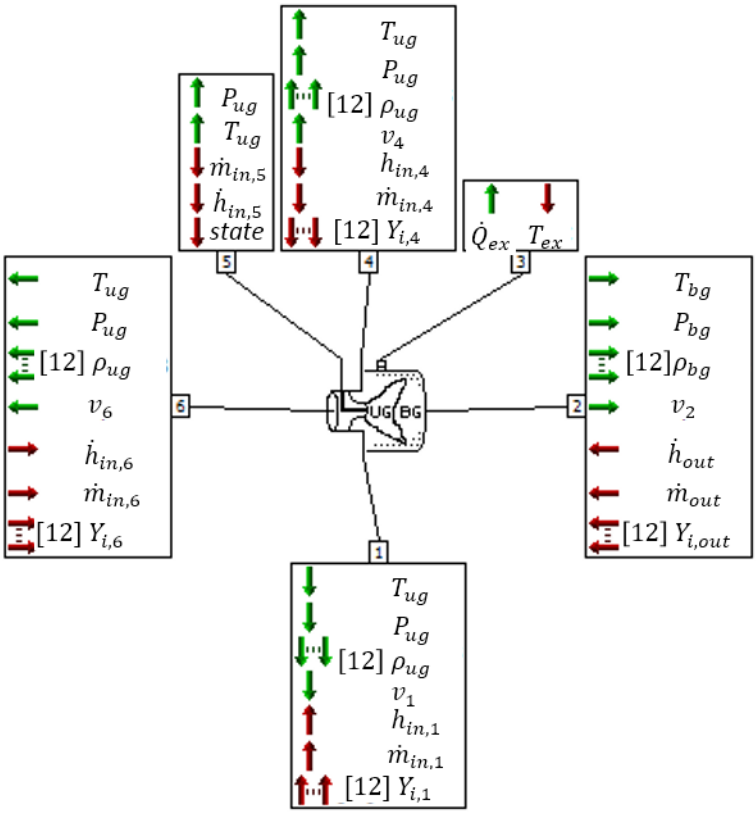

Figure 6.1 – Bond Graph of the 0D two-zone flame tube component. Ports are numbered from 1 to 6. Inputs are marked by red arrows and outputs are symbolised by green arrows. The variable *state* specifies the physical state of the fuel being fed into port 5.

6.1.1 Mass Balance, Density, Composition and Volume

Mass Balance

Mass balance is calculated for every species in the flame tube component by writing mass conservation for an open reactive system of the form:

$$\frac{dm_i}{dt} = \frac{d\left(\rho_i V\right)}{dt} = \sum_{k}^{in/out} \dot{m}_{i,k} + \dot{\Omega}_i \tag{6.1}$$

Total mass balance is given by:

$$\dot{m} = \sum_i \dot{m}_i \tag{6.2}$$

where the subscript k indicates an input/output port. $\dot{\Omega}_i$ is the reaction rate of the species i. In the presence of evaporating liquid fuel, the flow rate of evaporated fuel, $\dot{m}_F^{vap}$, is added to the gaseous fuel mass flow rate balance equation.

Liquid Fuel Evaporation

Liquid fuel is treated as a separate thermodynamic system exchanging mass and enthalpy with the gaseous phase. The fuel evaporation rate is written of the form:

$$\dot{m}_F^{vap} = \frac{m_F^{liq}}{\tau} \tag{6.3}$$

where m_F^{liq}, a state variable, is the current mass of liquid fuel in the combustion chamber and τ is the fuel and temperature dependent evaporation time scale. m_F^{liq} is solved by the integration of its derivative written of the form:

$$\dot{m}_F^{liq} = \dot{m}_{inj,F} - \dot{m}_F^{vap} \tag{6.4}$$

and where $\dot{m}_{inj,F}$ is the mass flow rate of injected liquid fuel. At every time step, the mass of evaporated fuel in the UG zone is also assumed as instantaneously mixed with the gaseous phase.

Density and Composition

Densities are state variables of the model. Thus, the solver calculates them by integrating their temporal derivatives, deduced from the mass balance of the flame tube:

$$\dot{\rho}_i = \frac{d\rho_i}{dt} = \frac{d}{dt}\left(\frac{m_i}{V}\right) \tag{6.5}$$

$$= \frac{\dot{m}_i V - m_i \cancel{\dot{V}}}{V^2} \tag{6.6}$$

$$\dot{\rho}_i = \frac{\dot{m}_i}{V} \tag{6.7}$$

The total density temporal derivative is given by:

$$\dot{\rho} = \sum \dot{\rho}_i \tag{6.8}$$

The species mass fractions are calculated using:

$$Y_i = \frac{\rho_i}{\rho} \tag{6.9}$$

The dynamic mixture viscosity is based on a linear temperature-dependent relation for every species i, depending on its mass fraction, Y_i.

$$\mu = \sum_i Y_i \left(\mu_{0,i} + \mu_{1,i} T\right) \tag{6.10}$$

Volume

The volume, V, is the volume corresponding to the combustion chamber volume.

6.1.2 Energy Balance, Temperature and Pressure

The differential form of the first law of thermodynamics is applied to the flame tube component as an open system, 6.12. Potential energy and the kinetic energy are neglected.

$$dU = \delta Q + \delta W + \sum_{k}^{in/out} h_k dm_k \tag{6.11}$$

$$= \delta Q - PdV + \sum_{k}^{in/out} h_k dm_k \tag{6.12}$$

The temporal variation gives:

$$\dot{U} = \dot{Q} - P\dot{V} + \sum_{k}^{in/out} h_k \dot{m}_k \tag{6.13}$$

$$Q = HR + Q_{ex} \tag{6.14}$$

$$\dot{HR} = \sum_{i} h_{f,i} \Omega_i \tag{6.15}$$

where U is the internal energy, h_k is the specific enthalpy of the mixture at port k and $\dot{m}_k$ is the mass flow rate at port k. The specific enthalpy h_i of a species i is evaluated at a given temperature by using the JANAF-YAWS polynomial formulation of specific heat at constant pressure, as a function of temperature. $h_{f,i}$ is the formation enthalpy of the species i. Heat flow, Q, includes combustion Heat Release (HR) and, Q_{ex}, the eventual contribution of conduction, convective and radiative heat flows in case of heat exchange between the thermodynamic system and its surrounding environment. W is the mechanical work yielded by the system.

According to equation 6.16 and equation 6.17, the energy balance equation 6.13 can be expressed in terms of enthalpy, equation 6.18.

$$H = U + PV \tag{6.16}$$

$$dH = dU + VdP + PdV \tag{6.17}$$

$$\dot{H} = \dot{Q} + V\dot{P} + \sum_{k}^{in/out} h_k \dot{m}_k \tag{6.18}$$

Total enthalpy is a state variable of the model.

Temperature

The temperature T represents the mean temperature of the gaseous mixture inside the flame tube component. It is computed from the flame tube mixture total enthalpy and composition, by means of an iterative procedure based on the Newton-Raphson method; its time derivative is used to compute the pressure derivative. Internal energy can be written of the form:

$$U = mu = m \int_T c_v dT = \sum_i m_i \int_T c_{v,i} dT = m \sum Y_i \int_T c_{v,i} dT \tag{6.19}$$

$$dU = dmu + mdu \tag{6.20}$$

$$\dot{U} = \dot{m} \sum_i Y_i \int_T c_{v,i} dT + m \sum_i \dot{Y}_i \int_T c_{v,i} dT + m \sum_i Y_i C_{v,i} \dot{T} \tag{6.21}$$

where c_v is the mixture specific heat at constant volume.
The injection of equation 6.21 in equation 6.13 enables a straightforward expression of $\dot{T}$.

$$\dot{m}\int_T c_v dT + m\sum \dot{Y}_i u_i + mc_v\dot{T} = \dot{Q} - P\dot{V} + h\dot{m}|^{in} - h\dot{m}|^{out} \tag{6.22}$$

$$\dot{T} = \frac{\sum m_i h_i + \dot{Q} - P\dot{V} - m\sum \dot{Y}_i u_i - \dot{m}\int_T c_v dT}{mc_v} \tag{6.23}$$

The species mass fraction derivatives are calculated by:

$$\dot{Y}_i = \frac{d}{dt}\left(\frac{m_i}{m}\right) = \frac{\dot{m}_i}{m} - Y_i\frac{\dot{m}}{m} \tag{6.24}$$

Pressure

Pressure is a state variable of the model. The perfect gas law, applied to the full flame tube control volume, is differentiated in order to get the pressure temporal derivative:

$$P = \rho r T \tag{6.25}$$

$$\dot{P} = \rho\left(\dot{r}T + r\dot{T}\right) + rT\sum \dot{\rho}_i \tag{6.26}$$

The temperature derivative $\dot{T}$ is given by equation 6.23, r is the gas mixture constant and $\dot{r}$ is its derivative:

$$r = \sum Y_i r_i \tag{6.27}$$

$$\dot{r} = \sum \dot{Y}_i r_i \tag{6.28}$$

where $\dot{Y}_i$ are given by equation 6.24.

6.2 Fresh Gas Characterisation

6.2.1 Mass Balance, Density, Composition and Volume

The gaseous flow ports 1, 4 and 6, and eventually the liquid fuel port 5, pour into the UG zone.

Mass Balance

A mass balance, $\dot{m}_{ug,i}$, is calculated for the i-th species in the UG zone, as well as the total mass flow rate $\dot{m}_{ug}$:

$$\frac{dm_{ug,i}}{dt} = \frac{d\left(\rho_{ug,i}V_{ug}\right)}{dt} = \sum_k^{in/out} \dot{m}_{k,i} - \dot{m}_{ug,i}^{\rightarrow bg} \tag{6.29}$$

$$\dot{m}_{ug,i}^{\rightarrow bg} = \dot{\Omega}_F\frac{m_{ug,i}}{m_{ug,F}} \tag{6.30}$$

$$\dot{m}_{ug} = \sum_i \dot{m}_{ug,i} \tag{6.31}$$

where $\sum_k^{in/out} \dot{m}_{k,i}$ is the sum of the species i mass flow rates through inlet/outlet ports and $\dot{m}_{ug,i}^{\rightarrow bg}$ is the rate at which the species i is transferred from the unburned zone to the burned zone. In the case of liquid fuel injection, liquid fuel is treated as a separated thermodynamic system exchanging mass and enthalpy with the fresh gases during the evaporation process. The mixing of the gaseous flows is assumed as being instantaneous. Fuel is assumed to be evaporated in the fresh gas region.

Density and Composition

Fresh gas densities are state variables of the model, written as it follows:

$$\rho_{ug,i} = \frac{m_{ug,i}}{V_{ug}} \tag{6.32}$$

The total fresh gas density is the sum of the fresh gas species densities:

$$\rho_{ug} = \sum \rho_{ug,i} \tag{6.33}$$

The time derivatives of fresh gas densities are given by:

$$\dot{\rho}_{ug,i} = \frac{\dot{m}_{ug,i}V_{ug} - m_{ug,i}\dot{V}_{ug}}{V_{ug}^2} = \frac{\dot{m}_{ug,i}}{V_{ug}} - \rho_{ug,i}\frac{\dot{V}_{ug}}{V_{ug}} \tag{6.34}$$

$$\dot{\rho}_{ug} = \sum \dot{\rho}_{ug,i} \tag{6.35}$$

The UG species mass fractions are calculated as:

$$Y_{ug,i} = \frac{\rho_{ug,i}}{\rho_{ug}} \tag{6.36}$$

Volume

The UG volume is also a state variable of the model. Starting from the relation $V_{ug} = \frac{m_{ug}}{\rho_{ug}}$, the derivation gives:

$$\frac{dV_{ug}}{dt} = \frac{d}{dt}\left(\frac{mrT}{P}\right)_{ug} \tag{6.37}$$

$$= \frac{1}{P}\left(\dot{m}rT + m\dot{r}T + mr\dot{T}\right)_{ug} - \frac{\dot{P}}{P}V_{ug} \tag{6.38}$$

$$\dot{V}_{ug} = V_{ug}\left(\frac{\dot{m}_{ug}}{m_{ug}} + \frac{\dot{r}_{ug}}{r_{ug}} + \frac{\dot{T}_{ug}}{T_{ug}} - \frac{\dot{P}}{P}\right) \tag{6.39}$$

where r_{ug} is the UG mixture gas constant, and $\dot{r}_{ug}$ is its derivative. Based on UG species gas constants r_i, they are respectively calculated as:

$$r_{ug} = \sum Y_{ug,i}r_i \tag{6.40}$$

$$\dot{r}_{ug} = \sum \dot{Y}_{ug,i}r_i \tag{6.41}$$

$$\dot{Y}_{ug,i} = \frac{\dot{m}_{ug,i}}{m_{ug}} - Y_{ug,i}\frac{\dot{\rho}_{ug}}{\rho_{ug}} \tag{6.42}$$

6.2.2 Energy Balance, Temperature and Pressure

The energy balance equation for an open system, equation 6.18, is applied to the UG region:

$$\dot{H}_{ug} = \dot{Q}_{ug} + V_{ug}\dot{P} + \sum_{k}^{in/out} h\dot{m}_{ug,k} - h\dot{m}_{ug}^{\rightarrow bg} \tag{6.43}$$

in which

$$\delta Q_{ug} = \delta Q\frac{V_{ug}}{V} \tag{6.44}$$

$$V_{ug} \ll V \tag{6.45}$$

$$\delta Q_{ug} \simeq 0 \tag{6.46}$$

The term $\sum_{k}^{in/out} h\dot{m}_{ug,k}$ represents the balance of the enthalpy fluxes through inlet/outlet ports, and $h\dot{m}_{ug}^{\rightarrow bg}$ is the rate at which fresh gas enthalpy is transferred from the unburned zone to the burned zone. The unburned mixture temperature and its derivative are computed from the UG mixture total enthalpy and composition, by an iterative procedure based on the Newton-Raphson method. According to the hypothesis of homogeneous pressure in the flame tube volume, the pressure derivative is given by equation 6.26.

6.2.3 Aerodynamic Pressure Drop, Turbulent Intensity and Integral Length Scale

Pressure is assumed to be the same in the UG and BG zones. However, as previously mentioned and shown in Figure 5.34, the turbulent velocity fluctuations are correlated to the relative pressure drop, $\frac{\Delta P_t}{P_{ug,t}}$, by a linear trend. Indeed, according to Figure 5.33, the fresh gases turbulent intensity is modelled by:

$$\left.\frac{u'}{u'_0}\right|_{ug} = 0.56 \left(\frac{\Delta P_t}{\Delta P_{ug,t}}\right) \left(\frac{P_{ug,t}}{\Delta P_t}\right)_0 + 0.56 \tag{6.47}$$

where $\left.\frac{u'}{u'_0}\right|_{ug}$ is the UG turbulent intensity normalised by its baseline value, and $\left(\frac{\Delta P_t}{P_{ug,t}}\right)_0$ is the baseline value of the relative pressure drop in the LES database. Relative pressure drop is expressed by:

$$\frac{\Delta P_t}{P_{ug,t}} = \alpha \frac{r_{ug}}{2} \left(\frac{\dot{m}_{ug}\sqrt{T_{ug}}}{A_{tube} P_{ug,t}}\right)^2 \tag{6.48}$$

where $\frac{\dot{m}_{ug}\sqrt{T_{ug}}}{P_{ug,t}}$ is the corrected mass flow rate, α is a constant, r_{ug} is the UG perfect gas constant and A_{tube} is a representative cross-section of the flame tube.

The integral length scale variable, l_T, is a required physical variable to close the equations system the 0D CFM flame tube model. l_T can be estimated from a CFD computation and according to [50], for a given geometry, it does not change by changing operating conditions. For PRECCINSTA, it is assumed that integral scale is equal to the diameter of the flame at the anchoring point on the swirler nozzle, which is 7mm.

6.3 Combustion Description

A lumped two-in-one reaction, proposed by [100], is used for describing the generic oxygenated fuel oxidation:

$$\begin{aligned} &\alpha_1 \left(C_x H_y O_z + \left(x + \frac{y}{4} - \frac{z}{2}\right) O_2 \longrightarrow x CO_2 + \frac{y}{2} H_2O\right) \\ &+ (1-\alpha_1) \left(C_x H_y O_z + \frac{x-z}{2} O_2 \longrightarrow x CO + \frac{y}{2} H_2\right) \end{aligned} \tag{6.49}$$

where α_1 is defined by considering the atomic conservation of C, H and O, as:

$$\alpha_1 = \frac{\left(0.98\left(4x + y - 2z\right)/\phi - 2(x-z)\right)}{2x + y} \tag{6.50}$$

and where ϕ is the fuel-air equivalence ratio given by:

$$\phi = \left(\frac{Y_F}{Y_A}\right)\left(\frac{Y_A}{Y_F}\right)_{st} \tag{6.51}$$

Y_F and Y_A are the respective mass fractions of fuel and air, and the subscript st stands for stoichiometric. The reaction rate $\dot{\Omega}_i$ for a species i is expressed as:

$$\dot{\Omega}_i = \upsilon_i \frac{M_i}{M_F} \dot{\Omega}_F \tag{6.52}$$

where $\dot{\Omega}_F$ is the fuel consumption rate, M_i is the Molar weight of the species i and υ_i is its stoichiometric coefficient in the chemical reaction, equation 6.49.

The fuel consumption rate $\dot{\Omega}_F$ is expressed of the form:

$$\dot{\Omega}_F = \rho_{ug} Y_{ug,F} S_L A_m \Xi \tag{6.53}$$

where ρ_{ug} is the UG density, $Y_{ug,F}$ is the UG fuel mass fraction, S_L is the laminar flame speed, A_m is the mean flame surface, and Ξ is the flame surface wrinkling, Figure 6.2, defined as:

$$\Xi = \frac{A_T}{A_m} \tag{6.54}$$

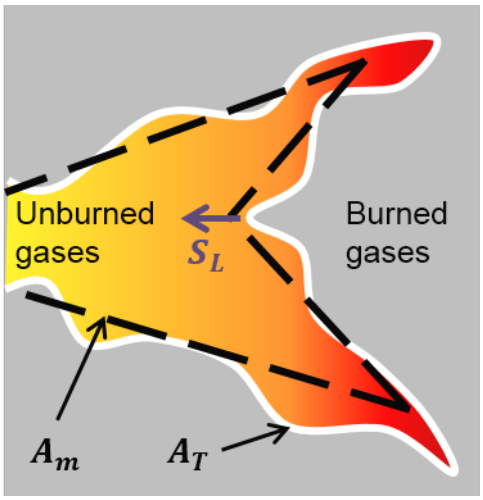

Figure 6.2 – Schematic representation of mean and turbulent flame surfaces and laminar flame speed.

The mean flame surface A_m, and the flame wrinkling Ξ are modelled using the LES database, and their modelling is presented below.

6.3.1 The Mean Flame Surface

According to the CFM paradigm, the mean flame surface is linked to the UG volume, since the volume is defined as being wrapped by the flame from one side, and delimited by the inlet of the combustion chamber from the other side. Here a geometric approach and a semi-empirical correlation approach based on LES results are investigated. The idea behind the geometric approach is that if the flame follows a geometrical pattern, its surface can be calculated by means of an easy and reliable extrapolation, increasing the predictability of 0D model. However, a geometrical pattern would be hardly identified in cases of spray combustion and counter-swirling flows. Accordingly, a semi-empirical approach seems to be easier to establish and probably more likely to yield more accurate results; nevertheless, it should target several types of burner technologies in order to provide a wide range of applications.

Geometric Representation

The first modelling option is a geometric approach that represents the mean flame surface as a combination of cones resulting in a truncated double cone, Figure 6.3. That representation allows a parametric calculation of the flame surface and fresh gases volume. Based on the

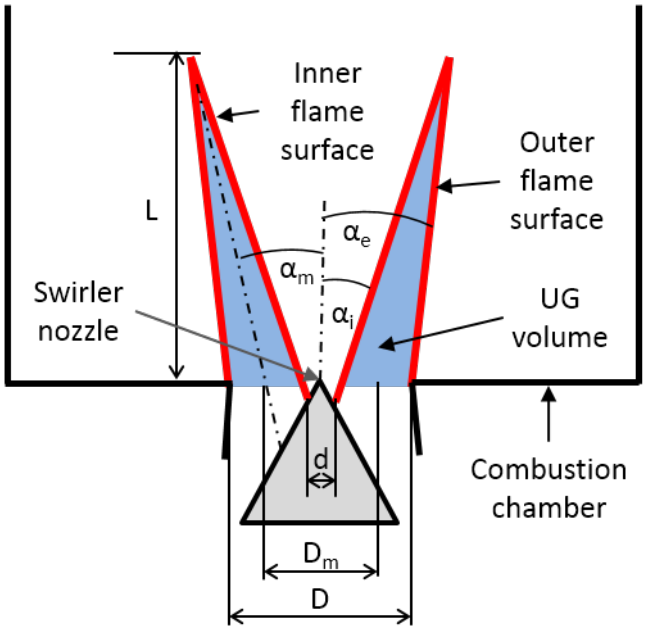

Figure 6.3 – PRECCINSTA M flame represented as a truncated double cone. D is the swirler diameter, d is the diameter corresponding to the flame anchor point on the swirler nozzle, L is the height of the flame, α_i and α_e are respectively the internal and external angles formed by the flame branches with the vertical direction, and α_m is the mean angle.

anchoring point diameter, d, evaluated from the LES results, and the swirler diameter, D, a mean diameter, D_m, is calculated, equation 6.55. A mean cone angle, α_m, is considered as the average between the internal and external angles of the flame, α_i and α_e, and it is evaluated from the LES results. The vertical flame length, L, is the variable which allows to completely determine the relationship between UG volume and UG mean flame surface. The angles, diameters and flame vertical length are related by the following formulae:

$$D_m = \frac{D+d}{2} \tag{6.55}$$

$$\alpha_i = \arctan\frac{D_m - d}{2L} + \tan\alpha_m \tag{6.56}$$

$$\alpha_e = \arctan\frac{D_m - D}{2L} + \tan\alpha_m \tag{6.57}$$

The mean surface is the sum of the internal and external flame surfaces S_i and S_e.

$$S_i = \frac{\pi L}{\cos\alpha_i}\left(L\tan\alpha_i + LD_i\right) \tag{6.58}$$

$$S_e = \frac{\pi L}{\cos\alpha_e}\left(L\tan\alpha_e + LD_e\right) \tag{6.59}$$

$$A_m = S_i + S_e \tag{6.60}$$

The unburned gases volume is deduced by a boolean subtraction of a truncated cone from another, Figure 6.4

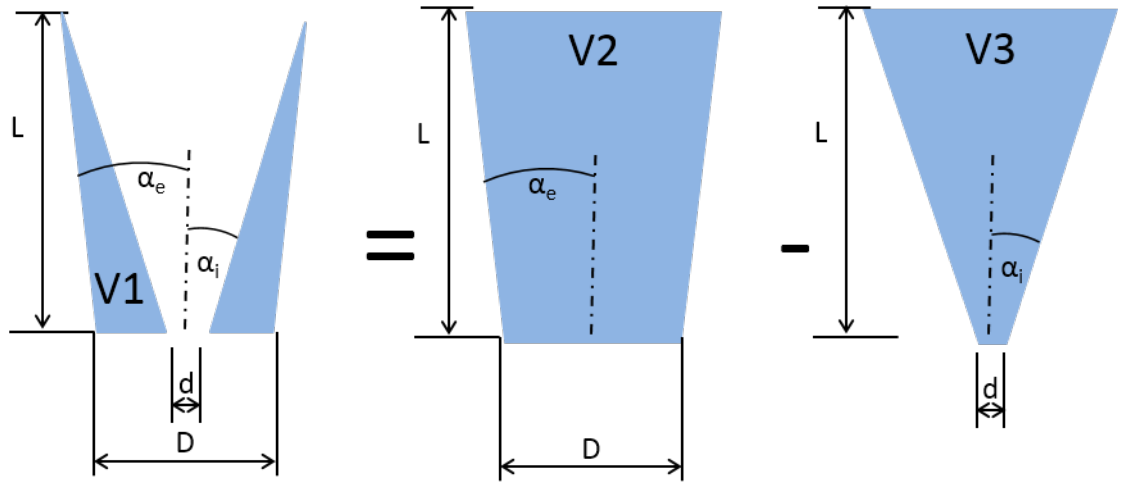

Figure 6.4 – Decomposition of the truncated double cone; the UG volume, Volume 1 (V_1) is obtained by removing Volume 3 (V_3) from Volume 2 (V_2).

$$V_3 = \frac{\pi L}{3} \tan {\alpha_i}^2 \left(L^2 + \frac{3}{2} \frac{L D_i}{\tan \alpha_i} + \frac{3}{4} \frac{D_i^2}{\tan {\alpha_i}^2} \right) \tag{6.61}$$

$$V_2 = \frac{\pi L}{3} \tan {\alpha_e}^2 \left(L^2 + \frac{3}{2} \frac{L D_e}{\tan \alpha_e} + \frac{3}{4} \frac{D_e^2}{\tan {\alpha_e}^2} \right) \tag{6.62}$$

$$V_1 = V_2 - V_3 \tag{6.63}$$

The resulting pattern of the geometrical modelling approach, Figure 6.5, is close to the pattern observed in the LES computations, except for one point at which V_{ug} is over six times greater than the baseline value. That point corresponds to the richest case for which $\phi = 1.5$. It can be noticed that the slope generated by the geometric model is slightly steeper than the LES-based slope.

Correlation from the LES database

The second option is to establish a correlation between normalized mean flame surfaces and UG volumes given by the LES database, of the form:

$$A_m = A_{m,0} \cdot a_m \left(v \right) \tag{6.64}$$

$$v_{ug} = \frac{V_{ug}}{V_{ug,0}} \tag{6.65}$$

where a_m is a correlation which is function of the normalised UG volume, v_{ug}. A linear dependency is identified between V_{ug} and A_m from the LES results, Figure 6.6, aside from the richest point. The point of exception rather seems to be reached with a log law of the form:

$$a_m = 0.216 \log \left(v_{ug} \right) + 1.148 \tag{6.66}$$

A combination of the linear trend f_1 and logarithmic trend f_2 can be formed by using a smoothing function expressed by:

$$a_m = smooth(f_1, f_2) = \frac{1}{2} \left(f_1 + f_2 + (f_1 - f_2) \tanh \left(\frac{v_{ug} - v_{ug}^*}{\zeta_0} \right) \right) \tag{6.67}$$

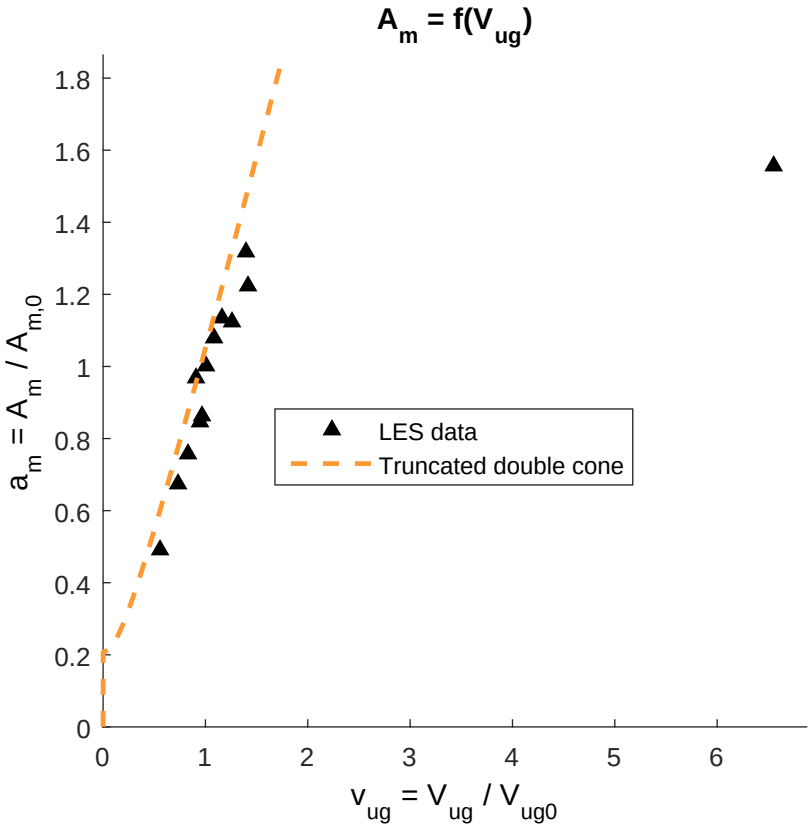

Figure 6.5 – Variation of normalised mean flame surface, a_m, with respect to normalised UG volume, v_{ug}; comparison between LES data and the truncated double cone geometrical model.

where v_{ug}^{*} is the value of normalised fresh gas volume at which the shift from the linear trend to the logarithmic trend is expected, and ζ_0 is a coefficient for adjusting the steepness of the shift. However, further investigations should be done before using the smoothing function $smooth(f_1, f_2)$ for incorporating the point corresponding to the case $\phi = 1.5$ in a flame surface estimator a_m.

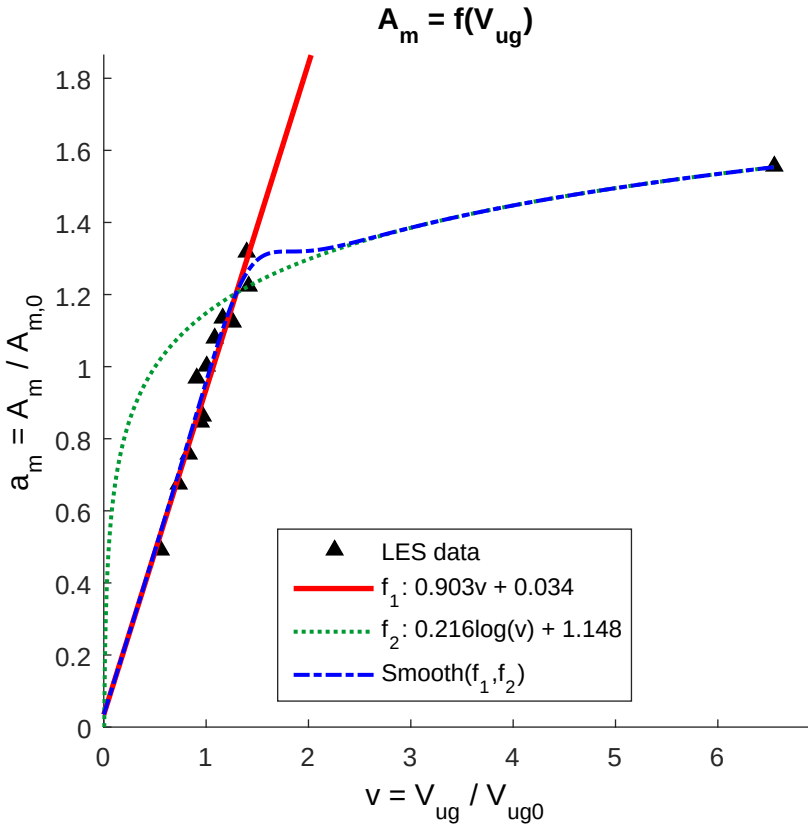

Figure 6.6 – Variation of a_m with respect to v_{ug}; comparison between LES data, the linear fit f_1, the log fit f_2, and a smoothed combination of f_1 and f_2.

For $V_{ug} < 2V_{ug,0}$, A_m can be written as

$$A_m = A_{m,0} \cdot a_m \tag{6.68}$$

where

$$a_m = 0.903 v_{ug} + 0.034 \tag{6.69}$$

The comparison between the geometrical approach and the correlation, Figure 6.7, shows that the semi-empirical correlation is the closest to the LES results.

6.3.2 The Laminar Flame Speed and Thickness

Laminar Flame Speed

For a given fully evaporated fuel, the laminar flame speed, when the oxidiser is pure air, depends on FAeR, pressure and temperature:

$$S_L = S_L(\phi, T, P) \tag{6.70}$$

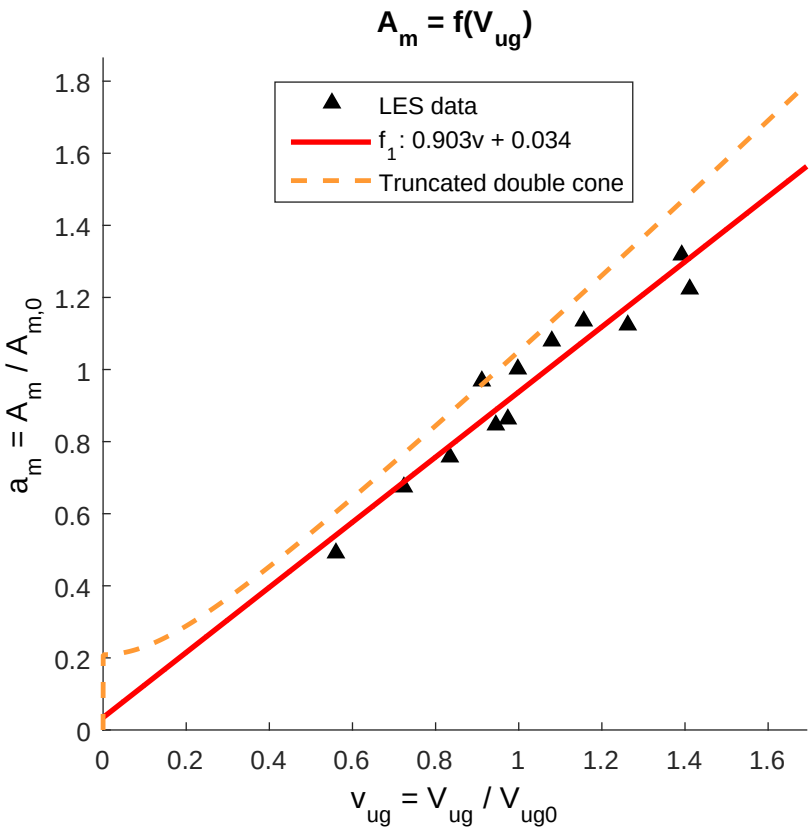

Figure 6.7 – Variation of a_m with respect to v_{ug}; comparison between LES data, the linear fit f_1 and the truncated double cone geometrical model.

According to section 5.4.1, the LES predictions of $S_L^{eff,LES}$ in the PRECCINSTA case featured a nearly constant offset in comparison with results given by laminar flame speed correlations, and that offset was investigated in section 5.1.3 and seemed to be due to numerical peculiarities and also to minor numerical instabilities. The offset was eliminated after normalising the respective $S_L^{eff,LES}$ by $S_{L,0}^{eff,LES}$, the laminar flame speed given by LES at the baseline point detailed in Table 5.6. Consequently, in the 0D flame tube model, S_L has to be written of the form:

$$S_L = \frac{S_{L,0}^{eff,LES}}{S_{L,0}\left(\phi, T_{ug}, P\right)} S_L\left(\phi, T_{ug}, P\right) \tag{6.71}$$

For methane, a correlation by Metghalchi&Keck [82] is used.

$$S_L\left(\phi, T_{ug}, P\right) = a_1 \left[1 + a_2\left(\phi - 1\right) + a_3\left(\phi - 1\right)^2\right] \left(\frac{T_{ug}}{T_{ug,ref}}\right)^{b_1} \left(\frac{P}{P_{ref}}\right)^{b_2} \tag{6.72}$$

where the a_i and b_i are constant coefficients, $T_{ug,ref}$ is a reference temperature and P_{ref} a reference pressure, Table 6.1. This correlation was experimentally validated for:

$$298K < T_{ug} < 650K,\ 1 < P < 40bar,\ 0.8 < \phi < 1.2$$

Table 6.1 – Coefficients of the correlation by [82] for the laminar speed of a methane flame.

Coefficient	Value
a_1 [-]	0.382
a_2 [-]	0.237
a_3 [-]	-3.411
b_1 [-]	1.854
b_2 [-]	-0.434
$T_{ug,ref}$ $[K]$	298
P_{ref} $[Pa]$	1.0^5

For the sake of completeness, it is worth to say that flame speed models are also available for flame propagation through quiescent combustible mixtures in which the fuel is present in the form of a combination of multi-droplet and vapour [68]. Such a kind of approach seems to be interesting for dealing with more complex combustion chambers in which fuel is introduced as liquid phase.

Laminar Flame Thickness

The laminar flame thickness (diffusion thickness δ_L^0), equation 3.8, is a physical quantity that allows to describe the physical structure of a premixed flame. Such an information is widely used in turbulent combustion theory for understanding and characterising the combustion regime [28, 81]. Here the correlation by [9] is chosen for that purpose:

$$\delta_L = \frac{2\lambda_{ug}}{\rho_{ug} c_{p_{ug}} S_L} \left(\frac{T_{bg}}{T_{ug}}\right)^{0.7} \tag{6.73}$$

where λ_{ug} is the thermal conductivity of the fresh gases mixture, and $c_{p_{ug}}$ is the unburned mixture specific heat at constant pressure.

6.3.3 The Flame Surface Wrinkling

According to the CFM formalism, combustion is assumed to occur within a thin sheet of wrinkled laminar flamelets. Several correlations are tested, and four flame surface wrinkling models are chosen from the literature.

Clavin and Williams Wrinkling Model

Studies conducted by [32] addressed the dynamics of wrinkled laminar flames for small values of turbulent velocity fluctuations. The effects of flame stretch and flame relaxation on the flame front were analysed, leading to the model expressed as:

$$\Xi = \sqrt{0.5\left(1+\sqrt{1+8C\left(\frac{u'}{S_L}\right)^2}\right)} \tag{6.74}$$

where C is the heat-to-reactant diffusivity ratio, approximately equal to unity. The turbulent correction to the flame speed involves an increase of the mean flame surface by wrinkling.

Ballal and Lefebvre Wrinkling Model

The correlation by Ballal and Lefebvre [68], 6.75, was proposed from a series of experiments on enclosed premixed turbulent flames. In these experiments, an effort was made in order to create conditions in which the separate effects of turbulence intensity and scale on burning velocity and flame structure could be determined. The scales encountered in a turbulent flow range in size from the Kolmogorov scale η, which represents the size of the smallest eddies in the flow, to the integral scale l_T, which represents the size of the largest eddies. For conditions of low turbulence ($u' < 2S_L$), it was found that burning velocity is increased due to the effect of turbulence in wrinkling the flame, thereby extending its surface area, as first noted by [38].

$$\Xi = \sqrt{1+0.003\left(\frac{u' l_T}{S_L \delta_L}\right)^2} \tag{6.75}$$

According to [68], conditions of high turbulence ($u' < 10S_L$) would yield a combustion regime, in which small eddies of unburned mixture intersperse a fairly thick matrix of burned gases.

Bradley Wrinkling Model

An attempt was made by Bradley [17] to explicitly account for the effect of integral length scale l_T, and the effect of thermo-diffusive properties of the mixture through the Lewis number Le on wrinkling.

$$\Xi = 1 + \frac{0.95}{Le}\sqrt{\frac{l_T}{\delta_L}\frac{u'}{S_L}} \tag{6.76}$$

The correlation expressed in equation 6.76 was developed based on stretched flames and the analysis of local flamelet quenching, and tested in applications that included spherical detonations and continuous swirling combustion.

ITNFS Model

The Intermittent Turbulence Net Flame Stretch Model (ITNFS) is based on an efficiency function that evaluates the stretch rate of turbulent premixed flames. It was initially developed by [81], using DNS of a counter-rotative vortex pair interacting with a plane flame, as well

as experimental data for characterising a statistical distribution of all the turbulent length scales acting on a flame front. A similar efficiency function, was proposed by [28, 29] and tested in the TFLES model, used in this study for the 3D database. The efficiency function proposed in [28, 29], Γ_c was used in the equilibrium wrinkling model:

$$\Xi_{eq} = 1 + \frac{2}{S_L}\sqrt{\Gamma_c \nu_T} \tag{6.77}$$

where ν_T is the turbulent kinematic viscosity calculated from l_T and the turbulent kinetic energy, k, as:

$$\nu_T = 0.009 l_T \sqrt{k} \tag{6.78}$$

$$k = \frac{3}{2}u'^2 \tag{6.79}$$

Testing of the Wrinkling Correlations

When benchmarked against the LES results without any adjustment, the wrinkling models do not quite match with the PRECCINSTA database values, Figure 6.8, except for the model by [32], which gave results of the same order as the LES results.

Therefore the following modification is performed for adding a new degree of freedom to correlations to better fit the LES results:

$$\Xi_0 = 1 + \kappa_j \left(\hat{\Xi}_j - 1\right) \tag{6.80}$$

where κ_j is an adjustment coefficient chosen for the $j-th$ correlation in order to provide the best possible fit with the LES results, Table 6.2.

Table 6.2 – Adjustment coefficients for the wrinkling models implemented in the 0D flame tube model.

Model	Ballal & Lefebvre	Bradley	Clavin & Williams	ITNFS
κ_j	0.25	0.2	0.84	0.35

After the adjustment, the four wrinkling models globally gave results of almost the same order as the LES results, Figure 6.9. The trend observed on LES results was fairly captured for the change of inlet mass flow rate, especially by the correlations by Bradley [17] and Clavin & Williams [32]. In the case of Fuel to Air ratio variations, the evolution of the flame surface wrinkling as predicted by the LES computations as a slightly growing trend. Even though that trend is not observed in system simulation predictions, the four flame wrinkling correlations tested in this work provide results within the same order of magnitude as LES results. Concerning the evolution of flame wrinkling with the variation of T_{ug}, the low amplitudes of the fluctuations of Ξ associated to the amplitudes of T_{ug} variations do not seem to be linked to premixed turbulent flame dynamics. These fluctuations of Ξ are rather of the same order of magnitude as the confidence level of the flame wrinkling predicted by LES computations. Regarding the flame wrinkling response to the variations of FAeR, the correlations by Bradley [17] and Lefebvre [68] give the closest results to the LES results. The evolution of wrinkling with the increase of pressure is also well predicted by the Bradley correlation given by [17]. Overall, the Bradley correlation [17], equation 6.76, provides the best response when compared to the LES results. However, further assessments of these four wrinkling correlations are necessary, and should be based on configurations even more representative of modern aeronautical combustors.

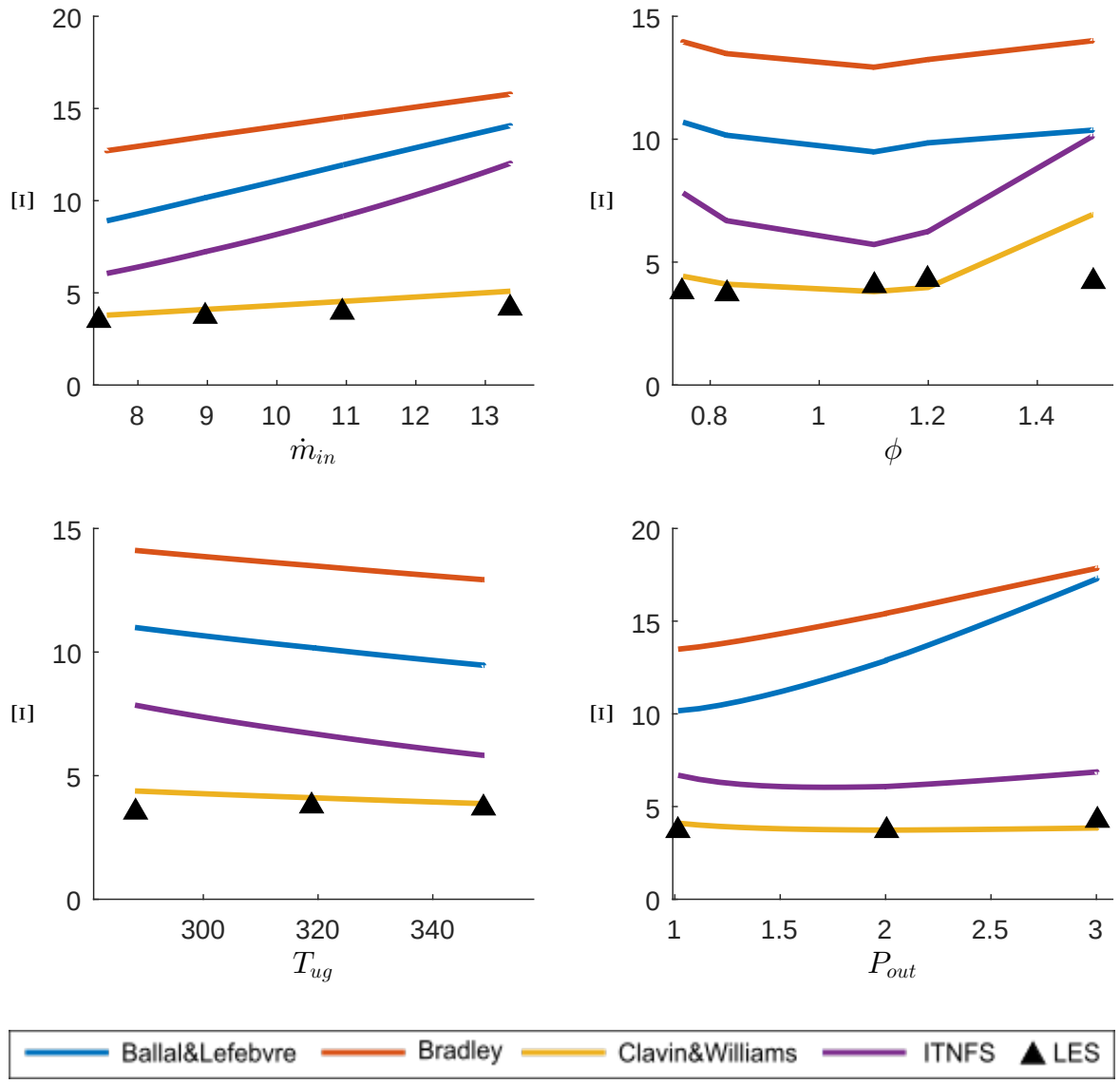

Figure 6.8 – Evolution of the wrinkling through the parametric variations; LES compared to models by Ballal&Lefebvre [68], Bradley [17], Clavin&Williams [32] and ITNFS [28, 29] before applying the adjustment coefficients κ_i.

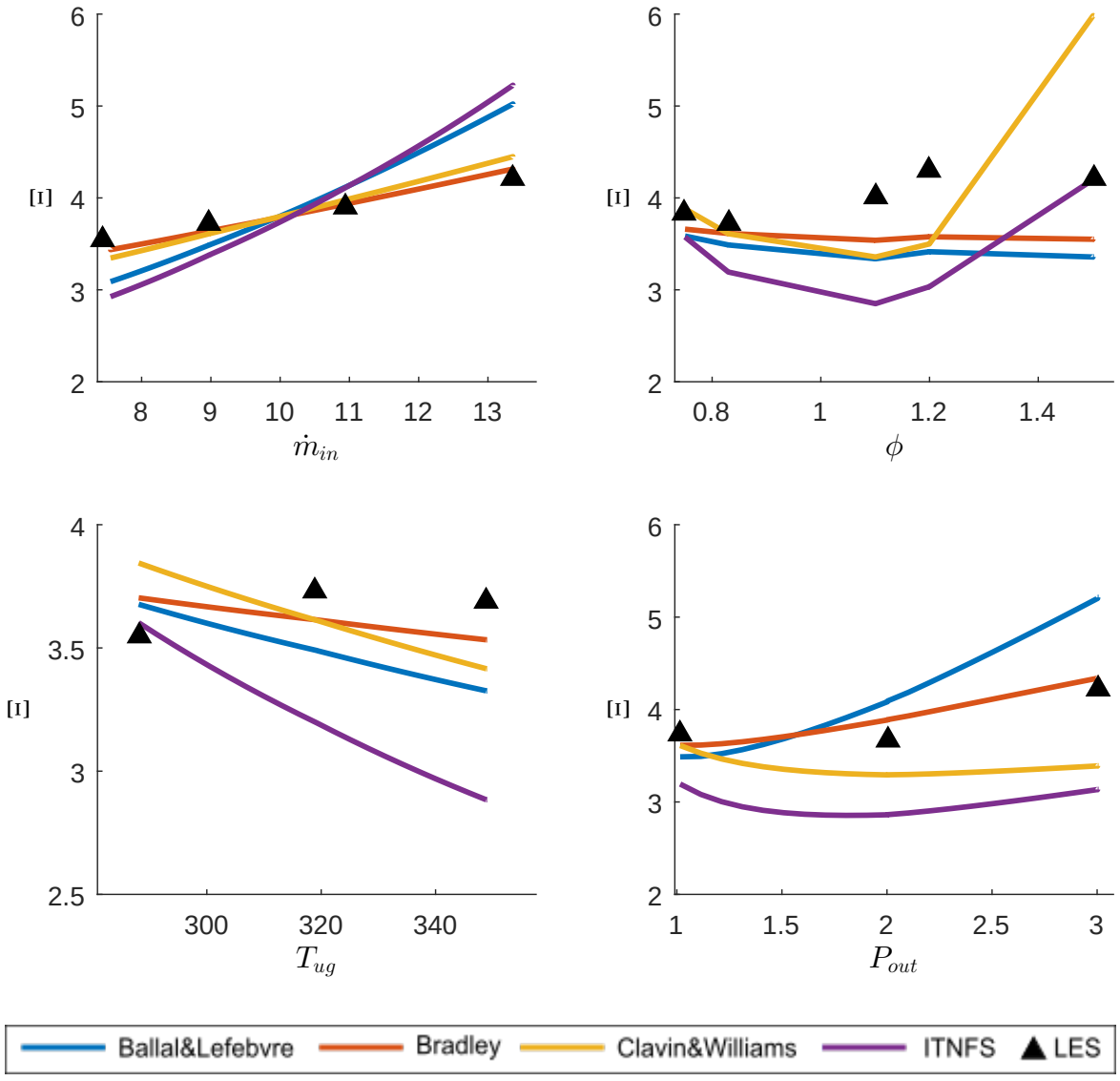

Figure 6.9 – Evolution of the wrinkling through the parametric variations; LES results compared to models by Ballal&Lefebvre [68], Bradley [17], Clavin&Williams [32] and ITNFS [28, 29]. The adjustment coefficients κ_i were optimized to fit at best the LES results.

6.4 Burned Gas Characterisation

6.4.1 Mass Balance, Density, Composition and Volume

The BG volume, V_{bg}, is calculated by simply removing the unburned volume of the combustion chamber from the total volume, and the BG mass is deduced from the total mass and the UG mass as it follows:

$$V_{bg} = V - V_{ug} \tag{6.81}$$

$$m_{bg,i} = m_i - m_{ug,i} \tag{6.82}$$

$$m_{bg} = \sum m_{bg,i} \tag{6.83}$$

Consequently, the BG density and composition calculation becomes straightforward.

$$\rho_{bg,i} = \frac{m_{bg,i}}{V_{bg}} \tag{6.84}$$

$$\rho_{bg} = \sum \rho_{bg,i} \tag{6.85}$$

$$Y_{bg,i} = \frac{m_{bg,i}}{m_{bg}} \tag{6.86}$$

6.4.2 Energy Balance, Temperature and Pressure

The specific BG enthalpy is first calculated from the total and UG enthalpies:

$$h_{bg} = \frac{(H - H_{ug})}{m_{bg}} \tag{6.87}$$

The iterative Newton-Raphson procedure is once again called for the calculation of T_{bg}:

$$T_{bg} = f^{-1}(h_{bg}) \tag{6.88}$$

Pressure is assumed to be the same in each of the UG and BG zones according to the CFM formalism.

6.5 Validation of the Flame Tube Model

The 0D flame tube model was validated against the LES results in system simulations representing the PRECCINSTA burner, using the software AMESim, featuring a variable time step solver. The flame tube component was connected to a source injecting air and a gaseous fuel, with a mass flow rate, temperature and FAeR control system. The outlet of the flame tube ends into a convergent exhaust duct with a 6:1 ratio and onto which an outlet pressure was imposed. No heat exchange was activated through the flame tube walls. Seven species were used, being the CH_4, O_2, N_2, CO, CO_2, H_2 and H_2O. Four simulations were performed. Each of these simulations was a transient in which one operating parameter was varied. The operating parameters were the inlet mass flow rate $\dot{m}_{in}$, the FAeR ϕ, the fresh gases temperature T_{ug} and outlet pressure P_{out}. The Bradley flame surface wrinkling correlation [17] was used throughout the validation.

6.5.1 Variation of Inlet Mass Flow Rate

The inlet mass flow rate starts at 7.4g/s and increases in three steps to reach 13.4g/s in a total simulation time of seven seconds, Figure 6.10. Passing from to the following mass flow rate, the flame tube component is subjected to transient operating conditions which translate into an unsteady combustion process computed by the 0D CFM combustion model approach. Below, in a first time, the steady state response of the 0D CFM flame to the change of operating conditions will be detailed. Then features describing the unsteady response of the flame to transient operating conditions will be approached and analysed. The flame tube is fed by a gaseous mixture characterised by a FAeR of 0.83, $T_{ug} = 320K$, and the outlet pressure is imposed at 1 atm.

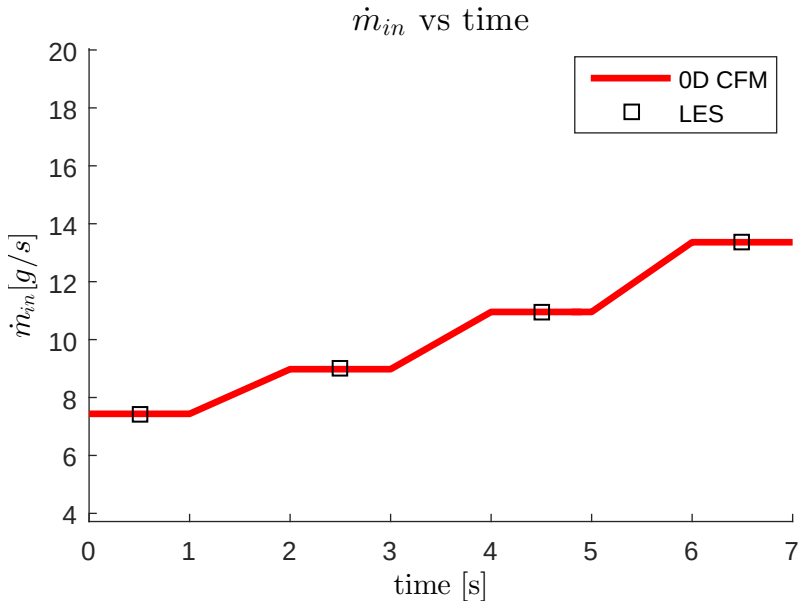

Figure 6.10 – Time variation of the inlet mass flow rate $\dot{m}_{in}$.

Comparison of the 0D Steady State Results to LES Results

The fresh gases volume predicted by the system simulation fairly agrees with the LES points, Figure 6.11, left sub-figure. Assuming the LES results as reference values, the right sub-figure of Figure 6.11 shows the percent error given by:

$$\epsilon = \frac{|\xi_n^{LES} - \xi_n^{0D}|}{\xi_n^{LES}} \times 100 \tag{6.89}$$

where ξ_n is the value of physical variable of interest at the operating point n, and the superscripts LES and $0D$ stand for the respective LES and 0D results.
The 0D UG density closely matches the LES UG density, Figure 6.12.

The turbulent velocity fluctuations differ from the LES reference at low mass flow rates, but converge towards a nearly perfect match at higher mass flow rates, Figure 6.13. Regarding the laminar flame speed, the 0D model renders an almost horizontal line while the LES reveals perturbations that grow with the increase of $\dot{m}_{in}$, Figure 6.14.

The flame thickness predicted by the system simulation is compared to the flame thickness post-processed from the LES results, Figure 6.15. Even though the numerical values are close, the trend of the flame thickness given by the 0D model is not quite the same as the decreasing slope shaped by the LES points. However, increasing the mass flow rate should not change the laminar flame thickness. The reason δ_L changes in the LES is probably the

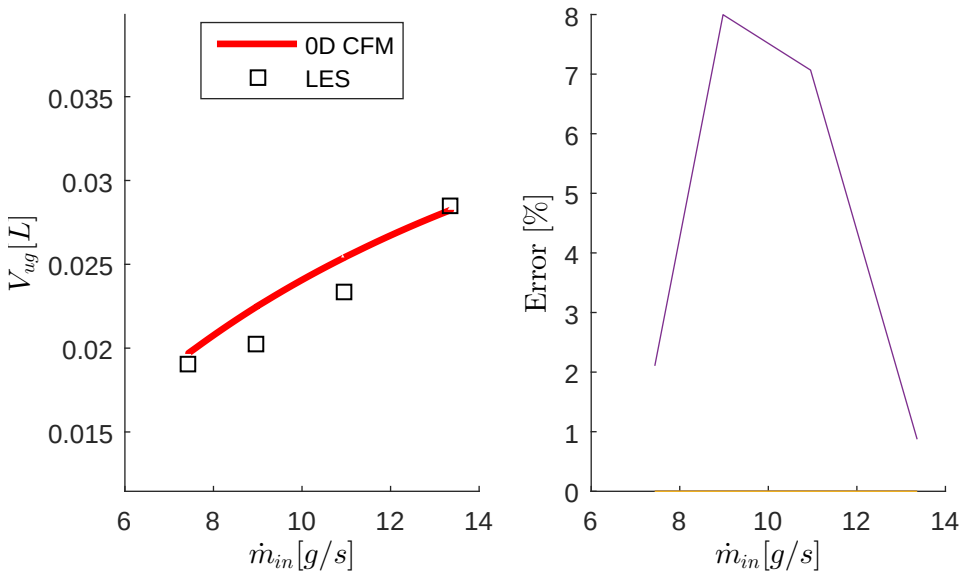

Figure 6.11 – Variation of the UG volume V_{ug} with the inlet mass flow rate $\dot{m}_{in}$.

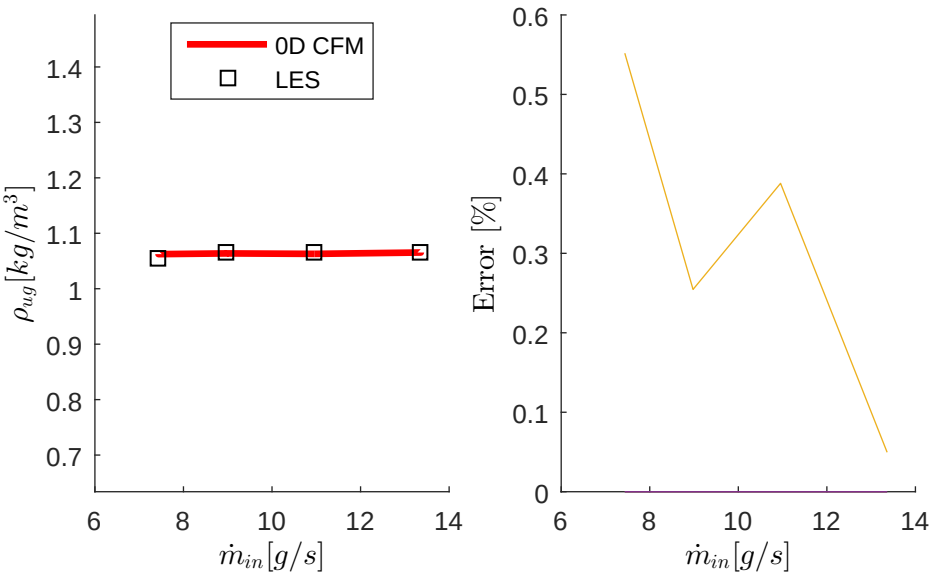

Figure 6.12 – Variation of the UG density ρ_{ug} with the inlet mass flow rate $\dot{m}_{in}$.

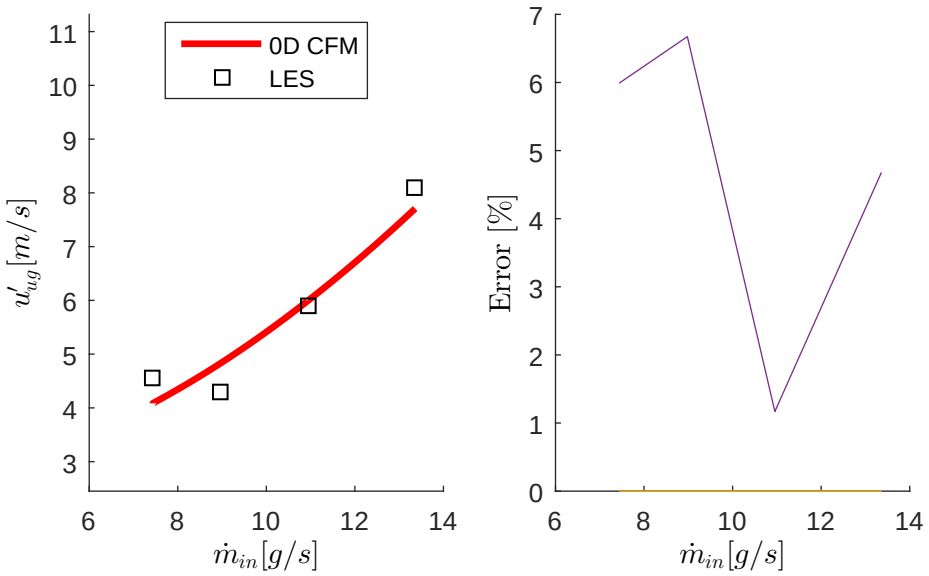

Figure 6.13 – Variation of the UG turbulent intensity u'_{ug} with the inlet mass flow rate $\dot{m}_{in}$.

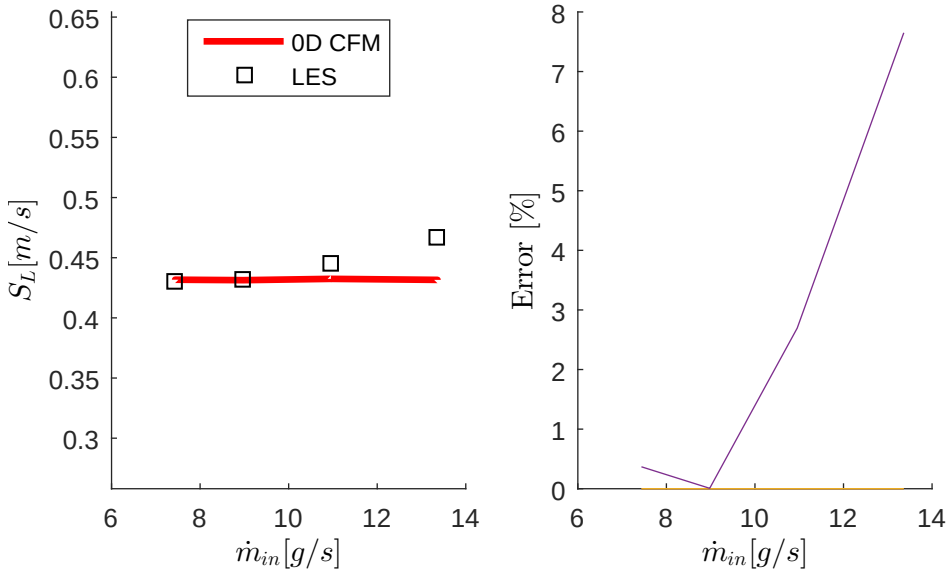

Figure 6.14 – Variation of the global laminar flame speed S_L with the inlet mass flow rate $\dot{m}_{in}$.

increase of the laminar flame speed, which is part of the denominator in the flame thickness correlation. The mean flame area pattern comparison, Figure 6.16, is quite satisfactory, but

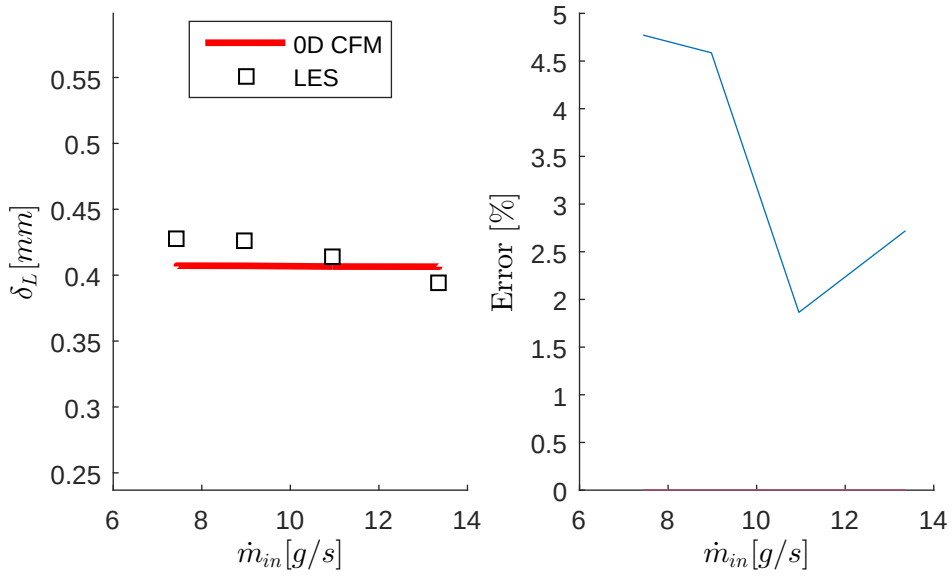

Figure 6.15 – Variation of the global laminar flame thickness δ_L with the inlet mass flow rate $\dot{m}_{in}$.

the wrinkling, Figure 6.17, in the flame tube model, has a slightly steeper slope than the LES points. The BG volume, Figure 6.18, and the pressure, Figure 6.20, are obviously the same in the system simulation and the CFD for the tested conditions.

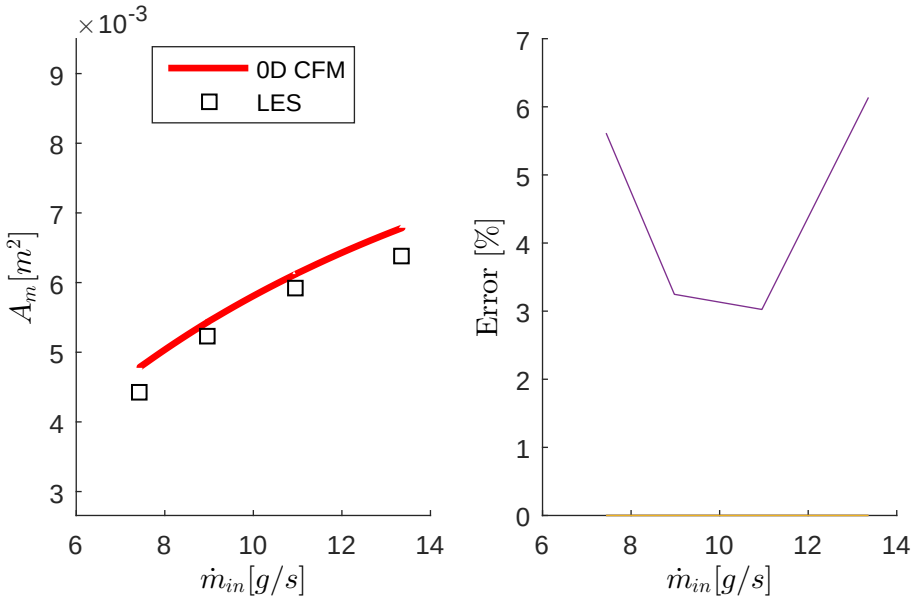

Figure 6.16 – Variation of the mean flame area A_m with the inlet mass flow rate $\dot{m}_{in}$.

As a consequence of the 0D CFM flame tube modelling approach, no CO was produced in that fuel lean simulation, while small quantities of CO were observed in LES results, Figure 6.22. Furthermore, CO_2 production was slightly overestimated by system simulation in comparison with LES results, Figure 6.23.

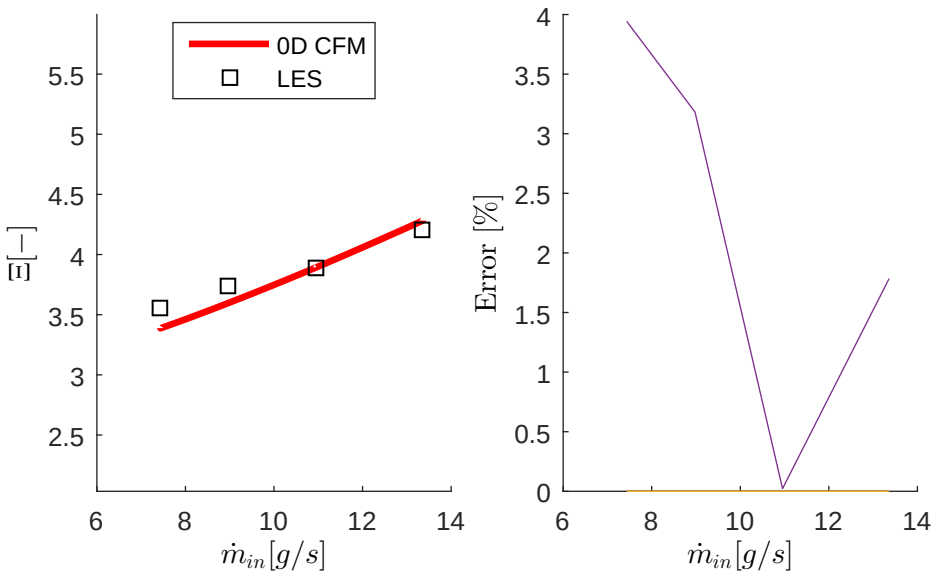

Figure 6.17 – Variation of the flame wrinkling Ξ with the inlet mass flow rate $\dot{m}_{in}$.

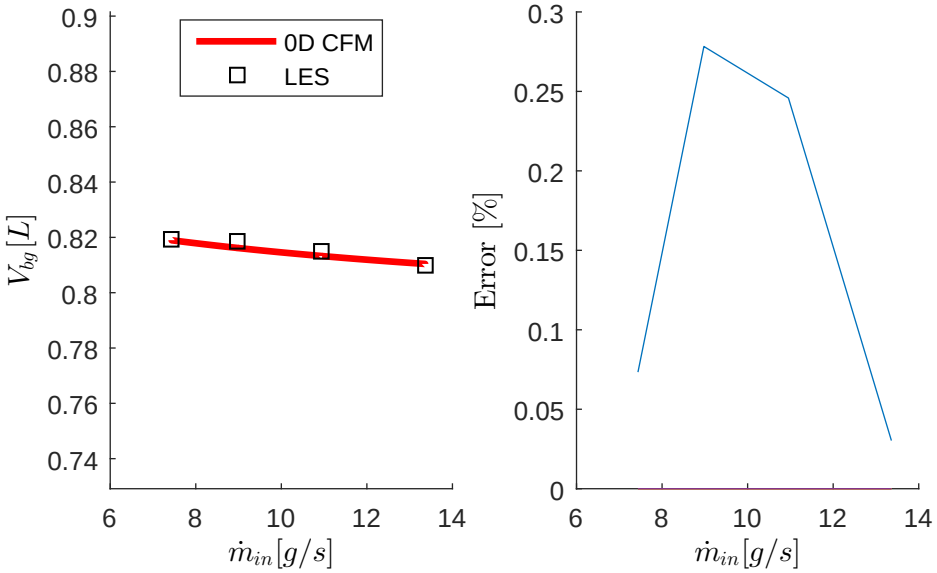

Figure 6.18 – Variation of the BG zone volume V_{bg} with the inlet mass flow rate $\dot{m}_{in}$.

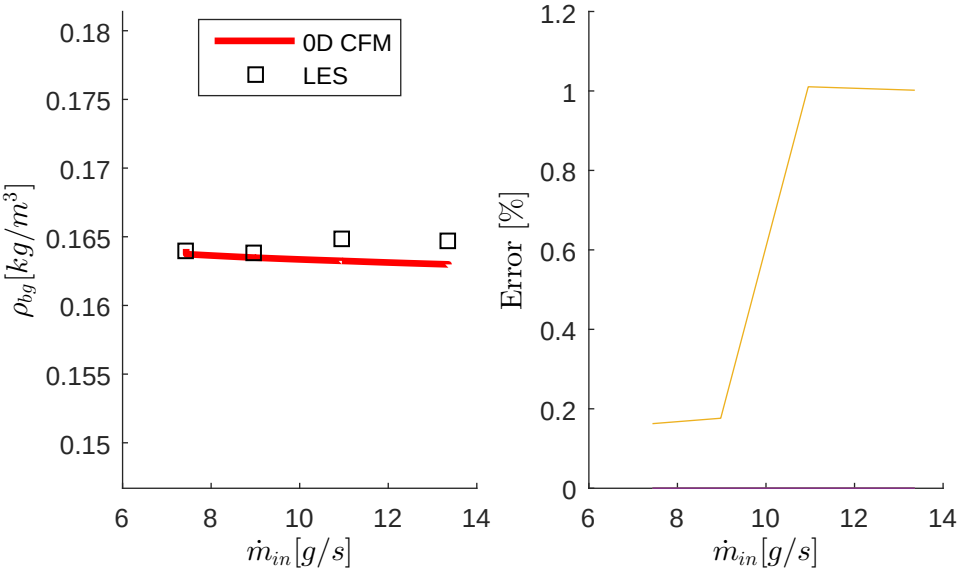

Figure 6.19 – Variation of the BG zone density ρ_{bg} with the inlet mass flow rate $\dot{m}_{in}$.

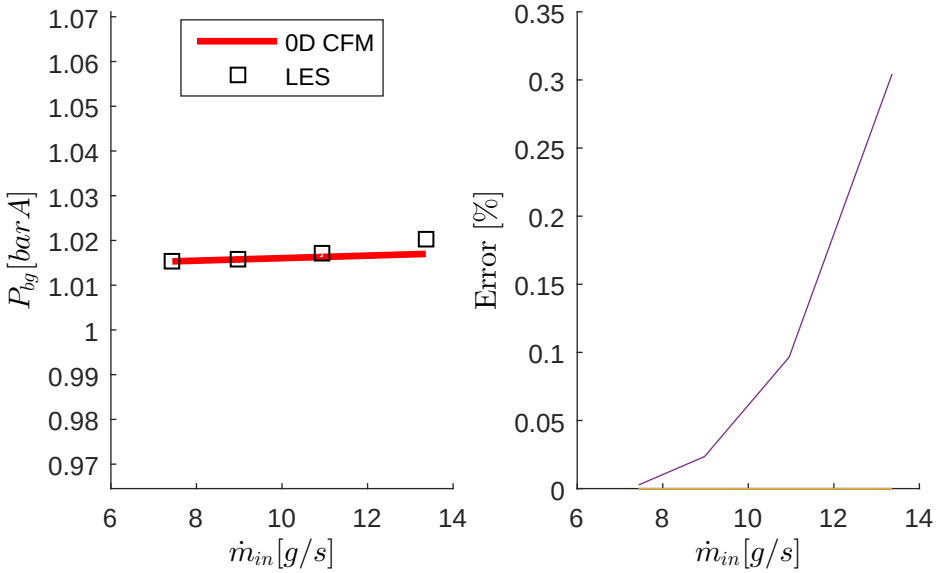

Figure 6.20 – Variation of the static pressure in the combustion chamber P_{bg} with the inlet mass flow rate $\dot{m}_{in}$.

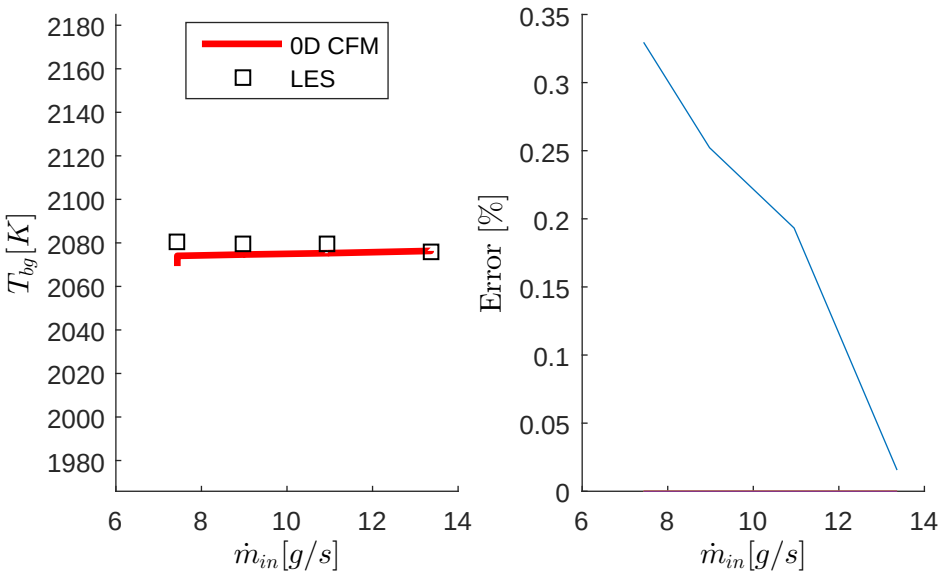

Figure 6.21 – Variation of the BG zone temperature T_{bg} with the inlet mass flow rate $\dot{m}_{in}$.

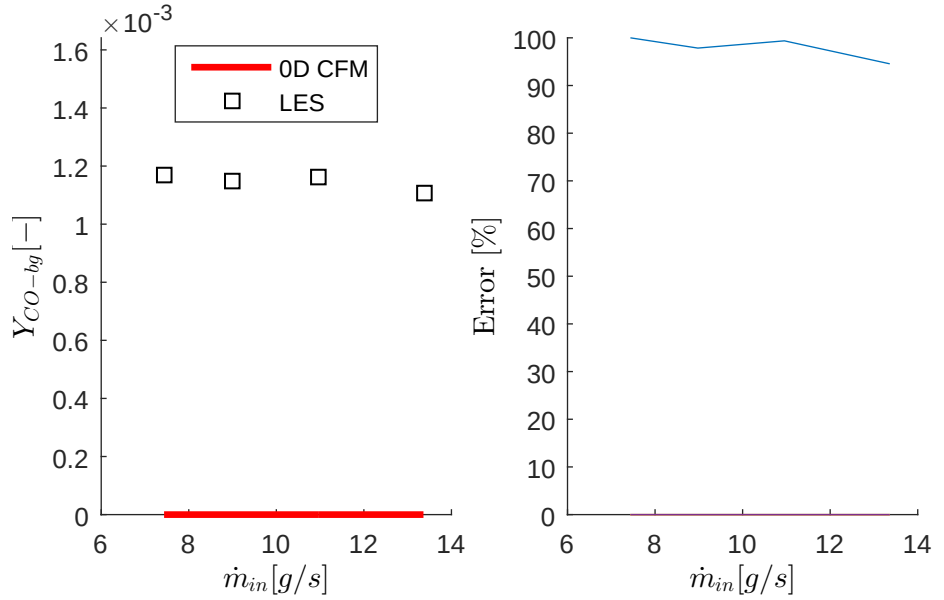

Figure 6.22 – Variation of the CO mass fraction in the BG zone with the inlet mass flow rate $\dot{m}_{in}$.

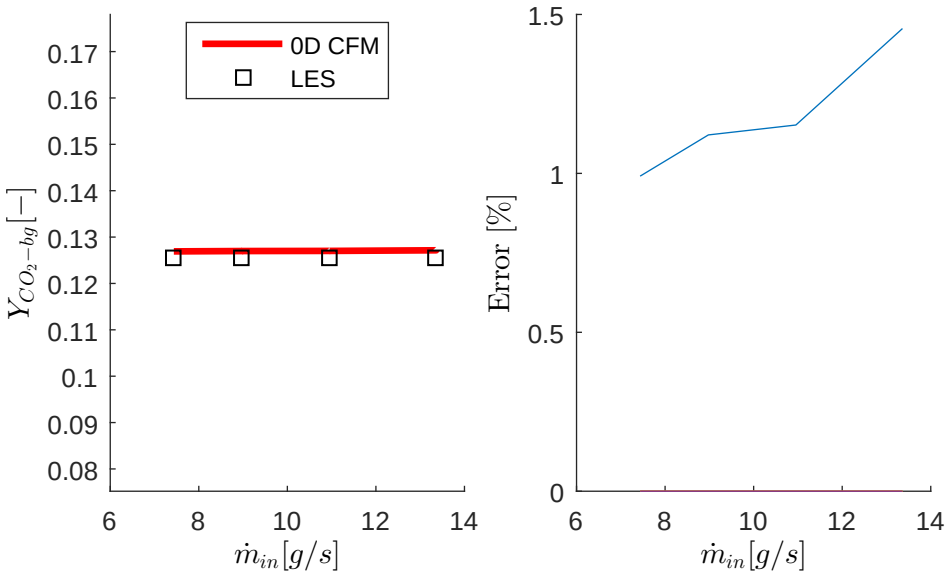

Figure 6.23 – Variation of the CO_2 mass fraction in the BG zone with the inlet mass flow rate $\dot{m}_{in}$.

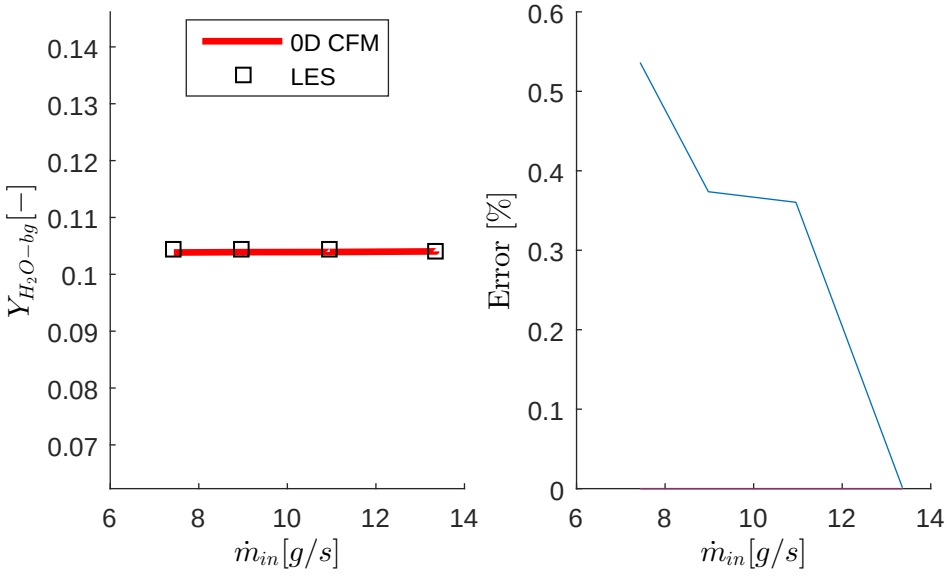

Figure 6.24 – Variation of the H_2O mass fraction in the BG zone with the inlet mass flow rate $\dot{m}_{in}$.

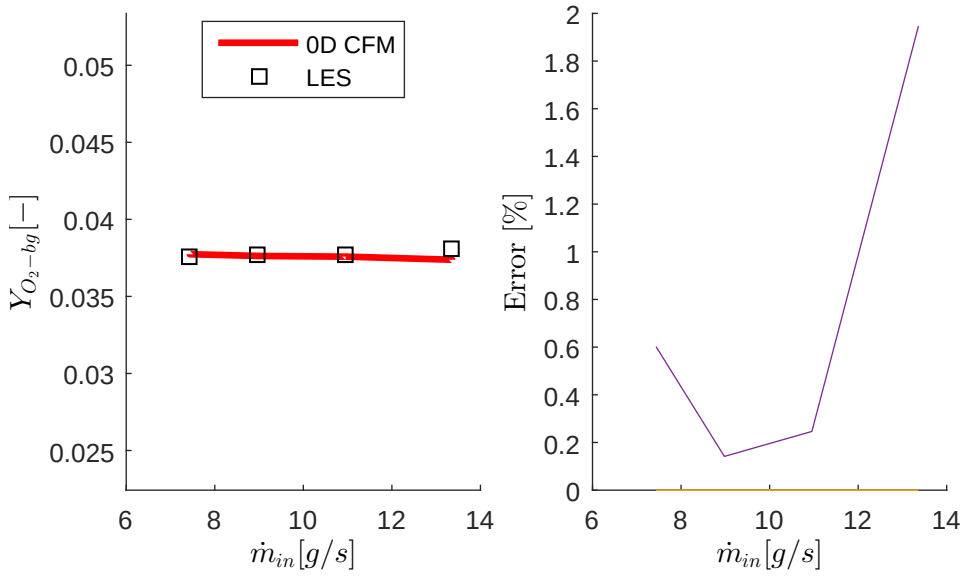

Figure 6.25 – Variation of the $O2$ mass fraction in the BG zone with the inlet mass flow rate $\dot{m}_{in}$.

Analysis of the 0D CFM Flame Tube Response to Transient Operating Conditions

Raising $\dot{m}_{in}$ by 81% increases the the UG zone turbulent velocity, u'_{ug}, Table 6.3a. As shown in Table 6.3b, as expected, neither laminar flame speed nor laminar flame thickness varied since ϕ remained constant during that transient simulation, and P_{ug} and T_{ug} were not affected by the increase of inlet mass flow rate. Conversely, an increase of mean flame surface and surface wrinkling was observed. The increase of A_m is coherent with the increase of fresh gas volume, Figure 6.11, and also consistent with the fact that S_L did not vary. The increase of Ξ is in agreement with the amplification of turbulent velocity fluctuations and the steadiness of S_L and δ_L, as well as the fact that l_T was assumed as being invariant throughout all this study. The fuel burning rate inside the 0D flame tube by the same percentage as $\dot{m}_{in}$.

Table 6.3 – Dynamic response of the UG zone and the flame to transients of inlet mass flow rate. Symbols: =: constant; ≃: negligible fluctuations; ↑: increase; ↓: decrease.

ρ_{ug}	$Y_{ug,F}$	T_{ug}	P_{ug}	u'_{ug}
=	=	=	≃	↑ 89%

(a) UG zone variables.

S_L	δ_L	A_m	Ξ	$\dot{\Omega}_F$
≃	≃	↑ 41.8%	↑ 27.5%	↑ 81%

(b) Flame variables.

In the BG zone the increase of V_{ug} caused a decrease of the BG volume, Figure 6.18. In addition, a slight increase of pressure was observed, Figure 6.20, and that is due to the overall mass increase in the flame tube.

In conclusion, the transient behaviour of the 0D CFM flame tube model is deemed consistent with the principles of aerothermochemistry of premixed turbulent combustion in an open volume.

6.5.2 Variation of Inlet Fuel to Air Ratio

In order to validate the impact of ϕ on combustion, the inlet mixture is enriched from an FAeR of 0.75 to 1.5 in 5 seconds, Figure 6.26. That choice allows to study the behaviour of the 0D model under lean, stoichiometric and rich fresh gas mixture conditions. In that simulation, subjecting the flame tube component to an increase of FAeR translates into an unsteady combustion process computed by the 0D CFM combustion model approach. Below, in a first time, the steady state response of the 0D CFM flame to the change of operating conditions will be detailed. Then features describing the unsteady response of the flame to transient operating conditions will be considered and analysed. The flame tube is fed by a gaseous mixture characterised by $\dot{m}_{in} = 8.98g/s$, $T_{ug} = 320K$, and the outlet pressure is imposed at 1 atm.

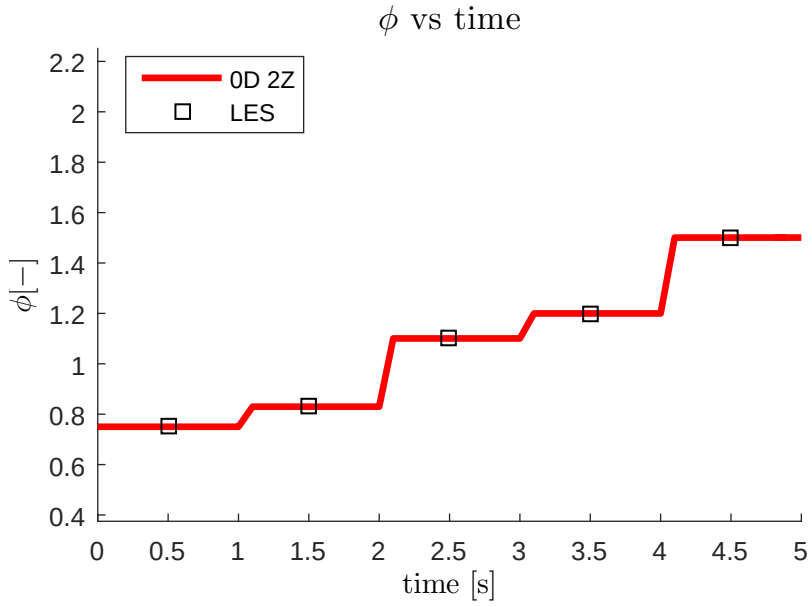

Figure 6.26 – Time variation of the inlet fuel to air equivalent ratio ϕ.

Comparison of the 0D Steady State Results to LES Results

In the UG zone, the fresh gas volume complies with the LES values until a FAeR of 1.2 and then diverges, Figure 6.27. The divergence of V_{ug} would be due to a divergence of S_L with respect to LES results discussed below. Fresh gas density results matches with the CFD results, Figure 6.28. However, the turbulent velocity fluctuations do not reproduce the pattern observed in the LES computations, Figure 6.29, but a good match is observed for three operating points being $\phi = 0.75$, $\phi = 1.1$ and $\phi = 1.5$. As a matter of fact, the LES pattern of u', oscillating with the increase of ϕ, does not seem to follow a regular trend. This makes difficult the interpretation and the validation of these results.

The laminar flame speed, Figure 6.30, is correctly predicted with respect to the LES results except for $\phi = 1.5$. The correlation used for S_L was not backed by experimental measurements with $\phi > 1.2$. Therefore, the discrepancies of S_L for $\phi > 1.2$ is due to a bad extrapolation. That was predictable according to Figure 5.21. Other correlations should be considered for rich mixtures. The flame thickness matches with the reference until $\phi = 1.2$, Figure 6.31, and the observed errors at $\phi = 1.5$ are related to errors in the estimation of S_L. System simulation results of mean flame surface show a fairly good match with the CFD results also until $\phi = 1.2$, Figure 6.32. Between $\phi = 1.2$ and $\phi = 1.5$, A_m is overestimated as a consequence of the underestimation of S_L, as observed in Figure 6.30. Nevertheless the

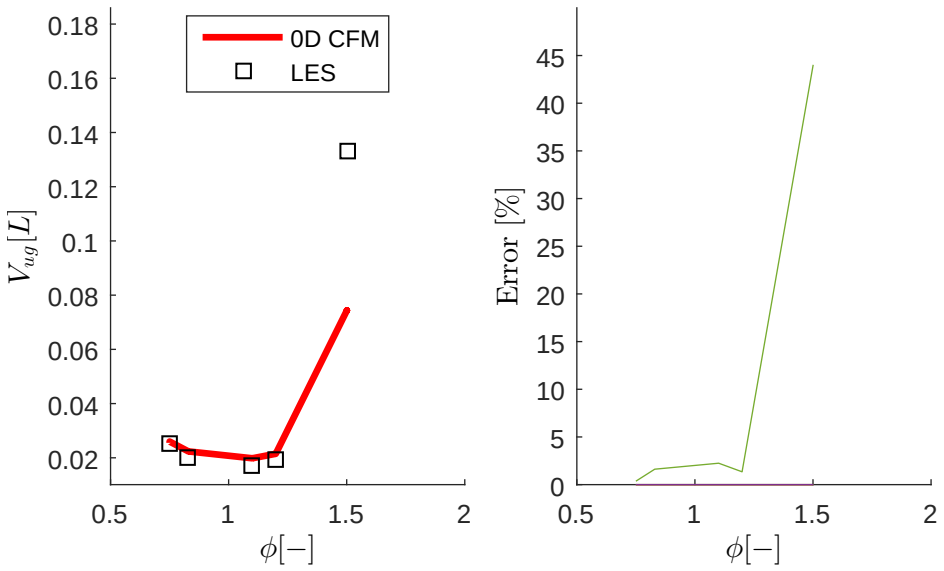

Figure 6.27 – Variation of the UG volume V_{ug} with the inlet fuel to air equivalent ratio ϕ.

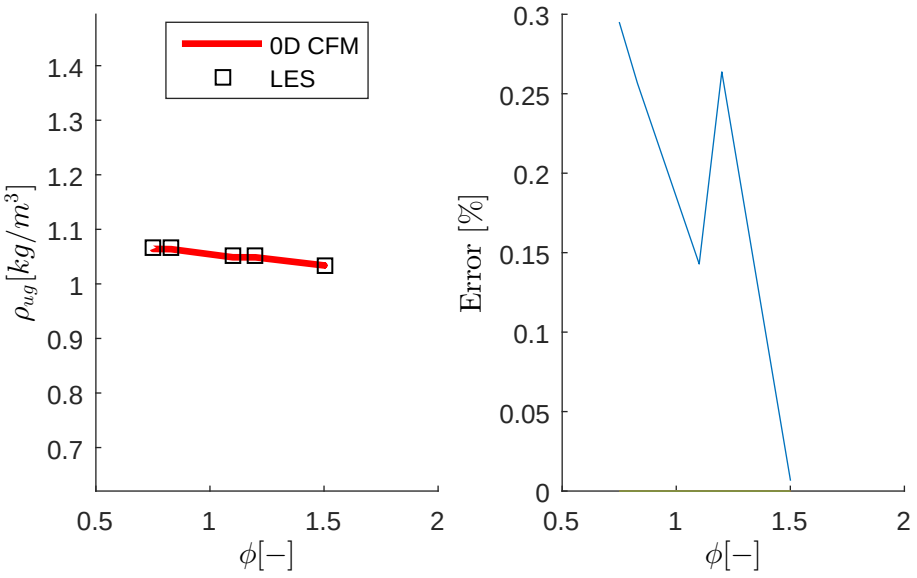

Figure 6.28 – Variation of the UG density ρ_{ug} with the inlet fuel to air equivalent ratio ϕ.

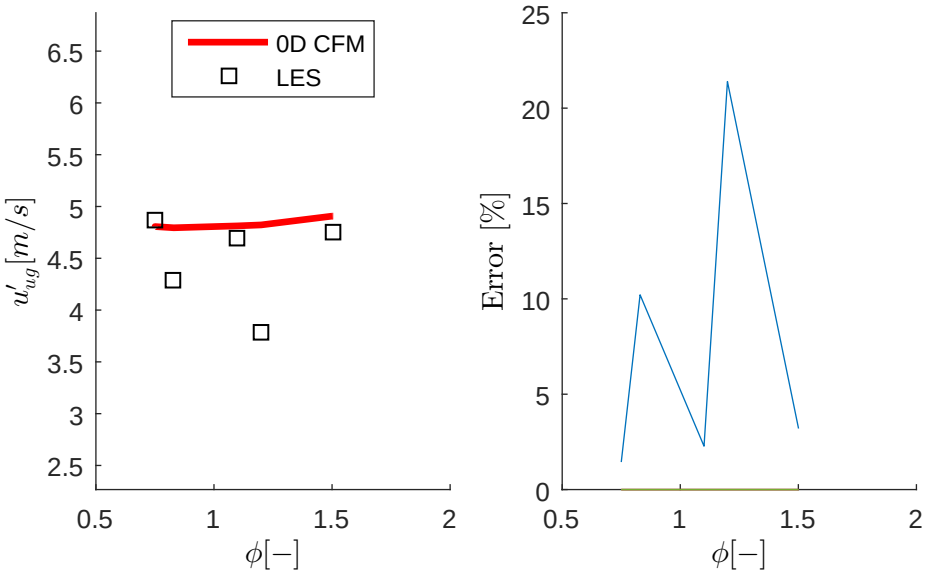

Figure 6.29 – Variation of the UG turbulent intensity u'_{ug} with the inlet fuel to air equivalent ratio ϕ.

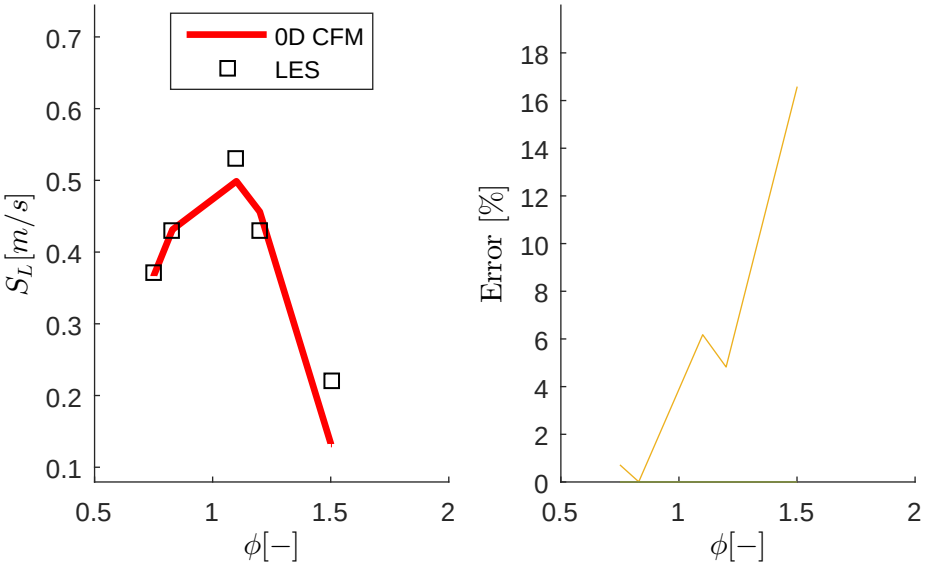

Figure 6.30 – Variation of the global laminar flame speed S_L with the inlet fuel to air equivalent ratio ϕ.

0D CFM approach remains coherent and to an increase of the mean surface corresponds an increase of the UG volume. The values of flame wrinkling given by system simulation and LES do not match, Figure 6.33. That was an expectable outcome since 0D and LES flame wrinkling predictions did not seem to match. However, the global error rate could be deemed as roughly acceptable.

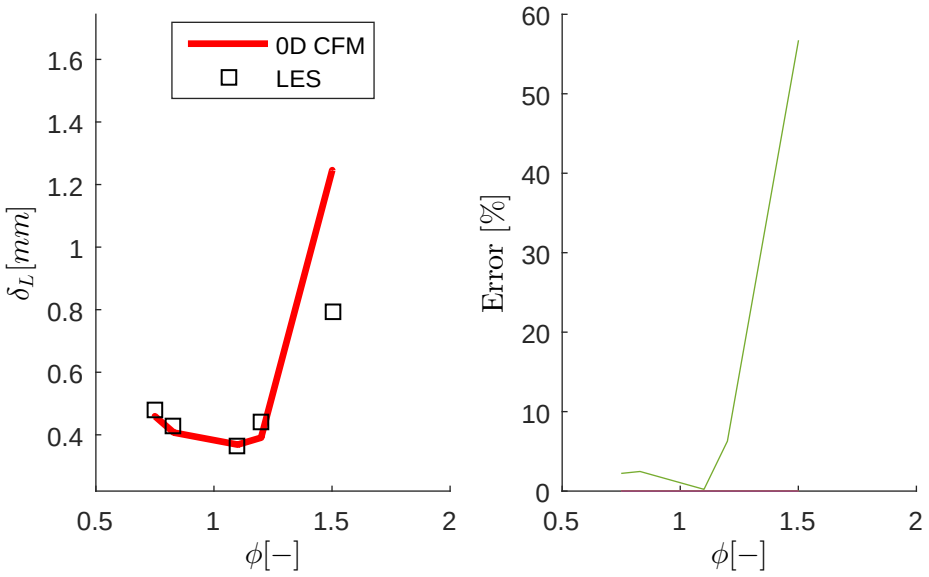

Figure 6.31 – Variation of the global laminar flame thickness δ_L with the inlet fuel to air equivalent ratio ϕ.

In the BG zone, the volume, Figure 6.34, and density, Figure 6.35, are in good agreement with the LES results until $\phi = 1.2$. Pressure results of the system simulation fit well with the all the LES points, Figure 6.36. BG temperature shows a good match as well with a maximal error of 1.4%, Figure 6.37.

It is worth to add a few comments about BG temperature. In fact, even though T_{bg} matches very well with the CFD reference, Figure 6.21, system simulation and LES BG compositions are not exactly the same. Regarding the BG compositions, significant differences are observed between system simulation results and LES results. Due to the fact that in the LES, no H_2 is included and two steps chemistry activated in the LES, equation 5.21 and equation 5.22, differs from the lumped reaction incorporated in the 0D flame tube model, high discrepancies were expected. For instance, in the BG zone and for $\phi > 0.83$, the 0D CFM model underestimated Y_{CO}, Figure 6.38, and overestimated Y_{CO_2}, Figure 6.38, with respect to CFD. Y_{H_2O} was underestimated in the BG zone, Figure 6.40, which is linked to the presence of hydrogen, Figure 6.42.

Analysis of the 0D CFM Flame Tube Response to Transient Operating Conditions

Passing from a lean to stoichiometric UG mixture without changing its thermodynamic state, Table 6.4a, caused S_L to increase and δ_L to decrease, Table 6.4b. Also as summarized in Table 6.4b for a raise of ϕ from 0.75 to 1.1, while reducing the mean flame surface and flame wrinkling, the fuel burning rate was increased. An increase of S_L was matched by a decrease of V_{ug} for $\phi < 1.1$, Figure 6.27, which matches with the decrease of A_m. In addition, to an increase of the laminar flame speed corresponds a decrease of the laminar flame thickness. Conversely, passing from $\phi = 1.1$ to $\phi = 1.5$ decreased the laminar flame speed and increased A_m, δ_L and Ξ. These changes led globally to an increase of the fuel burning rate. The

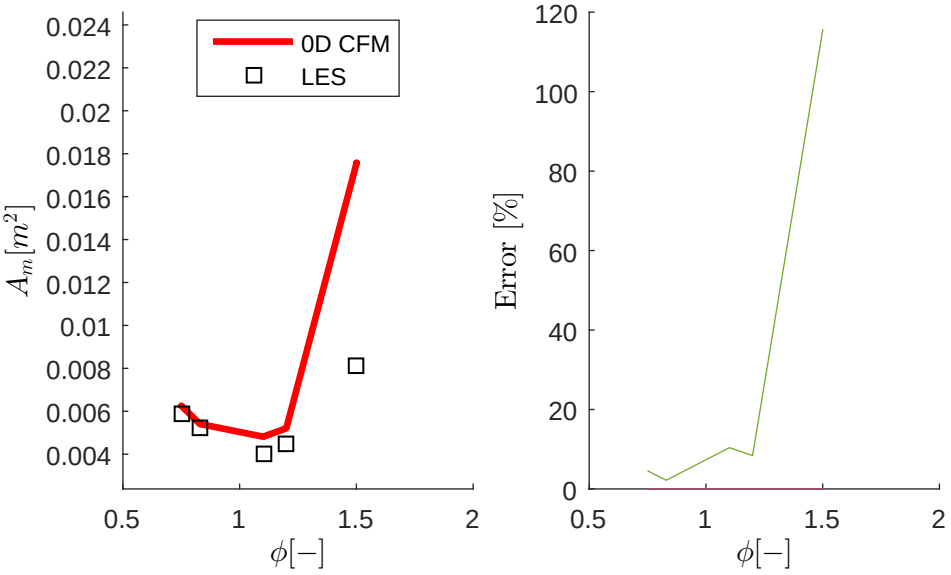

Figure 6.32 – Variation of the mean flame area A_m with the inlet fuel to air equivalent ratio ϕ.

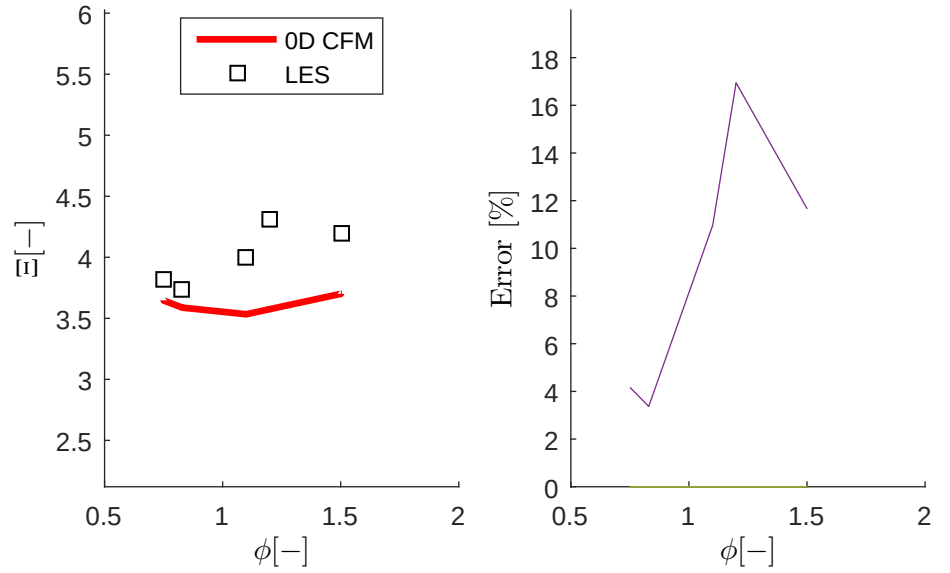

Figure 6.33 – Variation of the flame wrinkling Ξ with the inlet fuel to air equivalent ratio ϕ.

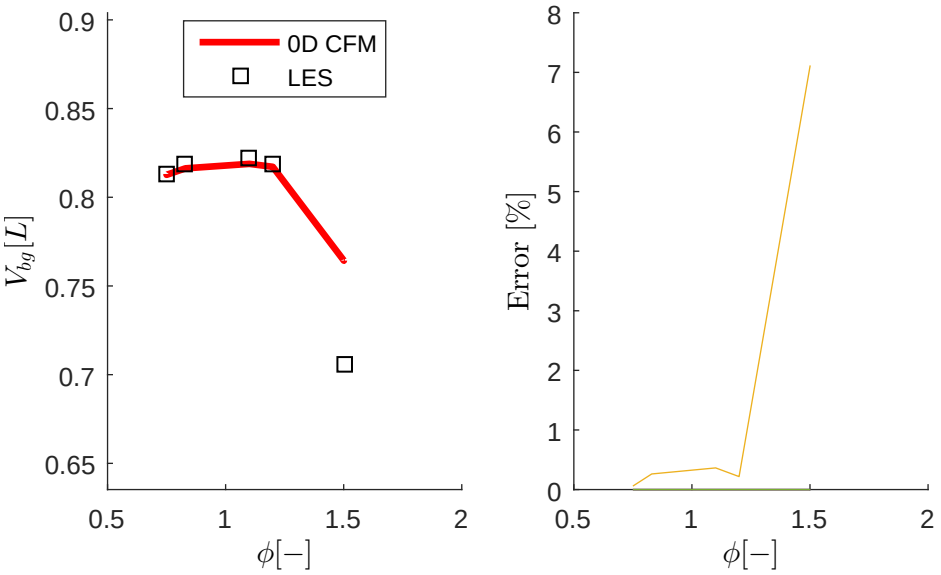

Figure 6.34 – Variation of the BG zone volume V_{bg} with the inlet fuel to air equivalent ratio ϕ.

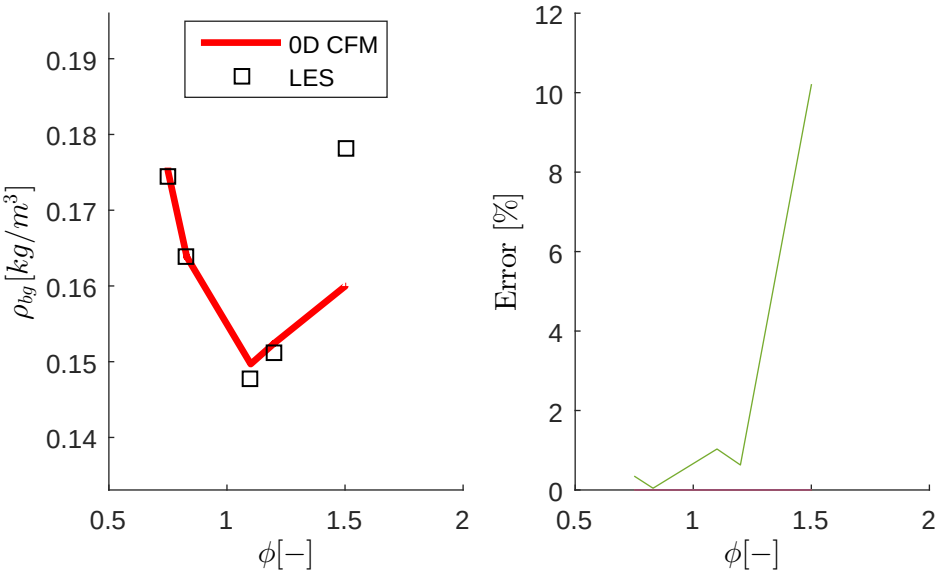

Figure 6.35 – Variation of the BG zone density ρ_{bg} with the inlet fuel to air equivalent ratio ϕ.

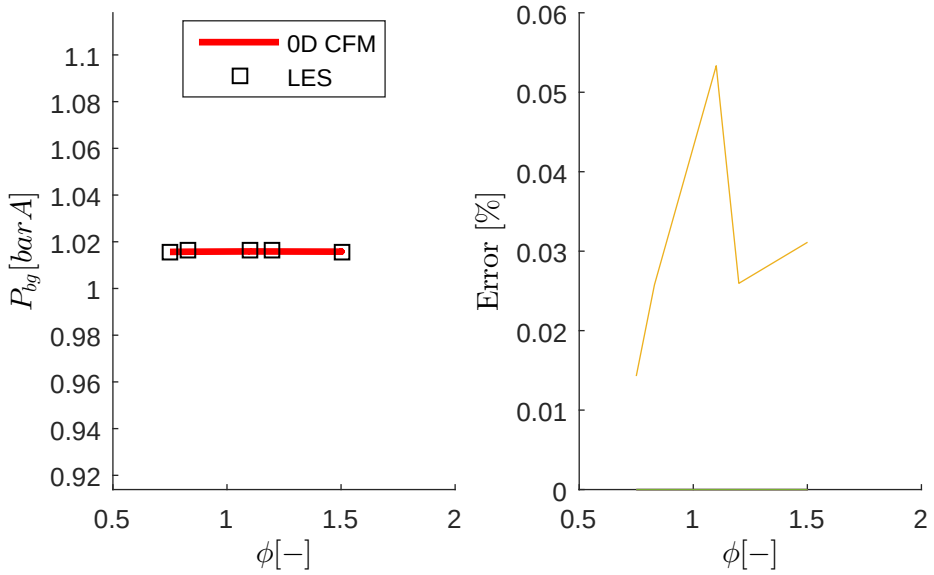

Figure 6.36 – Variation of the static pressure in the combustion chamber P_{bg} with the inlet fuel to air equivalent ratio ϕ.

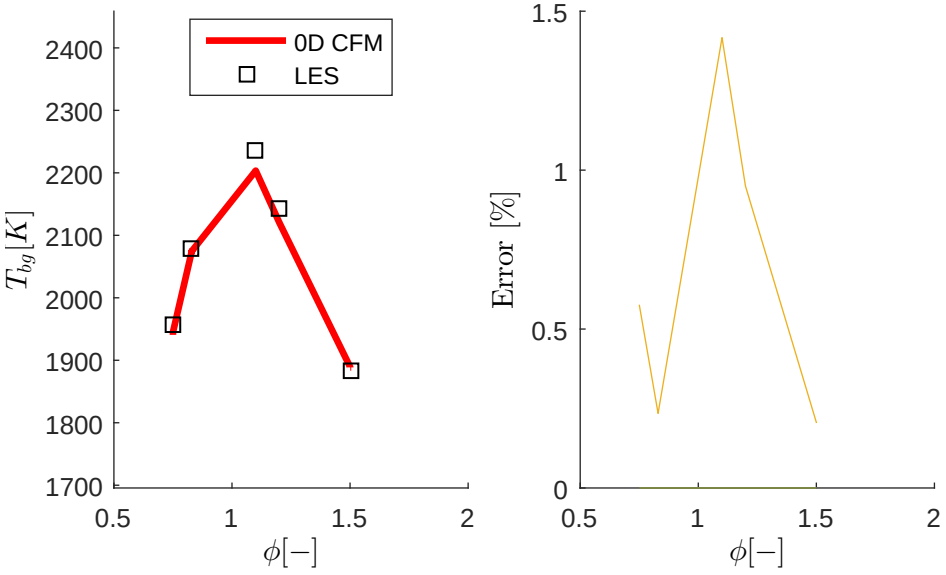

Figure 6.37 – Variation of the BG zone temperature T_{bg} with the inlet fuel to air equivalent ratio ϕ.

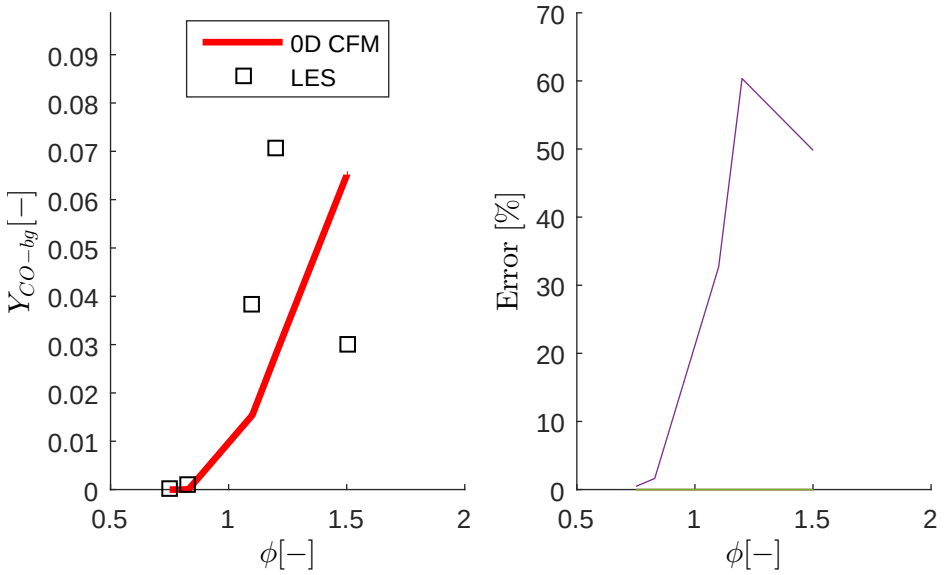

Figure 6.38 – Variation of the CO mass fraction in the BG zone with the inlet fuel to air equivalent ratio ϕ.

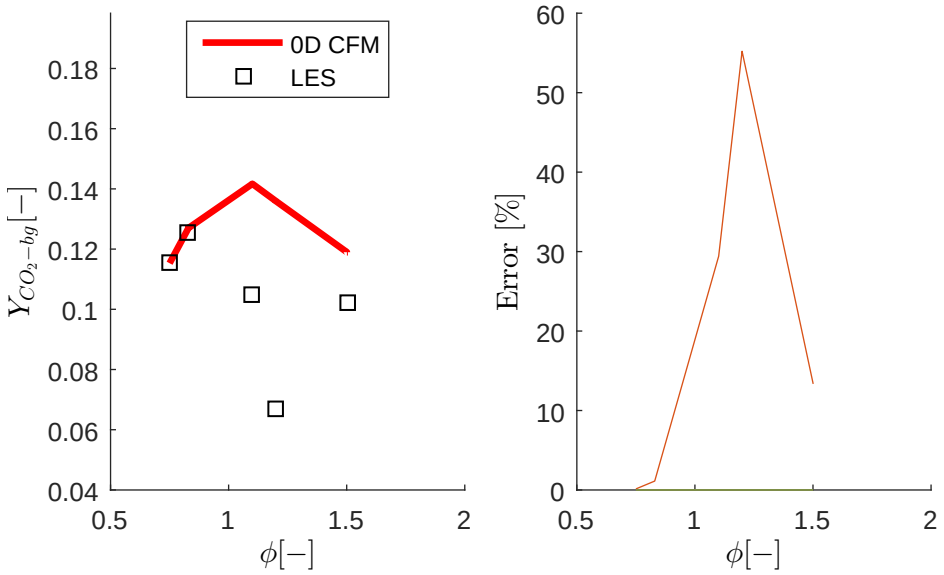

Figure 6.39 – Variation of the CO_2 mass fraction in the BG zone with the inlet fuel to air equivalent ratio ϕ.

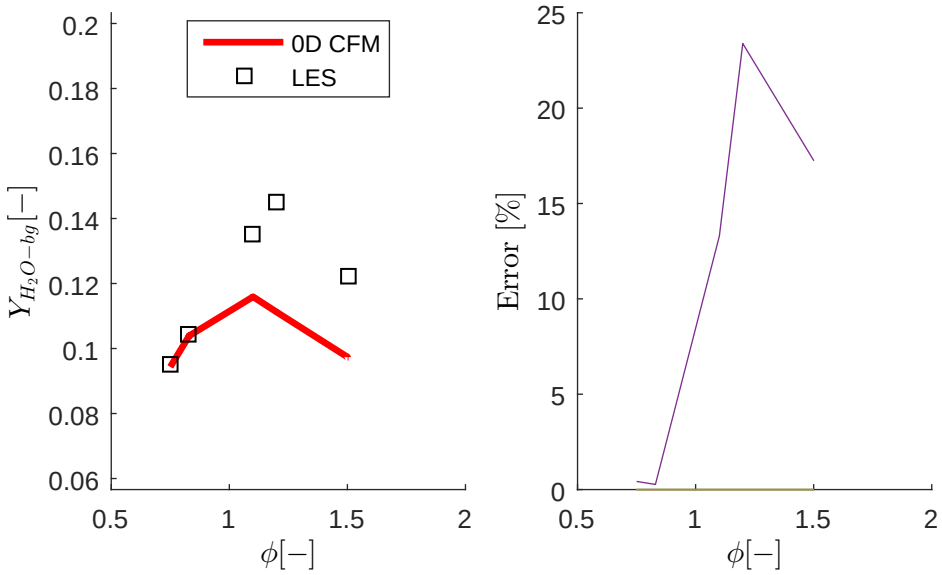

Figure 6.40 – Variation of the H_2O mass fraction in the BG zone with the inlet fuel to air equivalent ratio ϕ.

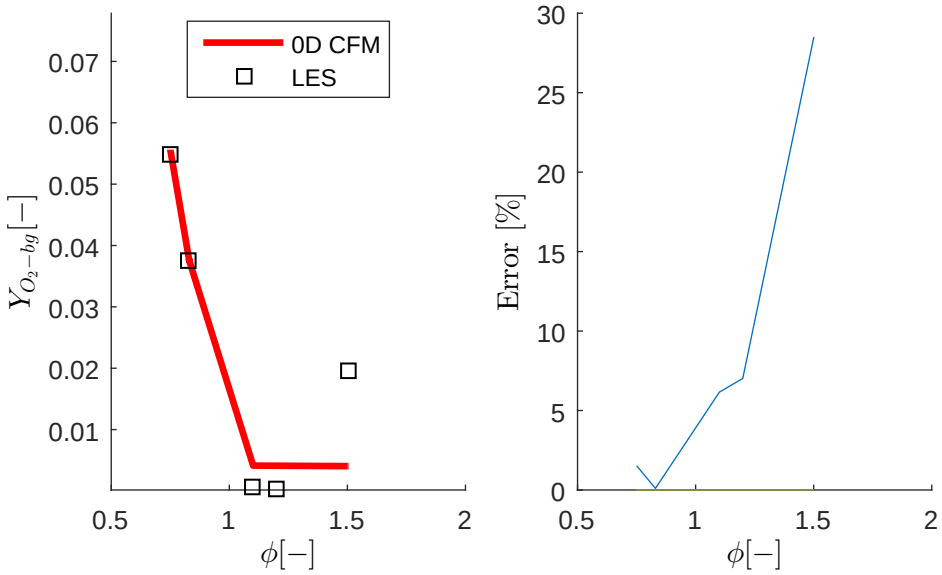

Figure 6.41 – Variation of the $O2$ mass fraction in the BG zone with the inlet fuel to air equivalent ratio ϕ.

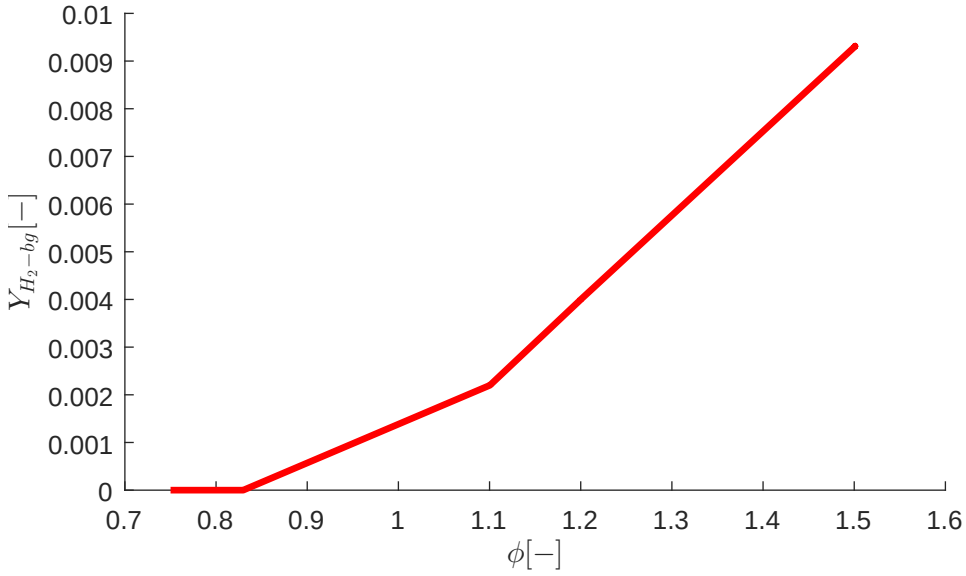

Figure 6.42 – Variation of the H_2 mass fraction in the BG zone with the inlet fuel to air equivalent ratio ϕ.

decrease of S_L is consistent with the increase of V_{ug} for $\phi > 1.1$, Figure 6.27, which is linked to the increase of A_m. It is worth to add that a decrease of ρ_{ug} was noticed, Figure 6.28, and that is due to the substitution of oxygen by methane which has a lower molecular weight.

Table 6.4 – Dynamic response of the UG zone and the flame to transients of ϕ.

ϕ	ρ_{ug}	$Y_{ug,F}$	T_{ug}	P_{ug}	u'_{ug}
0.75 to 1.1	$\downarrow$ 1.5%	$\uparrow$ 43%	$=$	$\simeq$	$\simeq$
1.1 to 1.5	$\downarrow$ 1.4%	$\uparrow$ 34%	$=$	$\simeq$	$\simeq$

(a) UG zone variables.

ϕ	S_L	δ_L	A_m	Ξ	$\dot{\Omega}_F$
0.75 to 1.1	$\uparrow$ 37%	$\downarrow$ 20%	$\downarrow$ 23%	$\downarrow$ 3%	$\uparrow$ 44%
1.1 to 1.5	$\downarrow$ 73%	$\uparrow$ 238%	$\uparrow$ 264%	$\uparrow$ 5%	$\uparrow$ 34%

(b) Flame variables.

Concerning the response of the 0D model in terms of turbulent velocity and wrinkling, the evolution of turbulent velocity, 6.4a, in conjunction with the evolutions laminar flame speed and thickness, 6.4b, may not seem sufficient for a conclusion.

However, the explanation for the response in terms of flame wrinkling seems straightforward when considering the increase of the ratio ${}^{u'}/_{S_L}$, Figure 6.43, along with the increase of ${}^{l_T}/_{\delta_L}$, Figure 6.44, as well as the product of those two terms, Figure 6.45. Indeed, the Bradley flame wrinkling model [17] used in this simulation, equation 6.76, clearly expresses Ξ as being proportional to $\sqrt{\frac{u'}{S_L}\frac{l_T}{\delta_L}}$. In spite of the uncertainties in the estimations of u', S_L, δ_L and the representation of l_T as being constant, the prediction of wrinkling surface can be considered as roughly acceptable.

Regarding the BG zone, the fluctuations of the BG volume, Figure 6.34, are coherent with those of V_{ug}, Figure 6.27, and the variations of ρ_{bg}, Figure 6.35, along with the changes of BG temperature, Figure 6.37, seem coherent. Indeed, as ϕ is increased, to 1.1, heat release

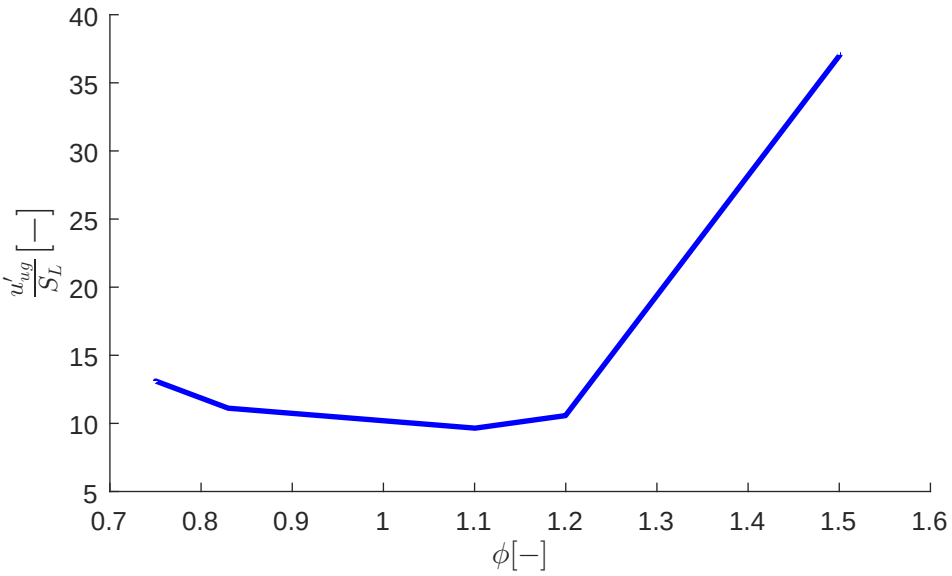

Figure 6.43 – Variation of ${}^{u'_{ug}}/_{S_L}$ with the inlet fuel to air equivalent ratio ϕ.

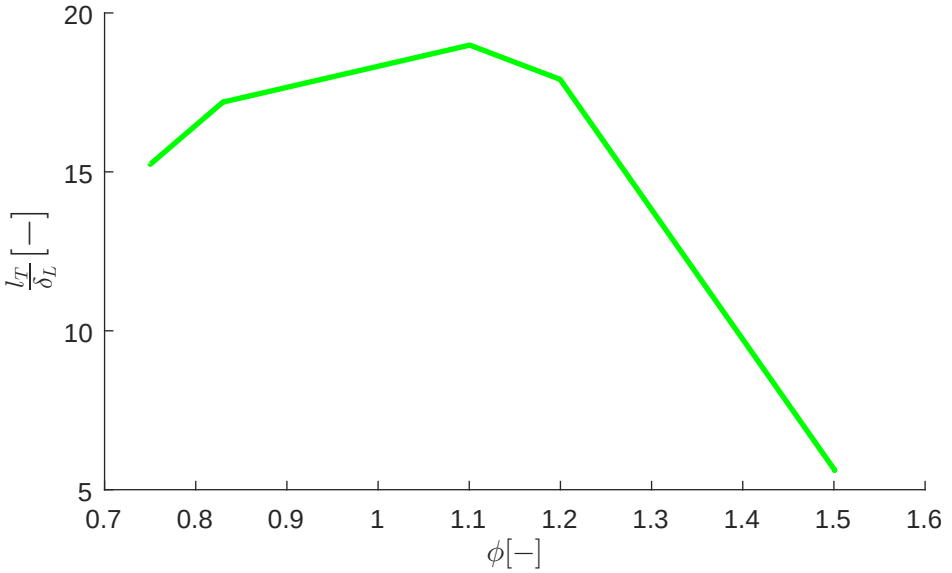

Figure 6.44 – Variation of ${}^{l_T}/_{\delta_L}$ with the inlet fuel to air equivalent ratio ϕ.

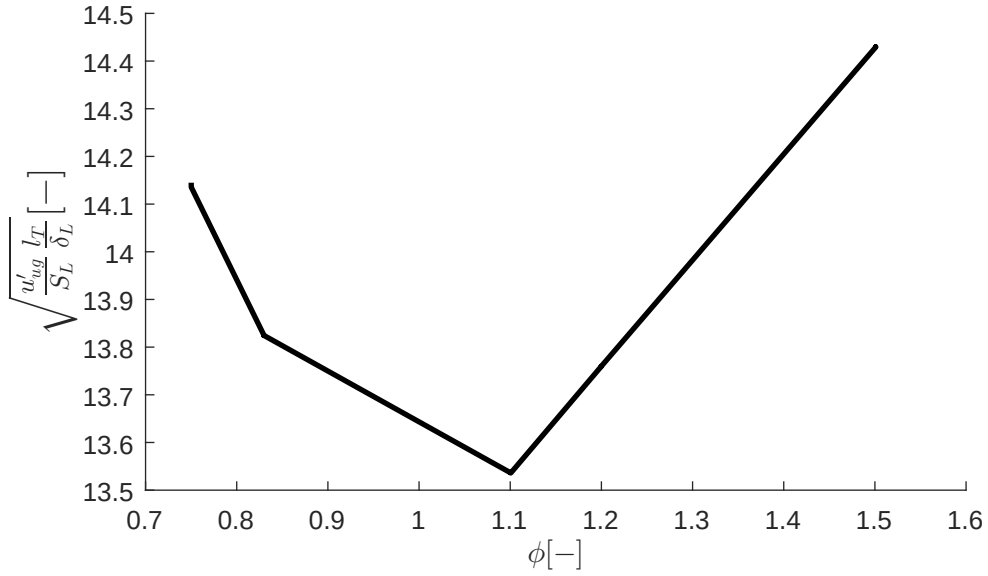

Figure 6.45 – Variation of $\sqrt{\frac{u'_{ug}}{S_L}\frac{l_T}{\delta_L}}$ with the inlet fuel to air equivalent ratio ϕ.

increases to reach its maximum value, which yields an increase of the BG temperature and a decrease of the BG density. Concerning the BG composition, the trends of fuel combustion products mass fractions, CO, CO_2, H_2O and H_2, were qualitatively captured, respectively Figure 6.38, Figure 6.39, Figure 6.40 and Figure 6.42. The evolution of the oxygen mass fraction in the BG zone was also fairly reproduced, Figure 6.41. Moreover, extending the present modelling approach by the introduction of a CO/CO_2 equilibrium model would be an interesting perspective.

6.5.3 Variation of Inlet Mixture Temperature

The inlet temperature is raised from 288K to 350K in 5 seconds, Figure 6.46. The flame tube is fed by a gaseous mixture characterised by $\dot{m}_{in} = 8.98g/s$, $\phi = 0.83$, and the outlet pressure is imposed at 1 atm. In that simulation, subjecting the flame tube component to an increase of UG temperature translates into an unsteady combustion process computed by the 0D CFM combustion model approach. Below, in a first time, the steady state response of the 0D CFM flame to the change of operating conditions will be detailed. Then features describing the unsteady response of the flame to transient operating conditions will be considered and analysed.

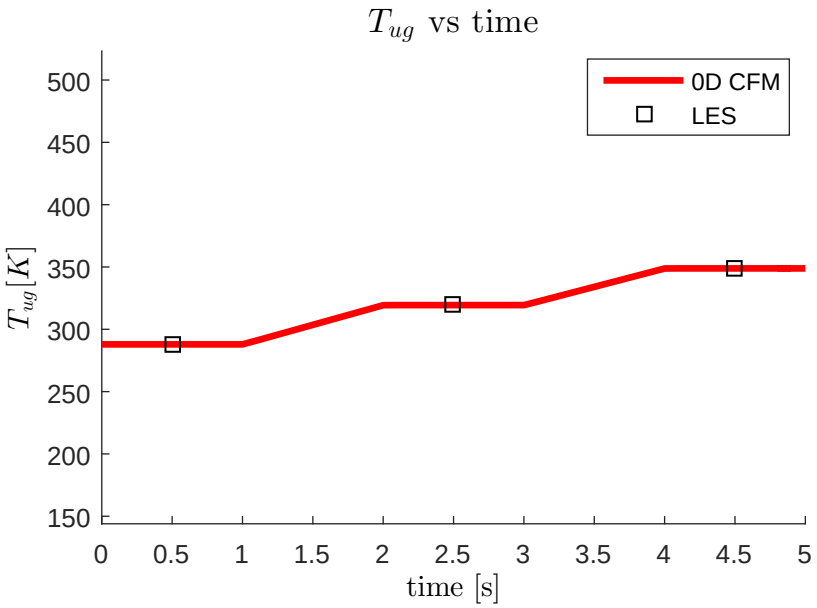

Figure 6.46 – Time variation of the UG temperature T_{ug}.

Comparison of the 0D Steady State Results to LES Results

The 0D model fairly catches the V_{ug} trend but with an offset, Figure 6.47. Conversely, the evolution of the turbulent velocity fluctuations is in contradiction with the CFD results, Figure 6.49. The 3D and 0D UG densities match, Figure 6.48.

The laminar flame speed Figure 6.50, thickness, Figure 6.51, mean surface, Figure 6.52, and wrinkling, Figure 6.53, fairly agree with the LES results.

The BG volume, Figure 6.54, and BG density, Figure 6.55, predicted by system simulation closely match with the CFD results. The same goes for pressure, Figure 6.56, and BG temperature, Figure 6.57.

As expected, the BG species mass fractions computed by the 0D CFM flame tube model do not match with the LES results for the same reasons mentioned in section 6.5.2, which are the absence of H_2 from the LES species set on one side, and the absence of CO/CO_2 equilibrium model from the 0D approach on the other side. However, two exceptions of results match were observed, namely for H_2O, Figure 6.60, and O_2, Figure 6.61. One could notice that CO levels predicted by LES are low in comparison to CO_2 levels.

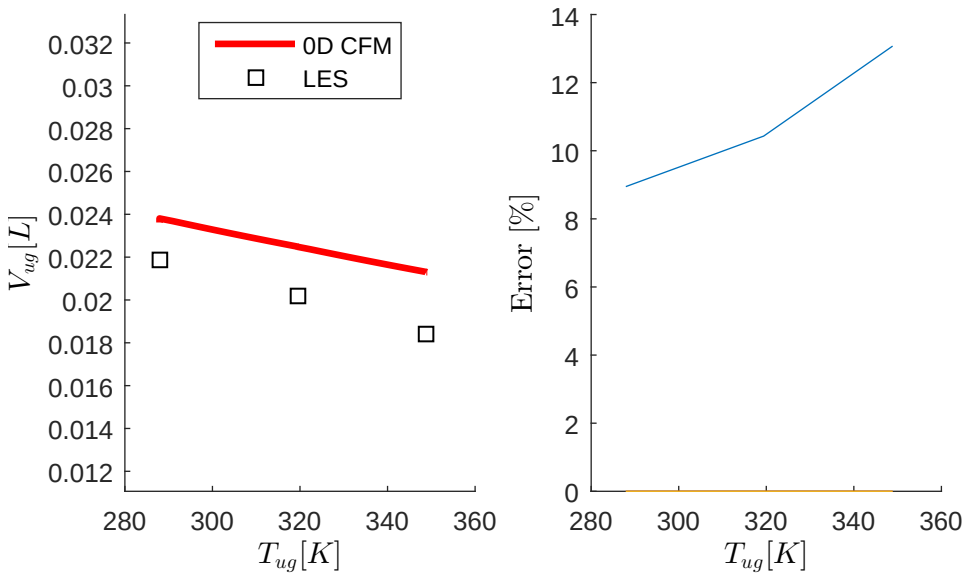

Figure 6.47 – Variation of the UG volume V_{ug} with the UG temperature T_{ug}.

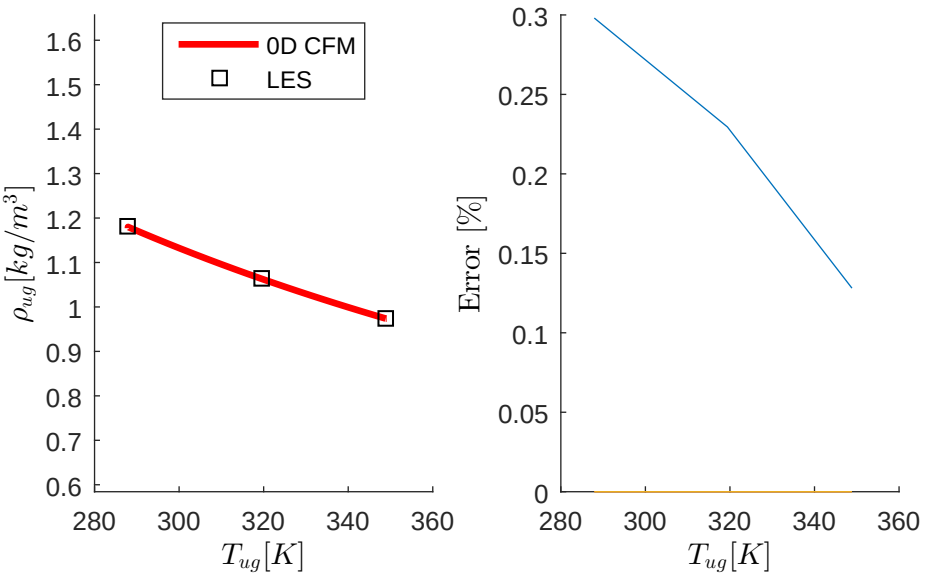

Figure 6.48 – Variation of the UG density ρ_{ug} with the UG temperature T_{ug}.

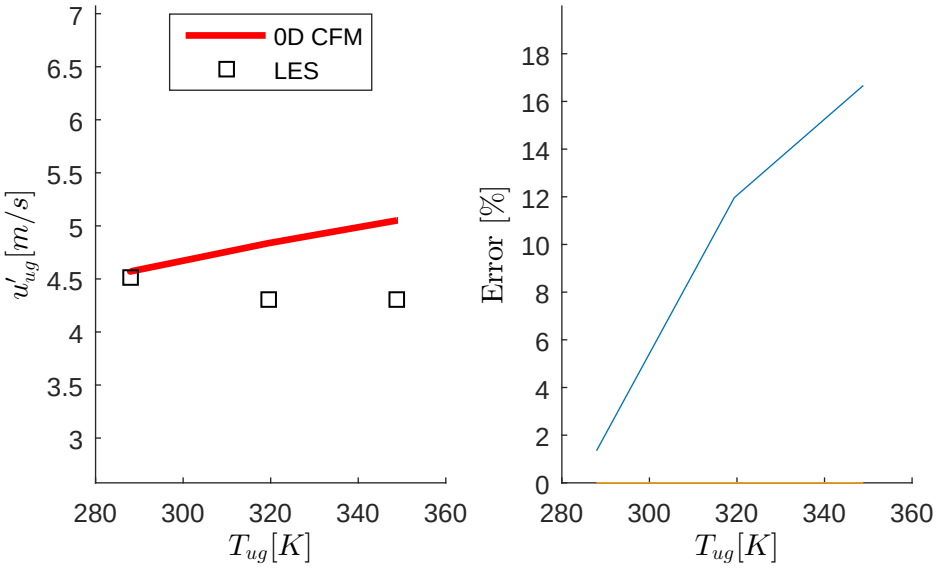

Figure 6.49 – Variation of the UG turbulent intensity u'_{ug} with the UG temperature T_{ug}.

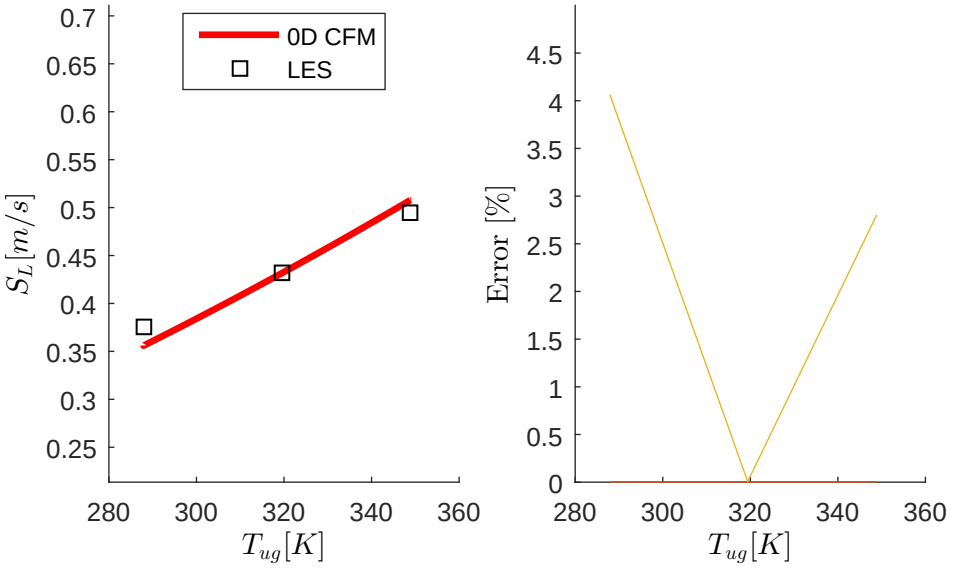

Figure 6.50 – Variation of the global laminar flame speed S_L with the UG temperature T_{ug}.

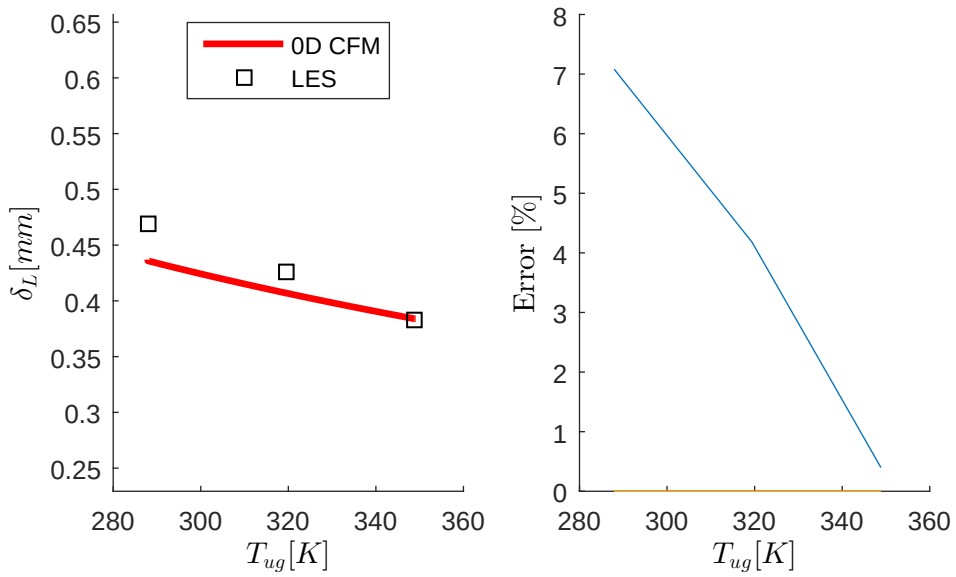

Figure 6.51 – Variation of the global laminar flame thickness δ_L with the UG temperature T_{ug}.

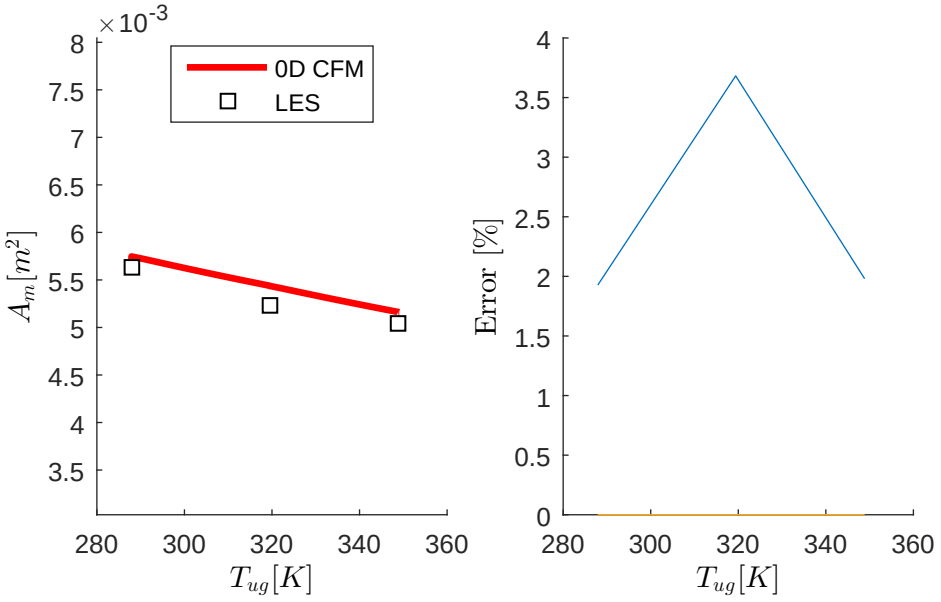

Figure 6.52 – Variation of the mean flame area A_m with the UG temperature T_{ug}.

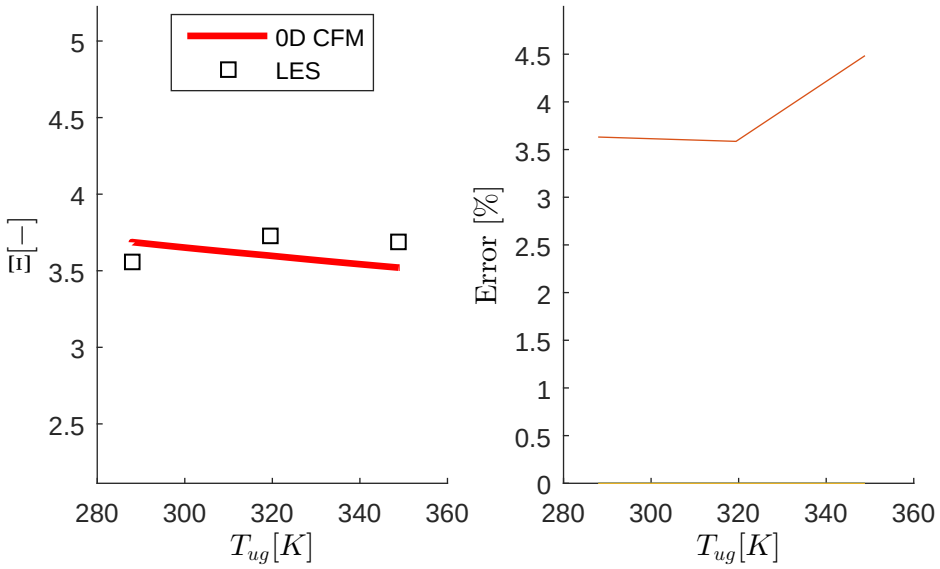

Figure 6.53 – Variation of the flame wrinkling Ξ with the UG temperature T_{ug}.

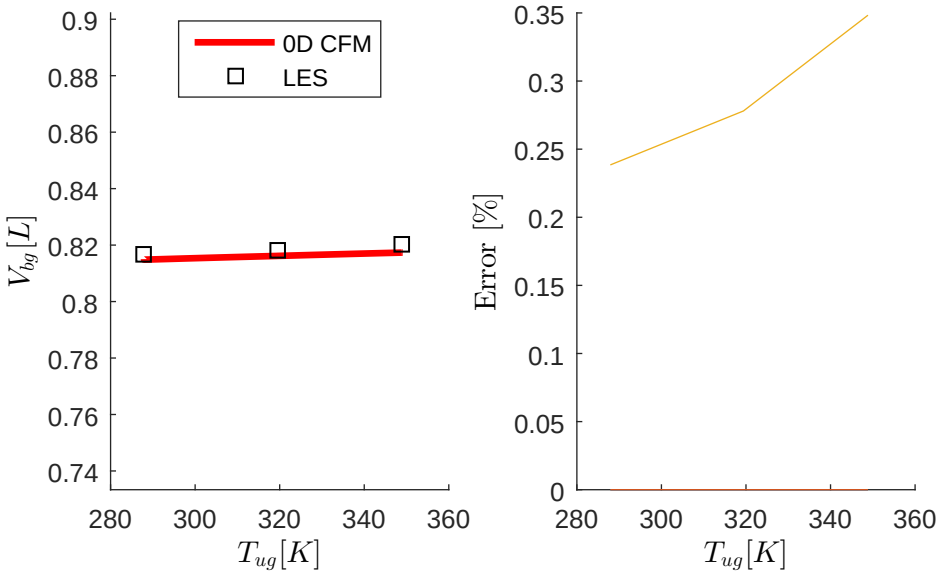

Figure 6.54 – Variation of the BG zone volume V_{bg} with the UG temperature T_{ug}.

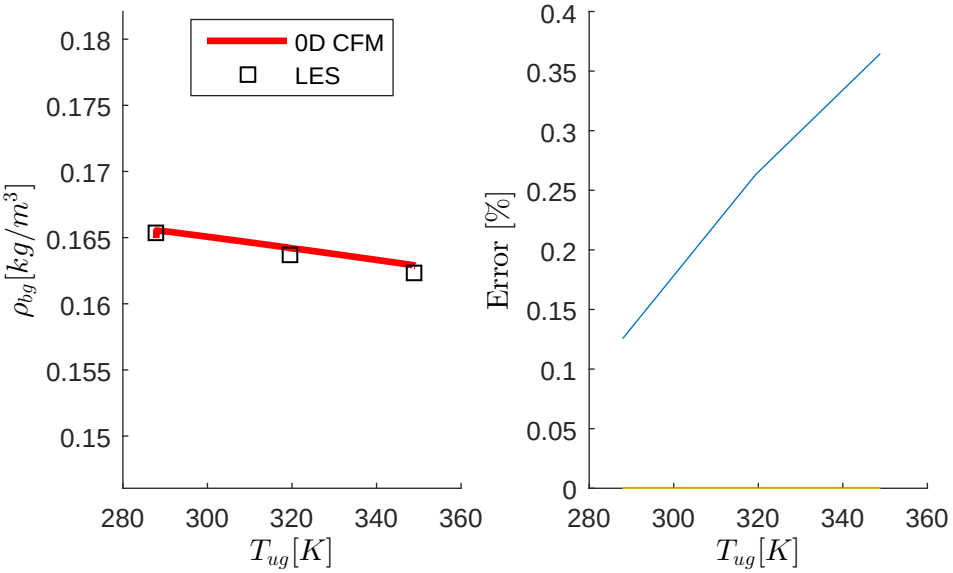

Figure 6.55 – Variation of the BG zone density ρ_{bg} with the UG temperature T_{ug}.

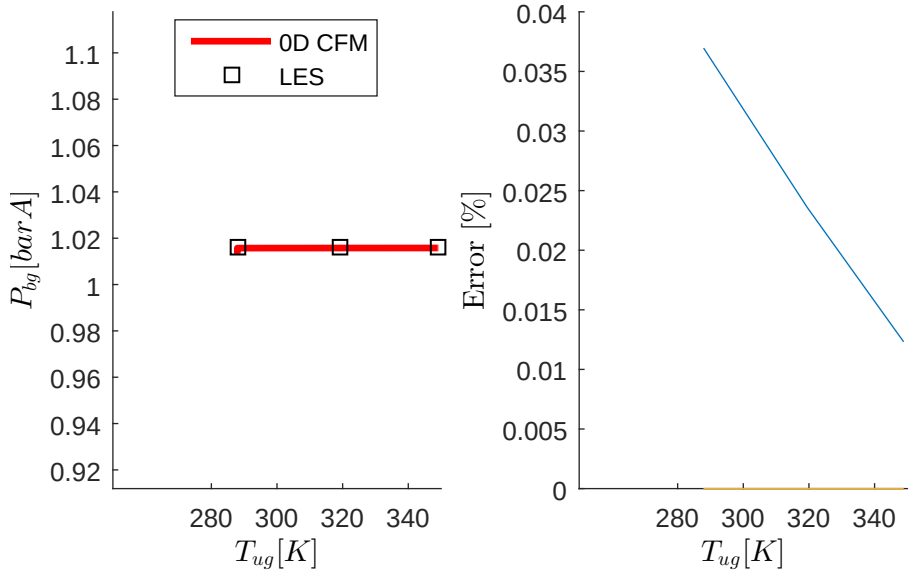

Figure 6.56 – Variation of the static pressure in the combustion chamber P_{bg} with the UG temperature T_{ug}.

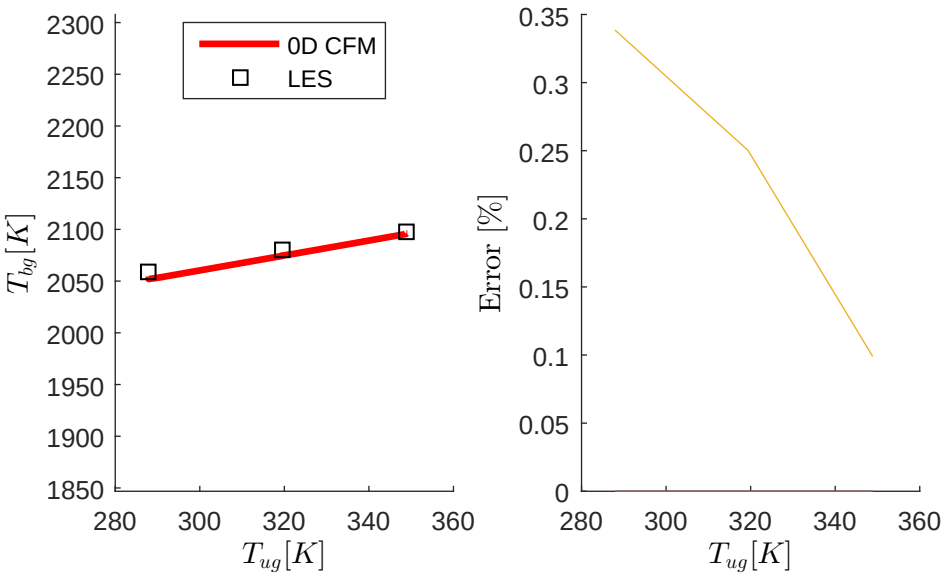

Figure 6.57 – Variation of the BG zone temperature T_{bg} with the UG temperature T_{ug}.

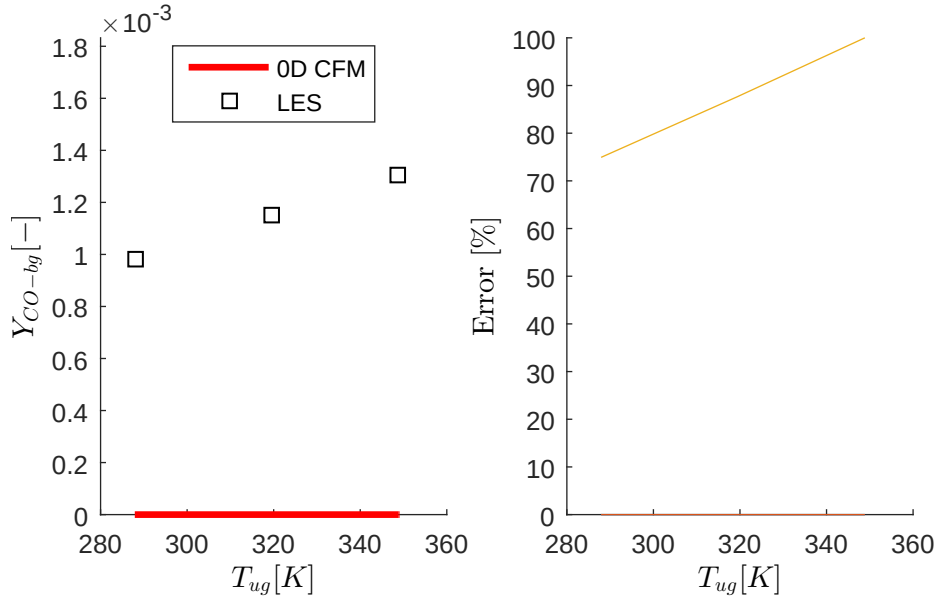

Figure 6.58 – Variation of the CO mass fraction in the BG zone with the UG temperature T_{ug}.

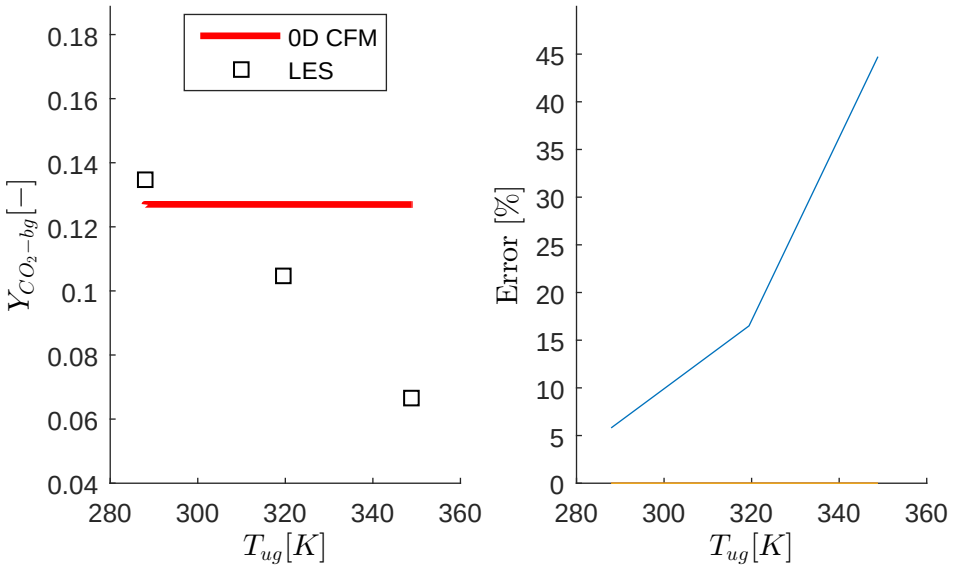

Figure 6.59 – Variation of the CO_2 mass fraction in the BG zone with the UG temperature T_{ug}.

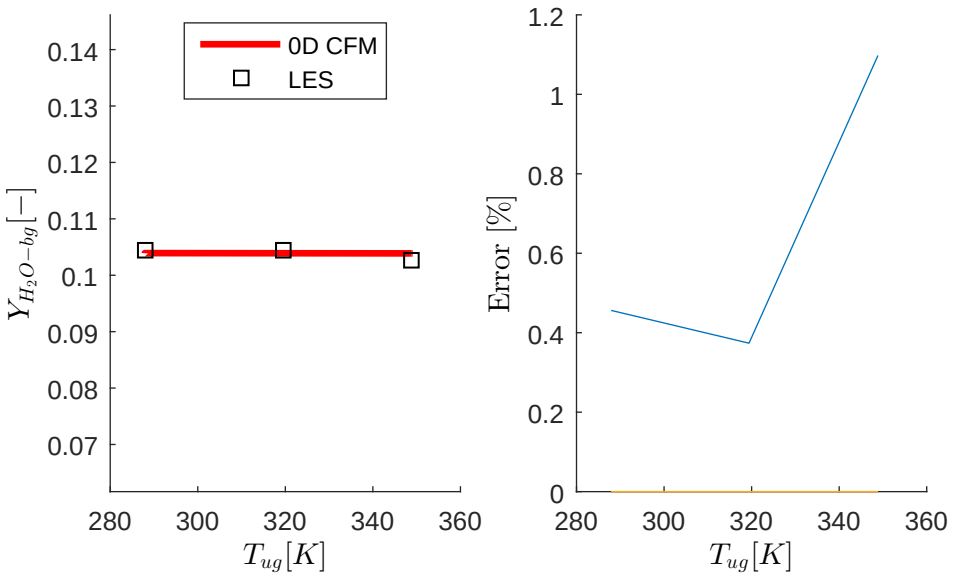

Figure 6.60 – Variation of the H_2O mass fraction in the BG zone with the UG temperature T_{ug}.

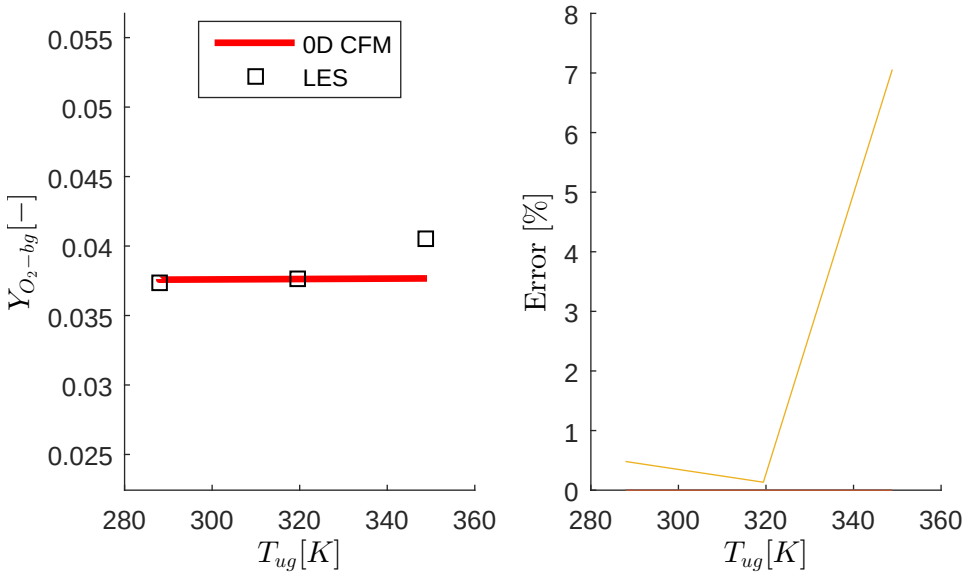

Figure 6.61 – Variation of the O_2 mass fraction in the BG zone with the UG temperature T_{ug}.

Analysis of the 0D CFM Flame Tube Response to Transient Operating Conditions

The dynamic response of the variables characterising the UG zone and the flame to transients of UG temperature is summarised in Table 6.5. Raising T_{ug} caused the UG density to decrease, but increased laminar flame speed, which decreased the fresh gas volume in return, Figure 6.47. The decrease of V_{ug} generated a decrease of mean flame surface. Also according to Table 6.5b, surface wrinkling decreased with the increase of UG temperature.

Table 6.5 – Dynamic response of the UG zone and the flame to transients of UG temperature.

ρ_{ug}	$Y_{ug,F}$	T_{ug}	P_{ug}	u'_{ug}
$\downarrow$ 17.5%	=	$\uparrow$ 21.5%	=	$\uparrow$ 11%

(a) UG zone variables.

S_L	δ_L	A_m	Ξ	$\dot{\Omega}_F$
$\uparrow$ 43%	$\downarrow$ 12%	$\downarrow$ 10%	$\downarrow$ 5%	$\simeq$

(b) Flame variables.

In details, as S_L builds up with the raise of T_{ug}, it overcompensates the decrease of fresh gas density, leading to an overall decrease of the heat diffusivity coefficient, $\frac{\lambda}{\rho_{ug} c_{p_{ug}}}$. As a consequence, δ_L is reduced. The increase of S_L is greater than both the increase of u'_{ug} and the decrease of δ_L. According to the work presented in [17], assuming that the roles of S_L, δ_L, u'_{ug} and l_T are equally important in the flame surface wrinkling process, the decrease of Ξ obtained by means of the herein analysed system simulation seems plausible.

Regarding the BG zone, as more heat is generated due to the increase of fresh gas temperature, ρ_{bg} diminishes, Figure 6.55, pressure does not change, Figure 6.56, and T_{bg} increases, Figure 6.57. Therefore, the thermodynamic behaviour of the 0D flame tube model is rather realistic. However, another case featuring steeper temperature transients and larger

temperature ranges should be considered. In the frame of the herein detailed temperature transients, no variations of BG composition were expected and no changes of species mass fractions were observed.

6.5.4 Variation of Outlet Static Pressure

The outlet pressure evolves from 1bar to 3bar in 5 seconds, Figure 6.62. The flame tube is fed by a gaseous mixture characterised by $\dot{m}_{in} = 8.98g/s$, $T_{ug} = 320K$, and $\phi = 0.83$. In that simulation, subjecting the flame tube component to an increase of outlet pressure translates into an unsteady combustion process computed by the 0D CFM combustion model approach. Below, the steady state response of the 0D CFM flame to the change of operating conditions will be detailed in a first time. Then features describing the unsteady response of the flame to transient operating conditions will be considered and analysed.

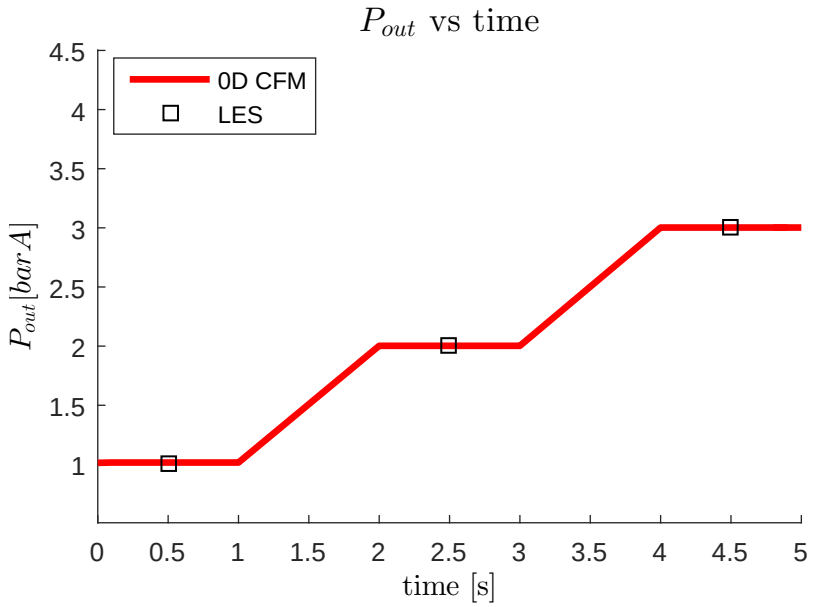

Figure 6.62 – Time variation of the outlet pressure P_{out}.

Comparison of the 0D Steady State Results to LES Results

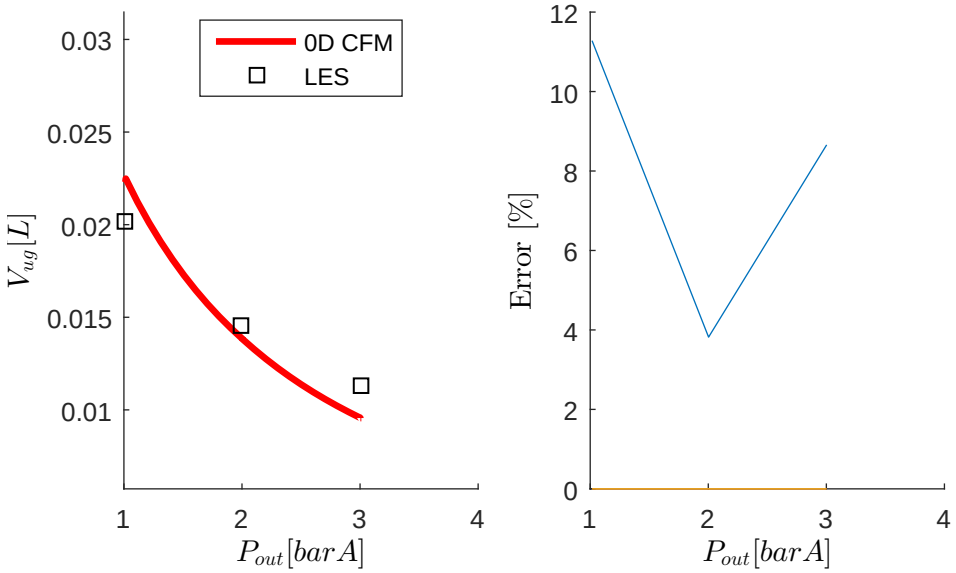

Figure 6.63 – Variation of the UG volume V_{ug} with the outlet pressure P_{out}.

Concerning the UG variables, fresh gas volume computations give results of the same order as LES results and predict a trend decreasing with the increase of P_{out}, slightly steeper than the trend given by LES, Figure 6.63. The 0D fresh gas density results match with the 3D results, Figure 6.64. Turbulent velocity of the fresh gas is computed with an acceptable accuracy with respect to LES results, especially at $P_{out} = 3bar$, Figure 6.65.

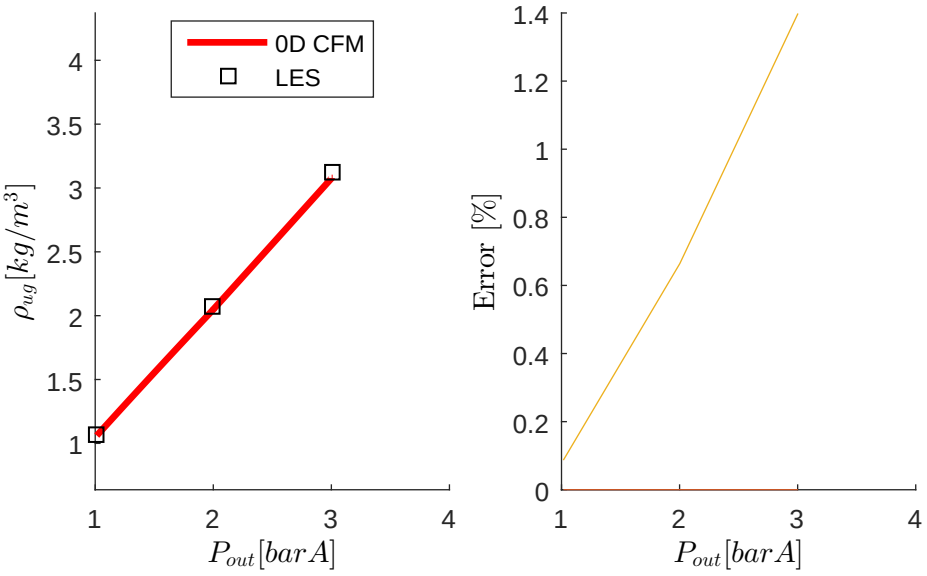

Figure 6.64 – Variation of the UG density ρ_{ug} with the outlet pressure P_{out}.

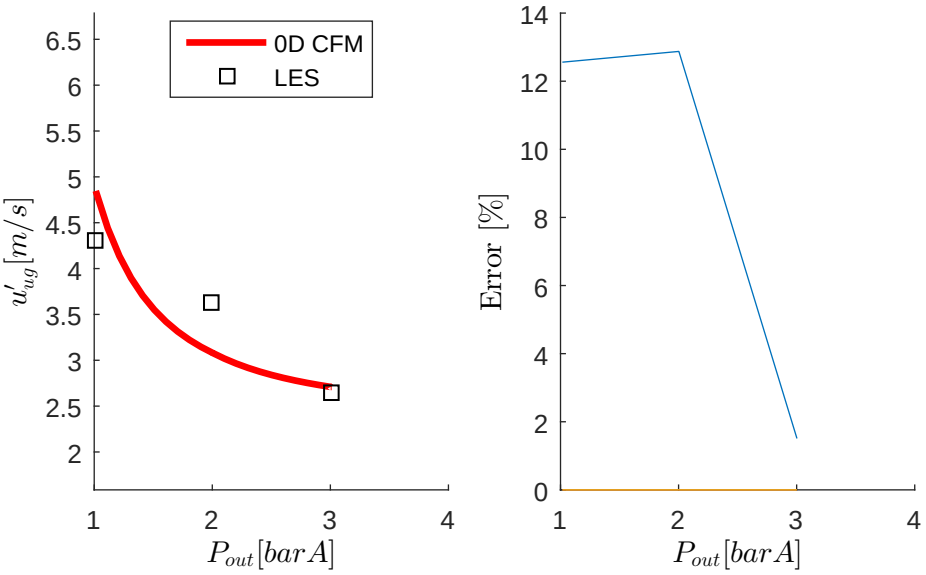

Figure 6.65 – Variation of the UG turbulent intensity u'_{ug} with the outlet pressure P_{out}.

Laminar flame speed and thickness results are in good agreement with CFD results, respectively Figure 6.66 and Figure 6.67. A good match with LES results is also obtained for A_m, Figure 6.68, and Ξ, Figure 6.69.

The characterisation of the BG thermodynamic variables is quite accurate with respect to the characterisation computed by means of LES. In details, BG volume, Figure 6.70, burned gas density, Figure 6.71, BG pressure, Figure 6.72, and temperature, Figure 6.73.

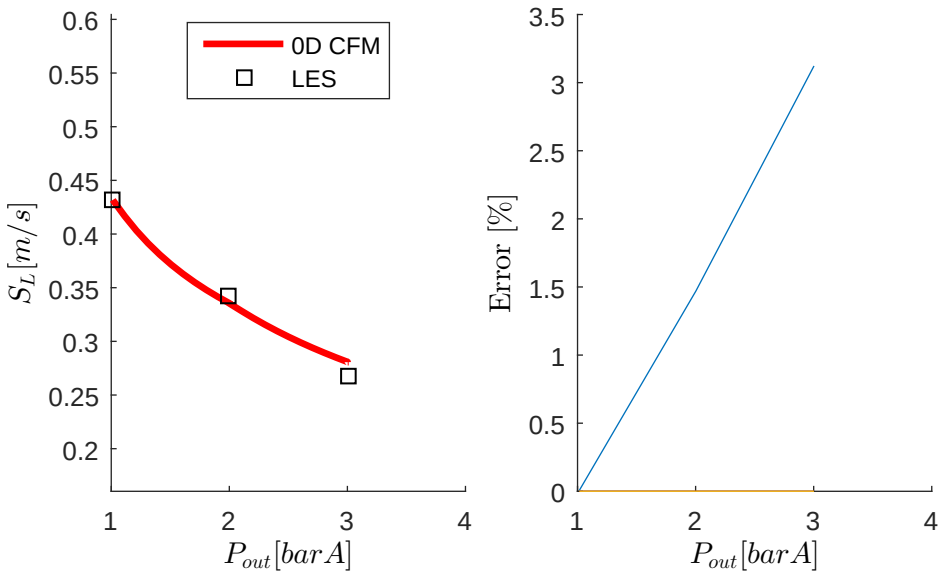

Figure 6.66 – Variation of the global laminar flame speed S_L with the outlet pressure P_{out}.

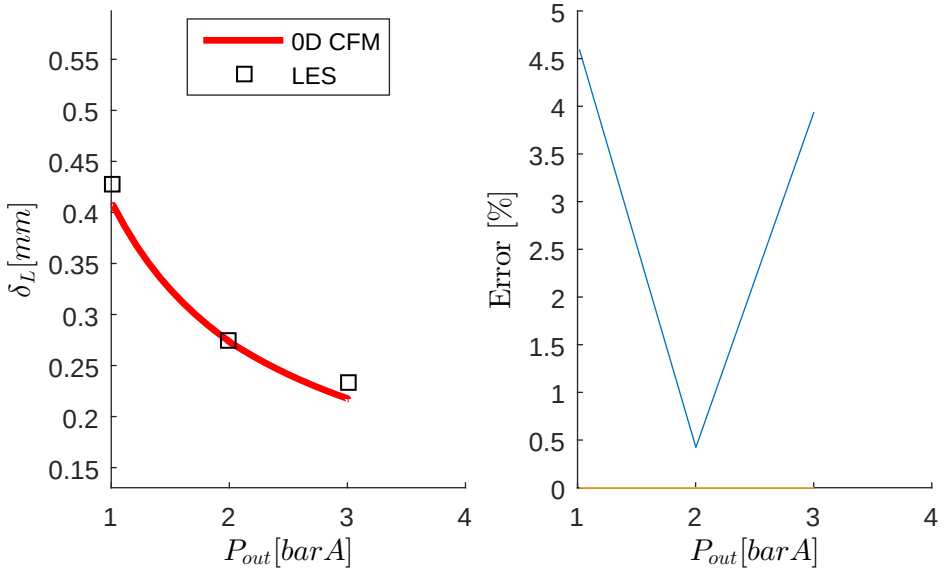

Figure 6.67 – Variation of the global laminar flame thickness δ_L with the outlet pressure P_{out}.

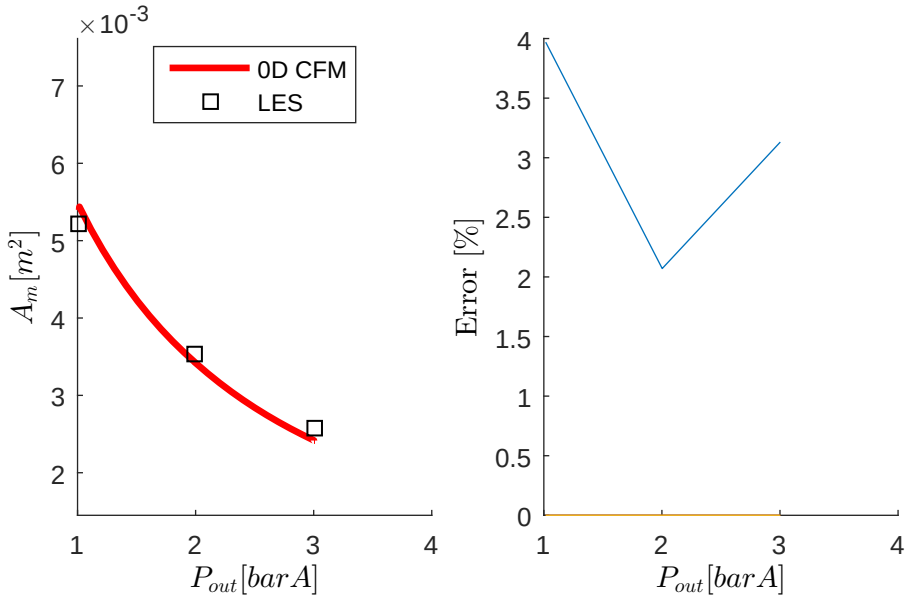

Figure 6.68 – Variation of the mean flame area A_m with the outlet pressure P_{out}.

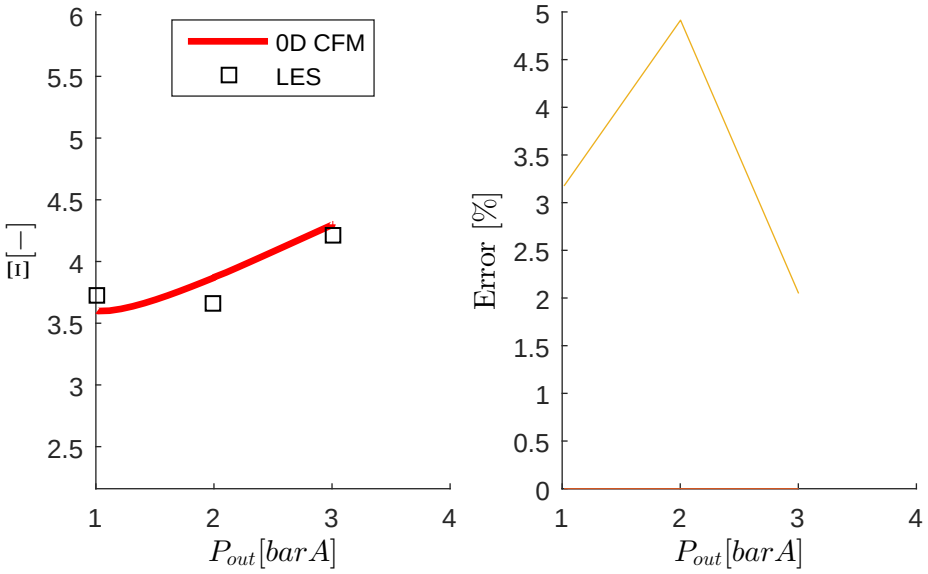

Figure 6.69 – Variation of the flame wrinkling Ξ with the outlet pressure P_{out}.

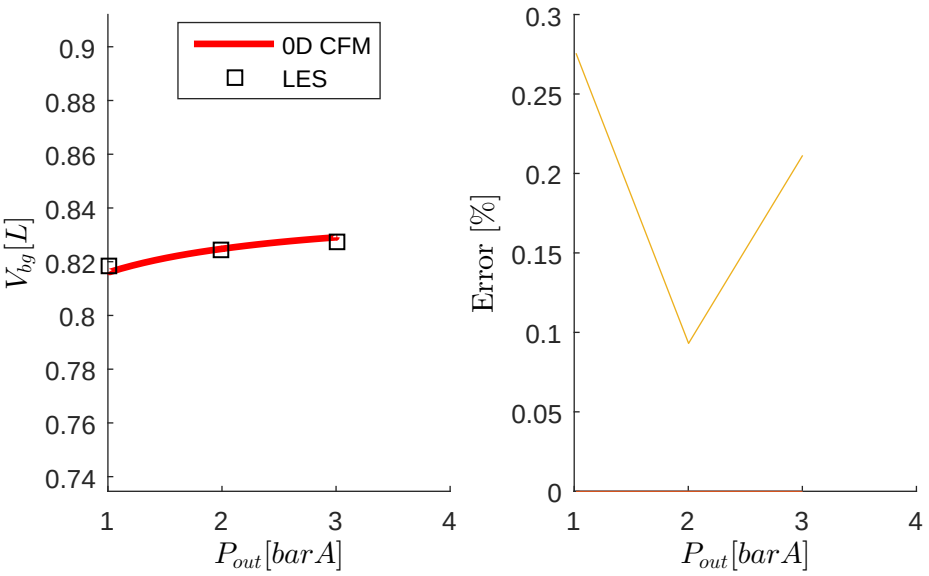

Figure 6.70 – Variation of the BG volume V_{bg} with the outlet pressure P_{out}.

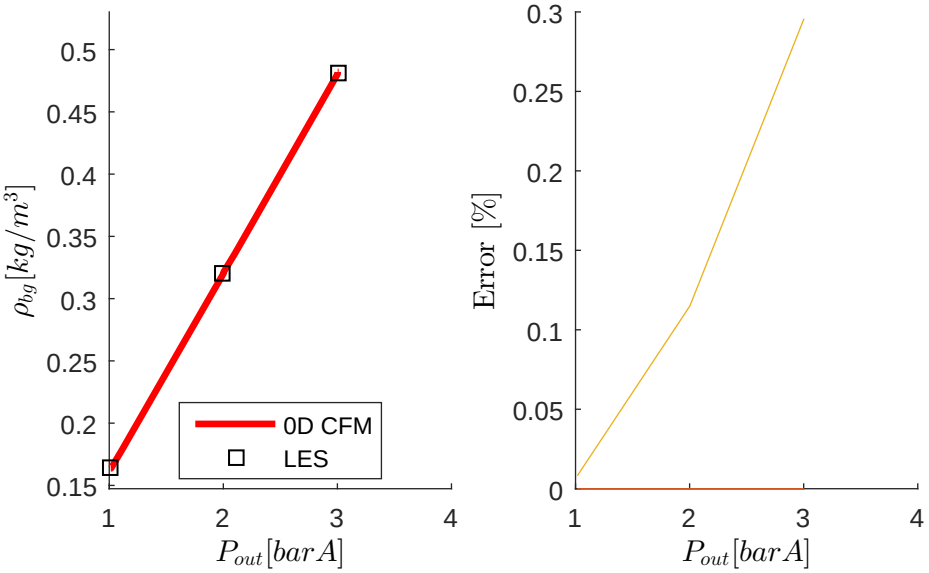

Figure 6.71 – Variation of the UG density ρ_{bg} with the outlet pressure P_{out}.

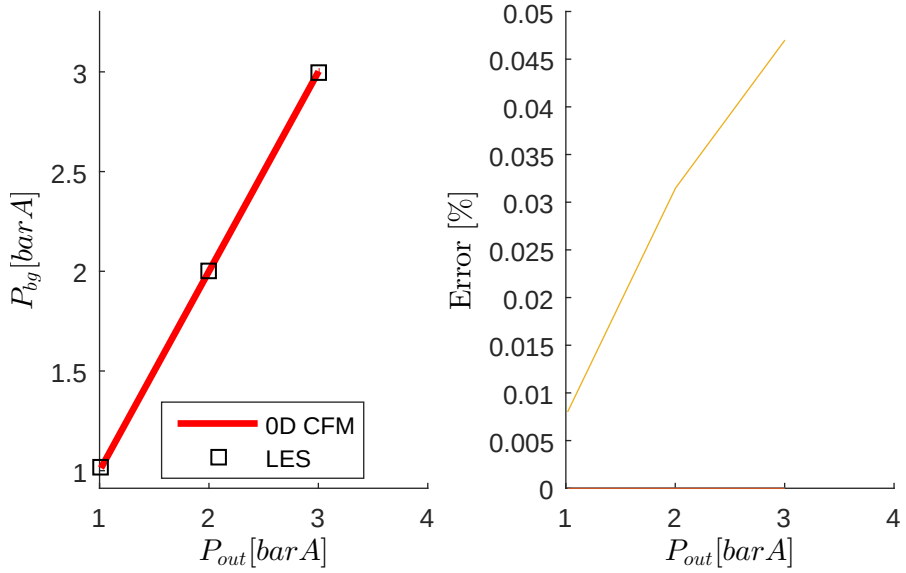

Figure 6.72 – Variation of the static pressure in the combustion chamber P_{bg} with the outlet pressure P_{out}.

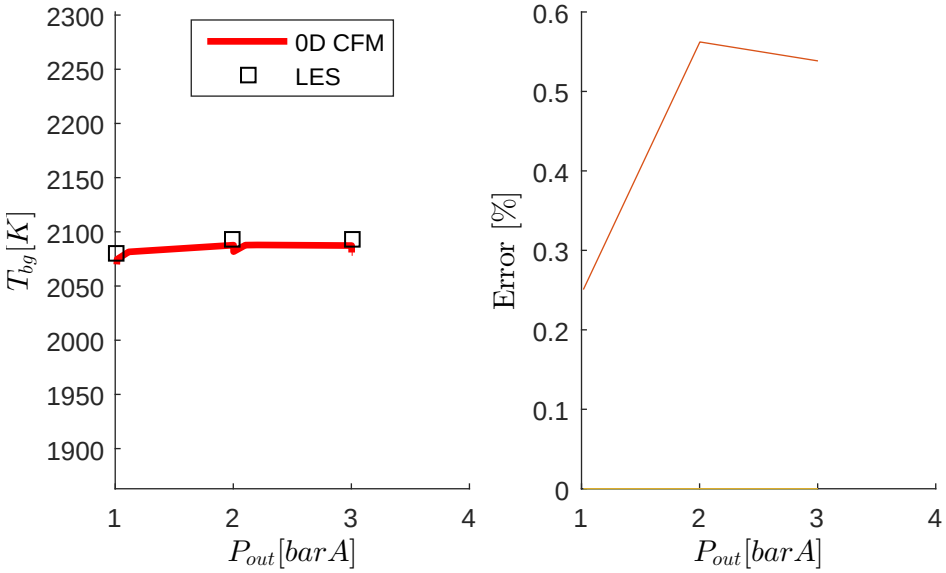

Figure 6.73 – Variation of the BG temperature T_{bg} with the outlet pressure P_{out}.

Mass fractions of species constituting the burned gas mixture are also well predicted except for CO, Figure 6.74, which is not estimated by using a CO/CO_2 equilibrium model in the 0D CFM flame tube approach. In details, according to Figure 6.75 and Figure 6.76, respective CO_2 and H_2O mass fractions discrepancies with respect to LES results do not exceed 1.1% and O_2 mass fractions estimated by the 0D model differ from LES estimations by less than 4%, Figure 6.77.

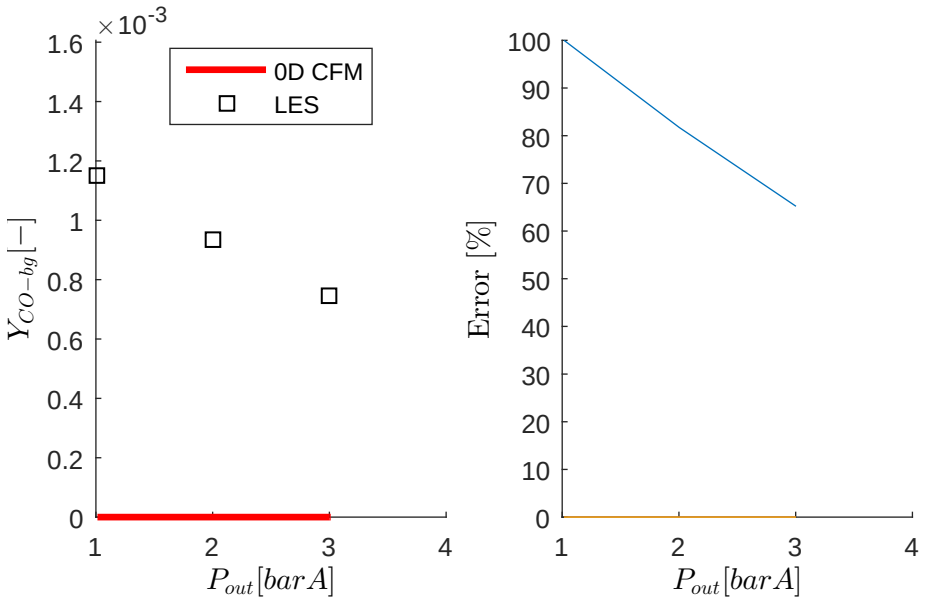

Figure 6.74 – Variation of the CO mass fraction in the BG zone with the outlet pressure P_{out}.

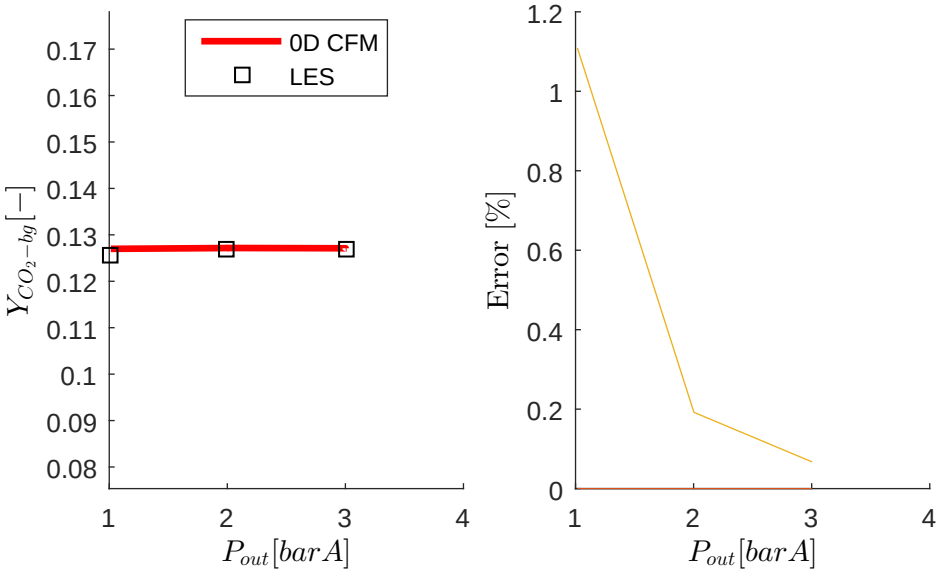

Figure 6.75 – Variation of the CO_2 mass fraction in the BG zone with the outlet pressure P_{out}.

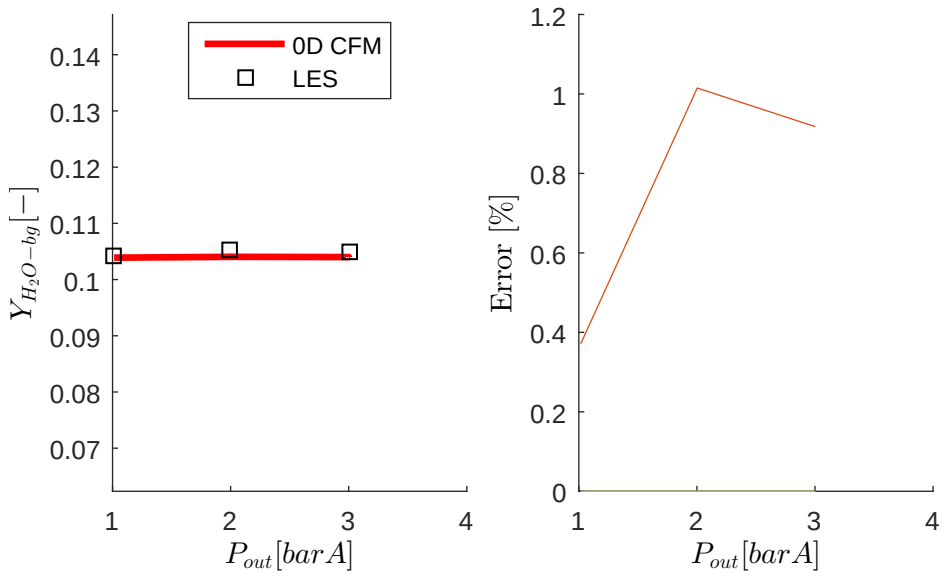

Figure 6.76 – Variation of the H_2O mass fraction in the BG zone with the outlet pressure P_{out}.

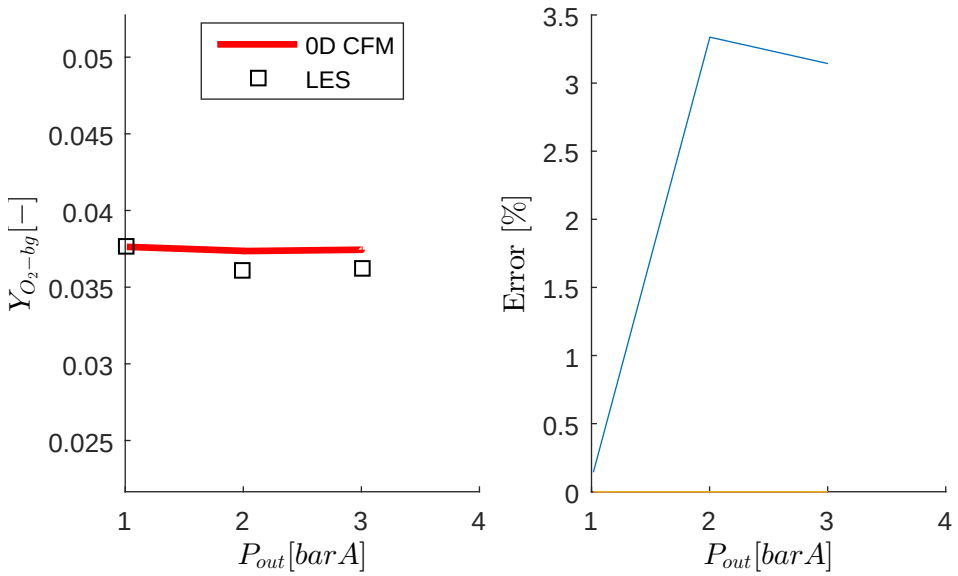

Figure 6.77 – Variation of the O_2 mass fraction in the BG zone with the outlet pressure P_{out}.

Analysis of the 0D CFM Flame Tube Response to Transient Operating Conditions

According to Figure 6.63, the pressure build-up imposed on the 0D flame tube compressed the UG gas, which obviously reduced the fresh gas volume and increased the UG density, Figure 6.64. That increase of density translated into a decrease of flow velocity which was relflected by the drop of turbulent velocity fluctuations by 44%, as observed in Table 6.6a.

Table 6.6 – Dynamic response of the UG zone and the flame to transients of outlet pressure.

ρ_{ug}	$Y_{ug,F}$	T_{ug}	P_{ug}	u'
$\uparrow$ 189%	$=$	$\simeq$	$\uparrow$ 200%	$\downarrow$ 44%

(a) UG variables.

S_L	δ_L	A_m	Ξ	$\dot{\Omega}_F$
$\downarrow$ 35%	$\downarrow$ 47%	$\downarrow$ 56%	$\uparrow$ 19.4%	$\simeq$

(b) Flame variables.

As shown in Table 6.6b, in addition to a decrease of S_L, the increase of P_{out} seems to cause the reduction of the laminar flame thickness. In fact, the increase of fresh gas density translates into a greater decrease of the heat diffusivity coefficient, $\frac{\lambda}{\rho_{ug} c_{p_{ug}}}$, than the decrease of S_L, Figure 6.66. This globally leads to a decrease of laminar flame thickness, which is in agreement with the observations and analysis detailed in [9]. Mean flame surface is also reduced as an inevitable consequence of the UG volume decrease. Concerning flame wrinkling, on one hand the slowing down of turbulent velocity slightly exceeds the decrease of laminar flame speed. On the other hand, the decrease of δ_L by 47% combined with a supposedly constant integral length scale, l_T, seems to be the dominant variation that affected flame surface wrinkling in this transient simulation. The overall fuel burning rate did no change.

On the BG side, a increase of V_{bg}, Figure 6.70, is observed against the previously mentioned decrease of UG volume, and an obvious increase of burned gas density, Figure 6.71, comes in response to the BG pressure raise, Figure 6.72. Finally, the burned gas mixture composition does not change in a statistically significant way in this simulation.

Conclusions

The results of the simulations are in a globally good agreement with the LES results, with CPU times of the order of half a second for physical times of the order of five seconds, and without any numerical instabilities or any difficulty to convergence. Some discrepancies with LES database results are due to the limits of the laminar flame speed correlation, in particular for $\phi > 1.2$. Other mismatches are due to non-justified fluctuations of the LES variables, namely u'. Flame surface wrinkling is fairly predictive for responses to variations of mass flow rate, temperature and pressure, but it does not comply with the wrinkling fluctuations observed in the LES variations of FAeR. The compositions of the burned mixture computed by the 0D model differs from the compositions obtained in the CFD database, and that is due to different combustion chemical reactions, different formulations of the reaction rates, the absence of H_2 in the LES setup, and the absence of CO/CO_2 equilibrium model in the post-flame region.

Part IV

A Non-Premixed Burner Case

Chapter 7

Large Eddy Simulation of an Aeronautical Burner Sector

In chapters 5 and 6, premixed combustion of a swirling flame in an experimental test rig was addressed. In what follows, multi-regime combustion in one sector of a rotorcraft turboshaft combustor is investigated by means of the DTFLES combustion model with the AVBP software. The numerical setup and data of the combustor case simulation were given by courtesy of the rotorcraft engine maker, SAFRAN Helicopter Engines. The aim of these investigations is to use reactive LES to gather phenomenological understanding of turbulent combustion with variable mixture fraction in a real aeronautical gas turbine, for system simulation modelling purposes. In a first step, based on CFD results, the main flow streams were characterised and the major recirculation zones were identified. Then, regions witnessing premixed and non-premixed combustion regimes were localised. In the following step, combustion variables were filtered by using the normalised Takeno flame index [46, 61], in order to quantify the respective contributions of each combustion regime in the combustor. Finally, all the gathered information was used to build a simplified combustion scenario that represents the real combustion process. That scenario allowed to define the constraints to be respected and the perimeter to be covered, by combustion modelling for the system simulation approach.

7.1 Simulation Setup and Preliminary Analysis

7.1.1 Case Description

The herein considered reverse-flow combustion chamber is designed for a rotorcraft turboshaft that powers modern multi-role helicopters. The annular reverse-flow combustion chamber is similar to the simplified representation in Figure 7.1. The schematic features inner and outer annuli, a number of counter-swirling injectors and an elbowed flame tube. High-pressure air travels through the annuli: part of the air mass flow reaches the injectors and the primary air inlets, and the other part enters the flame tube by crossing multi-perforated walls; liquid fuel is fed through the injectors separately from the air flow, Figure 7.2. The elementary angular sector of the combustor includes one counter-swirl injector. A DTFLES simulation of one sector of the combustion chamber was prepared and run for several flow-through time units by a team from SAFRAN Helicopter Engines. Compressible Navier-Stokes equations were solved. All the species were supposed to be gaseous and assumed to behave as ideal gases. Species thermochemical properties were characterized by JANAF tables [118]. The Lewis number, Le, was unity for all the species. Viscosities were modelled by using Sutherland's law [120]. Steady flows with fully developed turbulence and stable flames were considered in this study. Hence, turbulence production and destruction balance was assumed to be null. Accordingly, the Smagorinsky-Lilly subgrid scale model was used [115]. The CFD mesh was

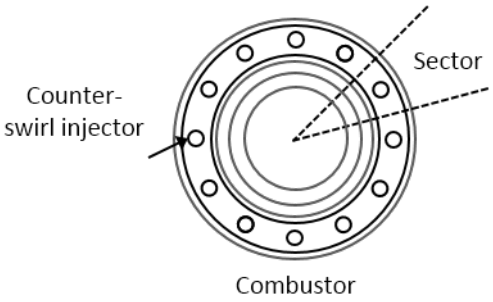

Figure 7.1 – Schematic of an annular combustion chamber featuring 12 counter-swirl injectors.

composed of 37.87×10^6 linear tetrahedral cells. The smallest length was 4.45×10^{-2}mm, and the mesh contained 6.65×10^6 nodes. The LW numerical scheme was used. The $smu2$ factor, controlling the damping of very strong gradients or shocks, and the $smu4$ factor, controlling the damping of high frequency wiggles, were respectively set in AVBP to 0.1 and 0.01.

Boundary Conditions

As shown in Figure 7.2, the computational domain starts at section 3, right upstream the second compressor stator vanes, where an air mass flow inlet condition is applied. The computational domain ends at the combustor exhaust, section 4, upstream the gas generator turbine, where a pressure condition is imposed. The inlet and outlet conditions properly represent the acoustic waves propagation and reflection, thanks to the NSCBC conditions [86, 97]. A fuel mass flow rate is applied on section 3.5. On flame tube walls and neighbouring annuli walls, large diameter holes were meshed as explicit computational flow path sections; multiperforations were represented as porous surfaces with equivalent mass fluxes conditions. Streamwise angles of the multiperforations as well as gyration effects were previously assessed by the rotorcraft engine maker by means of prior experimental characterisation, and the resulting mathematical formulations were incorporated into the AVBP source code. External annuli walls and outer walls were represented as solid walls. Shear stress was modelled on all walls by computing non-dimensional near-wall velocity, u^+, as a logarithmic function of non-dimensional distance to the wall, y^+ [27]. All the walls were assumed as adiabatic.

Combustion Model

The DTFLES combustion model [69], commonly used in the french aerospace industry, was selected for studying the present case. The flame thickening factor equals five grid points. Kerosene/air combustion is modelled by the reduced chemical scheme 2S_KERO_BFER [48]. This scheme takes into account six species ($KERO$, O_2, CO_2, CO, H_2O and N_2) and two reactions:

$$\mathrm{KERO} + 10O_2 \longrightarrow 10CO + 10H_2O \tag{7.1}$$

$$CO + \frac{1}{2}O_2 \longleftrightarrow CO_2 \tag{7.2}$$

The KERO fuel [76] is supposed as composed of n-decane ($C_{10}H_{22}$), an aromatic component (C_9H_{12}) and a naphtenic component (C_9H_{18}), the exact composition being described in Table 7.1. The KERO oxidation reaction, equation 7.1, is irreversible, whereas the CO-CO_2 equilibrium reaction, equation 7.2, is reversible. The rates of the reactions, equations 7.1 and

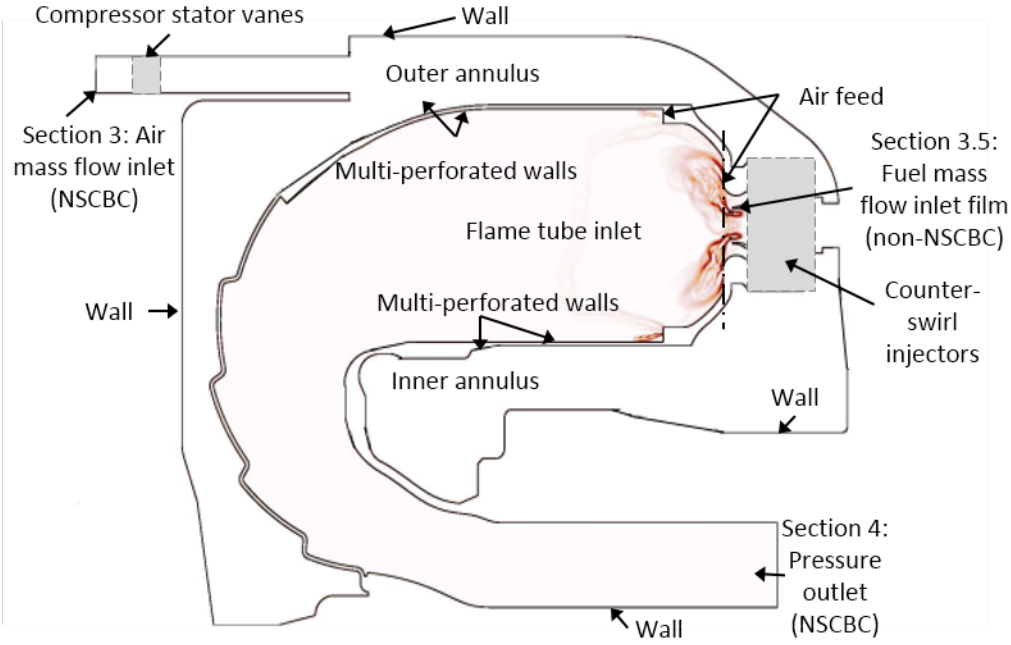

Figure 7.2 – Combustor sector computational domain and boundary conditions; boundary layer laws were applied on all the walls.

Table 7.1 – Composition of the KERO surrogate by [76].

Species	Type	Mass fraction [-]	Molar weight [g/mol]
$C_{10}H_{22}$	Linear	0.767	142.284
C_9H_{12}	Aromatic	0.132	120.1916
C_9H_{18}	Naphtenic	0.101	126.241
$C_{9.74}H_{20.05}$	KERO surrogate	1.0	137.195

7.2, are respectively given by:

$$R_1 = A_1 f_1(\phi) \left[\text{KERO }\right]^{n_{F,1}} \left[O_2\right]^{n_{O_2,1}} \exp\left(-\frac{E_{a,1}}{RT}\right) \tag{7.3}$$

$$\begin{aligned} R_2 &= R_{2_f} + R_{2_r} \\ &= A_2 f_2(\phi) \left(\left[CO\right]^{n_{CO,2}} \left[O_2\right]^{n_{O_2,2}} - \left[CO_2\right]^{n_{CO_2,2}}\right) \exp\left(-\frac{E_{a,2}}{RT}\right) \end{aligned} \tag{7.4}$$

where, for the reaction j, R_j is the reaction rate progress, A_j is the pre-exponential factor, f_j is a pre-exponential adjustment function, function of the mixture equivalence ratio, ϕ, $E_{a,j}$ is the activation energy and $n_{i,j}$ is the reaction exponent for the species i. Subscripts f and r represent forward and reverse reactions identifiers. According to [48], for equation 7.3, the values of activation energy, pre-exponential factor and reaction exponents were fitted to match the flame speed in the lean regime at the temperature of 300K and the pressure of 1atm, while f_1 was tuned in order to allow the 2S_KERO_BFER mechanism to recover flame speeds for rich mixtures; for equation 7.4, the values of activation energy, pre-exponential factor and reaction exponents were adjusted to correctly predict the flame temperature and the CO levels in burned gases, while f_2 was calibrated to correct the post-flame zone thickness and to help the mixture in quickly reaching equilibrium states. These values are summarized

in Table 7.2.

Table 7.2 – Activation energy, $E_{a,j}$, pre-exponential factor, A_j, and reaction exponents, $n_{i,j}$, used in the 2S_KERO_BFER mechanism [48].

Reaction	KERO oxidation (7.1)	CO-CO_2 equilibrium (7.2)
Activation energy [cal/mol]	4.15×10^4	2.0×10^4
Pre-exponential factor (cgs)	8.0×10^{11}	4.5×10^{10}
Reaction exponents [-]	$n_{F,1}$ 0.55 $n_{O_2,1}$ 0.90	$n_{CO,2}$ 1.00 $n_{O_2,2}$ 0.50 $n_{CO_2,2}$ 1.00

The values presented in Table 7.2 were validated in cases of laminar premixed flames at pressures ranging from 1atm to 12atm, fed by fresh gases at temperatures ranging from 300K to 700K, and diluted by Exhaust Gas Recirculation (EGR) at rates up to 15% in mass.

7.1.2 Preliminary Analysis

Before attempting to apply the formalism presented in section 5.1 to the present case, the results of the numerical simulation computed by the turboshaft maker were analysed in terms of flow velocity and combustion regimes. The analysis was focused on a volume designated as the flame region, bounded by the flame tube walls, a cut plane across the injectors and a cut plane located at a given height from the injectors outlet section, Figure 7.3. Indeed, the flame was localised within this volume by the presence of Heat Release Rate Density[1], $HRRD$, above a certain threshold. The flame penetration length, L_p, is the axial distance from the flame tube sector inlet to the tip of an iso-surface of $HRRD$ threshold. According

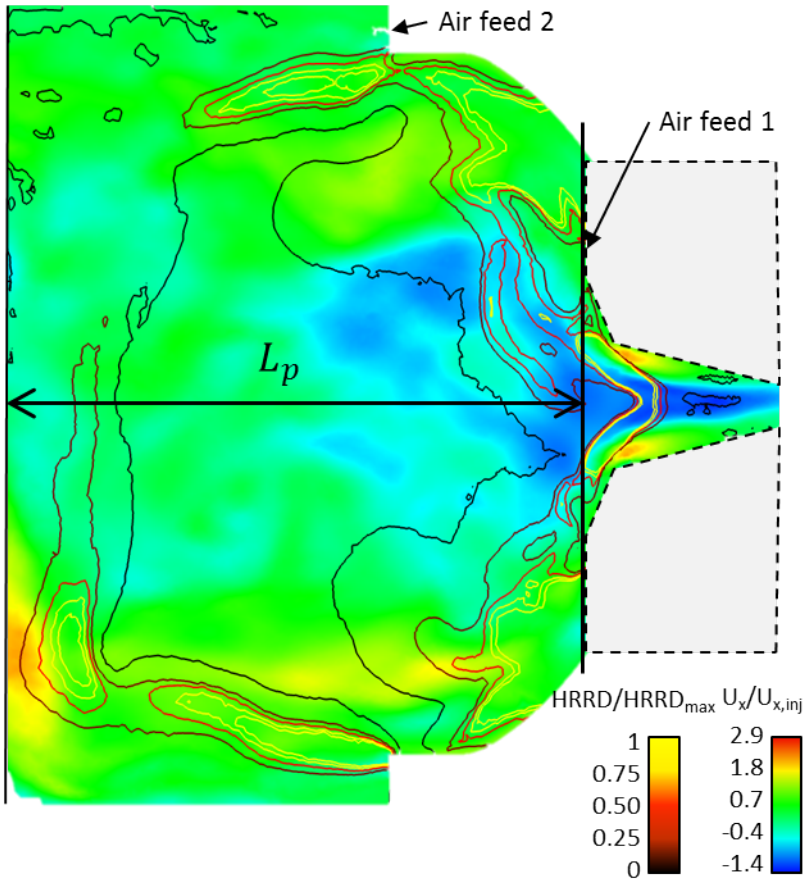

Figure 7.3 – 2D view of the time averaged axial velocity, U_x, normalized by its value inside the injector, $U_{x,inj}$, with superimposed contours of $HRRD$, normalised by its maximum value.

to Figure 7.3, blue shades witness recirculation zones and negative axial velocities along the flame tube sector axis and inside the inner injector. A detailed analysis of these features is presented in the following section.

Velocity Profiles Analysis

Axial, azimuthal and radial velocity profiles inside the flame region were post-processed over several cut planes, Figure 7.4, defined by their respective axial positions normalised by the flame penetration length, L_p. On each plane, only the points located inside the flame tube were considered, and their radial positions were normalised by the outer injector radius, R_{inj}.

[1] Heat release rate per unit of volume.

Axial, azimuthal and radial velocities were normalised by their reference values, which are their respective averages at the flame tube inlet, $l = 0$. These reference values are designated by the subscript 0.

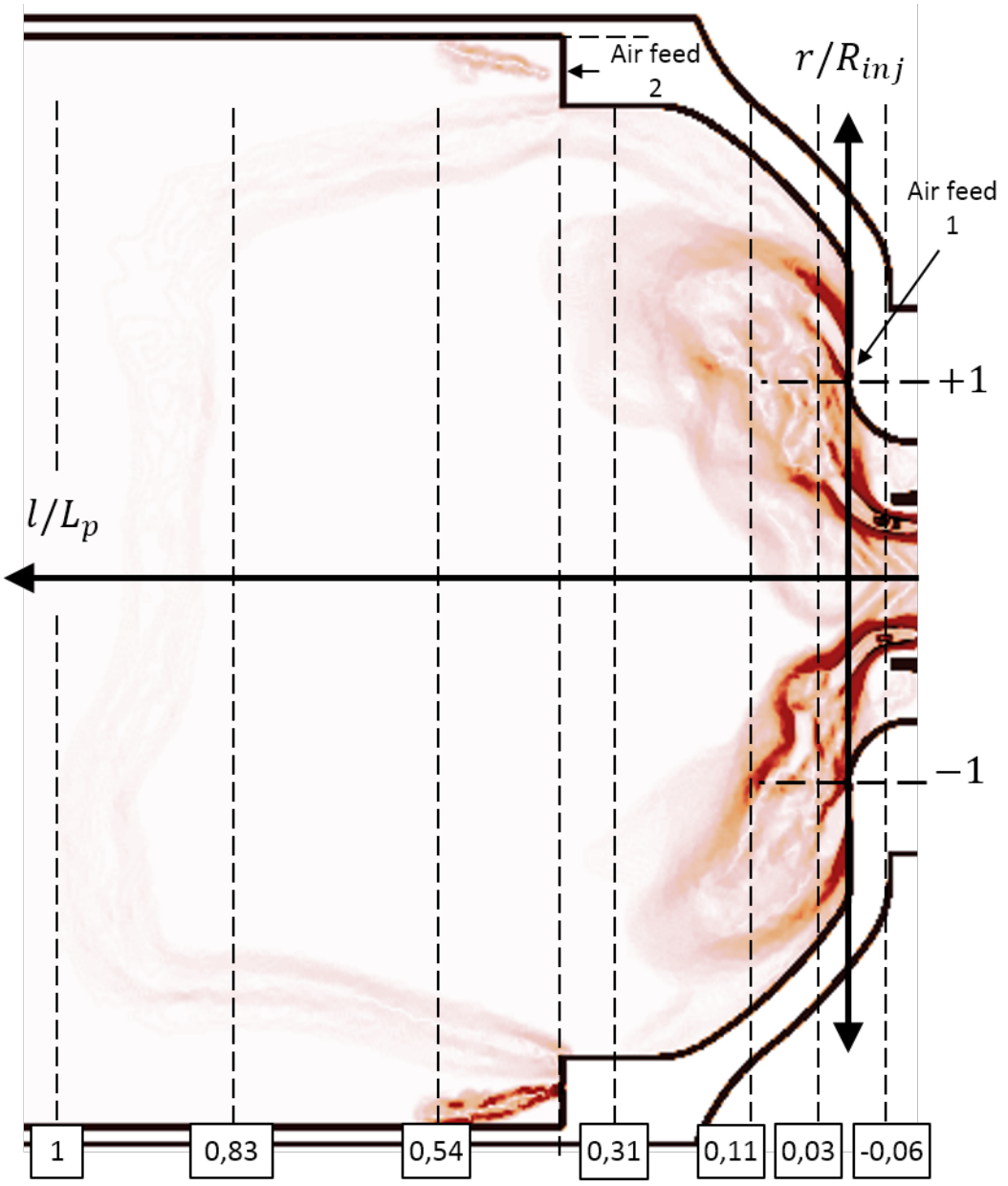

Figure 7.4 – Axial coordinates of the velocity profile analysis planes, l, normalised by the flame penetration length, L_p.

Radial profiles of normalised axial velocities, Figure 7.5, show a parabola of negative mean values of ${}^{U_x}/_{U_{x,0}}$ around the center, ${}^{r}/_{R_{inj}} = 0$, from inside the inner injector, ${}^{l}/_{L_p} = -0.06$, to the position ${}^{l}/_{L_p} = 0.31$. That evidence of central backflow along the axis of the injectors, which is in agreement with Figure 7.3, seems to vanish in the vicinity of the axial position ${}^{l}/_{L_p} = 0.54$. That central backflow of burned gases potentially reaches unburned gases, as soon as it crosses the plane positioned at ${}^{l}/_{L_p} = 0.03$. Furthermore, the coexistence of positive and negative axial velocities, detected at every plane for $\left|{}^{r}/_{R_{inj}}\right| > 0$, would confirm the presence of recirculation zones.

Radial profiles of normalised azimuthal velocities, ${}^{U_\theta}/_{U_{\theta,inj}}$, are shown in Figure 7.6. The

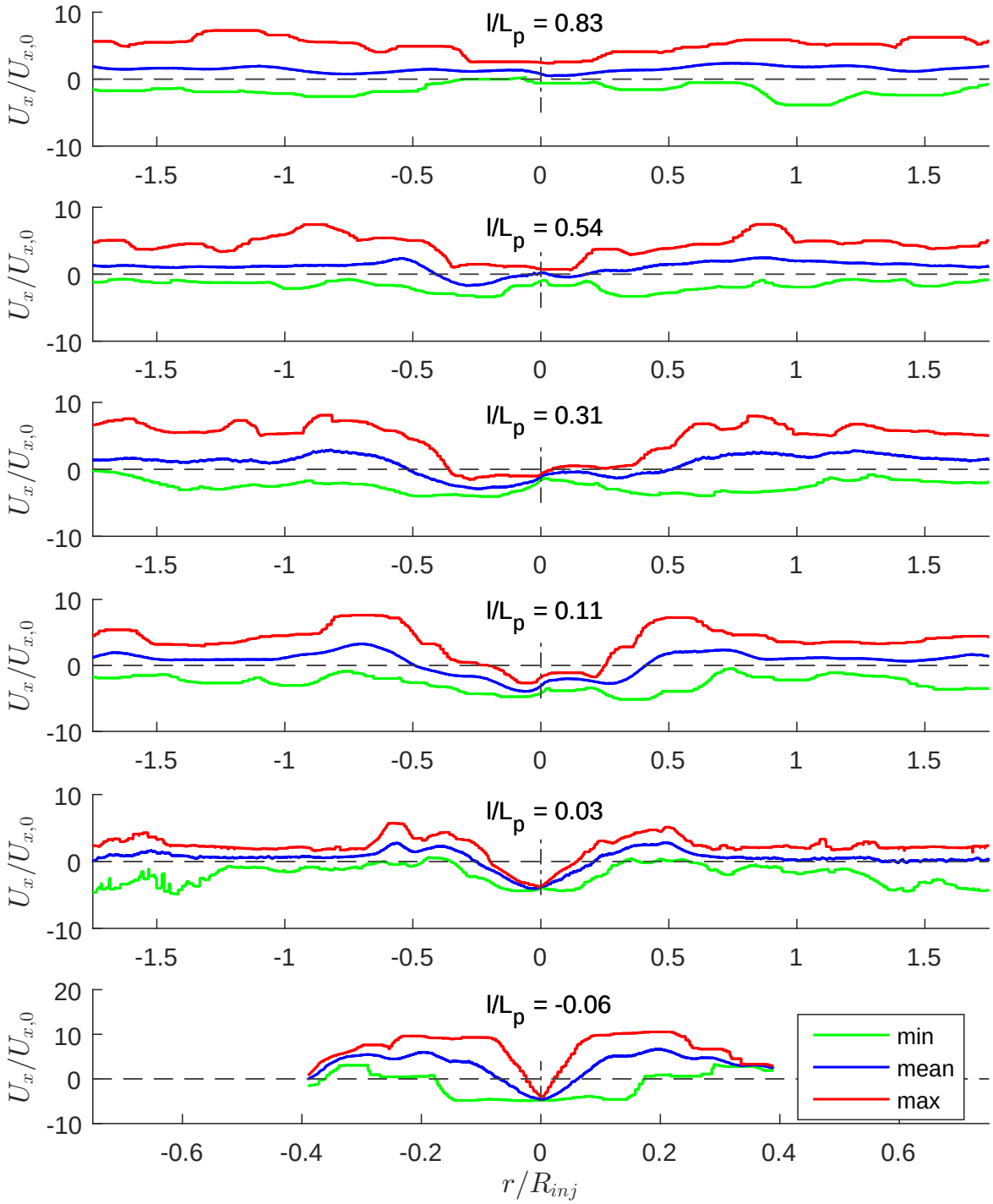

Figure 7.5 – Time-averaged axial velocities, U_x, normalised by the mean axial velocity at the injectors outlet section, with respect to the radius, r, normalised by the outer injector outlet radius, R_{inj}, at several axial normalised coordinates, $^{l}/_{L_p}$.

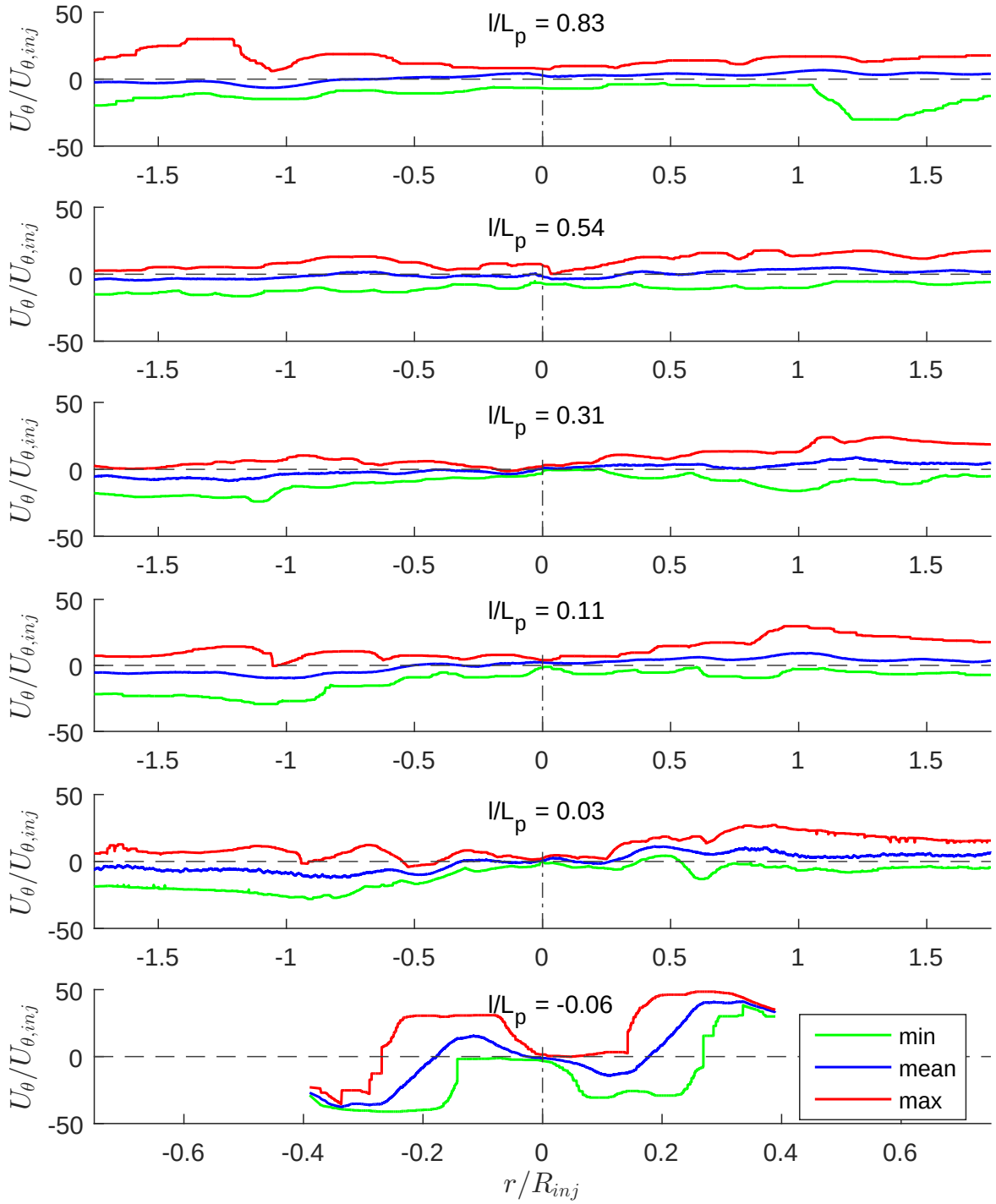

Figure 7.6 – Time-averaged azimuthal velocities, U_θ, normalised by the mean azimuthal velocity inside the inner injector, with respect to the radius, r, normalised by the outer injector outlet radius, R_{inj}, at several axial normalised coordinates, $^{l}/_{L_p}$.

mean value curves are anti-symmetrical as expected because of the swirling injectors. Inside the inner injector, at ${}^{l}/_{L_p} = -0.06$, mean azimuthal velocity goes through negative and positive peaks for $\left|{}^{r}/_{R_{inj}}\right| = 0.1$ and $\left|{}^{r}/_{R_{inj}}\right| = 0.3$. These pairs of peaks are signatures of a counter-swirl motion. Outside the injectors, the velocity profiles flatten and the radial peak-to-peak distances raise.

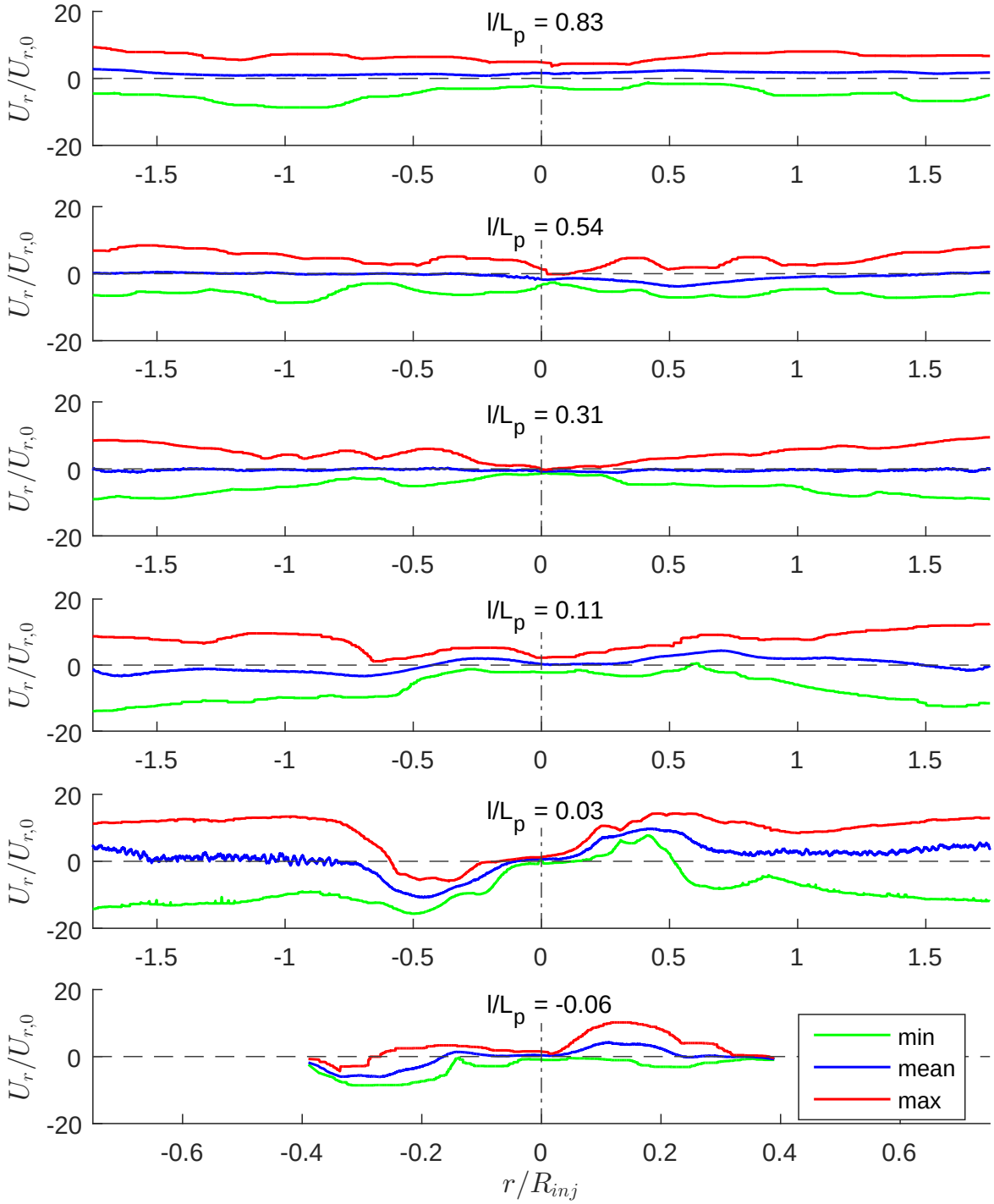

Figure 7.7 – Time-averaged radial velocities, U_r, normalised by the mean radial velocity at the injectors outlet section, with respect to the radius, r, normalised by the outer injector outlet radius, R_{inj}, at several axial normalised coordinates, ${}^{l}/_{L_p}$.

Figure 7.7 displays radial profiles of normalised radial velocities, ${}^{U_r}/_{U_{r,0}}$. Mean radial velocities at positions from ${}^{l}/_{L_p} = -0.06$ to ${}^{l}/_{L_p} = 0.11$ are anti-symmetrical. That witnesses

the divergence of the stream flowing out of the injectors; that divergence is due to the swirling motion and burner section enlargement.

Moreover, local turbulent velocity fluctuations where post-processed as:

$$u_i'(\vec{x}) = \sqrt{\langle \tilde{U}_i^2(\vec{x}) \rangle - \langle \tilde{U}_i(\vec{x}) \rangle^2} \tag{7.5}$$

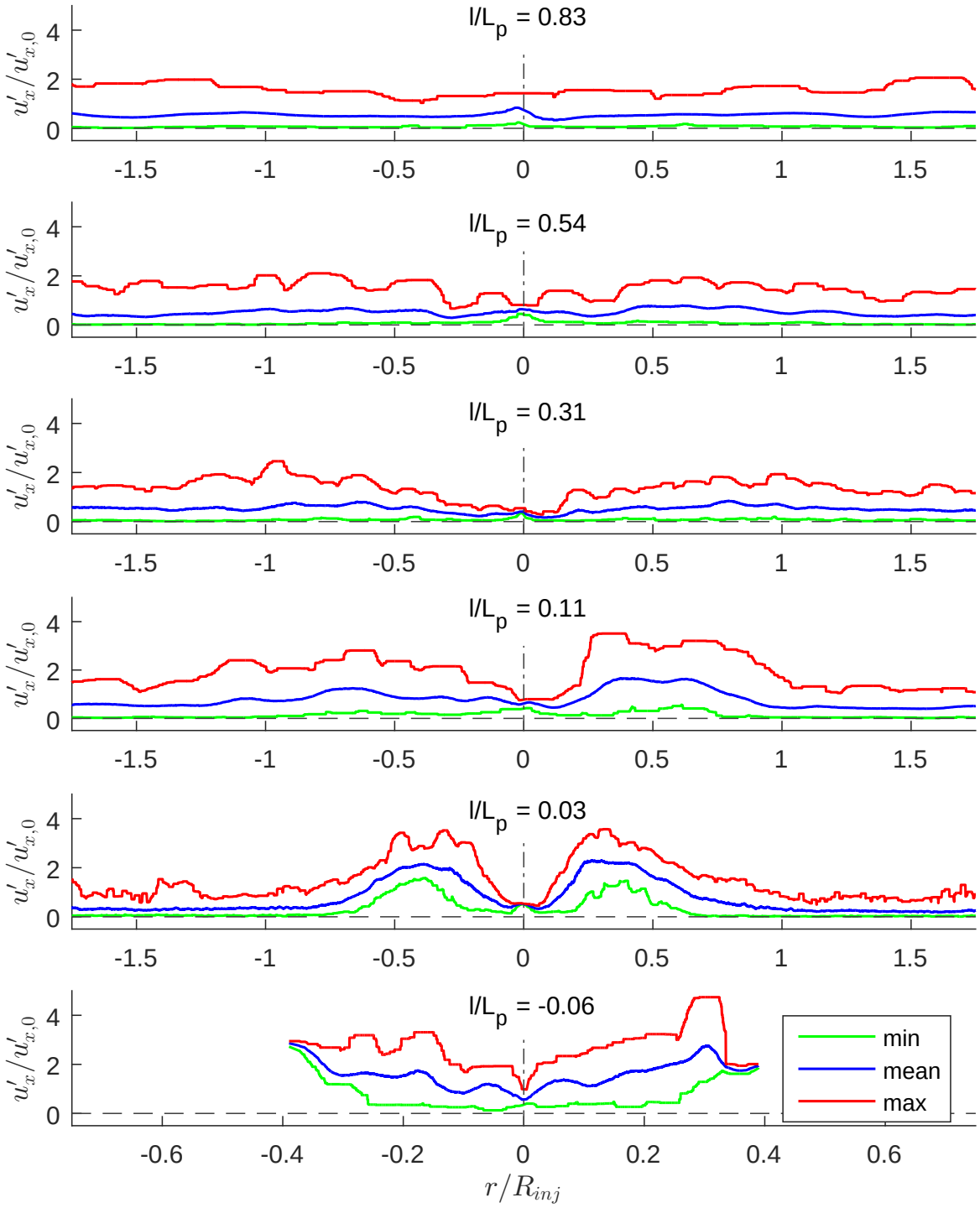

Figure 7.8 – Time-averaged axial turbulent velocities, u_x', normalised by the mean axial turbulent velocity at the injectors outlet section, with respect to the radius, r, normalised by the outer injector outlet radius, R_{inj}, at several axial normalised coordinates, $^{l}/_{L_p}$.

Radial profiles of axial turbulent velocity, u'_x, normalised by its mean value at the injectors outlet section, $u'_{x,0}$, are shown in Figure 7.8. Inside the inner injector, the mean profile of ${}^{u'_x}/_{u'_{x,0}}$ goes through a minimum at the center, and increases radially. That trend is consistent with the presence of an axial backflow discussed above. At the injectors outlet, ${}^{u'_x}/_{u'_{x,0}}$ reaches a peak on a circle at $\left|{}^{r}/_{R_{inj}}\right| = 0.4$, then stabilises at a lower level starting from $\left|{}^{r}/_{R_{inj}}\right| = 0.75$. The peak is due to the section enlargement at the outlet of the injectors. That circular peak widens and flattens at ${}^{l}/_{L_p} = 0.11$, and becomes progressively jammed further downstream. At ${}^{l}/_{L_p} = 0.83$, axial turbulent velocity profiles are almost flat, but their maximal value remains close to $2u'_{x,0}$. Radial profiles of normalised azimuthal and radial turbulent velocities, respectively shown in Figure 7.9 and Figure 7.10, are similar to axial turbulent profiles.

In addition, in order to evaluate the time-averaged global velocity magnitude along the flame tube, the mean velocity norm, U, was computed of the form:

$$U = \langle\sqrt{U_x^2 + U_y^2 + U_z^2}\rangle \tag{7.6}$$

As shown in Figure 7.11, from the inner injector to the air feed 2 section, U greatly decreases, due to the flame tube section enlargement. That decrease is beneficial for flame stabilisation. An increase of mean velocity is then observed for ${}^{l}/_{L_p} > 0.8$, which is probably due to thermal expansion resulting from combustion.

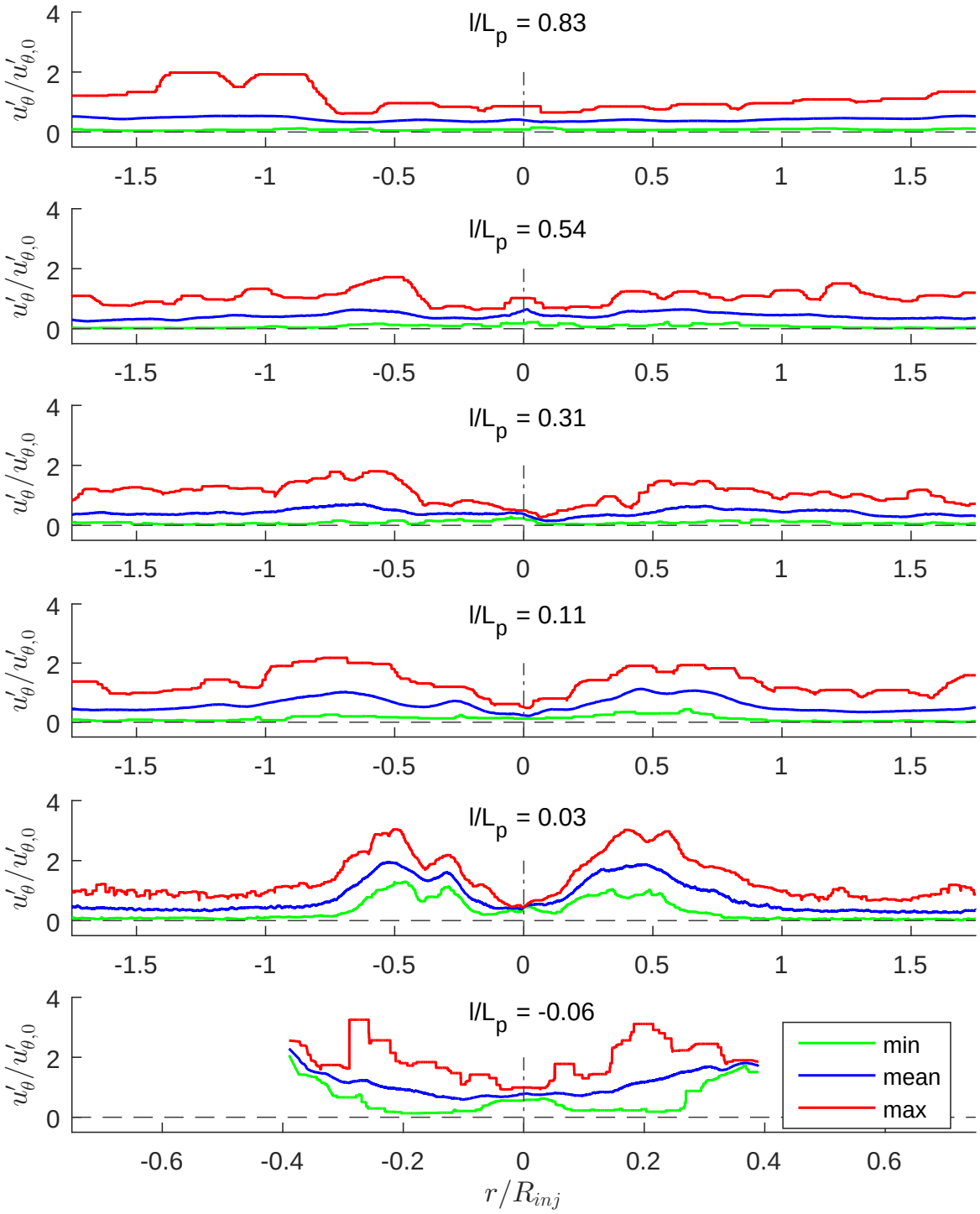

Figure 7.9 – Time-averaged azimuthal turbulent velocities, u'_θ, normalised by the mean azimuthal turbulent velocity at the injectors outlet section, with respect to the radius, r, normalised by the outer injector outlet radius, R_{inj}, at several axial normalised coordinates, $^{l}/_{L_p}$.

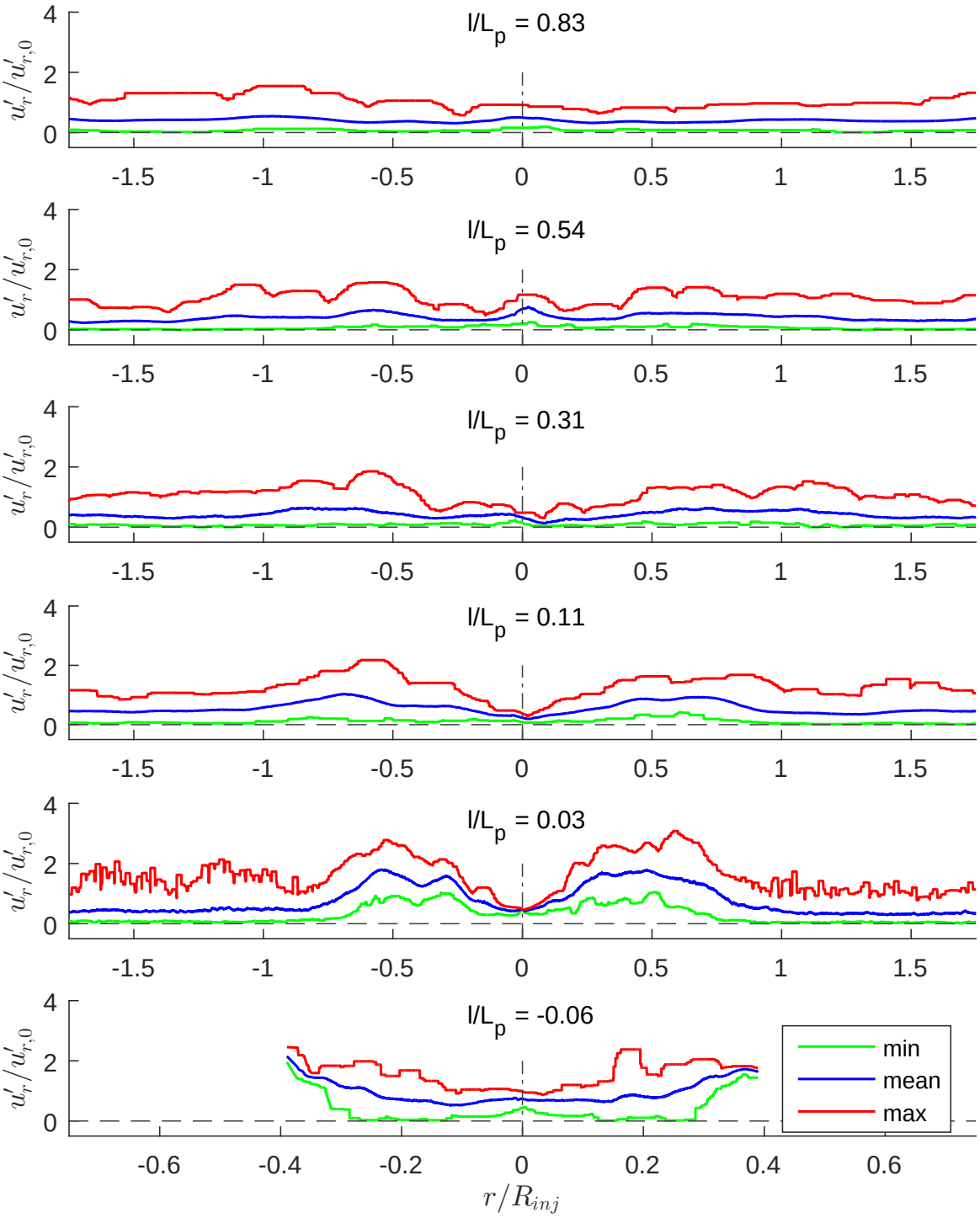

Figure 7.10 – Time-averaged radial turbulent velocities, u'_r, normalised by the mean radial turbulent velocity at the injectors outlet section, with respect to the radius, r, normalised by the outer injector outlet radius, R_{inj}, at several axial normalised coordinates, $^{l}/_{L_p}$.

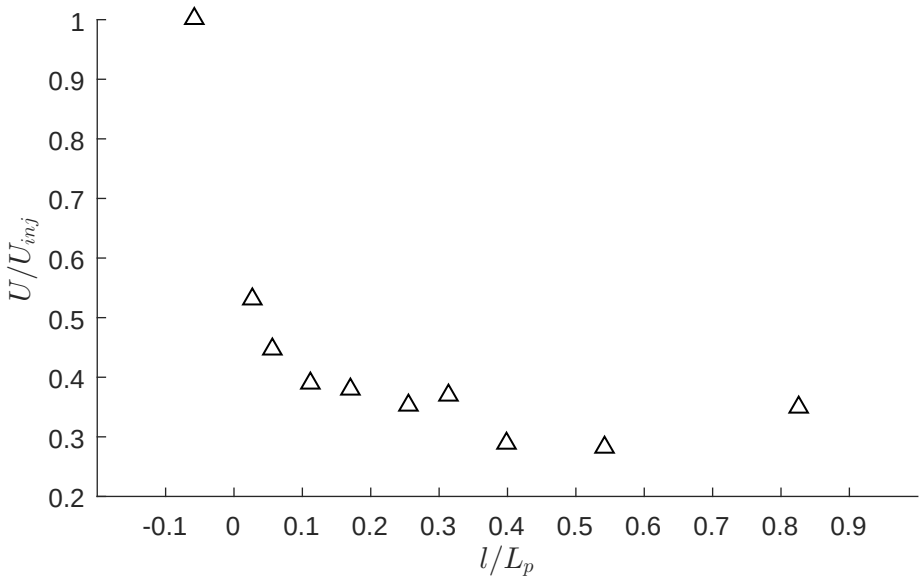

Figure 7.11 – Time-averaged mean velocity, U, normalised by mean velocity inside the injector, U_{inj}, along the normalised axial coordinate, $^{l}/_{L_p}$.

Reactive Zones Localisation

The structures of the reactive zones feature complex patterns of both anchored and lifted flames. According to Figure 7.12, the fuel oxidation reaction, equation 7.1, reaches its maximal rate in a small annulus, aerodynamically stabilised close to the fuel injection zone, and over a wider area, anchored at the air feed 1 height. These two zones are connected by a twisted reactive stream, which is most probably due to swirl and gas recirculation vortices. Another stream of fuel oxidation was observed, anchored at the air feed 2 hieght, transversely crossing the flame tube sector.

According to Figure 7.13, in the frame of the analysis of the CO/CO_2 equilibrium, equation

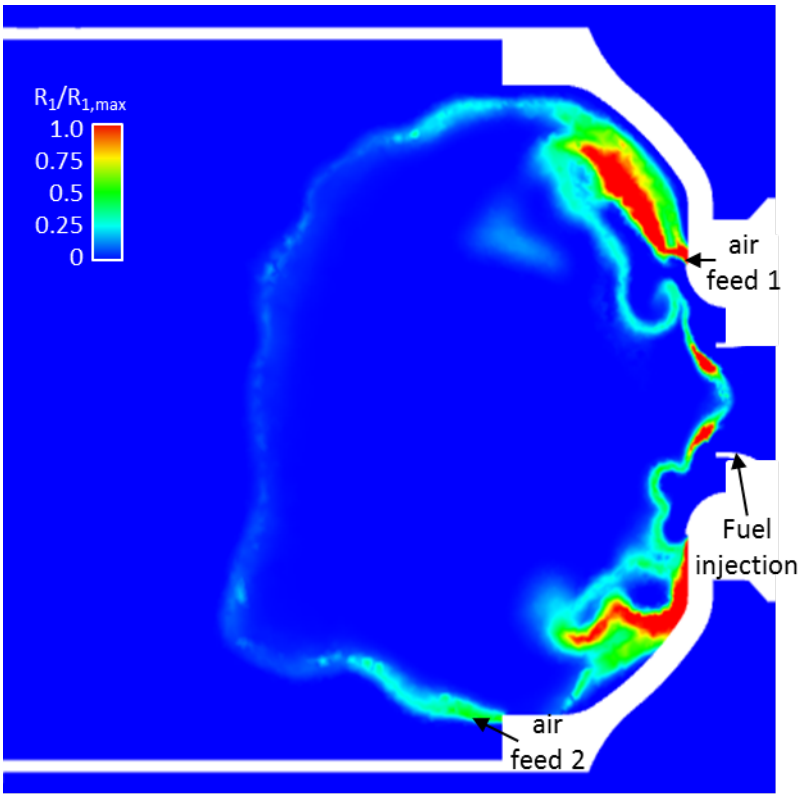

Figure 7.12 – 2D view of the time averaged combustion reaction rate, R_1, equation 7.3, normalised by its maximum value.

7.2, zones of CO_2 dissociation were observed inside the inner injector, downstream and around the flame region. This is probably due to the fact that the zone neighbouring the injectors is characterised by high temperatures and high mixture equivalence ratios, and in the zone further downstream, both temperatures and gases residence times are high.

Heat Release Field Analysis

The control of reactants mixedness is an important aspect in non-premixed combustion chambers design. Indeed, mixture heterogeneities are inherent to the fuel injection technology and mixture dilution through holes and multi-perforations all along the flame tube. Therefore, the study of the respective contributions of premixed and non-premixed flames to the global heat release rate was addressed. For that matter, a normalised Takeno flame index, G_{FO}, initially proposed by [46, 61], was applied to the time averaged solution of the preliminary

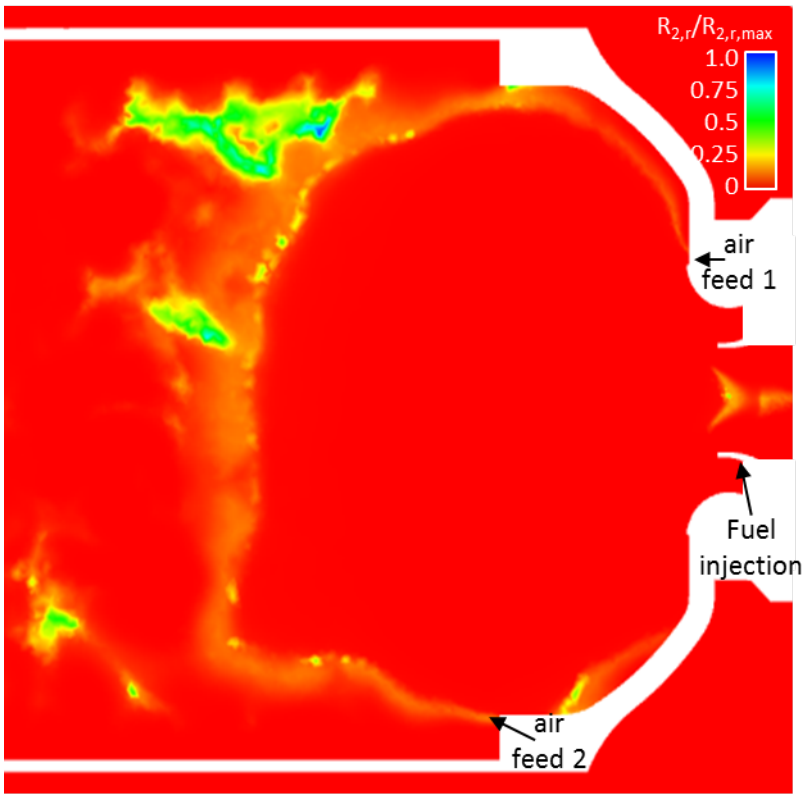

Figure 7.13 – 2D view of the time averaged CO_2 dissociation reaction rate, $R_{2,r}$, normalised by its maximum value.

LES computation :

$$G_{FO} = \frac{\nabla Y_F \times \nabla Y_{O_2}}{|\nabla Y_F \times \nabla Y_{O_2}|} \tag{7.7}$$

G_{FO} was set to zero where no chemical reaction rate was detected. Therefore, G_{FO} assumes the value of -1 for diffusion combustion, 0 if there is no combustion and 1 for premixed combustion. Figure 7.14 shows a central longitudinal cut plane of the flame tube sector, with a zoom-in over the flame region. The plane is coloured by $HRRD$, normalised by its maximum value in the combustion chamber. In addition to the central zones of high $HRRD$ inside the inner injector and close to the injectors outlets, another high $HRRD$ zone is visible downstream the air feed 2. This is consistent with what observed in Figure 7.12 and Figure 7.13. Contours of normalized Takeno flame index, superimposed to the normalised $HRRD$ field, highlight several zones of premixed and non-premixed combustion. According to Figure 7.14, a green contour inside the inner injector indicates the presence of an inner v-shaped non-premixed flame zone. That zone, in the vicinity of the fuel injection region, witnesses a backflow of hot burned gases and $CO - CO_2$ equilibrium reaction, equation 7.2, as it was observed in Figure 7.13. Another non-premixed flame zone, the outer non-premixed zone, is bounded by two green contours. The first contour is anchored at the air feed 1 height, and wraps around the pocket of burned gases. The second contour is anchored at the air feed 2 height. That region seems to constitute an interface where streams of unburned fuel or carbon monoxide join the air flows coming in through air feeds 1 and 2. Concerning premixed combustion zones, a first region is located close to the inner injector walls, and it is bounded by the burned gases pocket and the blue contours anchored at the air feed 1 height. A second premixed combustion zone is anchored at the air feed 2 height and floats downstream the outer non-premixed zone. According to Figure 7.12 and Figure 7.13, that second premixed

zone is probably related to the $CO - CO_2$ equilibrium reaction.

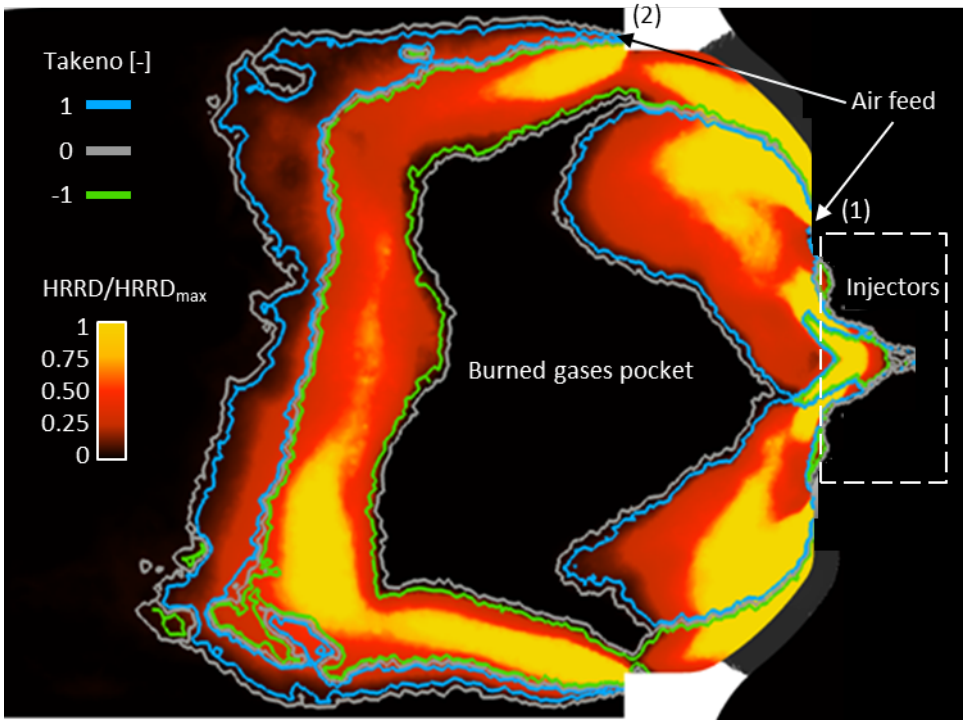

Figure 7.14 – 2D view of the time-averaged $HRRD$ field in the combustor flame tube, normalised by its maximum value, $HRRD_{max}$, with contours of normalised Takeno flame index.

Temperature Field Analysis

For a more detailed analysis of the unburned mixture heterogeneities, two indicators were simultaneously considered: the first being the mixture temperature as a function of the corresponding unburned gases fuel mixture fraction and the second being the normalised Takeno flame index, equation 7.7. The local fuel mass fraction of unburned gases, $Y_{ug,F}$, is equal to the local fuel mixture fraction, Z_F, defined by:

$$Z_F = Z_C + Z_H \tag{7.8}$$

$$Z_C = M_C \sum_k \frac{n_k^C Y_k}{M_k} \tag{7.9}$$

$$Z_H = M_H \sum_k \frac{n_k^H Y_k}{M_k} \tag{7.10}$$

where n_k^C and n_k^H are the respective numbers of carbon and hydrogen atoms per molecule of the species k, M_k is the molecular mass of the species k, and Y_k is the species k mass fraction.

Figure 7.15 shows a 2D cut plane along the flame tube axis, coloured by mixture temperature, T, normalised by the mean turbine inlet temperature, T_4. According to Figure 7.15, inside the injector, the conical zone of non-premixed combustion is characterised by a higher temperature in comparison to its neighbouring area burning as a premixed flame. The large brush of non-premixed flame anchored at the air feed 1 height also has a high temperature. The outer premixed combustion zone is rather characterised by a low temperature and seems to correspond to a lean-burning premixed flame zone. That is in agreement with what was observed in that region by the analysis of $HRRD$ and reaction rates fields, Figure 7.12 and Figure 7.13. The link between variable unmixedness and temperature was further assessed by drawing scatter plots of T/T_4 as a function of Z_F, Figure 7.16, at the planar sections designated in Figure 7.4.

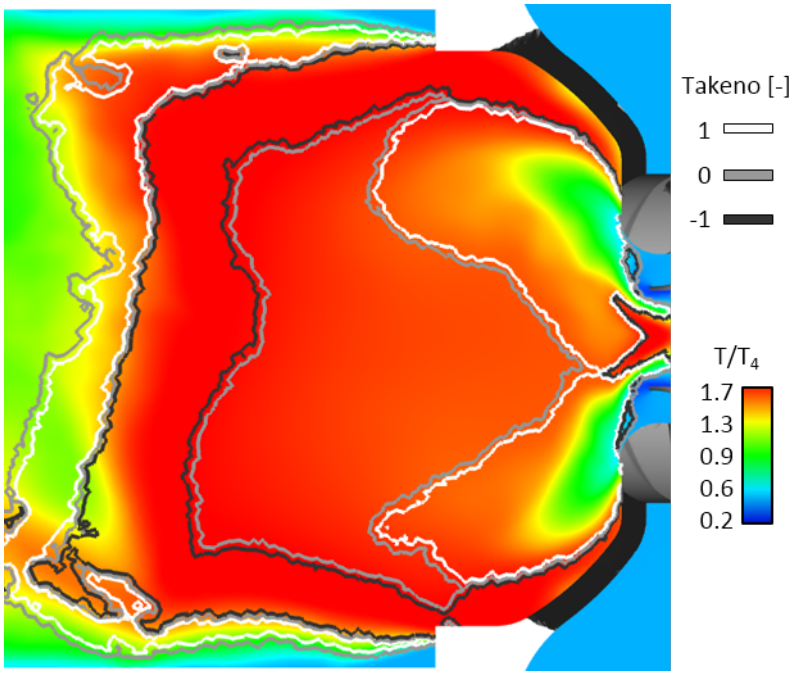

Figure 7.15 – 2D view of the mixture temperature field in the combustor flame tube, normalised by T_4, and Takeno flame index contours.

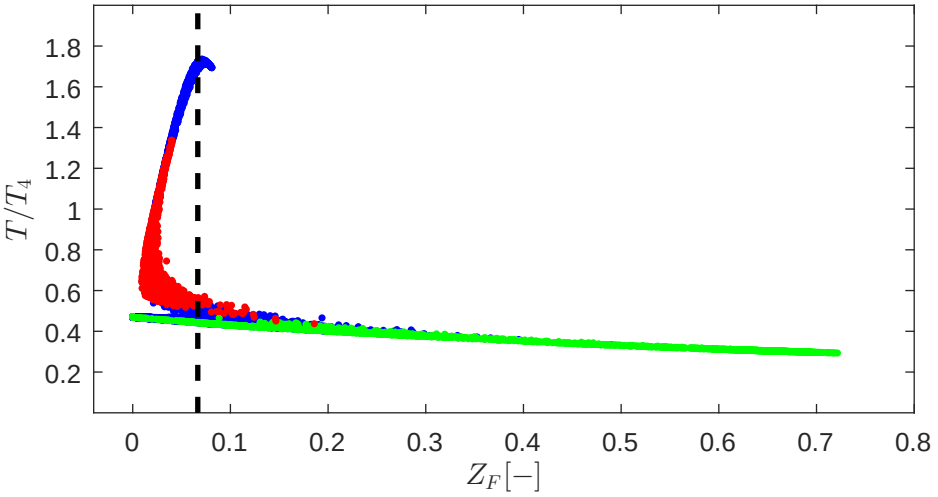

(a) Scatter plot at section $^{l}/_{L_p} = -0.06$.

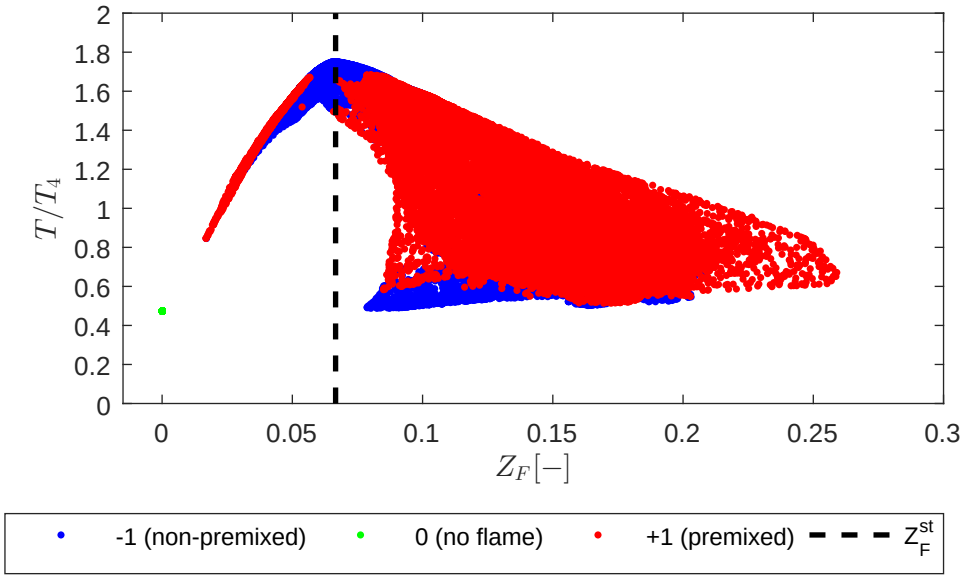

(b) Scatter plot at section $^{l}/_{L_p} = 0.03$.

Figure 7.16

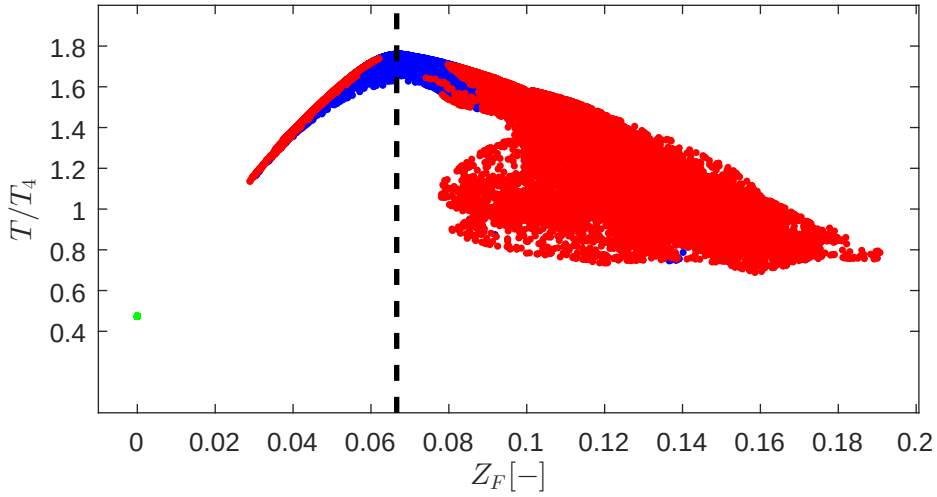

(c) Scatter plot at section $^{l}/_{L_p} = 0.11$.

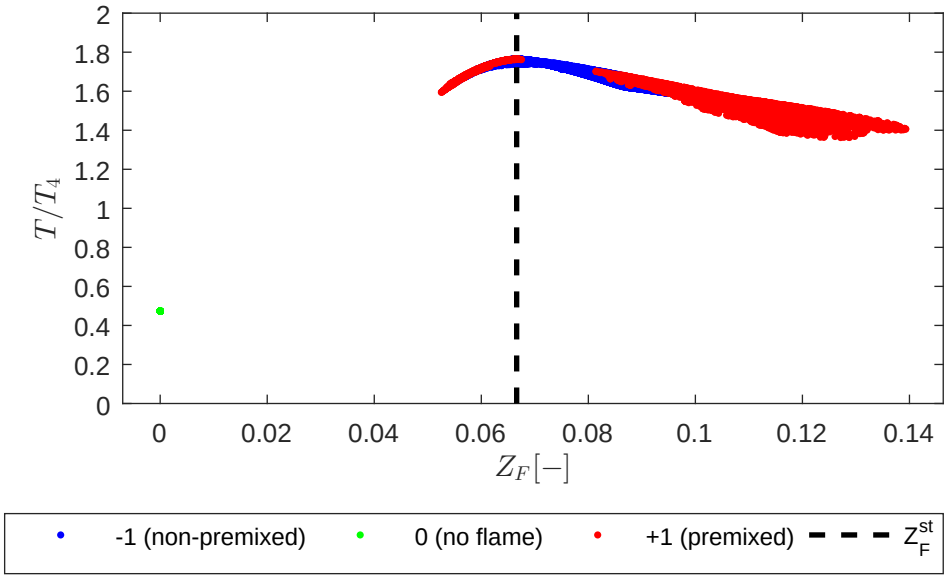

(d) Scatter plot at section $^{l}/_{L_p} = 0.31$.

Figure 7.16

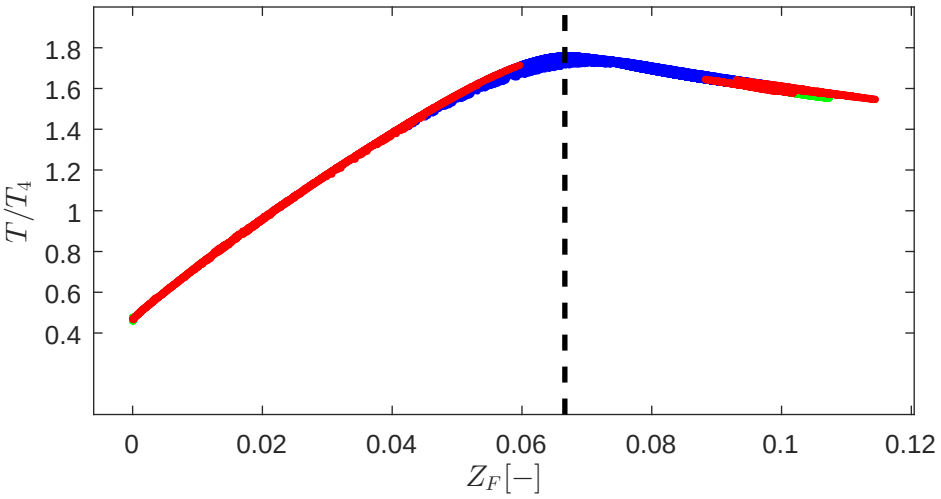

(e) Scatter plot at section $^{l}/_{L_p} = 0.54$.

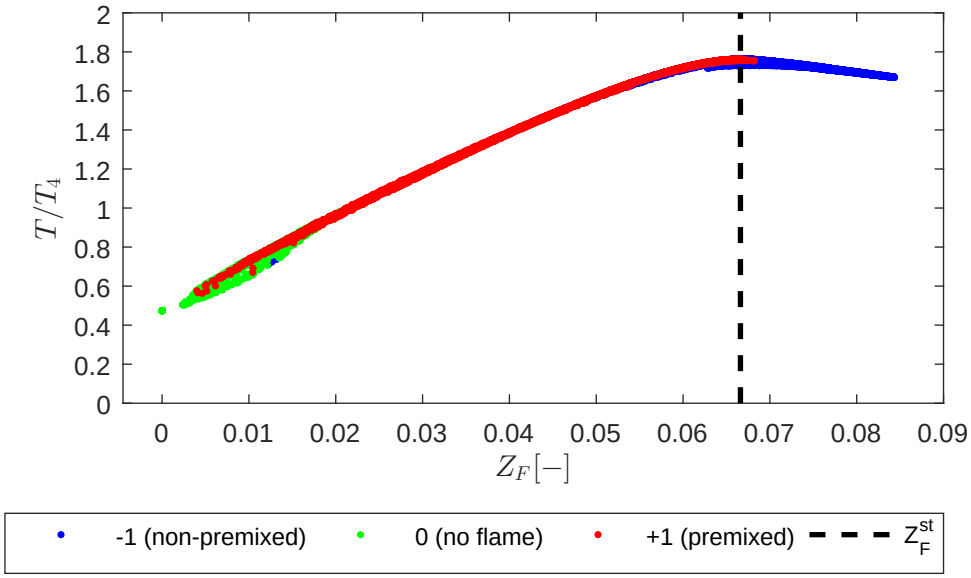

(f) Scatter plot at section $^{l}/_{L_p} = 0.83$.

Figure 7.16 – Scatter plots of mixture temperature normalised by the mean turbine inlet temperature, T_4, with respect to the fuel mixture fraction, and coloured depending on the normalised Takeno flame index: dashed line indicates the stoichiometric value of Z_F, red dots indicate points of premixed combustion, blue dots indicate points of non-premixed combustion and green dots indicate points with no combustion.

On the first scatter plot, Figure 7.16a, slightly upstream the flame tube inlet, blue spots indicate non-premixed combustion at the temperature peak, centred at stoichiometry. However, a few blue spots also appear at lower temperatures, spread on a broader range of Z_F. The cold diffusion oxidation would be due to oxidation of fresh gases by burned gases. In any case, that region is not a standard diffusion flame region. Red spots of premixed combustion spread on a slope of lean fuel mixture fraction and reach temperatures colder than T_4, as noticed in Figure 7.15. Many green points of fresh gas can be observed, mostly on the fuel rich side; this is expected as the plane is located in the region where the fuel is injected. Cold diffusion oxidation is induced by an axial backflow of hot burned gas that reaches the zone of fuel injection. Indeed, as represented in Figure 7.17, Central Recirculation Zones (CRZ), favoured by section enlargement and swirl vortices, common in gas turbine burners[1], were identified. These CRZs entrain peripheral burned gas towards the axis of the flame tube sector, where it flows towards the injectors. That counter-streamwise flow of burned gases would trigger the oxidation of some of the fresh gases available at the center of the inner injector.

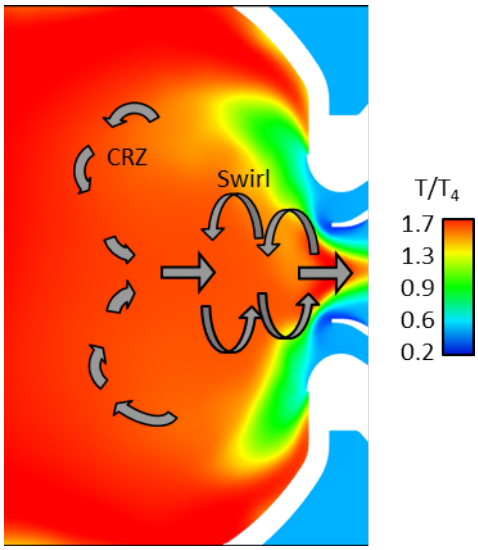

Figure 7.17 – 2D view of the mixture temperature field in the combustor flame tube, normalised by T_4, with a schematic representation of the flow streamlines. A CRZ is generated by the section enlargement in conjunction with a swirl vortex. In addition, swirl creates a depression zone draining burned gas counter-streamwise along the flame tube sector axis.

On the next two plots, Figure 7.16b and Figure 7.16c, premixed burning mixture is mostly rich, due to the proximity of the fuel injector to the planes located at $^{l}/_{L_p} = 0.03$ and at $^{l}/_{L_p} = 0.011$, and a wide range of Z_F is covered, which is due to the mixing of swirling air and fuel streams. A line of lean to near stoichiometric premixed combustion points is also observed. Non-premixed combustion can be observed within a narrow range around stoichiometry, at maximal temperature. In addition, diffusion points appear above stoichiometry at temperatures around $0.6T_4$, especially on Figure 7.16b. Further downstream in the flame tube, Figure 7.16d, most of combustion, either premixed and non-premixed, appears to occur close to stoichiometry and above it, at temperatures between $1.4T_4$ and $1.8T_4$. However, given the fact that no reactants are left at that section, even though G_{FO} indicates the presence of premixed combsution, the observed phenomenon is probably related to post-flame chemistry, and it does not match with any standard flame structure. At $^{l}/_{L_p} = 0.54$, most of premixed combustion is lean, Figure 7.16e, and at $^{l}/_{L_p} = 0.83$, Figure 7.16f, points of

[1]The presence of a CRZ of hot burned gases allows to stabilise the flame.

premixed combustion are observed together with points of diffusion combustion, ranging from stoichiometry to slightly rich equivalence ratios. This pattern is due to progressive dilution and mixing of reactants streaming towards the flame tube elbow along with a persistent trailing peripheral non-premixed stream tangent to the air jet coming in from air feed 2.

Conclusion

According to the preliminary analysis, the herein studied swirl combustor sector is characterized by complex counter-swirl, recirculation zones and backflow streams. These features, basically three-dimensional, cannot be accounted for in a 0D system modelling approach. However, a 0D model for system simulation of combustors should be capable of computing the right order of magnitude, at least, for mean flow velocity and turbulent velocity fluctuations whithin the flame tube. Furthermore, the 0D model should also account for the effects of main geometrical featuresas well as the influence of thermal expansion on mean and turbulent velocity fields.
Moreover, the present combustor sector hosts roughly as much premixed as non-premixed combustion, as well as anchored and lifted flames. Therefore, the formalism presented in section 5.2 has to be modified in order to handle the multiple flame types and the combustion scenario encountered in the flame tube sector, by preserving space-dependent patterns.

7.2 Determination of Flame and Turbulence Characteristics

Once identified the zones of premixed and non-premixed flames in the presently studied combustor sector, section 7.1.2, the next objective was to evaluate the balance between premixed and non-premixed combustion in the flame tube, and to characterise premixed flames from the perspective of a FSD paradigm, section . Therefore, a filter function based on G_{FO} was used and mathematical formulations, detailed below, were implemented in the AVBP source code, in order to extract the relevant information. Time-averaged and 3D space averaged post-processing were performed and, in addition, in order to preserve the complexity and the space-dependency of the flame structure, the plane-by-plane post-processing presented in section 7.1.2 was extended to include flame characteristics, as well.

7.2.1 Flame Type Identification

With the aim of applying the formalism presented in **part III** to a real rotorcraft combustor case, the progress variable definition should take into account the unburned mixture heterogeneities inherent to the injection technology and air dilution through the multi-perforations all along the flame tube. Accordingly, for this purpose, the oxygen burning process was selected for the chemical reactions progress evaluation. All the following mathematical developments are space and time dependent. For that matter, as a first step, the fuel mixture fraction, Z_F, previously defined in equation 7.8, was implemented in the source code and the oxygen mass fraction in unburned gas, Y_{ug,O_2}, was reconstructed by considering atomic conservation, as in the following expression:

$$Y_{ug,O_2} = Z_{O_2} = M_O \sum_k \frac{n_k^O Y_k}{M_k} \tag{7.11}$$

where n_k^O is the number of oxygen atoms per molecule of the species k, M_k is the molecular mass of the species k and Y_k is its mass fraction. In a second step, considering the fuel oxidation reaction, equation 7.1, the stoichiometric O_2 and CO mixture fractions, $Z^{st}_{O_2,1}$ and $Z^{st}_{CO,1}$, can be expressed of the form:

$$Z^{st}_{O_2,1} = 10\frac{M_{O_2}}{M_F} Z_F \tag{7.12}$$

$$Z^{st}_{CO,1} = 10\frac{M_{CO}}{M_F} Z_F \tag{7.13}$$

From the $CO-CO_2$ equilibrium reaction, equation 7.2, the stoichiometric O_2 mixture fraction $Z^{st}_{O_2,2}$ can be calculated as:

$$Z^{st}_{O_2,2} = \frac{1}{2}\frac{M_{O_2}}{M_{CO}} Z^{st}_{CO,1} = 5\frac{M_{O_2}}{M_F} Z_F \tag{7.14}$$

The above detailed developments allowed the deduction of the O_2 mass fraction in burned gases depending on the values of Z_{O_2}, $Z^{st}_{O_2,1}$ and $Z^{st}_{O_2,2}$ by:

$$Y_{bg,O_2} = \begin{cases} 0 & \text{if } Z_{O_2} \leq Z^{st}_{O_2,1} + Z^{st}_{O_2,2} \\ Z_{O_2} - Z^{st}_{O_2,1} - Z^{st}_{O_2,2} & \text{if } Z_{O_2} > Z^{st}_{O_2,1} + Z^{st}_{O_2,2} \end{cases}$$

Instantaneous oxygen burning progress was monitored at each computational node through the progress variable $\tilde{c}$, defined by the following formulation:

$$\tilde{c} = \frac{Y_{ug,O_2} - Y_{O_2}}{Y_{ug,O_2} - Y_{bg,O_2}} \tag{7.15}$$

In combination with the progress variable field, $\tilde{c}$, the Takeno flame index, G_{FO}, equation 7.7, was introduced into the computational routines, in order to separately characterise premixed and non-premixed flames. That characterisation concerns flame surface and reactants consumption rate. For this matter, a Heaviside function, H, was applied to the index G_{FO}, giving:

$$H \equiv H(G_{FO}) = \begin{cases} 0 & \text{if } G_{FO} < 1 \\ 1 & \text{if } G_{FO} = 1 \end{cases}$$

This allows to discriminate premixed flames from non-premixed flames.

7.2.2 Oxygen Burning Rate, and Flame Surface and Speed

The total oxygen burning rate, $\dot{\Omega}_{O_2}$, can be expressed by using equations 7.3 and 7.4, and the oxygen stoichiometric coefficients in the chemical reactions, equations 7.1 and 7.2, which gives:

$$\dot{\Omega}_{O_2} = -\int_V \dot{\omega}_{O_2} dV \tag{7.16}$$

with:

$$\dot{\omega}_{O_2} = M_{O_2} \left(10R_1 + 0.5R_2\right) \tag{7.17}$$

In the herein studied combustor, $\dot{\Omega}_{O_2}$, can be split into a rate consumed by premixed combustion, $\dot{\Omega}^p_{O_2}$ and another rate consumed by non-premixed flames, $\dot{\Omega}^n_{O_2}$, according to:

$$\dot{\Omega}_{O_2} = \dot{\Omega}^p_{O_2} + \dot{\Omega}^n_{O_2} \tag{7.18}$$

where:

$$\dot{\Omega}^p_{O_2} = -\int_V H\dot{\omega}_{O_2} dV \tag{7.19}$$

The global premixed O_2 consumption rate, $\dot{\Omega}^p_{O_2}$, can be expressed by means of a CFM paradigm reaction rate as:

$$\dot{\Omega}^p_{O_2} = \rho_{ug} S_L^{eff}\Big|^p \left(Y_{ug,O_2} - Y_{bg,O_2}\right)^p A_T^p \tag{7.20}$$

where ρ_{ug} is the UG density and $S_L^{eff}\Big|^p$ is the effective laminar flame speed in the premixed flame region. The total premixed flame surface, A^p_T, is written as:

$$A^p_T = \int_V H \left|\nabla \tilde{c}\right| \Xi_{sgs} dV \tag{7.21}$$

where Ξ_{sgs} is the sgs wrinkling efficiency function [33].
In addition to total flame surface assessment, local distributions of premixed and non-premixed flames were traced to depict a flame-type pattern, and eventually put it in perspective with the flow velocity profiles analysed in section 7.1.2. For each given plane j, the time-averaged resolved flame surface, $J_{\langle A_R \rangle}$, was calculated as:

$$J_{\langle A_R \rangle} = \sum_{l=1}^{N_j} \langle |\nabla \tilde{c}_l| \rangle_l dV_l \tag{7.22}$$

where N_j is the number of nodes on the plane j, $\langle |\nabla \tilde{c}| \rangle_n$ is the time-averaged resolved flame surface density at the node l and dV_l is its volume. The relative shares of premixed and

non-premixed resolved flame surfaces, respectively $J_{\langle A_R\rangle^p}$ and $J_{\langle A_R\rangle^n}$, were calculated by applying the filter function H, previously defined in section 7.2.1, by means of:

$$J_{\langle A_R\rangle} = J_{\langle A_R\rangle^p} + J_{\langle A_R\rangle^n} \tag{7.23}$$

$$J_{\langle A_R\rangle^p} = \sum_{l=1}^{N_j} \langle H_l\rangle \langle |\nabla \tilde{c}_l|\rangle_l dV_l \tag{7.24}$$

Concerning the laminar flame speed, the product of the UG mixture density, ρ_{ug}, by laminar flame speed conditioned to premixed flame regions, $S_L^{eff}\Big|^p$, was expressed of the form:

$$\rho_{ug} S_L^{eff}\Big|^p = \frac{\int_V H \rho_{ug} S_L^{eff} \left(Y_{ug,O_2} - Y_{bg,O_2}\right) |\nabla \tilde{c}| \, \Xi_{sgs} dV}{\int_V H \left(Y_{ug,O_2} - Y_{bg,O_2}\right) |\nabla \tilde{c}| \, \Xi_{sgs} dV} \tag{7.25}$$

Finally, the O_2 mass fraction participating to combustion, conditioned to premixed flame regions, was computed as:

$$\left(Y_{ug,O_2} - Y_{bg,O_2}\right)^p = \frac{\int_V H \left(Y_{ug,O_2} - Y_{bg,O_2}\right) |\nabla \tilde{c}| \, \Xi_{sgs} dV}{\int_V H \, |\nabla \tilde{c}| \, \Xi_{sgs} dV} \tag{7.26}$$

7.2.3 Turbulent Velocity Fluctuations

At every plane j, resolved turbulent velocity fluctuations are evaluated on the whole plane, inside the unburned gas regions, as well as in the premixed and non-premixed flame regions by using the following expressions:

$$J_{u'_{ug,i}} = \frac{1}{\sum_{l=1}^{N_j} \left(1 - \langle \tilde{c}_l \rangle\right)} \sum_{l=1}^{N_j} \left(1 - \langle \tilde{c}_l \rangle\right) \sqrt{\langle \tilde{U}_{i,l}^2 \rangle - \langle \tilde{U}_{i,l} \rangle^2} dV_l \tag{7.27}$$

$$J_{u'_{flame,i}} = \frac{1}{J_{\langle A_R\rangle}} \sum_{l=1}^{N_j} |\nabla \langle \tilde{c}_l \rangle| \sqrt{\langle \tilde{U}_{i,l}^2 \rangle - \langle \tilde{U}_{i,l} \rangle^2} dV_l \tag{7.28}$$

$$J_{u'^p_{flame,i}} = \frac{1}{J_{\langle A_R\rangle^p}} \sum_{l=1}^{N_j} \langle H_l \rangle |\nabla \langle \tilde{c}_l \rangle| \sqrt{\langle \tilde{U}_{i,l}^2 \rangle - \langle \tilde{U}_{i,l} \rangle^2} dV_l \tag{7.29}$$

$$J_{u'^n_{flame,i}} = \frac{1}{J_{\langle A_R\rangle^n}} \sum_{l=1}^{N_j} \left(1 - \langle H_l \rangle\right) |\nabla \langle \tilde{c}_l \rangle| \sqrt{\langle \tilde{U}_{i,l}^2 \rangle - \langle \tilde{U}_{i,l} \rangle^2} dV_l \tag{7.30}$$

where $J_{u'_{ug,i}}$ is the fresh gas turbulent velocity, $J_{u'_{flame,i}}$ is the turbulent velocity in the flame, and $J_{u'^p_{flame,i}}$ and $J_{u'^n_{flame,i}}$ are the turbulent velocities in the premixed and non-premixed parts of the flame, respectively; the index i indicates the component of the variable along the axis i. As global flame wrinkling is targeted, global turbulent velocity fluctuations were calculated for both flames and unburned gas zone, under the Homogeneous Isotropic Turbulence (HIT) assumption, from the turbulent kinetic energy, k, according to the following equations:

$$k_m = \frac{1}{2} \sum_i J_{u'_{m,i}}^2 \tag{7.31}$$

$$u'_m = u'_{m,HIT} = \sqrt{\frac{2k_m}{3}} \tag{7.32}$$

where the subscript m is a general notation to refer to ug, $flame$, $premixed\ flame$ and $non-premixed\ flame$, and $u'_{m,HIT}$ is the equivalent turbulent velocity fluctuation under the assumption of HIT.

7.3 Computation and Results

After the implementation of the equations detailed in section 7.2, starting from a stable computation solution, a simulation of the combustor sector was launched, with the setup described in section 7.1.1, for computing a few milliseconds of physical time. Flame and turbulence characteristics where then post-processed according to the mathematical formulations presented in section 7.2.

7.3.1 Oxygen Burning Rate, Flame Surface and Speed

Oxygen Burning Rate

The share of space-averaged premixed flame oxygen burning rate, Figure 7.18, fluctuates between 44% and 51 %, while the space and time-averaged oxygen burning rate is split into 49% of premixed combustion versus 51% of non-premixed combustion. These results confirm that premixed and non-premixed flames play equally important roles in terms of reactants consumption.

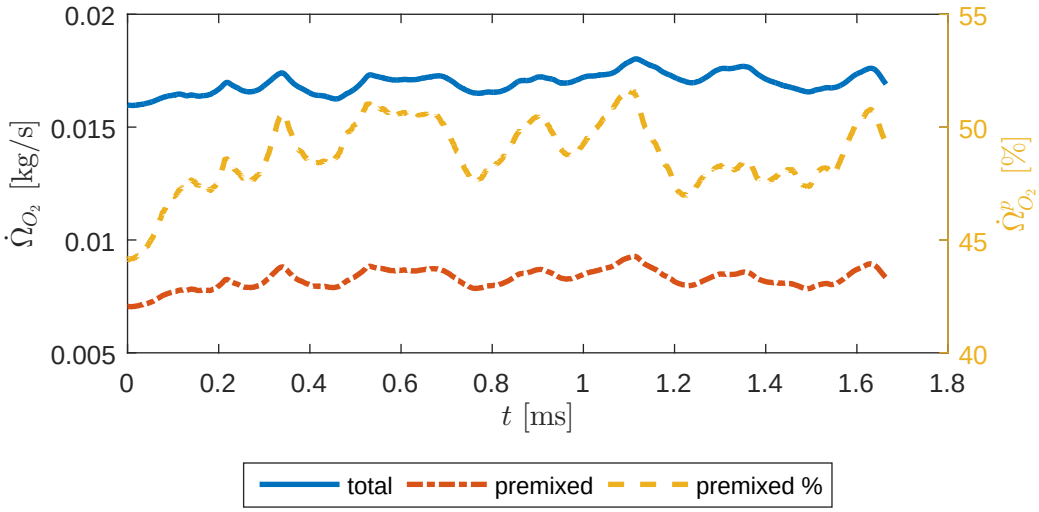

Figure 7.18 – Space-averaged total and premixed flame oxygen reaction rates: the total reaction rate is represented by the solid blue line, the premixed reaction rate is represented by the dashed and dotted red line, and the orange dashed line represents the percentage of oxygen reaction rate consumed by premixed combustion with respect to the total oxygen reaction rate.

Flame Surface

The shares of $\langle A_R \rangle^p$ and $\langle A_R \rangle^n$, and $\langle A_R \rangle$ are represented in Figure 7.19, with respect to the coordinate $^l/_{L_p}$. From the plane across the injectors to half flame penetration length, most of the resolved flame surface is associated to premixed combustion. However, the trend inverts downstream, where $\langle A_R \rangle$ is mostly linked to non-premixed combustion. The total resolved flame surface curve reaches its peak at the flame tube sector inlet and steeply decreases within the third of L_p, followed by a small peak at $^l/_{L_p} = 0.4$, probably due to the air mass flow rate injected at air feed 2, before annihilating. These quantitative observations are in agreement with the 2D view of $\langle A_R \rangle$, Figure 7.20, where most of the flame surface is located upstream the air feed 2 height, and a thin stream of flame surface can be observed at the air feed 2 height.

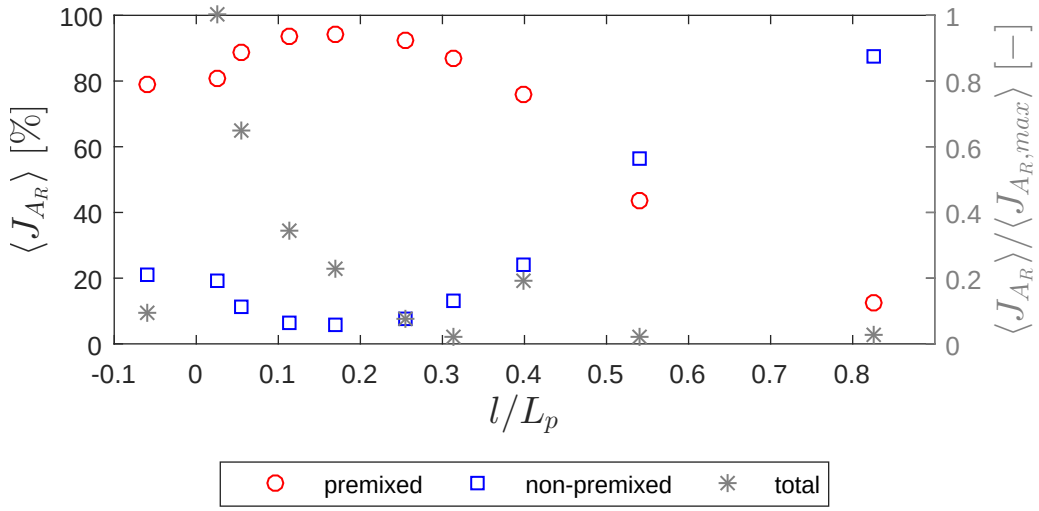

Figure 7.19 – Distribution of the time averaged resolved flame surface, $\langle J_{A_R} \rangle$, along the normalised axial coordinate, $^{l}/_{L_p}$: red circles and blue squares represent the respective shares of premixed and non-premixed flame surface, and the grey stars represent the total resolved flame surface computed at the given normalised axial positions.

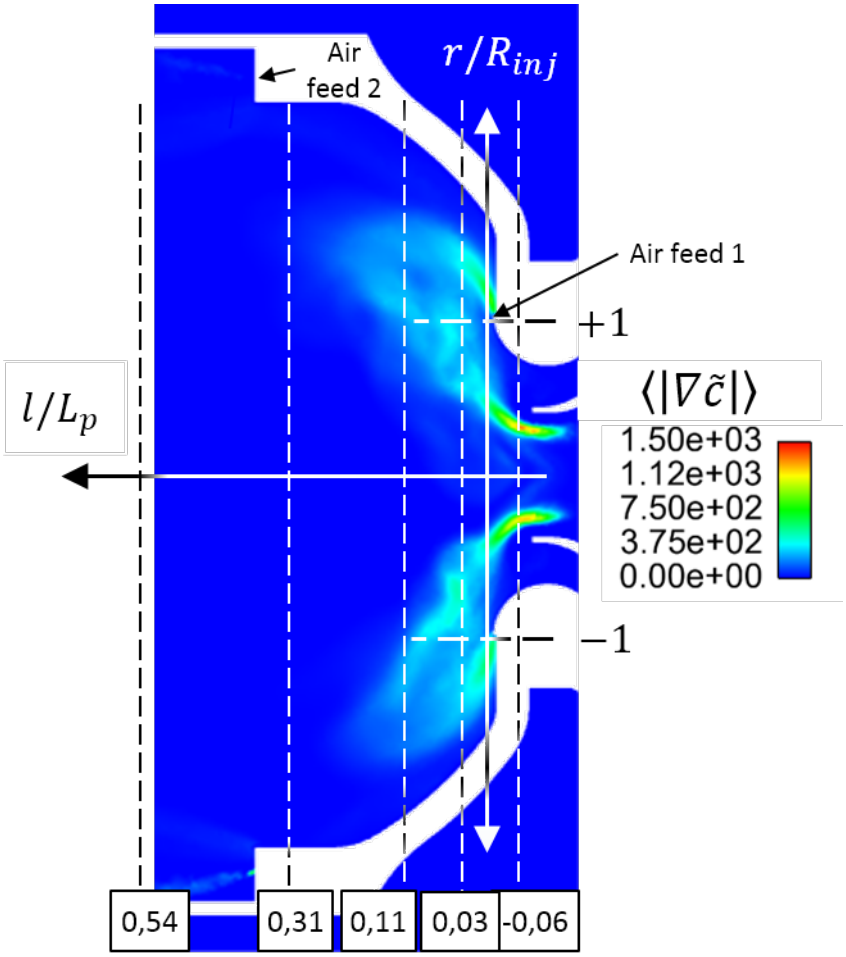

Figure 7.20 – 2D view of the time-averaged resolved flame surface density, $\langle |\nabla \tilde{c}| \rangle$.

Total turbulent flame surface, A_T, Figure 7.21, is associated to premixed combustion at 65 to 71%. That result is not exactly in line with the reaction rates balance shown in Figure 7.18. That is due to the fact that premixed and non-premixed flame structures are obviously different, and also because mixture heterogeneities in the flame tube induce spatial variations of the term $Y_{ug,O_2} - Y_{bg,O_2}$.

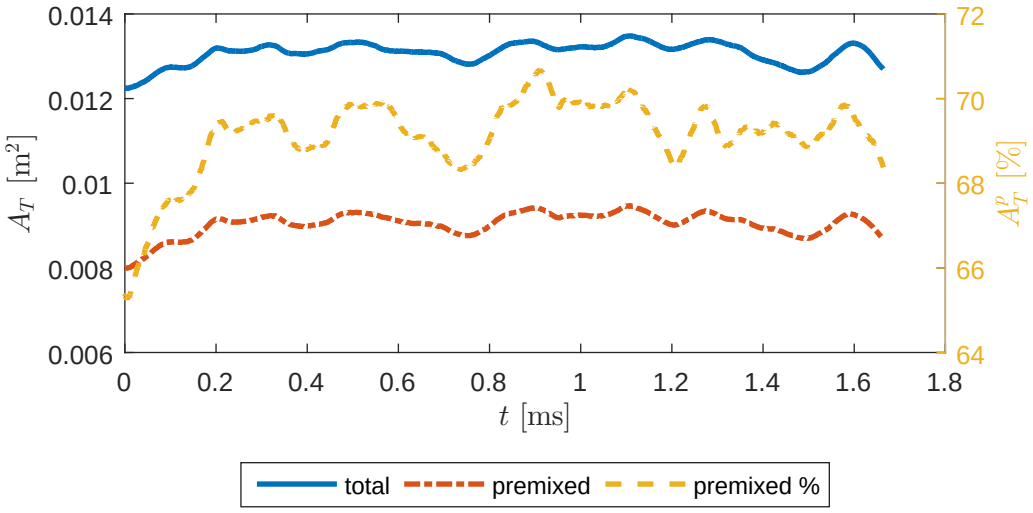

Figure 7.21 – Space-averaged turbulent flame surface, $A_T(t)$, and premixed turbulent flame surface, $A_T^p(t)$, and percentage of premixed turbulent flame surface with respect to total flame surface.

Flame Speed

Premixed laminar flame speed, Figure 7.22, fluctuates around an average value of 0.64 m/s. Unfortunately, that result was not easy to validate against results from the literature, since reactants temperature and FAER were highly heterogeneous in the flame tube sector. A more detailed post-processing, representing scatter plots of $S_L^{eff}\Big|^p$ as a function of local mixture density, temperature and equivalence ratio should be performed to fully validate this aspect. Nevertheless, the obtained $S_L^{eff}\Big|^p$ is a plausible order of magnitude for a kerosene surrogate and for the operating conditions of fresh gas temperatures and static pressures of the herein studied combustor, Figure 7.23.

7.3.2 Heat Release Rate

The $HRRD$ profiles with respect to the normalised radial coordinate of the flame tube sector, at the previously presented 2D planes, Figure 7.24, and along the axial normalised coordinate, Figure 7.4, show merely axisymmetrical patterns around the flame tube axis, and a fast decrease with the flame penetration length. The shares of non-premixed and premixed combustion in heat production vary depending on the axial position. These variations are synthesized in Figure 7.25, showing the percentages of $HRRD$ due to premixed and non-premixed combustions at several axial locations in the flame tube, together with the axial evolution of the total $HRRD$. At the injectors cross sections, almost 90% of the $HRRD$ is produced by diffusion flame, in spite of the fact that according to Figure 7.19, only 20% of the flame surface corresponds to non-premixed flame at the position $^l/_{L_p} = -0.06$. That high contribution of non-premixed combustion to $HRRD$ in contrast with the low percentage of diffusion flame surface is consistent with observations in Figure 7.16a, i.e. high temperature

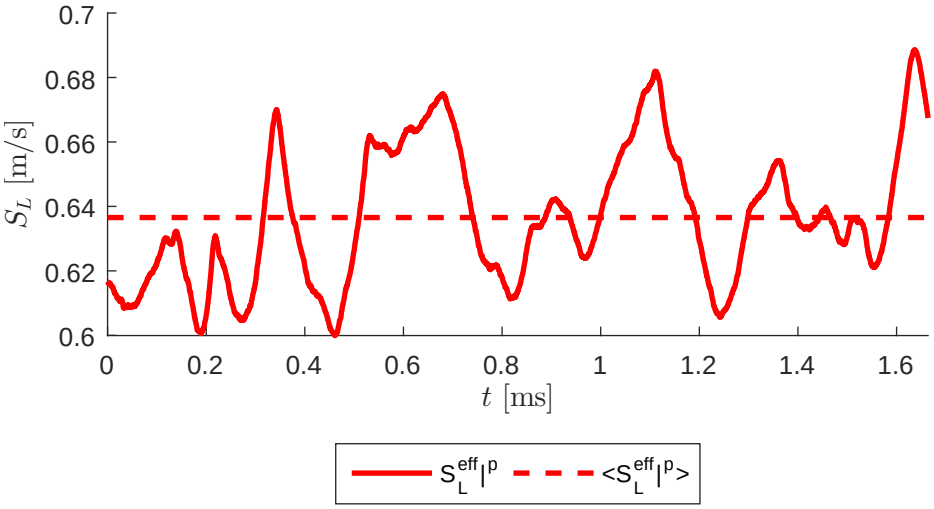

Figure 7.22 – Global instantaneous and time-averaged premixed laminar flame speed.

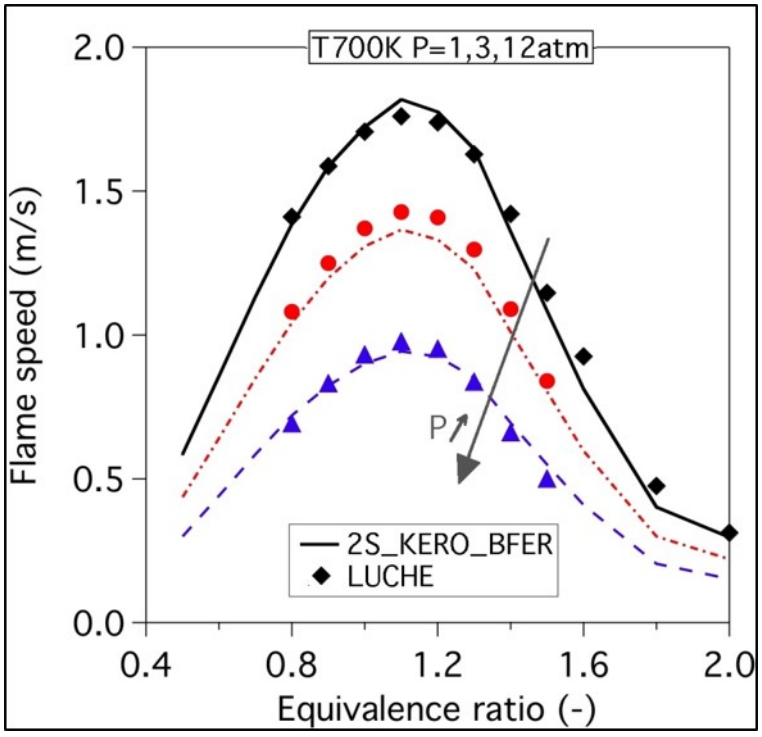

Figure 7.23 – Laminar flame speeds of the KERO fuel obtained with the chemical schemes 2S_KERO_BFER and LUCHE [76], respectively illustrated by lines and markers.

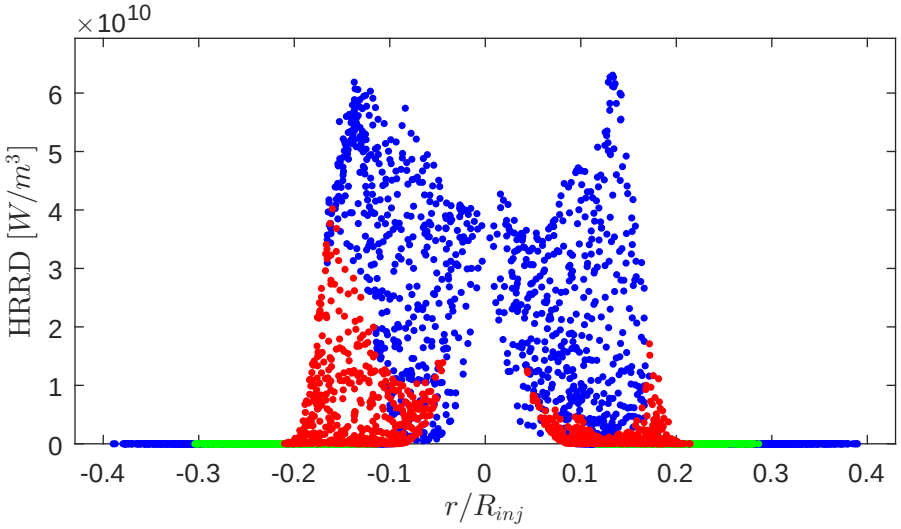

(a) Scatter plot at section $^{l}/_{L_p} = -0.06$.

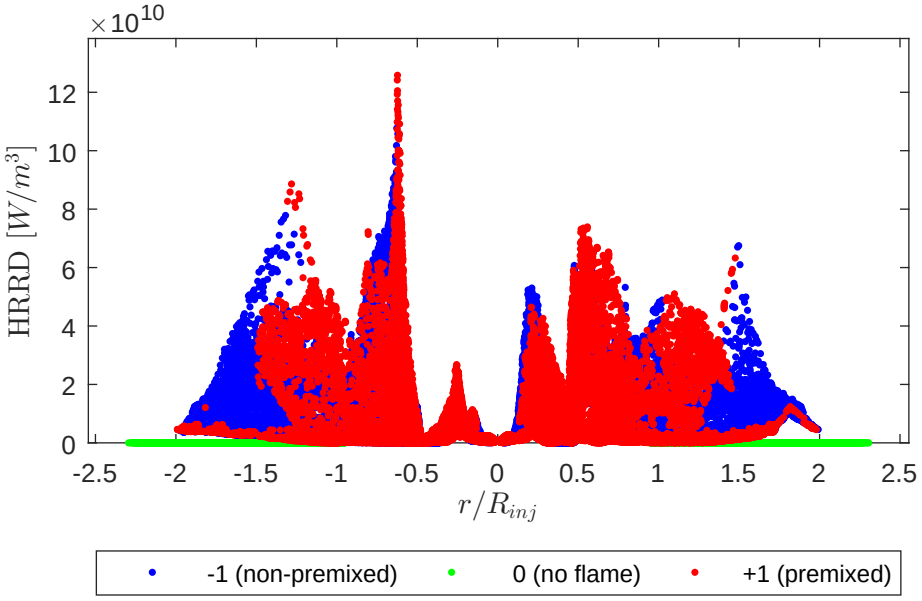

(b) Scatter plot at section $^{l}/_{L_p} = 0.03$.

Figure 7.24

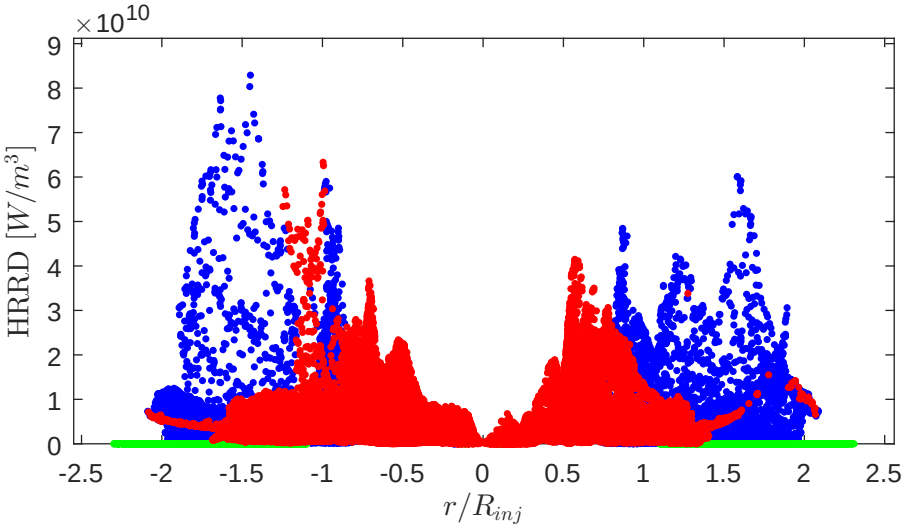

(c) Scatter plot at section $^{l}/_{L_p} = 0.11$.

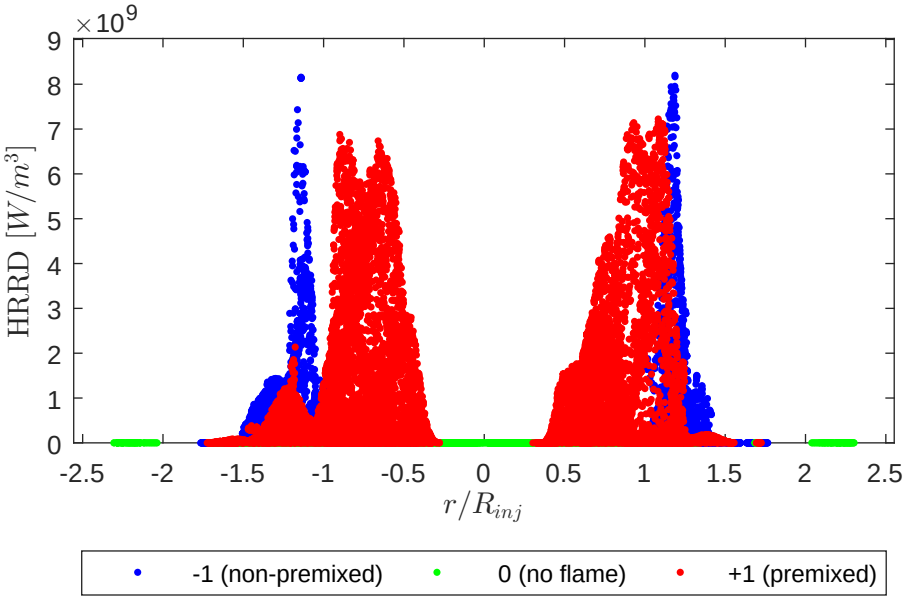

(d) Scatter plot at section $^{l}/_{L_p} = 0.31$.

Figure 7.24

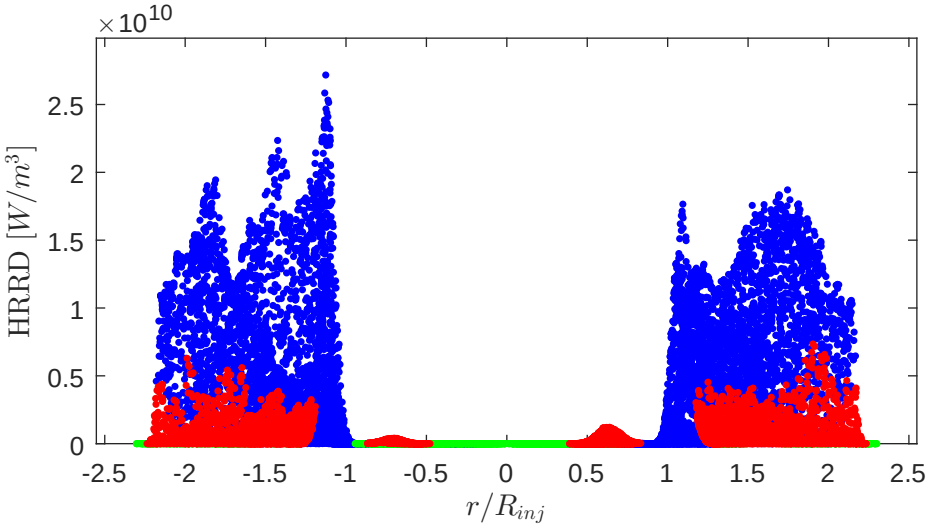

(e) Scatter plot at section $^{l}/_{L_p} = 0.54$.

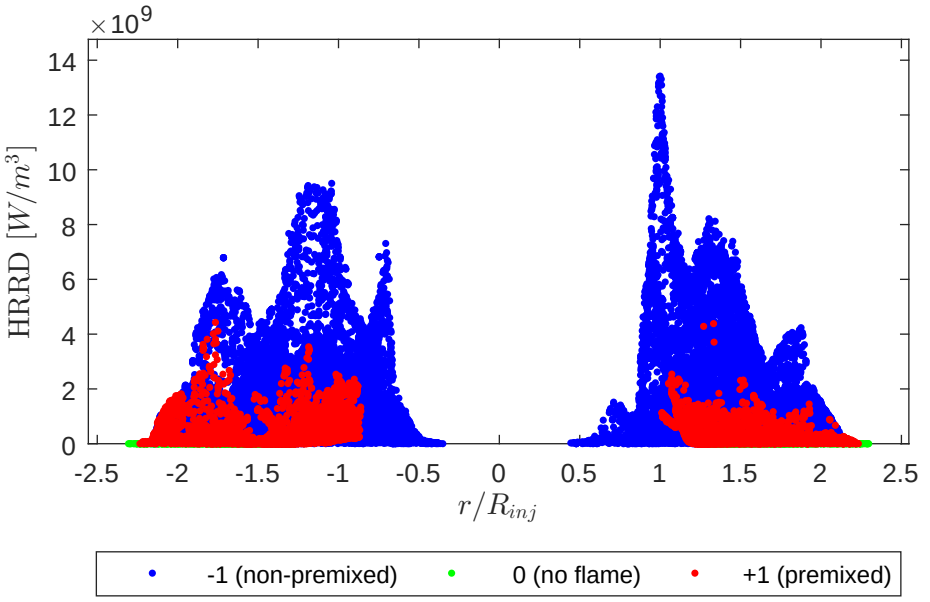

(f) Scatter plot at section $^{l}/_{L_p} = 0.83$.

Figure 7.24 – Scatter plots relative to different axial positions definied by the non-dimensional axial coordinate $^{l}/_{L_p}$ of time-averaged $HRRD$, with respect to the radius, r, normalised by R_{inj}, and coloured depending on the Takeno flame index.

levels corresponding to non-premixed flame points, in comparison to low temperature levels of premixed flame points. Slightly downstream the outer injector outlet, where the time-averaged $HRRD$ peaks at 10GW/m^3, the shares of heat production per volume are roughly equal between premixed and non-premixed combustion. From the flame tube inlet to the position $^{l}/_{L_p} = 0.31$, premixed combustion progressively yields more $HRRD$ than non-premixed combustion. However, downstream the position $^{l}/_{L_p} = 0.4$, more than 90% of the $HRRD$ is released by diffusion flame but the overall intensity of $HRRD$ is reduced. The small $HRRD$ peak at the position $^{l}/_{L_p} = 0.4$ is due to the air feed 2, shown in Figure 7.14. A piecewise study of the Heat Release Rate (HRR), inside parts of the flame region volume, would be more representative of local shares of premixed and non-premixed combustion inside the sector than the present planar analysis of $HRRD$. Unfortunately, HRR could not be computed on volume pieces of the sector.

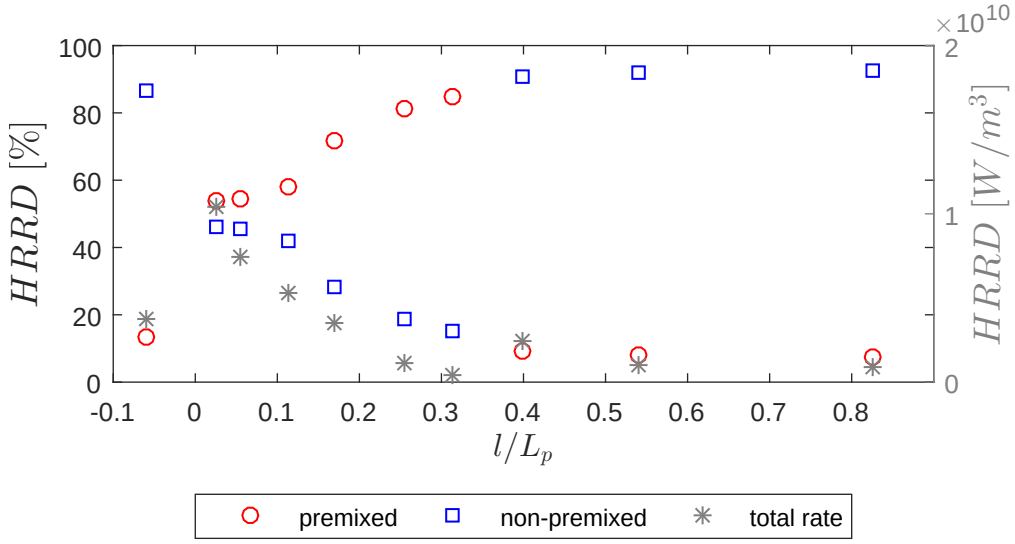

Figure 7.25 – Distribution of $HRRD$, along the normalised axial coordinate, $^{l}/_{L_p}$, and share of $HRRD$ between premixed and non-premixed flames.

Neverthless, HRR was computed for the full flame region, and the integration indicates that the respective premixed/non-premixed shares of global HRR, are 44% - 56%. Consequently, developing a 0D multi-flame model seems to be a suitable option for the simulation of combustion systems such as the herein studied gas turbine combustor.

7.3.3 Turbulent Velocity Fluctuations

A comparison was made, Figure 7.26, between the axial evolutions of the different turbulent velocities, defined in equation 7.32. Turbulent intensities in the fresh gas and in the flame increase between the injectors cross section plane and the first section inside the flame tube. This would be due to the additional air flow from the air feed 1 and the recirculation streams that reach the flame tube inlet. Downstream the flame tube inlet, the mixture turbulent intensity decreases until $^{l}/_{L_p} = 0.4$, while u'_{ug} decreases until $^{l}/_{L_p} = 0.17$ and u'_{flame} decreases until $^{l}/_{L_p} = 0.25$ and slightly increases at $^{l}/_{L_p} = 0.3$. At the latter coordinate, the air jet at the air feed 2 height seems to have more impact on fresh gases and premixed combustion than impact on the overall mixture and non-premixed combustion. The reasons for that behaviour remain unclear.
As shown in Figure 7.27, turbulent intensities corresponding to the gaseous mixture seemed

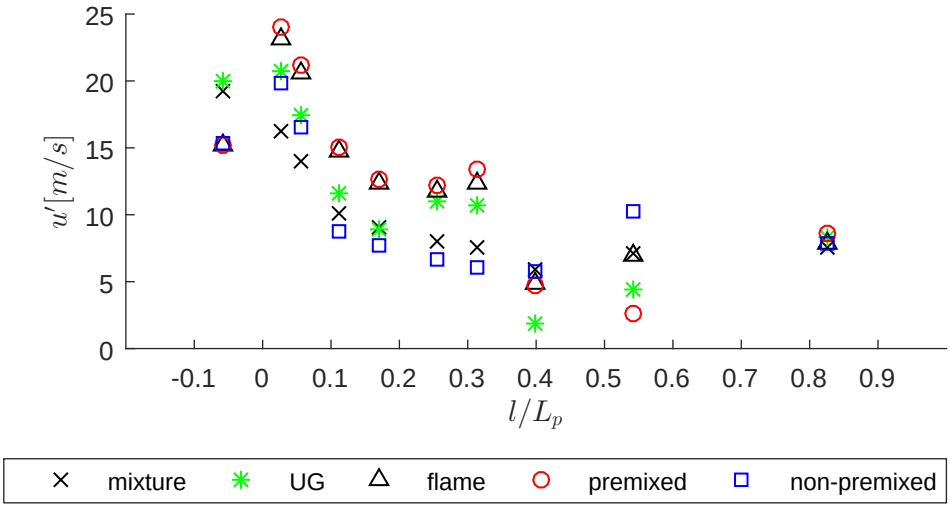

Figure 7.26 – Turbulent velocity fluctuations along the normalised axial coordinate, $^{l}/_{L_p}$: gaseous mixture represented by black x-marks, UG represented by green stars, flame represented by black triangles and premixed and non-premixed combustions represented by red circles and blue squares, respectively.

to be correlated to the non-dimensional aerodynamic pressure loss, $\frac{PL_{aero}}{PL_{aero,0}}$, of the form:

$$\frac{u'_{mixt}}{u'_{mixt,0}} = -0.4104\left(\frac{PL_{aero}}{PL_{aero,0}}\right)^2 + 1.1653\left(\frac{PL_{aero}}{PL_{aero,0}}\right) + 0.2564 \tag{7.33}$$

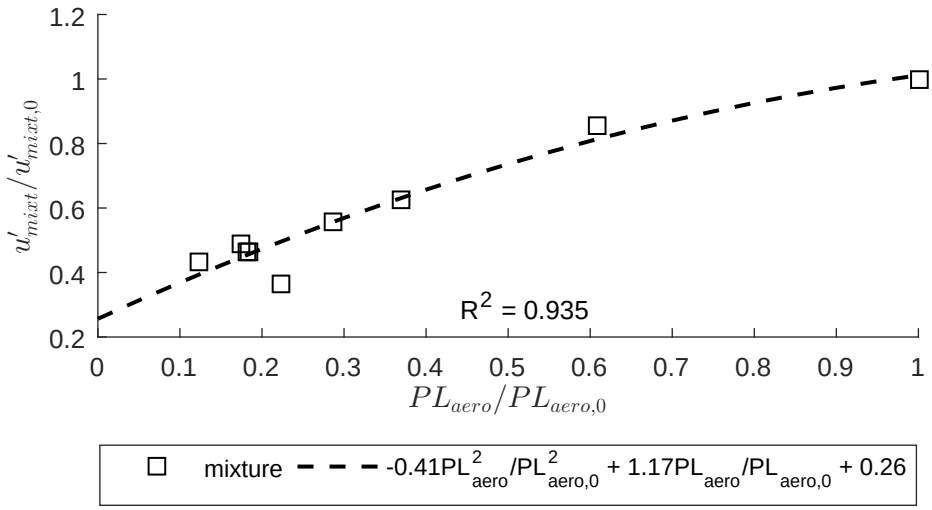

Figure 7.27 – Evolution of u'_{mixt}, normalised by their value at the flame tube sector inlet, $u'_{mixt,0}$, with normalised aerodynamic pressure drop, $\frac{PL_{aero}}{PL_{aero,0}}$, as computed in equation 7.34. Coefficients of the correlation function were rounded for the sake of readability.

$\frac{PL_{aero}}{PL_{aero,0}}$ was computed at every plane j by:

$$PL_{aero,j} = \frac{r_j}{2}\left(\frac{\dot{m}_j\sqrt{T_j}}{A_j P_{t,j}}\right)^2 \tag{7.34}$$

$$= \frac{r_j}{2}\left(\frac{\rho_j U_j\sqrt{T_j}}{P_{t,j}}\right)^2 \tag{7.35}$$

where P_t is the total pressure, r is the perfect gas constant and U is the modulus of time-averaged mean velocity , equation 7.6. Every given variable σ_j was computed as the average of the variable σ over the plane j.

Moreover, turbulence intensities in the premixed flame zone, u'^p_{flame}, normalised by their value at the injectors outlet, $u'^p_{flame,0}$, seemed to follow the non-dimensional modulus of time-averaged mean velocities, $\frac{U}{U_0}$, in a linear trend, as shown in Figure 7.28, given by:

$$\frac{u'^p_{flame}}{u'^p_{flame,0}} = 1.9582\frac{U}{U_0} - 0.8614 \tag{7.36}$$

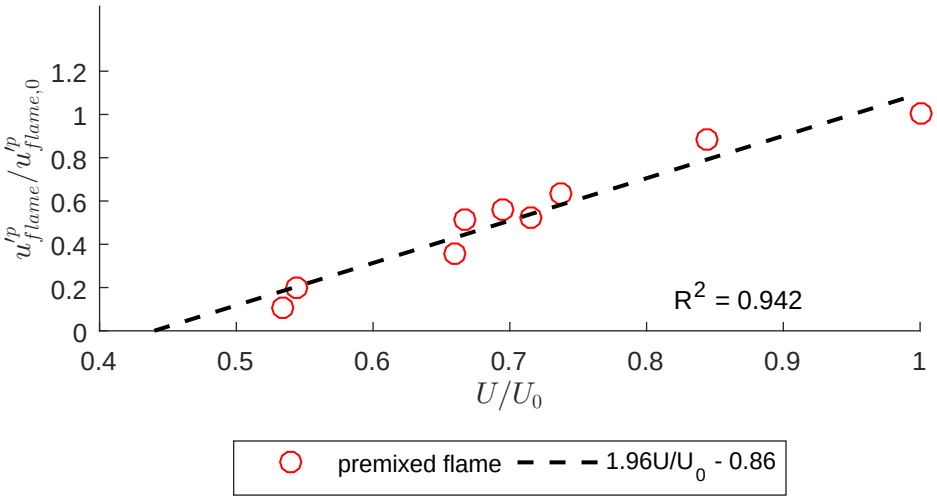

Figure 7.28 – Turbulent velocity fluctuations conditioned to premixed flame region, u', as functions of the normalised time-averaged mean velocity, $^U/_{U_0}$, as computed in equation 7.6.

Conclusion

A real aeronautical combustor sector was used for investigating the feasibility of a FSD-based model reduction. Specific formulations were implemented for flame-type-selective post-processing. Time-averaged, space-averaged and streamwise-dependent information was extracted and analysed. Features of the flow in the present case, such as axial backflow, seemed to have a local impact on flame structure and CO/CO_2 equilibrium chemistry. Therefore, CO/CO_2 equilibrium model would be necessary to be included in the 0D flame tube model. In addition, shares of premixed and non-premixed combustion were assessed in terms of reaction rate, heat release rate and flame surface. Premixed flames characterisation was performed to extract valuable information in order to feed a prospective 0D FSD-based combustion model. Turbulent intensity was analysed following a flame-type-based decomposition. For a complete

insight of the herein studied studied case, diffusion flames in the flame tube sector should be addressed as well as the mechanisms of transition from premixed to non-premixed combustion. Furthermore, the obtained results put in evidence that the best modelling option for system simulation of a real gas turbine combustor should feature a multi-flame combustion model to represent the combustion process in the flame tube. Accordingly, a network approach accounting for additional air mass flow sreams seems to be a valuable solution to simulate such a kind of system.

Part V

Conclusions and Perspectives

Conclusions

The present research project has targeted the investigation of a new physical approach to combustion modelling for gas turbine system simulation embedded in a multi-physical domain environment. The project context was thoroughly analysed with respect to environmental, economic and technological factors. The target application technology was studied. Indeed bibliographic research encompassed current gas turbine technologies as well as prospective concepts. The life cycle and design process were examined and the common simulation and modelling practices were identified. This helped in determining emerging needs in gas turbine combustor modelling and simulation for aeronautics. These needs include more synergy between system simulation and detailed 3D CFD component simulation. For instance, on one hand, advantage can be taken from detailed combustor flame tube simulations for synthesizing and interpreting information into 0D CFD flame tube models. On the other hand, accounting for physical phenomena occurring in the flame tube, as early as possible, by means of 0D CFD approaches during the combustor system design loop, would help in providing valuable input for 3D CFD approaches and detailed component design.

Concrete technical objectives were defined: the 0D flame tube model is expected to represent steady and transient behaviours of gas turbine combustors in terms of fuel vaporization, turbulent flow, thermochemistry and thermodynamics. The flame tube combustion model was planned to be embedded in a submodel component representative of the combustor PZ. It was built to be compatible with other components representing fuel injectors, compressors and turbines with a connectivity based on the Bond Graph approach. Care was taken to allow that component to be compatible with network approaches for flame tube simulation, including post-flame chemistry modelling. In a first time, a reference model was created. It was designed to be representative of the state-of-the-art engine performance models, along with pollutants prediction via semi-empirical correlations. It was then used to evaluate from qualitative and quantitative view points the achievements of the new combustion model which was meant to offer more detailed simulation of combustion physics.

For this matter, a detailed strategy was drawn based on the use of 3D CFD for a deep understanding of turbulent combustion. In a first step, for that matter, an envelope methane flame anchored at a swirler nozzle was studied by means of DTFLES of the single phase swirl burner PRECCINSTA in order to get a deep insight of the combustion process. A reference DTFLES computation was validated against experimental measurements, and several numerical parameters were assessed to find an optimal numerical setup. Using the optimal setup, a baseline case was computed. Flame responses to single parameter variations of FAeR, inlet temperature, inlet mass flow rates and pressures, were characterised by using specific post-processing of mean flame surfaces, wrinkling factors and laminar flame speeds. These characterisations were checked for consistency and validated against results from literature when possible, then normalised with respect to the baseline case results. Premixed turbulent combustion was addressed and resulted in the development of a 0D flame tube model. The flame tube model is based on the CFM formalism, a flame surface density technique originally introduced in 3D CFD approaches. It separates a fresh

gas zone from the burned gas by a flame front. The LES database results were used to model the terms of the global reaction rate equation controlling the 0D CFM flame tube model.

In details, two leads were investigated for the description of the evolution of mean flame surface with the fresh gas volume, the first lead being a geometric modelling approach, and the second lead being a semi-empirical correlation between normalised mean flame surface and normalised fresh gas volume. The semi-empirical correlation was more accurate than the geometric modelling approach for the available LES data. The geometric modelling approach did not seem suitable for the studied type of flame, in the frame of the PRECCINSTA case. Laminar flame speed is computed by means of the correlation given by Metghalchi&Keck [82], and scaled by using baseline results given by means of LES. A correlation was established between normalised aerodynamic pressure drop and turbulent velocity fluctuations, this last responsible for flame surface wrinkling. Four flame surface wrinkling models were compared with LES results, and it was found that the correlation given by Bradley [17] predicted the closest surface wrinkling to the LES results. System simulations were performed to validate the 0D CFM flame tube model against the LES database results. In these simulations, the flame tube component was subjected to transient operating conditions which translated into an unsteady combustion process computed by the 0D CFM combustion model approach. The system simulations showed good agreement with the LES results database for steady state operating conditions for what concerns UG and BG densities, volumes, temperatures and pressures, as well as mean flame surface, laminar flame speed and thickness, turbulent velocity fluctuations and surface wrinkling. However, discrepancies were observed for most of BG species mass fractions and most of the results relative to the case $\phi = 1.5$. Discrepancies of BG species mass fractions were expected because of the absence of H_2 from the species set of the LES computations, and also because two steps chemistry of the LES accounts for CO/CO_2 equilibrium while no CO/CO_2 equilibrium model was incorporated in the 0D flame tube model. Concerning the mismatching results obtained at $\phi = 1.5$, two main reasons are involved: First, the flame surface correlation was not accurate for that FAeR. Secondly, the flame speed correlation was used out of its domain of validation. These two causes add up to the lack of post-flame chemistry model, which would play an important role in rich combustion. Nevertheless, the new 0D CFM flame tube model succeeded in predicting unsteady thermodynamic behaviour of the UG and BG zones, and showed good capabilities of transient aero-thermo-chemistry simulation.

In a second step, non-premixed combustion was addressed in an investigation based on an annular reverse-flow helicopter combustor sector. That sector featured a pair of counter-swirling injectors separately feeding air and fuel into the flame tube. After a characterisation of the main flow streams and an identification of the major recirculation zones, regions witnessing premixed and non-premixed combustion regimes were localised. The structures of the reactive zones featured complex patterns of both anchored and lifted flames. Then, combustion solution variables were filtered by using the normalised Takeno flame index [46, 61], in order to quantify the respective contributions of each combustion regime in the combustor. Finally, all the gathered information was used to build a simplified combustion scenario that represents the real combustion process. Indeed, contours of normalised Takeno number revealed a stratification of zones of premixed and non-premixed combustion. The share of premixed and non-premixed combustion seemed roughly equal in terms of oxygen burning rate and slightly in favour of non-premixed combustion in terms of heat release. That scenario allowed to define the constraints to be respected, and the perimeter to be covered by the system simulation modelling approach.
Therefore, the best system simulation strategy for a gas turbine swirl combustor would be the use of a multi combustion regime flame tube model in conjunction with a network approach, allowing to feature dilution air mass flow rate paths all along the flame tube. Accordingly,

that combination would allow to discretise the flame tube streamwise to separately treat flame zones characterised by different FAeR and combustion regimes.

Perspectives

Improving the 0D CFM Flame Tube Model

The potential of the new 0D CFM flame tube model was demonstrated by the validation on the premixed burner case. That potential could be improved by implementing a pollutants modelling approach, by modifying mean flame surface and laminar flame speed correlations, and by going further with the CFD-based modelling approach.

Pollutants Modelling

The integration of post-flame chemistry in the flame tube model would be necessary for addressing the technical need to predict pollutant emissions identified in the bibliographic study. In addition, Post-flame chemistry modelling would also help in improving the description of the BG species composition and would yield a more accurate BG temperature computation. One interesting lead would be the integration of the CO and NO relaxation approaches, respectively CORA and NORA [14], based on tabulated detailed chemistry, and described in section 3.3.1. The interest of that approach is its accuracy, thanks to tabulated detailed chemistry, combined to reasonable CPU time cost when integrated into a 0D code.

Improving Turbulence and Flame Characteristics Prediction

Some improvements can be directly brought to the 0D CFM flame tube model by modifying mean flame surface, laminar flame speed and turbulent velocity correlations. For instance, the 0D CFM flame tube model can be improved by extending the validity domain of the normalised mean flame surface correlation for large variations of normalised fresh gas volume. This improvement should be operated by further analysis of LES results and additional LES computations. The LES computations would ideally correspond to realistic aeroengine configurations, which would allow fitting flame features of the 0D flame tube model to the LES results. Such a strategy would help in improving the predictive capabilities of the present 0D model and also ease its validation against experimental measurements. Another possible investigation direction is the investigation of the effect of heat exchange through the walls on flame wrinkling, stretching and quenching. In addition, supplementary post-processing could enable better assessment of turbulent features. As a matter of fact, l_T should be accurately computed like it was done in [50]. In addition, leads should be found for representing CRZ and backflow in the present modelling approach.

Application of the 0D CFM Flame Tube Model to a Real Aeronautical Combustor Case

The study of the aeronautical combustor sector in chapter 7 confirms the interest of a network approach similar to what was presented in [119] for combustor system simulations. Discretising the flame tube following a network approach would allow accounting for mixture fraction heterogeneities. Accordingly, the whole combustor could be represented by discretising its External Annulus (EA) and Internal Annulus (IA) as interconnected networks of capacitive components linked together by resistive components, and its Flame Tube (FT) as a line of 0D CFM flame tube components, Figure 7.29.

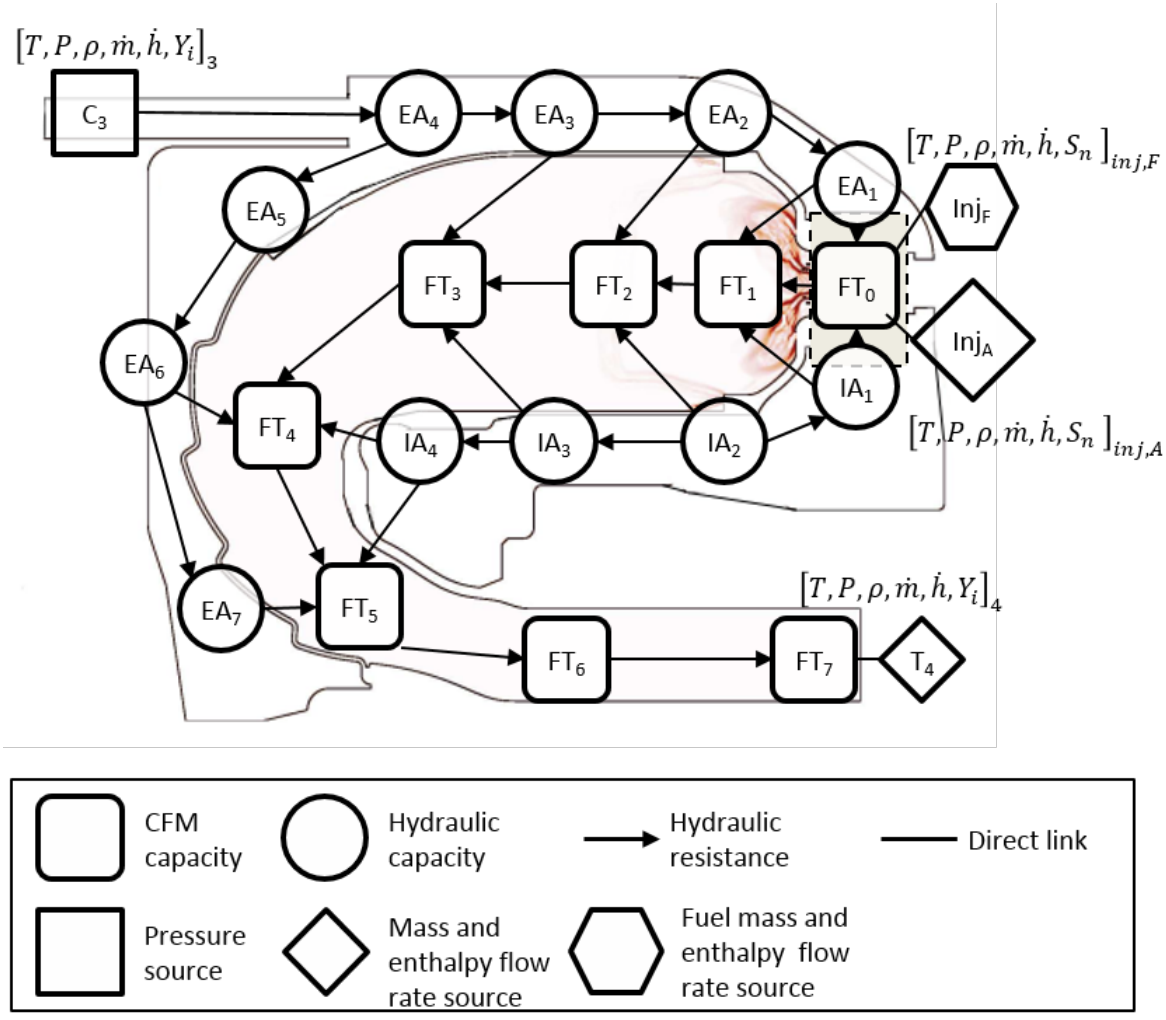

Figure 7.29 – Sketch of a combustor simulation setup by network approach. The component C_3 represents the compressor outlet, EA_i are external annulus portions, IA_j are internal annulus portions, Inj_F is the fuel injector, Inj_A is the air injector, FT_k are 0D CFM flame tube components, and T_4 is the flame tube outlet.

Application to the Operation of an Aeronautical Turboshaft

Considering the current state-of-art system simulations of combustors described in section 2.2.2, the presently developed 0D CFM model can already be benchmarked against the reference 0D flame tube model detailed in appendix A2, eventhough it does not address non-premixed combustion. Moreover, thanks to the choice of the development platform, accounting for the most important physical domain, the turboshaft model can be easily completed to a control loop to validate new control strategies and engine performance on new flight paths such as low-noise landing or on new mission profiles. The system simulation will be possibly extended to a complete rotorcraft system.

Development of a Partially Premixed Flame Tube Model

As shown in chapter 7, the 0D CFM flame tube model developed in this thesis should be extended to address non-premixed combustion, and improved in many respects, in order to tackle fairly predictive simulations of real turboshaft burners. The Partially Premixed Flame Model (PPFM) would be an extension of the 0D CFM submodel to a combination of premixed and non-premixed combustions, Figure 7.30. Premixed combustion would be represented by a premixed reaction rate, $\dot{\Omega}^{p}_{O_2}$, similar to the reaction rate detailed in equation 6.53. A diffusion reaction rate, $\dot{\Omega}^{n}_{O_2}$, should also be established. However, it is not a straightforward task. Indeed, as discussed in chapter 3, a turbulent diffusion flame is often very unsteady and it does not propagate. Non premixed flames should be characterised by their mean surfaces, but also by their scalar dissipation rates of mixture fractions, which are highly space-dependant. Therefore, effort should be deployed in order to propose a consistent reduction solution for scalar dissipation rates. Moreover, a transfer rate between premixed and non-premixed flame types has to be specified depending on hypotheses that should be formulated thanks to analysis of thorough LES results.

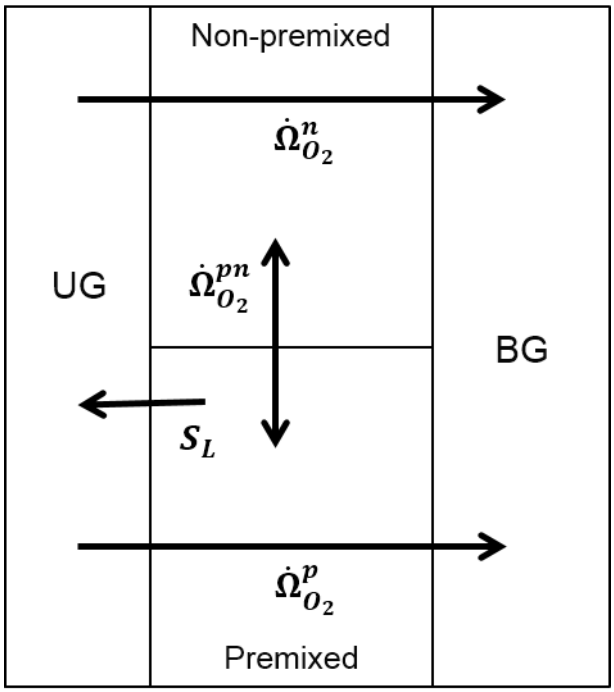

Figure 7.30 – Schematic representation of the prospective 0D PPFM model.

References

[1] Douglas L Allaire, Ian A Waitz, and Karen E Willcox. A comparison of two methods for predicting emissions from aircraft gas turbine combustors. In *ASME Turbo Expo 2007: Power for Land, Sea, and Air*, pages 899–908. American Society of Mechanical Engineers, 2007. , 14, 24, 38

[2] International Air Transport Association. IATA Technology Roadmap, June 2013. , 3

[3] Robert S Barlow. Laser diagnostics and their interplay with computations to understand turbulent combustion. *Proceedings of the Combustion Institute*, **31**[1]:49–75, 2007. 32

[4] H Barths, N Peters, N Brehm, A Mack, M Pfitzner, and V Smiljanovski. Simulation of pollutant formation in a gas-turbine combustor using unsteady flamelets. In *Symposium (International) on Combustion*, **27**, pages 1841–1847. Elsevier, 1998. 38

[5] R. W. Bilger, S. B. Pope, K. N.C. Bray, and J. F. Driscoll. Paradigms in turbulent combustion research. *Proceedings of the Combustion Institute*, **30**[1]:21–42, 2005. , 25, 29, 32, 33

[6] RW Bilger. Turbulent flows with nonpremixed reactants. In *Turbulent reacting flows*, pages 65–113. Springer, 1980. 32

[7] RW Bilger. Turbulent diffusion flames. *Annual Review of Fluid Mechanics*, **21**[1]:101–135, 1989. 32

[8] RW Bilger. Conditional moment closure for turbulent reacting flow. *Physics of Fluids A: Fluid Dynamics*, **5**[2]:436–444, 1993. 33

[9] Richard J Blint. The relationship of the laminar flame width to flame speed. *Combustion Science and Technology*, **49**[1-2]:79–92, 1986. , 25, 51, 98, 144

[10] Mathieu Boileau, Gabriel Staffelbach, Benedicte Cuenot, Thierry Poinsot, and Claude Bérat. LES of an ignition sequence in a gas turbine engine. *Combustion and Flame*, **154**[1]:2–22, 2008. 33

[11] Roland Borghi and Michel Destriau. *La combustion et les flammes*. Editions Technip, 1995. 28

[12] Guillaume Boudier, LYM Gicquel, Thierry Poinsot, D Bissieres, and C Bérat. Comparison of LES, RANS and experiments in an aeronautical gas turbine combustion chamber. *Proceedings of the Combustion Institute*, **31**[2]:3075–3082, 2007. 20

[13] P. Boudier, S. Henriot, T. Poinsot, and T. Baritaud. A model for turbulent flame ignition and propagation in spark ignition engines. In *Symposium (International) on Combustion*, **24**, pages 503–510, 1992. 31

[14] S Bougrine, S Richard, J-B Michel, and D Veynante. Simulation of CO and NO emissions in a SI engine using a 0D Coherent Flame Model coupled with a tabulated chemistry approach. *Applied Energy*, **113**:1199–1215, 2014. , 38, 191

[15] Sabre Bougrine. *0-dimensional modeling of the combustion of alternative fuels in spark ignition engines*. Theses, Ecole Centrale Paris, June 2012. , 27, 28

[16] Meherwan P. Boyce. *Gas turbine engineering handbook*. Butterworth-Heinemann, 2011. 32

[17] Derek Bradley. How fast can we burn? In *Symposium (International) on Combustion*, **24**, pages 247–262. Elsevier, 1992. , 28, 99, 100, 101, 102, 104, 123, 134, 188

[18] KNC Bray, M Champion, and Paul A Libby. The interaction between turbulence and chemistry in premixed turbulent flames. In *Turbulent Reactive Flows*, pages 541–563. Springer, 1989. 29

[19] KNC Bray and J Barrie Moss. A unified statistical model of the premixed turbulent flame. *Acta Astronautica*, **4**[3-4]:291–319, 1977. 29

[20] Pieter Cornelis Breedveld. *Physical systems theory in terms of bond graphs*. Twente University, 1984. 205

[21] Jan F. Broenink. Introduction to physical systems modelling with bond graphs. *SiE Whitebook on Simulation Methodologies*, pages 1–31, 1999. 205

[22] SP Burke and TEW Schumann. Diffusion flames. *Industrial & Engineering Chemistry*, **20**[10]:998–1004, 1928. 32

[23] TD Butler and PJ O'rourke. A numerical method for two dimensional unsteady reacting flows. In *Symposium (International) on Combustion*, **16**, pages 1503–1515. Elsevier, 1977. 31

[24] Sebastien Candel, Denis Veynante, Francois Lacas, Eric Maistret, Nasser Darabiha, and Thierry Poinsot. Coherent Flamelet Model: applications and recent extensions. *Recent advances in combustion modelling*, **6**:19–64, 1990. 31

[25] Sebastien M Candel and Thierry J Poinsot. Flame stretch and the balance equation for the flame area. *Combustion Science and Technology*, **70**[1-3]:1–15, 1990. 25, 29

[26] L Caracciolo and PA Rubini. Validation of a partially-premixed combustion model for gas turbine applications. In *ASME Turbo Expo 2006: Power for Land, Sea, and Air*, pages 731–742. American Society of Mechanical Engineers, 2006. , 54

[27] CERFACS. *The AVBP HandBook*, 2008. 56, 148

[28] Fabrice Charlette, Charles Meneveau, and Denis Veynante. A power-law flame wrinkling model for LES of premixed turbulent combustion part i: non-dynamic formulation and initial tests. *Combustion and Flame*, **131**[1]:159–180, 2002. , 98, 100, 101, 102

[29] Fabrice Charlette, Charles Meneveau, and Denis Veynante. A power-law flame wrinkling model for LES of premixed turbulent combustion part ii: dynamic formulation. *Combustion and Flame*, **131**[1]:181–197, 2002. , 100, 101, 102

[30] W.A. Chishty and M. Klein. Combustion and emission issues in gas turbines. Technical report, Institute of Aerospace Research, National Research Council Canada, 2009. , 36

[31] SH Chung and CK Law. An invariant derivation of flame stretch. *Combustion and Flame*, **55**[1]:123–125, 1984. 25

[32] P. Clavin and F. A. Williams. Effects of molecular diffusion and of thermal expansion on the structure and dynamics of premixed flames in turbulent flows of large scale and low intensity. *Journal of Fluid Mechanics*, **116**:251–282, 3 1982. , 99, 100, 101, 102

[33] O Colin, F Ducros, D Veynante, and Thierry Poinsot. A thickened flame model for Large Eddy Simulations of turbulent premixed combustion. *Physics of Fluids (1994-present)*, **12**[7]:1843–1863, 2000. , 31, 50, 171

[34] Olivier Colin and Michael Rudgyard. Development of high-order taylor–galerkin schemes for les. *Journal of Computational Physics*, **162**[2]:338–371, 2000. 59

[35] European Commission et al. Flightpath 2050, Europe's vision for aviation. *Report of the High Level Group on Aviation Research*, **10**:50266, 2011. , 3

[36] Committee on Aeronautical Technologies, National Research Council. *Aeronautical Technologies for the Twenty-First Century*. The National Academies Press, 1992. 37, 213

[37] G Damköhler. Der einfluß der turbulenz auf die flammengeschwindigkeit, 1940. 29

[38] Gerhard Damköhler. The effect of turbulence on the flame velocity in gas mixtures. 1947. 99

[39] Pascale Domingo, Luc Vervisch, Sandra Payet, and Raphael Hauguel. Dns of a premixed turbulent v flame and LES of a ducted flame using a FSD-PDF subgrid scale closure with FPI-tabulated chemistry. *Combustion and Flame*, **143**[4]:566–586, 2005. 21, 34

[40] A. Dopelheuer and M. Lecht. Influence of engine performance on emission characteristics. In *RTO-Symposium of AVT on Gas Turbine Engine Combustion, Emissions and Alternative Fuels*, pages 12–16, 1998. 37

[41] James F Driscoll. Turbulent premixed combustion: Flamelet structure and its effect on turbulent burning velocities. *Progress in Energy and Combustion Science*, **34**[1]:91–134, 2008. , 25, 28, 29, 78, 83

[42] D. Veynante1 JM Duclos and J. Piana. Experimental and theoretical analysis of flame surface density modelling for premixed turbulent combustion. *Direct Numerical Simulation for Turbulent Reacting Flows*, page 147, 1996. 31

[43] Gordon L Dugger and Sheldon Heimel. Flame speeds of methane-air, propane-air, and ethylene-air mixtures at low initial temperatures. 1952. , 72

[44] E. Knudsen and H. Pitsch. Capabilities and limitations of multi-regime flamelet combustion models. *Combustion and Flame*, **159**[1]:242–264, 2012. 34

[45] JH Ferziger and TAREK ECHEKKI. A simplified reaction rate model and its application to the analysis of premixed flames. *Combustion science and technology*, **89**[5-6]:293–315, 1993. 25

[46] Benoit Fiorina, O Gicquel, L Vervisch, S Carpentier, and N Darabiha. Approximating the chemical structure of partially premixed and diffusion counterflow flames using FPI flamelet tabulation. *Combustion and flame*, **140**[3]:147–160, 2005. , 33, 147, 161, 188

[47] TJ Foster, CW Wilson, M Pourkashanian, and A Williams. Measurement and prediction of NO and NO_2 emissions from aero engines. In *RTO Meeting proceedings*, 1999. 35

[48] B Franzelli, E Riber, M Sanjosé, and T. Poinsot. A two-step chemical scheme for kerosene–air premixed flames. *Combustion and Flame*, **157**[7]:1364–1373, 2010. , 148, 149, 150

[49] Benedetta Giulia Franzelli. *Impact of the chemical description on direct numerical simulations and Large Eddy Simulations of turbulent combustion in industrial aero-engines*. PhD thesis, Institut National Polytechnique de Toulouse, 2011. , 55, 56

[50] Bénédicte Galmiche. *Experimental characterization of expanding laminar and turbulent flames*. Theses, Université d'Orléans, April 2014. , 52, 91, 191

[51] Max Giraud and Joël Silet. Turbines à gaz aéronautiques et terrestres. *Techniques de l'ingénieur. Génie mécanique*, [B4410a]:B4410a–1, 1992. , 14, 19

[52] Guillaume Godel. *Modélisation de sous-maille de la combustion turbulente: développement d'outils pour la prédiction de la pollution dans une chambre aéronautique*. PhD thesis, INSA de Rouen, 01/01/2010. 38

[53] Air Transport Action Group. Aviation: Benfits Beyond Borders, July 2016. 3

[54] WR Hawthorne, DS Weddell, and HC Hottel. Mixing and combustion in turbulent gas jets. In *Symposium on Combustion and Flame, and Explosion Phenomena*, **3**, pages 266–288. Elsevier, 1948. 32

[55] Jérôme Hélie and Arnaud Trouvé. A modified Coherent Flame Model to describe turbulent flame propagation in mixtures with variable composition. *Proceedings of the Combustion Institute*, **28**[1]:193–201, 2000. 34

[56] Ueli Honegger. *Gas turbine combustion modeling for a Parametric Emissions Monitoring System*. Master's thesis, Kansas State University, 01/01/2007. , 37, 213, 214

[57] D. C. Karnopp, D. L. Margolis, and R. C. Rosenberg. *System Dynamics: A Unified Approach*. John Wiley, 1990. 205

[58] Greg Kelsall and Christian Troger. Prediction and control of combustion instabilities in industrial gas turbines. *Applied thermal engineering*, **24**[11]:1571–1582, 2004. 53

[59] A Yu Klimenko. Multicomponent diffusion of various admixtures in turbulent flow. *Fluid dynamics*, **25**[3]:327–334, 1990. 33

[60] Alex Y Klimenko and Robert William Bilger. Conditional moment closure for turbulent combustion. *Progress in energy and combustion science*, **25**[6]:595–687, 1999. 33

[61] E Knudsen and H Pitsch. A general flamelet transformation useful for distinguishing between premixed and non-premixed modes of combustion. *Combustion and flame*, **156**[3]:678–696, 2009. , 33, 147, 161, 188

[62] Ghislain Lartigue. *Simulation des grandes échelles et instabilités de combustion*. PhD thesis, Institut National Polytechnique de Toulouse, 2004. , 54

[63] Peter Lax and Burton Wendroff. Systems of conservation laws. *Communications on Pure and Applied Mathematics*, **13**[2]:217–237, 1960. 59

[64] Guillaume Lecocq. *Approches hybrides combinant chimie complexe, description statistique et densité de surface de flamme pour la simulation aux grandes échelles de l'auto-inflammation, l'allumage par bougie et la flamme de prémélange dans les moteurs à allumage commandé*. PhD thesis, INSA de Rouen, 01/01/2010. 31

[65] DS Lee, G Pitari, V Grewe, K Gierens, JE Penner, A Petzold, MJ Prather, U Schumann, A Bais, T Berntsen, et al. Transport impacts on atmosphere and climate: Aviation. *Atmospheric Environment*, **44**[37]:4678–4734, 2010. 3

[66] AH Lefebvre. Theoretical aspects of gas turbine combustion performance. Technical report, College of Aeronautics Cranfield, 1966. , 22

[67] Arthur Henry Lefebvre. Fuel effects on gas turbine combustion-liner temperature, pattern factor, and pollutant emissions. *Journal of Aircraft*, **21**[11]:887–898, 1984. 36, 37, 213

[68] Arthur Henry Lefebvre, Dilip R. Ballal, and Donald W. Bahr. *Gas turbine combustion: alternative fuels and emissions*. CRC Press Boca Raton, FL, 2010. , 17, 18, 19, 34, 35, 36, 37, 71, 78, 98, 99, 100, 101, 102

[69] JP Légier, T Poinsot, and D Veynante. Dynamically thickened flame Large Eddy Simulation model for premixed and non-premixed turbulent combustion, summer program 2000. *Center for Turbulence Research, Stanford, USA*, pages 157–168, 2000. , 31, 55, 148

[70] GD Lewis. Prediction of NO_x emissions. In *ASME 1981 International Gas Turbine Conference and Products Show*, pages V002T06A023–V002T06A023. American Society of Mechanical Engineers, 1981. 213

[71] GEORGED LEWIS. A new understanding of no (x) formation. In *International Symposium on Air Breathing Engines, 10 th, Nottingham, England*, pages 625–629, 1991. 37, 213

[72] Paul A Libby and Forman A Williams. A presumed pdf analysis of partially premixed turbulent combustion. *Combustion science and technology*, **161**[1]:351–390, 2000. 34

[73] Amable Linan and Antonio Crespo. An asymptotic analysis of unsteady diffusion flames for large activation energies. *Combustion science and technology*, **14**[1-3]:95–117, 1976. 32

[74] Louis Tsague, Joseph Tsogo, and Thomas Tamo Tatietse. Prediction of the production of nitrogen oxide in turbojet engines. *Atmospheric Environment*, **40**[29]:5727–5733, 2006. 37

[75] Louis Tsague, Thomas Tamo Tatietse, John Ngundam, and Joseph Tsogo. Prediction of emissions in turbojet engines exhausts: relationship between nitrogen oxides emission index ($EINO_x$) and the operational parameters. *Aerospace Science and Technology*, **11**[6]:459–463, 2007. 214

[76] Jocelyn Luche. *Obtention de modèles cinétiques réduits de combustion : application à un mécanisme de kérosène*. PhD thesis, 2003. Thèse de doctorat dirigée par Boettner, Jean-Claude Chimie - Physique. Cinétique chimique Orléans 2003. , 148, 149, 176

[77] Bernie MacIsaac and Roy Langton. *Gas Turbine Propulsion Systems*, **49**. Wiley, 2011. , 11, 12, 13, 14, 78

[78] Frank E. Marble and James E. Broadwell. The Coherent Flame Model for turbulent chemical reactions, 1977. 29

[79] M Matalon and BJ Matkowsky. Flames as gasdynamic discontinuities. *Journal of Fluid Mechanics*, **124**:239–259, 1982. 25

[80] W. Meier, P. Weigand, X. R. Duan, and R. Giezendanner-Thoben. Detailed characterization of the dynamics of thermoacoustic pulsations in a lean premixed swirl flame. *Combustion and Flame*, **150**[1]:2–26, 2007. , 54, 59, 61, 62, 63, 64, 65, 66, 67, 68

[81] C Meneveau and T Poinsot. Stretching and quenching of flamelets in premixed turbulent combustion. *Combustion and Flame*, **86**[4]:311–332, 1991. , 21, 98, 99

[82] M Metghalchi and JC Keck. Laminar burning velocity of propane-air mixtures at high temperature and pressure. *Combustion and flame*, **38**:143–154, 1980. , 25, 71, 72, 73, 98, 188

[83] Yasuhiro Mizobuchi, Shigeru Tachibana, Junji Shinio, Satoru Ogawa, and Tadao Takeno. A numerical analysis of the structure of a turbulent hydrogen jet lifted flame. *Proceedings of the Combustion Institute*, **29**[2]:2009–2015, 2002. 21

[84] Chowdhury G. Moniruzzaman and Fangqun Yu. A 0D aircraft engine emission model with detailed chemistry and soot microphysics. *Combustion and Flame*, **159**[4]:1670–1686, 2012. 14, 38

[85] David Nicol, Philip C Malte, Jenkin Lai, Nick N Marinov, David T Pratt, and Robert A Corr. NO_x sensitivities for gas turbine engines operated on lean-premixed combustion and conventional diffusion flames. In *ASME 1992 International Gas Turbine and Aeroengine Congress and Exposition*, pages V003T06A012–V003T06A012. American Society of Mechanical Engineers, 1992. 35

[86] F Nicoud and T Poinsot. Boundary Conditions for Compressible Unsteady Flows. *Absorbing Boundaries and Layers, Domain Decomposition Methods: Applications to Large Scale Computers*, page 78, 2001. 55, 148

[87] North Atlantic Treaty Organization. Performance prediction and simulation of gas turbine engine operation. 2002. , 12, 13

[88] Belkacem Ould Bouamama and Geneviève Dauphin-Tanguy. Modélisation par bond graph: Éléments de base pour l'énergétique. *Techniques de l'ingénieur. Génie énergétique*, [BE8280], 2006. , 206

[89] Henry M. Paynter. *Analysis and design of engineering systems*. MIT press, 1961. 205

[90] François Pecquery, Vincent Moureau, Ghislain Lartigue, Luc Vervisch, and Anthony Roux. Modelling nitrogen oxide emissions in turbulent flames with air dilution: Application to LES of a non-premixed jet-flame. *Combustion and Flame*, **161**[2]:496–509, 2014. 38

[91] N Peters. The turbulent burning velocity for large-scale and small-scale turbulence. *Journal of Fluid Mechanics*, **384**:107–132, 1999. , 29, 30, 83

[92] Norbert Peters. Local quenching due to flame stretch and non-premixed turbulent combustion. *Combustion Science and Technology*, **30**[1-6]:1–17, 1983. 32

[93] Norbert Peters. Laminar diffusion flamelet models in non-premixed turbulent combustion. *Progress in energy and combustion science*, **10**[3]:319–339, 1984. 32

[94] Norbert Peters. *Turbulent combustion*. Cambridge university press, 2000. 28, 29

[95] T Poinsot, T Echekki, and MG Mungal. A study of the laminar flame tip and implications for premixed turbulent combustion. *Combustion science and technology*, **81**[1-3]:45–73, 1992. 25

[96] Thierry Poinsot and Denis Veynante. *Theoretical and numerical combustion*. T. Poinsot, 2012. , 21, 25, 26, 27, 29, 31, 32

[97] T.J Poinsot and S.K Lelef. Boundary conditions for direct simulations of compressible viscous flows. *Journal of computational physics*, **101**[1]:104–129, 1992. 55, 148

[98] SB Pope. The evolution of surfaces in turbulence. *International journal of engineering science*, **26**[5]:445–469, 1988. 29

[99] Aerospace & Defense Practice. Global Civil Helicopter Market Growth Dynamics with focus on Emergency Medical Services, 2012. 3

[100] S. Richard, S. Bougrine, G. Font, F-A Lafossas, and F. Le Berr. On the reduction of a 3D CFD combustion model to build a physical 0D model for simulating heat release, knock and pollutants in si engines. *Oil & Gas Science and Technology-Revue de l'IFP*, **64**[3]:223–242, 2009. , 91, 212

[101] Stéphane Richard, Olivier Colin, O. Vermorel, A. Benkenida, C. Angelberger, and D. Veynante. Towards Large Eddy Simulation of combustion in spark ignition engines. *Proceedings of the Combustion Institute*, **31**[2]:3059–3066, 2007. 31

[102] Nader K Rizk, Ju S Chin, Andre W Marshall, and Mohan K Razdan. Predictions of NO_x formation under combined droplet and partially premixed reaction of diffusion flame combustors. *Journal of engineering for gas turbines and power*, **124**[1]:31–38, 2002. , 24

[103] NK Rizk and HC Mongia. A semianalytical emission model for diffusion flame, rich/lean, and premixed lean combustors. In *ASME 1993 International Gas Turbine and Aeroengine Congress and Exposition*, pages V002T05A003–V002T05A003. American Society of Mechanical Engineers, 1993. 36

[104] NK Rizk and HC Mongia. Emissions predictions of different gas turbine combustors. In *AIAA, Aerospace Sciences Meeting & Exhibit, 32 nd, Reno, NV*, 1994. 36, 37, 213, 214

[105] Vincent Robin. *Contribution à la modélisation des écoulements turbulents réactifs partiellement pré-mélangés*. PhD thesis, Ecole Nationale Supérieure de Mécanique et d'Aérotechnique, 01/01/2007. 34

[106] NA Røkke, JE Hustad, and S Berg. Pollutant emissions from gas fired turbine engines in offshore practice: Measurements and scaling. In *ASME 1993 International Gas Turbine and Aeroengine Congress and Exposition*, pages V03AT15A021–V03AT15A021. American Society of Mechanical Engineers, 1993. 37, 213

[107] David A Rosenberg, Patton M Allison, and James F Driscoll. Method to measure flame index in a partially-premixed gas turbine combustor. In *51st AIAA Aerospace Sciences Meeting, Grapevine, TX*, pages 2013–1181, 2013. 33

[108] R. C. Rosenberg. Exploiting bond graph causality in physical system models. *Journal of dynamic systems, measurement, and control*, **109**[4]:378–383, 1987. 205

[109] M Sébastien Roux. *Influence de la modélisation du mélange air/carburant et de l'étendue du domaine de calcul dans la simulation aux grandes échelles des instabilités de combustion. Application à des foyers aéronautiques.* PhD thesis, Université de Montpellier II, 2007. , 54, 59, 61, 62, 63, 64, 65, 66, 68

[110] Sebastien Roux, G. Lartigue, Thierry Poinsot, U. Meier, and Claude Bérat. Studies of mean and unsteady flow in a swirled combustor using experiments, acoustic analysis, and Large Eddy Simulations. *Combustion and Flame*, **141**[1]:40–54, 2005. 54

[111] Pierre Sagaut and Dimitris Drikakis. Large Eddy Simulation. *Encyclopedia of Aerospace Engineering*, 2010. 21

[112] Robert Sausen, Ivar Isaksen, Volker Grewe, Didier Hauglustaine, David S Lee, Gunnar Myhre, Marcus O Köhler, Giovanni Pitari, Ulrich Schumann, Frode Stordal, et al. Aviation radiative forcing in 2000: An update on ipcc (1999). *Meteorologische Zeitschrift*, **14**[4]:555–561, 2005. 3

[113] J Schwarzenbach and KF Gill. *System modelling and control*. J. Wiley, 1978. 14

[114] Lartigue Selle, Ghislain Lartigue, Thierry Poinsot, R Koch, K-U Schildmacher, W Krebs, B Prade, P Kaufmann, and Denis Veynante. Compressible Large Eddy Simulation of turbulent combustion in complex geometry on unstructured meshes. *Combustion and Flame*, **137**[4]:489–505, 2004. , 54

[115] Joseph Smagorinsky. General circulation experiments with the primitive equations: I. the basic experiment*. *Monthly weather review*, **91**[3]:99–164, 1963. 54, 147

[116] Gregory P. Smith, David M. Golden, Michael Frenklach, Nigel W. Moriarty, Boris Eiteneer, Mikhail Goldenberg, C. Thomas Bowman, Ronald K. Hanson, Soonho Song, William C. Gardiner, Vitali V. Lissianski, and Zhiwei Qin. GRI-Mech 3.0. 51

[117] D Brian Spalding. Development of the eddy-break-up model of turbulent combustion. In *Symposium (International) on Combustion*, **16**, pages 1657–1663. Elsevier, 1977. 29

[118] Daniel R Stull and Harold Prophet. JANAF thermochemical tables. Technical report, DTIC Document, 1971. 54, 147

[119] Peter J Stuttaford and Philip A Rubini. Preliminary gas turbine combustor design using a network approach. In *ASME 1996 International Gas Turbine and Aeroengine Congress and Exhibition*, pages V003T06A026–V003T06A026. American Society of Mechanical Engineers, 1996. , 23, 192

[120] William Sutherland. Lii. the viscosity of gases and molecular force. *The London, Edinburgh, and Dublin Philosophical Magazine and Journal of Science*, **36**[223]:507–531, 1893. 54, 147

[121] J Swithenbank, I Poll, MW Vincent, and DD Wright. Combustion design fundamentals. In *Symposium (International) on Combustion*, **14**, pages 627–638. Elsevier, 1973. , 14, 23, 37

[122] Arnaud Trouvé and Thierry Poinsot. The evolution equation for the flame surface density in turbulent premixed combustion. *Journal of Fluid Mechanics*, **278**:1–31, 1994. 25

[123] A. Tsalavoutas, M. Kelaidis, N. Thoma, and K. Mathioudakis. Correlations adaptation for optimal emissions prediction. *Proceedings of GT2007: ASME Turbo Expo 2007: Power for Land, Sea and Air GT*, **27060**, 2007. 36

[124] Mark G Turner, Andrew Norris, and Joe Veres. High fidelity 3D simulation of the GE90. *AIAA Paper*, **3996**:2003, 2003. 37

[125] Stephen R Turns et al. *An introduction to combustion*, **287**. McGraw-hill New York, 1996. 29

[126] United States. Federal Aviation Administration. *Rotorcraft flying handbook*, **4**. Federal Aviation Administration, 2000. , 10

[127] Vincent Fichet, Mohamed Kanniche, Pierre Plion, and Olivier Gicquel. A reactor network model for predicting 5NO_x6 emissions in gas turbines. *Fuel*, **89**[9]:2202–2210, 2010. 14, 37, 38

[128] P. Wang, N. A. Platova, J. Fröhlich, and U. Maas. Large Eddy Simulation of the PRECCINSTA burner. *International Journal of Heat and Mass Transfer*, **70**:486–495, 2014. , 53, 54

[129] Gareth Williams. Combustion theory. Addison-Wesley, 1985. 25

[130] H Yamashita, M Shimada, and T Takeno. A numerical study on flame stability at the transition point of jet diffusion flames. In *Symposium (International) on Combustion*, **26**, pages 27–34. Elsevier, 1996. 33

A1 - The System Simulation Development Environment

About LMS Imagine.Lab Amesim

The LMS Imagine.Lab software suite is a multi-domain simulation environment. The user connects various validated components to predict multi-disciplinary system performance. Thanks to application-specific simulation, a variety of subsystems in multiple physical domains can be assessed (hydraulic, pneumatic, mechanic, electrical, thermal, electromechanical). The software suite encompasses Amesim, Ameset and Amerun.
The Amesim Platform is the core of the Amesim software. It offers a user-friendly environment for 1D system simulation. Its physically conservative multi-port modelling of physical components as well as its block-diagram approach for control systems enables the coupling of all its libraries together. To create a system simulation model in Amesim, components from different physical domains are assembled. The physical libraries have been developed through engineering services and partnerships with customers. Amesim is based on the Bond graph theory and distinguishes four operation modes:

1. Sketch mode: in which the different components are linked.
2. Submodel mode: in which the physical submodel associated to each component is chosen.
3. Parameter mode: in which the parameters for each submodel are set.
4. Run mode: in which the simulation is started and results analysed.

Ameset is the component design environment that allows creating and editing the components, in which submodel codes are encapsulated, while Amerun is an interface for efficient simulation running for the end-user.

Bond Graph Theory

The concept of bond graphs was originated by [89]. The idea was further developed by [57, 108]. By means of the formulation by [20], of a framework based on thermodynamics, bond-graph model description evolved to a systems theory. Bond graphs are a domain-independent graphical description of dynamic behaviour of physical systems [21]. This means that systems from different domains (e.g. electrical, mechanical, hydraulic, acoustical, thermodynamic, material) are described using a common formalism. Bond graphs are based on energy and energy exchange. Physical analogies between domains are established in terms

of fluxes and efforts. Bond-graph modelling is a tool for engineering systems, especially when different physical domains are involved. Furthermore, bond-graph submodels can be seen as objects: bond-graph modelling is a form of object-oriented physical systems modelling. Bond graphs are labelled and directed graphs, in which the vertices represent submodels and the edges represent an ideal energy connection between power ports. The vertices are idealised descriptions of physical phenomena and denote the relevant aspects of the dynamic system behaviour. It can be bond graphs itself, thus allowing hierarchical models, or it can be a set of equations in the variables of the ports (two at each port). The edges are labelled bonds. They denote point-to-point connections between submodel ports. When preparing for simulation, the bonds are embodied as two-signal connections with opposite directions. Furthermore, a bond has a power direction and a computational causality direction. The internals of the submodels give preferences to the computational direction of the bonds to be connected. The eventually assigned computational causality dictates which port variable is computed as a result (output) and consequently, the other port variable is the cause (input). Since bond graphs can be mixed with block-diagram parts, bond-graph submodels can have power ports, signal inputs and signal outputs as their interfacing elements. Transformation to a bond graph leads to a domain independent model.
A Bond Graph example is illustrated in Figure 31. Assuming A and B are two connected elements, The arrow symbolizes a physical bond through which a flux f goes from A to B. The flux is associated to an effort e.

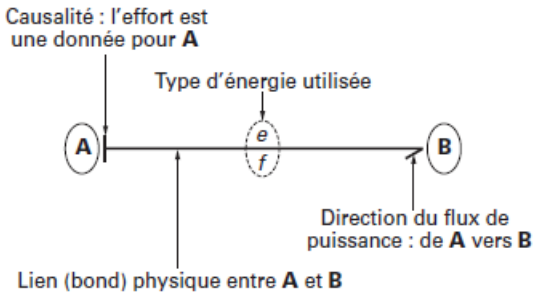

Figure 31 – Example of a bond graph representation. [88]

The physical behaviour of Bond Graph elements is defined by the algebraic equation that lies within and sets a relation between the flux variable, the effort variable at the element bond graph arc and their derivatives. The three major types of elements are Resistive (R), Capacitive (C) and Inertial (I) element types, which can be respectively defined by:

$$R : \alpha_R (f, e) = 0 \tag{37}$$
$$C : \alpha_C (f, \dot{e}) = 0 \tag{38}$$
$$I : \alpha_I \left(\dot{f}, e\right) = 0 \tag{39}$$

where α_i are algebraic functions, f is a flux and e is an effort. Based on the bond graph theory, the power P of a Resistive, Capacitive or Inertial element is given by the product of the effort and the flux variables on the element bond graph arc:

$$P = e \times f \tag{40}$$

A2 - The Global 0D Burner Modelling Approach

Building a 0D Reference Model

As a comparison tool for the models under development, a reference model is needed. Hence a generic black-box-type combustor is created. In order to reflect the existent system simulation codes, this component , depicted in Figure 32, is an open volume that represents a full flame tube.

According to the Bond Graph formalism, the flame tube component is designated as an aerothermal Capacity (C) receiving mass flow rates and returning static pressure. This choice gives a large array of connectivity possibilities while giving the freedom to incorporate all the eventually required mathematical modelling for aero-thermochemistry. Therefore, the 0D flame tube model must be able to handle a reactive/non-reactive gaseous mixture that flows through it, as well as to deal with gaseous/liquid fuel injection. Information describing the interaction of the thermodynamic system contained into the combustion chamber with its external environment is exchanged at the six ports of the component. In details, ports 1, 4 and 6 are inlets and port 2 is an outlet. All these flow ports handle gaseous mixtures of up to twelve species, being oxygenated hydrocarbon fuel $C_xH_yO_z$, N_2, O_2, $H2$, H_2O, CO, CO_2, NO, NO_2, HC, $NH3$ and *soot*. Port 5 is an inlet restricted to fuel, feeding the flame tube mass and enthalpy flow rates of liquid or gaseous fuel. Port 3 is a thermal port that receives the wall temperature information, designated by T_{ex}, and allows heat exchange between the flame tube system and its surrounding environment, represented by the variable Q_{ex}. The mixture is considered as ideal gas and as homogeneous in the control volume. The pressure and the turbulent kinetic energy field are assumed to be uniform in the control volume V.

Mass Balance, Density, Composition and Volume

Mass Balance

Mass balance is calculated for every species in the flame tube component by writing mass conservation for an open reactive system of the form:

$$\frac{dm_i}{dt} = \frac{d\left(\rho_i V\right)}{dt} = \sum_{k}^{in/out} \dot{m}_{i,k} + \dot{\Omega}_i \tag{41}$$

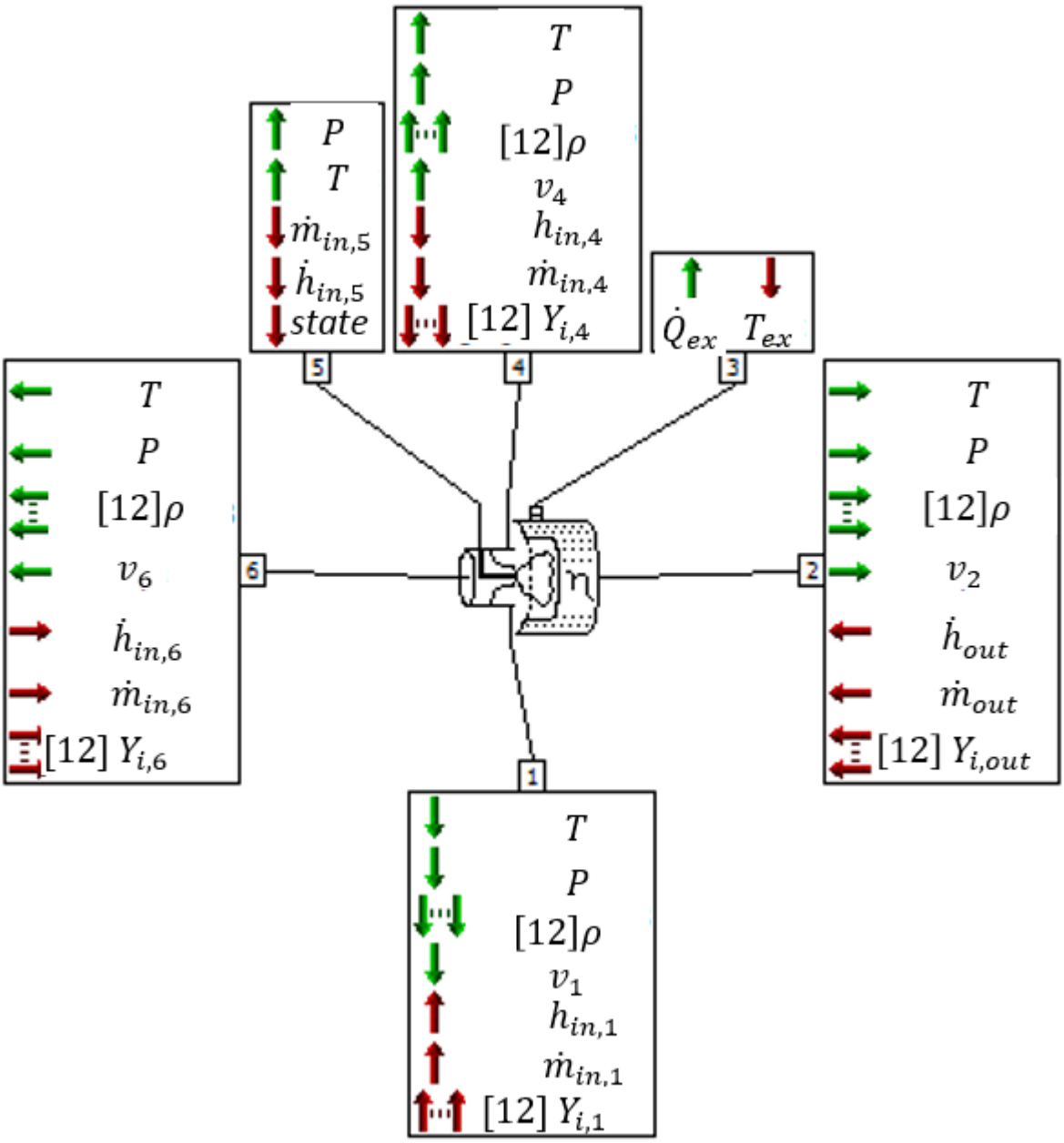

Figure 32 – Bond Graph of the 0D one-zone flame tube component. Ports are numbered from 1 to 6. Inputs are marked by red arrows and outputs are symbolised by green arrows. The variable *state* specifies the physical state of the fuel being fed into port 5.

Total mass balance is given by:

$$\dot{m} = \sum_i \dot{m}_i \tag{42}$$

where the subscript k indicates an input/output port. $\dot{\Omega}_i$ is the reaction rate of the species i. In the presence of evaporating liquid fuel, the flow rate of evaporated fuel, $\dot{m}_F^{vap}$, is added to the gaseous fuel mass flow rate balance equation.

Liquid Fuel Evaporation

Liquid fuel is treated as a separate thermodynamic system exchanging mass and enthalpy with the gaseous phase. The fuel evaporation rate is written of the form:

$$\dot{m}_F^{vap} = \frac{m_F^{liq}}{\tau} \tag{43}$$

where m_F^{liq}, a state variable, is the current mass of liquid fuel in the combustion chamber and τ is the fuel and temperature dependent evaporation time scale. m_F^{liq} is solved by the integration of its derivative written of the form:

$$\dot{m}_F^{liq} = \dot{m}_{inj,F} - \dot{m}_F^{vap} \tag{44}$$

and where $\dot{m}_{inj,F}$ is the mass flow rate of injected liquid fuel. At every time step, the mass of evaporated fuel in the UG zone is also assumed as instantaneously mixed with the gaseous phase.

Density and Composition

Densities are state variables of the model. Thus, the solver calculates them by integrating their temporal derivatives, deduced from the mass balance of the flame tube:

$$\dot{\rho}_i = \frac{d\rho_i}{dt} = \frac{d}{dt}\left(\frac{m_i}{V}\right) \tag{45}$$

$$= \frac{\dot{m}_i V - m_i \cancel{\dot{V}}}{V^2} \tag{46}$$

$$\dot{\rho}_i = \frac{\dot{m}_i}{V} \tag{47}$$

The total density temporal derivative is given by:

$$\dot{\rho} = \sum \dot{\rho}_i \tag{48}$$

The species mass fractions are calculated using:

$$Y_i = \frac{\rho_i}{\rho} \tag{49}$$

The dynamic mixture viscosity is based on a linear temperature-dependent relation for every species i, depending on its mass fraction, Y_i.

$$\mu = \sum_i Y_i \left(\mu_{0,i} + \mu_{1,i} T\right) \tag{50}$$

Energy Balance, Temperature and Pressure

The differential form of the first law of thermodynamics is applied to the flame tube component as an open system, 52. Potential energy and the kinetic energy are neglected.

$$dU = \delta Q + \delta W + \sum_k^{in/out} h_k dm_k \tag{51}$$

$$= \delta Q - PdV + \sum_k^{in/out} h_k dm_k \tag{52}$$

The temporal variation gives:

$$\dot{U} = \dot{Q} - P\dot{V} + \sum_k^{in/out} h_k \dot{m}_k \tag{53}$$

$$Q = HR + Q_{ex} \tag{54}$$

where U is the internal energy, h_k is the specific enthalpy of the mixture at port k and $\dot{m}_k$ is the mass flow rate at port k. The specific enthalpy h_i of a species i is evaluated at a given temperature by using the JANAF-YAWS polynomial formulation of specific heat at constant pressure, as a function of temperature. Heat flow, Q, includes combustion Heat Release (HR) and, Q_{ex}, the eventual contribution of conduction, convective and radiative heat flows in case of heat exchange between the thermodynamic system and its surrounding environment. W is the mechanical work yielded by the system.

According to equation 55 and equation 56, the energy balance equation 53 can be expressed in terms of enthalpy, equation 57.

$$H = U + PV \tag{55}$$

$$dH = dU + VdP + PdV \tag{56}$$

$$\dot{H} = \dot{Q} + V\dot{P} + \sum_k^{in/out} h_k \dot{m}_k \tag{57}$$

Total enthalpy is a state variable of the model.

Temperature

The temperature T represents the mean temperature of the gaseous mixture inside the flame tube component. It is computed from the flame tube mixture total enthalpy and composition, by means of an iterative procedure based on the Newton-Raphson method; its time derivative

is used to compute the pressure derivative. Internal energy can be written of the form:

$$U = mu = m\int_T c_v dT = \sum_i m_i \int_T c_{v,i} dT = m\sum Y_i \int_T c_{v,i} dT \tag{58}$$

$$dU = dmu + mdu \tag{59}$$

$$\dot{U} = \dot{m}\sum_i Y_i \int_T c_{v,i} dT + m\sum_i \dot{Y}_i \int_T c_{v,i} dT + m\sum_i Y_i C_{v,i}\dot{T} \tag{60}$$

where c_v is the mixture specific heat at constant volume.
The injection of equation 60 in equation 6.13 enables a straightforward expression of $\dot{T}$.

$$\dot{m}\int_T c_v dT + m\sum \dot{Y}_i u_i + mc_v\dot{T} = \dot{Q} - P\dot{V} + h\dot{m}|^{in} - h\dot{m}|^{out} \tag{61}$$

$$\dot{T} = \frac{\sum m_i h_i + \dot{Q} - P\dot{V} - m\sum \dot{Y}_i u_i - \dot{m}\int_T c_v dT}{mc_v} \tag{62}$$

The species mass fraction derivatives are calculated by:

$$\dot{Y}_i = \frac{d}{dt}\left(\frac{m_i}{m}\right) = \frac{\dot{m}_i}{m} - Y_i\frac{\dot{m}}{m} \tag{63}$$

Pressure

Pressure is a state variable of the model. The perfect gas law, applied to the full flame tube control volume, is differentiated in order to get the pressure temporal derivative:

$$P = \rho r T \tag{64}$$

$$\dot{P} = \rho\left(\dot{r}T + r\dot{T}\right) + rT\sum \dot{\rho}_i \tag{65}$$

The temperature derivative $\dot{T}$ is given by equation 62, r is the gas mixture constant and $\dot{r}$ is its derivative:

$$r = \sum Y_i r_i \tag{66}$$

$$\dot{r} = \sum \dot{Y}_i r_i \tag{67}$$

where $\dot{Y}_i$ are given by equation 63.

Density and Composition

Gas densities are state variables of the model, written as it follows:

$$\rho_i = \frac{m_i}{V} \tag{68}$$

The total gas density is the sum of the gas species densities:

$$\rho = \sum \rho_i \tag{69}$$

The time derivatives of gas densities are given by:

$$\dot{\rho}_i = \frac{\dot{m}_i}{V} \tag{70}$$

$$\dot{\rho} = \sum \dot{\rho}_i \tag{71}$$

Combustion Description

A lumped two-in-one reaction, proposed by [100], is used for describing the generic oxygenated fuel oxidation:

$$\begin{aligned} &\alpha_1 \left(C_x H_y O_z + \left(x + \frac{y}{4} - \frac{z}{2} \right) O_2 \longrightarrow x CO_2 + \frac{y}{2} H_2O \right) \\ &+ (1 - \alpha_1) \left(C_x H_y O_z + \frac{x - z}{2} O_2 \longrightarrow x CO + \frac{y}{2} H_2 \right) \end{aligned} \tag{72}$$

where α_1 is defined by considering the atomic conservation of C, H and O, as:

$$\alpha_1 = \frac{\left(0.98 \left(4x + y - 2z\right) / \phi - 2(x - z)\right)}{2x + y} \tag{73}$$

$$\tag{74}$$

and where ϕ is the fuel-air equivalence ratio given by:

$$\phi = \left(\frac{Y_F}{Y_A} \right) \left(\frac{Y_A}{Y_F} \right)_{st} \tag{75}$$

Y_F and Y_A are the respective mass fractions of fuel and air, and the subscript st stands for stoichiometric. The reaction rate $\dot{\Omega}_i$ for a species i is expressed as:

$$\dot{\Omega}_i = \upsilon_i \frac{M_i}{M_F} \dot{\Omega}_F \tag{76}$$

where $\dot{\Omega}_F$ is the fuel consumption rate, M_i is the Molar weight of the species i and υ_i is its stoichiometric coefficient in the chemical reaction, equation 72. The fuel consumption rate, $\dot{\Omega}_F$, is given by:

$$\dot{\Omega}_F = \begin{cases} \eta_{comb} \dot{m}_F & \text{if } \phi \leq \phi_{max} \\ \dfrac{\phi_{max}}{\phi} \dot{m}_F & \text{if } \phi > \phi_{max} \end{cases}$$

where η_{comb} is a semi-empirical combustion efficiency ratio and ϕ_{max} is the equivalence ratio at which combustion of a given fuel can still occur.

Global Correlations for Pollutant Emissions

Some of the correlations found in literature, discussed in section 3.3, were implemented in the reference submodel and tested. In general, the pollutant Emissions Index, EI, is expressed as the mass of pollutant species in gram, per kilogram of fuel (g/kg). However, EI can also be expressed in volume parts per million (ppmv).

Carbon Monoxide

eico Rizk [104] proposed a correlation for CO emissions, which includes the PZ temperature, T_{pz}, assumed to be equal to T, the mean chamber pressure, P, and a mean evaporation characteristic time, t_{evap}, given by:

$$EI_{CO} = 0.18 \times 10^9 \exp\left(7800/T_{pz}\right)/P^2 \left(t - 0.4t_{evap}\right) \left(\Delta P/P\right)^{0.5} \tag{77}$$

NOx

einox Rgarding NO_x emissions estimations, correlations with exponential term and pressure and/or temperature dependency were included in the 1-zone model, given by:

$$EI_{NO_x} = 7.5 \times 10^{-6} \exp(8.28 \times 10^{-3} T) \quad [70] \tag{78}$$

$$EI_{NO_x} = 3.32 \times 10^{-6} \exp(0.008T) P^{0.5} \, [ppmv] \quad [71] \tag{79}$$

$$EI_{NO_x} = 32.0 \exp\left[\frac{T - 826}{194} + \frac{6.29 - 100 \times war}{53.2}\right] \left(\frac{P}{2.965 \times 10^6}\right)^{0.4} \quad [36] \tag{80}$$

In equation 80, war is the water vapour to air ratio, dedicated to wet low-NO_x technologies featuring water vapour addition to the combustion chamber. The war ratio was set to zero in the presently detailed model since peculiar technologies such as the wet low-NO_x were out of the scope of the present work. Correlations with air mass flow rate, $\dot{m}_A$, or fuel mass flow rate, $\dot{m}_f$, eventually featuring FAER, were also considered but considerably simplified due to the fact that the combustion chamber was represented by one single component. For instance, a correlation by Lefebvre[67] includes the gaseous mixture average residence time, t_{res}, expressed as $\dfrac{V}{\dot{m}_A}$ in what follows:

$$EI_{NO_x} = 9.0 \times 10^{-8} \frac{\exp(0.01 T_{st})}{\dot{m}_A T_{pz}} V P^{1.25} \tag{81}$$

Two other relations are respectively given by:

$$EI_{NO_x} = 18.1 \Phi^{0.72} \dot{m}_A^{0.3} P^{1.42} \, [ppmv] \quad [106] \tag{82}$$

$$EI_{NO_x} = 62.0 \exp(-635/T) \phi^{1.4} P^{0.5} \quad [56] \tag{83}$$

Other correlations with exponential term, P, T, and residence time t_{res}, NOx formation

time t_{form} and/or evaporation time t_{vap} were also considered:

$$EI_{NO_x} = 29.0 \exp(-21670/T) \left[1 - \exp(-250 t_{form})\right] P^{0.66} \quad [56] \tag{84}$$

$$EI_{NO_x} = 15 \times 10^{14} \left(t - 0.5 t_{vap}\right)^{0.5} \exp(71100/T_{st}) P^{-0.05} \left(\frac{\Delta P}{P}\right)^{-0.5} \quad [104] \tag{85}$$

$$\tag{86}$$

One final correlation, proposed by [75], was impemented and is given by:

$$EI_{NO_x} = B \exp\left(-\frac{21640}{T_f^{0.97}}\right) \left(\frac{V_{pz}^{0.44} P^{0.26}}{\dot{m}_A^{0.52} T_m^{0.62}}\right) \quad [75] \tag{87}$$

$$B = 58.0 T_3^{1.53} \left(\phi m_f\right)^{0.03} Ma^{0.3} P^{0.26}$$

where T_3 is the burner inlet temperature, T_f is the flame temperature, here computed as adiabatic combustion temperature, T_m is the mean mixture tempeature, which is equivalent to T, and Ma is the Mach number. That correlation obviously requires a certain level of flame tube discretisation in order to give its best level of accuracy .

Validation

The reference 0D flame tube model was subjected to a thorough validation process, in order to check the capability of the model to represent the basic aerothermal phenomena that current global flame tube models are able to represent. Validation is done for gaseous fuel

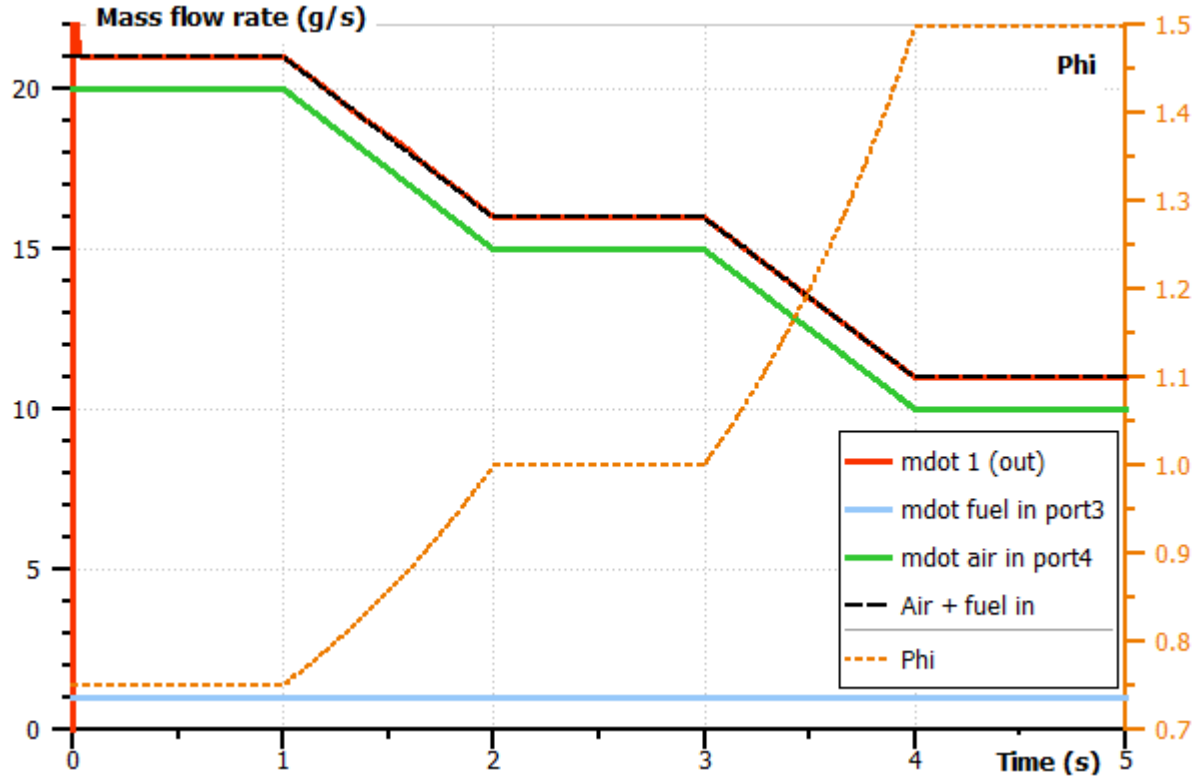

Figure 33 – Validation case - Input and output mass flow rate.

first. Several steady-state and transient scenarios were tested. Air mass flow rate is set as a variable input, as depicted in Figure 33. The air mass flow rate evolves through five one-second steps:

1. Steady at $20g/s \Rightarrow \phi = 0.749$
2. Decrease from $20g/s$ to $14.985g/s \Rightarrow \phi$ goes from 0.749 to 1.0
3. Steady at $14.985g/s \Rightarrow \phi = 1.0$
4. Decrease from $14.985g/s$ to $10g/s \Rightarrow \phi$ goes from 1.0 to 1.499
5. Steady at $10g/s \Rightarrow \phi = 1.499$

As shown in Figure 34, temperature, T, rises to around 2400K, increases in step 2 as ϕ gets closer to unit, until it reaches the maximum arround 2625K. As $\dot{m}_A$ further decreases, starting from step 4, T decreases in a nearly linear fashion until it settles to 2263K.
Starting from 101344Pa, Pressure, shown in Figure 35 continuously decreases as ϕ increases

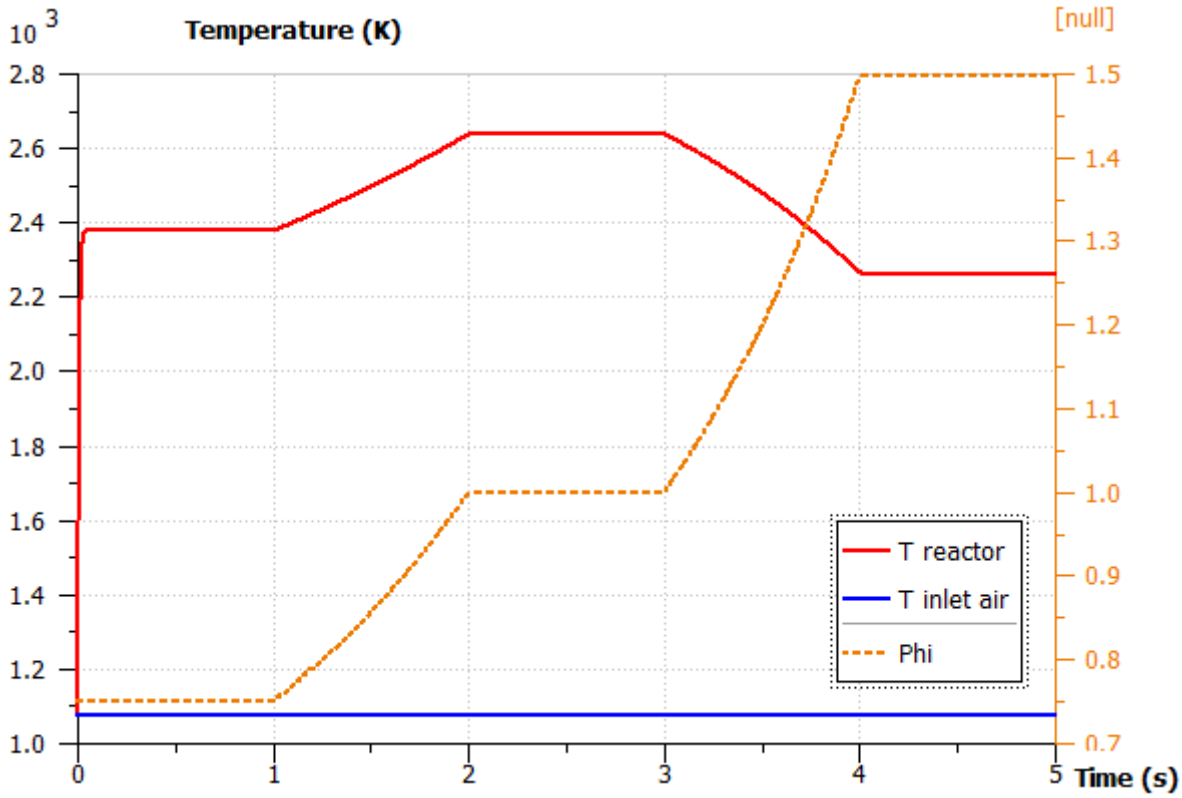

Figure 34 – Monophasic validation case - Temperature.

and at step 5, P is equal to 101334Pa. The 10Pa decrease is negligible with respect to pressure's absolute value. That pressure variation is a conjunction of air mass flow rate decrease as well as temperature rise and decrease.
The species mass fractions temporal evolution is plotted in Figure 36. From start and until the end of step 2 which ends after two seconds, excess in O_2 is observed. At stoichiometry, Y_{O_2} is null while CO_2 and H_2O mass fractions are at maximal level. At $t = 3s$, H_2 and CO traces appear. In the meanwhile, H_2O and CO_2 mass fractions diminish.

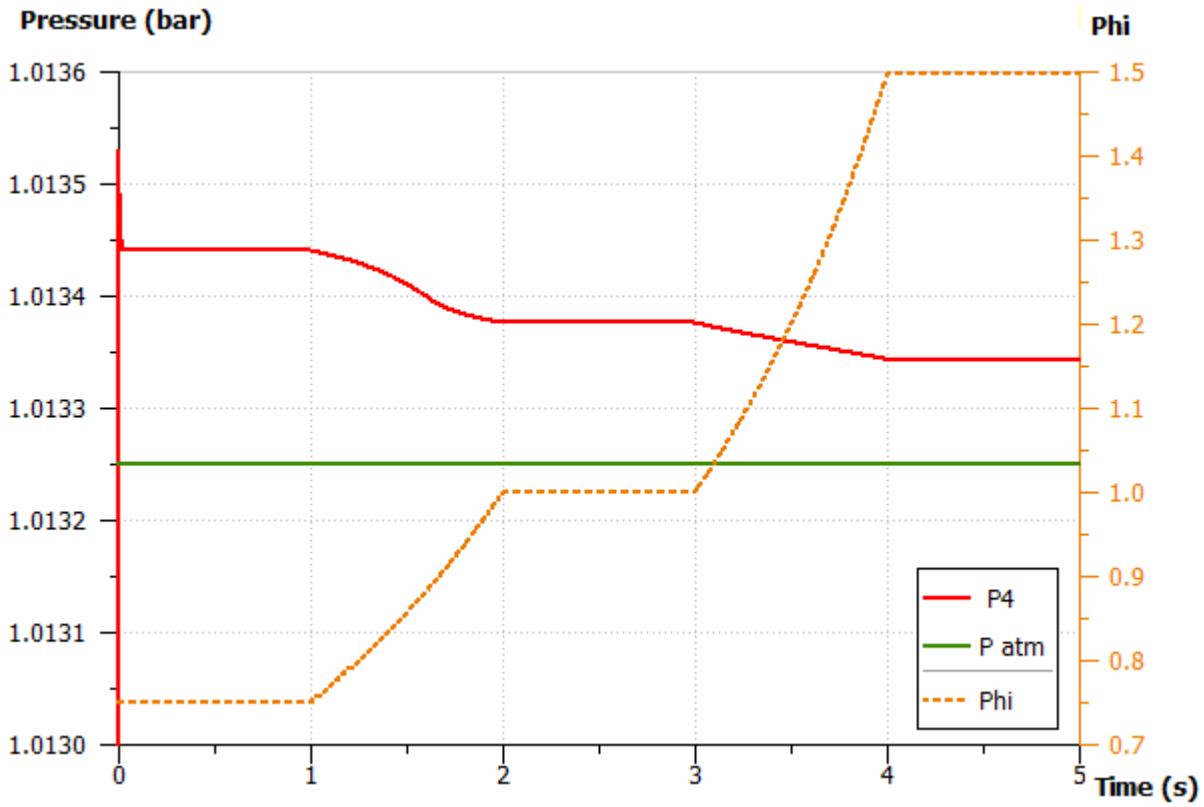

Figure 35 – Monophasic validation case - Pressure.

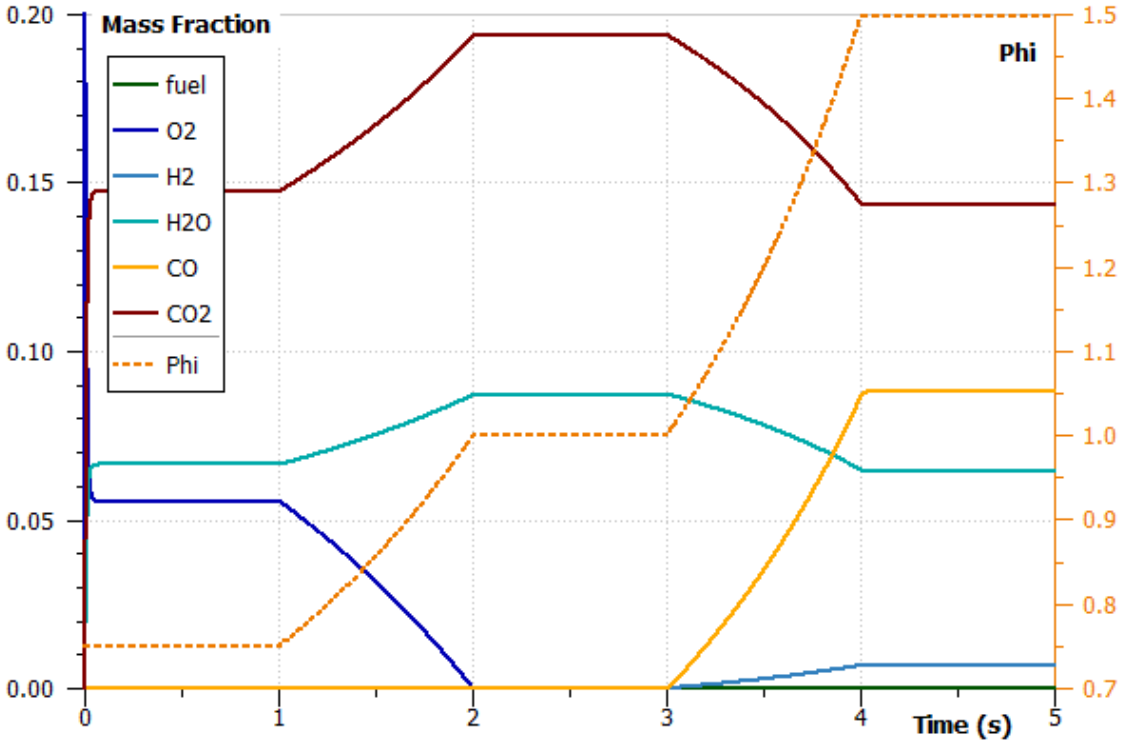

Figure 36 – Monophasic validation case - Species mass fraction.

Two-phase cases featuring constant and variable air mass flow rate were also tested. The evaporation process reduces temperature in the burner, as shown in Figure 37. Afterwards, pollutant emissions prediction was added to the burner submodel.

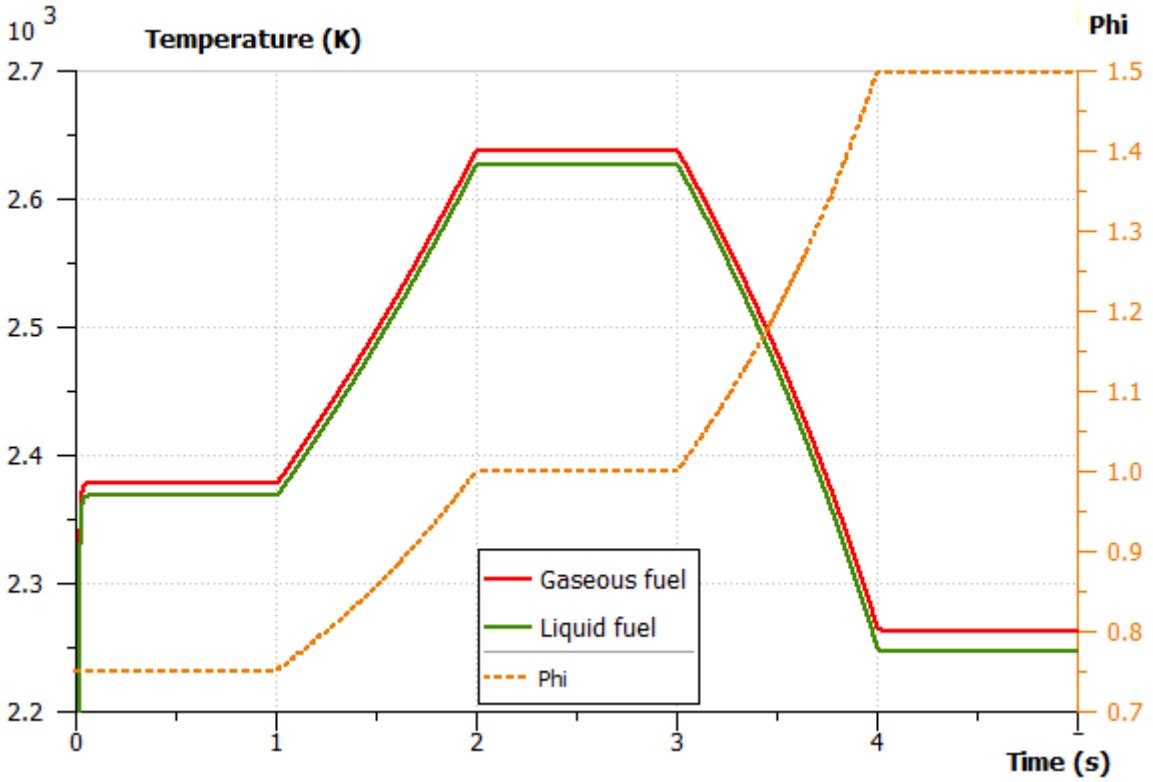

Figure 37 – Evaporation effect: when liquid fuel is injected, evaporation absorbs heat from the gaseous mixture within the burner due to the fuel latent heat of evaporation.

Temperature-dependency of the evaporation time constant has been set by the following expression:

$$\tau = 9e - 6 + \frac{1e - 4}{T} \tag{88}$$

Some of the NOx correlations were tested in the previously detailed validation case. Figure 38 presents the NOx prediction results. The absolute values generated in this test case are not relevant since no re-adaptation to experimental data was made. Nevertheless, most of these correlations follow the high-NOx route trend shown in Figure 3.7 when ϕ is close to unity.

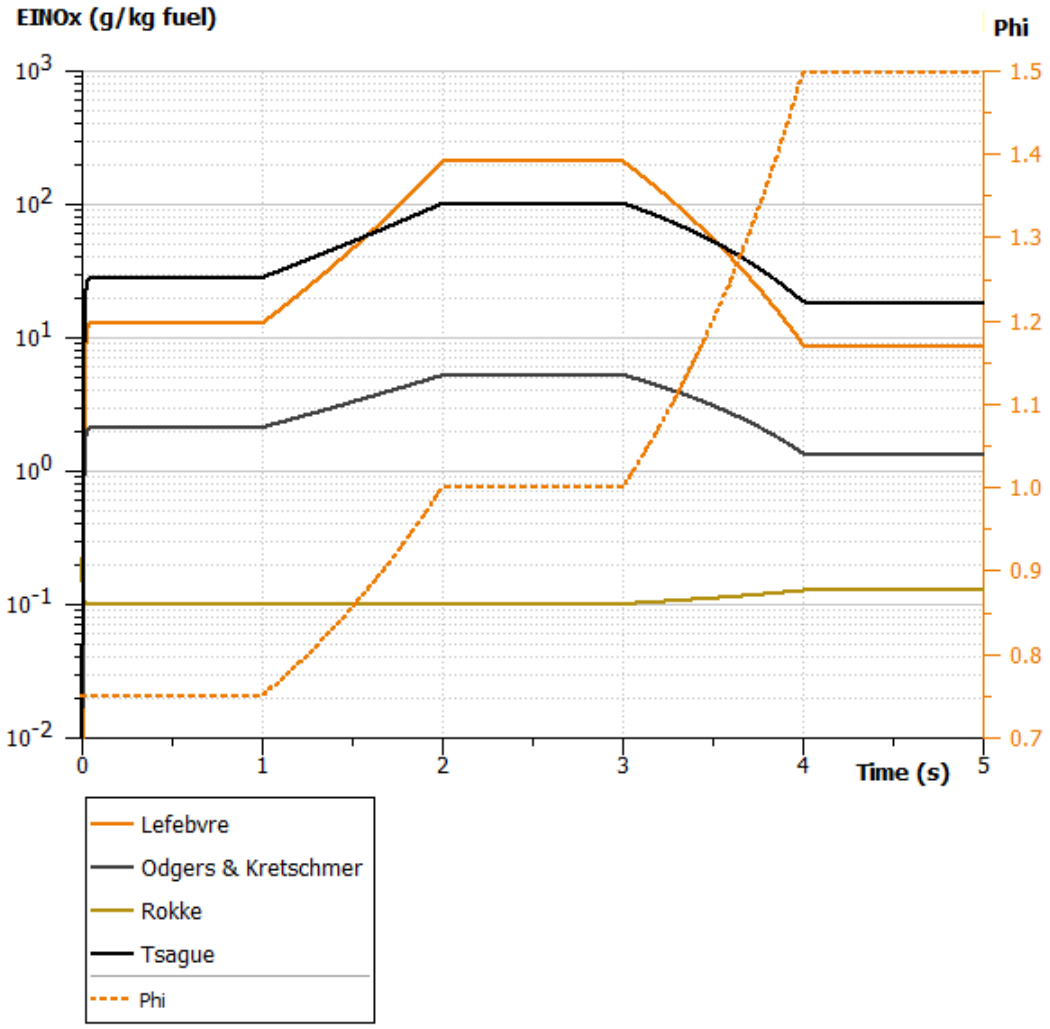

Figure 38 – Monophasic validation case - NOx emissions index.

Titre : Modélisation des turbomachines: Dérivation d'un modèle phénoménologique de combustion pour la simulation de transitoires sur hélicoptères

Mots clefs : Turbines à gaz, combustion, simulation système, CFD.

Résumé : Ce travail propose l'investigation d'une approche physique 0D/1D modélisant les brûleurs de turbines à gaz, prenant en compte l'évaporation du carburant, la turbulence, la combustion, et permet la représentation de zones de dilution et l'implémentation de modèles de chimie des polluants. Il s'agit de sous-modèles répartis dans des composants assemblables dans un environnement numérique multi-domaines basé sur le formalisme de Bond Graph. Ceci permet, par exemple, l'assemblage de plusieurs volumes ouverts en un tube à flamme, l'ajout d'un compresseur et d'une turbine, ou bien aussi d'intégrer des chaînes de commande afin de représenter un hélicoptère complet. L'originalité de cette thèse réside dans l'application d'un paradigme de combustion 0D, issu d'une approche 3D élaborée chez IFP Energies nouvelles et appliquée avec succès aux moteurs alternatifs ainsi qu'à des turbines à gaz. Le sous-modèle intègre le formalisme de flamme cohérente qui distingue une zone de gaz frais d'une zone de gaz brûlés. Les deux zones sont séparées par une flamme turbulente. Le sous-modèle de tube à flamme décrit la flamme grâce à une synthèse issue de résultats de calculs CFD 3D validés par des expériences. En effet, des résultats de calculs LES d'un brûleur expérimental monophasique ont étés analysés pour caractériser la combustion turbulente prémélangée dans un brûleur à tourbilloneur. Enfin, un secteur de brûleur réel de turbomoteur a été étudié à l'aide de simulations CFD afin d'évaluer la pertinence du modèle de tube à flamme 0D/1D et de guider la modélisation permettant de compléter la nouvelle approche de simulation système des turbines à gaz.

Title : Gas Turbine Modelling: Phenomenological Combustion Model Derivation for Rotorcraft Transient Operation

Keywords : Gas turbines, combustion, system simulation, CFD.

Abstract : This work investigates a unique 0D/1D physical approach for gas turbine combustor modelling. It accounts for fuel evaporation, turbulence, combustion, and allows to represent dilution stages. Detailed pollutants formation models can also be added. The chosen formalism, based on the Bond Graph theory approach, allows to describe systems organised in a series of submodel components such as a series of open volumes forming a flame tube, or a combustor coupled to a compressor and turbine but they can also be combined with control and regulation devices in order to represent a complete rotorcraft. The essence of the PhD strategy is the application of a 0D combustion paradigm, obtained at IFP Energies nouvelles by formal reduction of 3D approaches for gas turbines. More in details, a new combustion model was developed integrating the Coherent Flame Model (CFM) formalism which allows to distinguish between fresh gases and burned gases separating them with a turbulent flame. The flame tube submodel features a physical description of the flame thanks to thorough understanding given by 3D CFD simulation results validated against experimental measurements. More specifically, LES results corresponding to a single phase test rig were analysed in order to characterise premixed turbulent combustion in a swirl burner. Finally, a real turboshaft combustor sector case was studied by means of CFD simulations to investigate the relevance of the 0D/1D flame tube model and to determine modelling strategies for the completion of the new gas turbine system simulation approach.

Université Paris-Saclay
Espace Technologique / Immeuble Discovery
Route de l'Orme aux Merisiers RD 128 / 91190 Saint-Aubin, France